國立臺灣大學理學院大氣科學所

博士論文

Department of Atmospheric Sciences
College of Science
National Taiwan University
Doctoral Dissertation

利用衛星測高觀測西北太平洋的上層海洋溫度結構

Upper Ocean Thermal Structure in the Western North Pacific from Satellite Altimetry

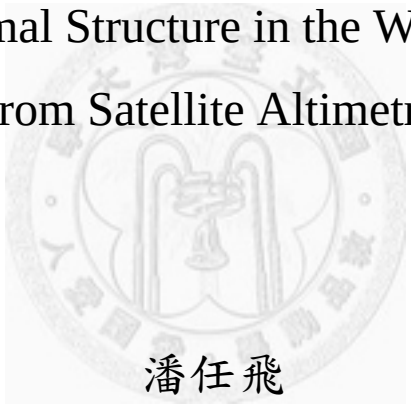

潘任飛

IamFei Pun

指導教授：林依依 博士

Advisor: I-I Lin, Ph.D.

中華民國 101 年 7 月

July 2012

致謝

首先，我衷心感謝我的指導老師林依依博士悉心的栽培與教導，把我從大學畢業的小伙子培育成博士的一員；雖然過程很漫長，一路走來當中有苦也有樂，但依依老師總是懷著一顆熱誠和樂觀的心來帶領我走在正確的道路上。在這裡我沒有華麗話語，只有真誠的感謝：依依，謝謝您！

另外，我要感謝我父母親的耐心教導與無私的支持。爸爸媽媽，我成功了！當然我要感謝我勞苦功高的太太在我背後默默的支持與體諒，她打點日常生活的一切和照顧好我們兩個可愛的小孩，讓我可以安心去做研究。老婆，I love you!! 我也要感謝我兩個摯愛的妹妹給我信心與祝福。

同時，我要感謝六位口試委員的建議，使這份論文至臻完善。我亦要謝謝遙測實驗室的各位對我的幫助與體諒，並維持了一個良好、舒適和融洽的學習環境，使大家可以互相學習和專心研究。在這裡我要特別感謝實驗室的大師姐瑪格對我的照顧與幫忙，減輕我不少的煩惱。

最後，謹以此文獻給我身邊所有最愛的朋友。在人生的路上總會有很多的挑戰與考驗，而博士畢業並不是代表結束，而是人生新一章的開始，在未來還有很多挑戰等著我，有您們的支持我定能一一克服所有我挑戰攀上成功的山峰！

摘要

近年來有很多研究指出颱風的強度變化是跟上層海洋(0-200m)的溫度結構有密切的關系。但是要在大洋中取得上層海洋溫度結構的資訊是非常困難的，傳統上只可以透過實測的方法。而傳統實測資料的時空分佈並不足以代表整個大洋的變化，對颱風強度的研究與預報造成相當大的阻礙。因此，本研究利用先進的衛星測高技術去估計西北太平洋的上層海洋溫度結構，目的是要去彌補海洋觀測資料的不足。

首先，本研究利用測高衛星的海水面高度資料透過簡單的兩層海洋模式去計算上層海洋的溫度結構，並利用這些資料去研究西北太平洋的超級颱風 Dianmu (2004)的強度變化。發現 Dianmu 的強度變化對海表面溫度冷卻(SST cooling)和動態上層海洋熱容量(dynamic UOHC)最敏感。在 2010 年臺灣美國合作的 ITOP 實驗期間，我們就利用這個兩層海洋模式透過衛星的測高資料去提供每天西北太平洋上層海洋溫度結構的資訊，對整個實驗有相當大的幫助。

由於兩層模式相對簡單，而且並不適用在整個西北太平洋上。所以本研究利用>38,000 個 Argo 實測的海洋溫度剖面去建立西北太平洋的線性回歸方法(REGWNP)，目的是要去改進衛星對上層海洋溫度結構的估計。之後，再利用>7,000 個獨立的 Argo 剖面去驗證 REGWNP 的估計。驗證的結果顯示 REGWNP 可以準確地估計西北太平洋的上層海洋溫度結構。在颱風季節，由 REGWNP 估計出來的 20°C 等溫線深度(D20)的誤差為 30m、26°C 等溫線深度(D26)的誤差為 20m、UOHC 的誤差為 20 kJ cm^{-2}、上層 100m 平均溫度(T100)的誤差為 1.5°C。另外也發現用 REGWNP 對比用傳統兩層模式估計出來的上層海洋溫度結構有顯著的改進；同時也非常接近用完整海洋模式計算出來的結果。

最後，研究過去西北太平洋颱風增強區域的海洋條件變化，發現從 1993 年到 2010 年之間，海洋暖渦(warm eddy)增加，冷渦(cold eddy)減少。水下溫度變化方面，在過去 18 年之間 D20、D26 和 UOHC 增加了 9-17%，而 T100 增加了 0.16-0.35°C。另外，正海水面異常(SSHA ≧ 10 cm)區域增加，負海水面異常(SSHA ≦ -10 cm)區域減少。這個結果顯示西北太平的海洋條件變得越來越有利颱風的增強作用。

關鍵詞：衛星測高、上層海洋溫度結構、颱風、海洋渦旋、海洋特徵。

Abstract

This thesis firstly demonstrates the importance of satellite-derived upper ocean thermal structure (UOTS) in typhoon research. Using a simple two-layer model, UOTS can be roughly derived from satellite altimetry and the intensity change of the Supertyphoon Dianmu (2004) is investigated. It is found that Dianmu's intensity is very sensitive to the during typhoon SST cooling and upper ocean heat content (UOHC). During 2010, UOTS was estimated on a daily basis from satellites for the use in the large international field experiment, Impact of Typhoons on the Ocean in the Pacific (ITOP), showing the advantage of satellite-derived UOTS in typhoon-ocean research.

Secondly, using >38,000 Argo temperature profiles, a linear regression method for the western North Pacific (i.e., REGWNP) is developed. Then, >7,000 *in situ* profiles are used to assess accuracy of REGWNP-derived UOTS. The results show that REGWNP is able to produce rather reliable UOTS. During the typhoon season, the rms difference for the depth of 20°C isotherm (D20), depth of 26°C isotherm (D26), UOHC and averaged temperature of the upper 100 m (T100) is less than 30 m, 20 m, 20 kJ cm^{-2}, and 1.5°C, respectively. Also, it is found that REGWNP outperforms the traditional two-layer approach and is comparable to a sophisticated full ocean model for producing real-time UOTS field.

Finally, based on the sea surface height anomaly (SSHA) record between 1993 and 2010, the long-term changes in ocean conditions in the western North Pacific main typhoon intensification region are investigated. It is found that the activity of warm eddies enhanced while cold eddies weakened. In terms of subsurface variability, D20, D26 and UOHC increased by 9-17%, meanwhile, T100 warmed by 0.16-0.35°C over the 18 years period. Furthermore, it is also found that the total area of positive SSHA ($\geqq$ 10 cm) features substantially increased while negative SSHA ($\leqq$ -10 cm) features deceased. These results suggest that the western North Pacific ocean conditions are becoming more favorable to typhoon intensification.

Keyword: satellite altimetry, upper ocean thermal structure, typhoon, ocean eddy, ocean feature.

Table of Contents

致謝……i
摘要……ii
Abstract……iii
Chapter 1 Introduction 1
1.1 Background and motivation 1
1.1.1 Importance of upper ocean thermal structure 1
1.1.2 Importance of ocean features 3
1.1.3 Estimation of upper ocean thermal structure 5
1.1.4 Ocean conditions in the western North Pacific 7
1.2 Objectives of the study 8
Chapter 2 Review of the two-layer reduced gravity model and its applications to typhoon research 11
2.1 Two-layer reduced gravity approach for the western North Pacific Ocean 11
2.2 Intensity change of Supertyphoon Dianmu (2004) 12
2.3 Implementation of the 2-layer in the ITOP experiment in 2010 17
Chapter 3 Linear regression technique 20
3.1 Data 20
3.1.1 In situ Argo temperature profiles 20
3.1.2 Merged and gridded satellite altimetry SSHA data 21
3.1.3 Satellite microwave SST data 23
3.2 Hydrographic characteristics in the western North Pacific Ocean 24
3.3 Relationship between SSHA and depth variation of isotherms 26
3.4 Linear regression technique 29
3.4.1 Procedure of developing regressions 30
3.4.2 The spatial pattern of the regressions 31
3.4.3 Treatment for mixed layer 33
3.5 Summary 34
Chapter 4 Validation of regression-derived altimetry-based upper ocean thermal structure in the western North Pacific Ocean 36
4.1 Validation 36
4.1.1 Validation for D20 37
4.1.2 Validation for D26 (i.e. warm water thickness) 38
4.1.3 Validation for UOHC and T100 39
4.1.4 Applicability of regression-derived D20, D26, UOHC and T100 for typhoon research 40
4.2 Comparison with the 2-layer, EASNFS full ocean model and AXBT data from ITOP field

experiment (2010) 41
4.2.1 Comparison with the 2-layer 41
4.2.2 Inter-comparison with EASNFS full ocean model and AXBT data from ITOP experiment 43
4.3 Accuracy in other isotherm depths 45
4.4 Summary 46
Chapter 5 Eddy identification and variability in the South Eddy Zone of the western North Pacific Ocean 48
5.1 Overview of existing eddy identification techniques 48
5.2 Satellite altimetry data 50
5.3 Automated eddy identification procedure 51
5.3.1 Contour lines of SSHA 51
5.3.2 Criteria for the eddy identification procedure 52
5.4 Results of eddy variability in the SEZ 55
5.4.1 Eddy number 55
5.4.2 Eddy amplitude 58
5.4.3 Eddy size 59
5.5 Discussion 61
5.5.1 Issue of the eddy identification method 61
5.5.2 Comparison with the results obtained using another eddy identification procedure 62
5.5.3 Issue of eddy variability and typhoon intensification in the SEZ 64
5.6 Summary 66
Chapter 6 Changes in ocean conditions in the western North Pacific typhoon intensification region 68
6.1 Typhoon intensification zone of the western North Pacific Ocean 68
6.2 Methodology and Data 69
6.3 Results 70
6.3.1 Variability in SST and SSHA 70
6.3.2 Variability in UOTS 71
6.3.3 Variability in ocean features 72
6.4 Discussion 73
6.4.1 Issue on satellite-estimated UOTS trends 73
6.4.2 Issue on the study domain 75
6.4.3 Issue on SSHA gridded data 76
6.5 Summary 77
Chapter 7 Conclusion and future work 78
References… 83

List of Tables

Table 1.1: Saffir-Simpson tropical cyclone scale based on 1-min maximum sustained wind speeds…. 94
Table 3.1: Additional quality control for Argo profiles. [1] WMO: World Meteorological Organization. 95
Table 3.2: Orbit parameters for T/P series and ERS series missions. 95
Table 3.3: The past and current altimetry missions used by AVISO to produce merged SSHA products. 96
Table 3.4: Correction applied to AVISO SSHA products. 96
Table 4.1: Root-mean-square error (°C) of T100 from EASNFS, 2-layer and REGWNP as compared with AXBTs on August 28, August 31 and September 1, 2010. 97
Table 4.2: Root-mean-square error (°C) of T100 from EASNFS, 2-layer and REGWNP as compared with Argos on August 28, August 31 and September 1, 2010. 97
Table 5.1: The number of warm (cold) eddies identified in each monthly SSHA contour map during May to October from 1993 to 2010. The months in which cold eddies outnumbered warm eddies are highlighted with bold text. 98
Table 5.2: Trends and changes in the numbers, amplitudes and radii of warm and cold eddies in the SEZ from 1993 to 2010. The trends are based on least squares fitting and the significance level is based on the t-test. 99
Table 5.3: Parameters used in the two-layer reduced gravity model, i.e., equations (2.1) and (2.2), for calculating D26 and associated UOHC. Each value is a seasonal (May-October) average of the SEZ mean. 99
Table 6.1: Linear trends and changes in D26, D20, UOHC and T100 in the SEZ over 1993-2010. The trends are based on least squares fitting and the significance level is based on the t-test. 100
Table 6.2: Linear trends and changes in D26, D20, UOHC and T100 in the Gyre over 1993-2010. The trends are based on least squares fitting and the significance level is based on the t-test. 100
Table 6.3: Linear trends and changes in the percentage of total area of warm, no and cold features in the SEZ over 1993-2010. The unit is %. The trends are based on least squares fitting and the significance level is based on the t-test. 101
Table 6.4: Linear trends and changes in the percentage of total area of warm, no and cold features in the Gyre over 1993-2010. The unit is %. The trends are based on least squares fitting and the significance level is based on the t-test. 101
Table 6.5: Comparison of recent estimates of heat content in the upper ocean. Heat storage is per unit area of ocean surface. 102

List of Figures

Figure 1.1: Average errors of tropical cyclone forecast in (a) track for the period 1989-2011 and (b) intensity for the period 1990-2011 for the Atlantic basin. [Courtesy of NOAA/National Hurricane Center (NHC), http://www.nhc.noaa.gov/verification/verify5.shtml]..... 103

Figure 1.2: A comparison of the thicknesses of the warm water layer (> 26°C) between (a) the climatology for September from the World Ocean Atlas 2001 (WOA01, Stephens et al. 2002), and (b) the satellite estimation on 24 September 2010 from the two-layer model (Pun et al. 2007)..... 104

Figure 1.3: (a) Relative geostrophic currents superimposed on an SSHA map from August 20, 2008. One can see that there are two distinct warm and cold eddies east of Taiwan. The warm eddy is associated with positive SSHA and anticyclonic flow, whereas the cold eddy is associated with negative SSHA and cyclonic flow. (b) A comparison of an *in situ* depth-temperature profile-1 of August 16, 2008 from Argo float and a profile of August from the World Ocean Atlas 2001 (WOA01, Stephens et al. 2002). The two profiles are depicted by blue and black curves, respectively. (c) the same as in (b), but the red curve depicts the Argo profile-2 of August 20, 2008. The locations of the profiles are indicated by yellow triangles in (a). 105

Figure 1.4: (a) 3-day averaged SST from 4-6 September 2003 from Tropical Rainfall Measuring Mission/Microwave Imager (TRMM/TMI). (b) Composite of SSHA measurements from TOPEX/Poseidon and Jason-1 for one 10-day cycle between 27 August and 5 September 2003. Their ground tracks are shown in light grey lines. The southern and northern eddy zones are indicated by green boxes..... 106

Figure 2.1: The schematic of satellite-derived upper ocean temperature profiles (i.e., UOTS) consisting of SST, MLD (mixed-layer depth), D26 (the depth of the 26°C isotherm, above which the water is regarded as warm), and D20 (the depth of the 20°C isotherm).107

Figure 2.2: (a) Composite of TOPEX/Poseidon and Jason-1 altimetry measurements for one cycle (10 days) between 5 and 14 Jun 2004 showing the pre-Dianmu SSHA. (b) △D26 (2-layer-derived D26 minus climatological D26), (c) 2-layer-derived D26, and (d) UOHC estimated from the 2-layer-derived profiles. Green stars and black triangle depict the *in situ* profiles found before and during the Dianmu's passage. Typhoon's intensity in Saffir-Simpson scale is shown in the legend of (a)..... 108

Figure 2.3: (a) Initial profiles along Dianmu's track used in the mixed-layer model experiment where *in situ* profiles are depicted in black, profiles along Dianmu's intensification location in red, along Dianmu's intensity maintenance location in green, along Dianmu's intensity decay location in blue. 109

Figure 2.4: The relationship between 5 parameters (self-induced SST cooling, dynamic UOHC, pre-typhoon SST, pre-typhoon UOHC and vertical wind shear) and typhoon's intensity.110

Figure 2.5: Composite of SST from the TMI and AMSR-E passes in (a) 13 Jun 2004 for

Pre-Dianmu and in (b) 18 Jun 2004 for after-Dianmu's passage..... 111
Figure 2.6: The 6 h intensity change of Dianmu with the 5 parameters, i.e., (a) self-induced SST cooling, (b) dynamic UOHC, (c) pre-typhoon SST, (d) pre-typhoon UOHC, and (e) vertical wind shear. 112
Figure 2.7: Operational daily two-dimensional maps of (a) SST, (b) SSHA, (c) D26, (d) UOHC, and (e) T100 on 24 September 2010. On the maps, color-coded triangles represent Argos searched within 2 days period; color-coded asterisks in (c) and (e) represent mooring measurements; black dots represent drifters and floats; and black curve with color-coded dots represents typhoon Malakas (2010)' track and intensity from the JTWC..... 113
Figure 2.8: Comparison of Argo float (black) and satellite-derived (red) temperature profiles. See Figure 2.7 for the profile's location (Profile 25)..... 114
Figure 2.9: Operational products of along the typhoon Malakas (2010) track: (a) UOTS, (b) SST, (c) SSHA, (d) D26, (e) UOHC, and (f) T100 on 24 September 2010 during the ITOP experiment. 115
Figure 3.1: The locations of Argo profiles in the western North Pacific used to establish the linear regressions of SSHA onto displacement of subsurface isotherms. Red dots depict a total of 38,556 profiles collected from May to October of 2000-2008. Four hydrographic zones, i.e., the Gyre, SEZ, IEZ and NEZ, are indicated. 116
Figure 3.2: 10-day ground tracks of TOPEX/Poseidon (red) and Jason-1 (blue) in the western North Pacific. 117
Figure 3.3: Schematic of current systems and associated eddy fields in the western North Pacific. Red and blue rings depict anti-cyclonically circulated warm eddies and cyclonically circulated cold eddies, respectively. The latitudinal band of the Gyre, SEZ, IEZ and NEZ are denoted. The current systems refer mainly to Qiu (2001). 118
Figure 3.4: All of the Argo profiles (grey curves) in September from 2000 to 2008 in (a) the Gyre, (b) the SEZ, (c) the IEZ and (d) the NEZ. The blue curves depict the mean profiles and the blue dots depict the mean depths of isotherms from D28 to D4. The arrows depict the base of thermocline, which is located at D10 in Gyre, D6 in SEZ and D7 in IEZ and NEZ..... 119
Figure 3.5: The monthly correlation coefficients between SSHA and displacements of the isotherms from 26°C to 4°C in (a) the Gyre, (b) the SEZ, (c) the IEZ and (d) the NEZ. The color code for each curves are shown in (a). The dashed line depicts the correlation of 0.6. Grey area masks the isotherms which are below the base of the thermocline..... 120
Figure 3.6: the schematic demonstrates the meaning of SSHA for the Gyre, SEZ, IEZ and NEZ. The profile of each zone is the mean profile averaged from 2000-2008 during May-October. The isotherms of which the variation can be described by SSHA are colored, whereas the correlation with SSHA is <0.6 are masked with grey, representing that they cannot be expressed by SSHA effectively, and the isotherms below the base of the thermocline are

masked in black. Generally, SSHA can reflect the variation in D26-D12 in the Gyre, D26-D6 in the SEZ, D18-D7 in the IEZ and NEZ. 121
Figure 3.7: Comparison of the near real-time (daily) and delay time (7-day) SSHA, which paired with Argo profiles in 2009 /May-October in (a) the Gyre, (b) the SEZ, (c) the IEZ and (d) the NEZ. 122
Figure 3.8: (a) and (b) show the slope and offset, respectively, in the eqn. (3.2) for D20 in September. (c) the corresponding correlation coefficient between the variation of D20 and SSHA, and (d) the number of profiles used to calculate the regressions. Grey areas in (a)-(c) represent the significance level that is less than 99%..... 123
Figure 3.9: (a) The correlation cross section from the equator to 40°N along 145°E in September from D26 down to D4. (b) Same as in (a), but for the slope. In (b), the slope less than 99% significance is marked in grey. 124
Figure 3.10: Comparison between the profiles from REGWNP (green), 2-layer (red) and Argo (black). The legend is also shown on the lower left plot. From the upper to lower rows represent the profiles from the NEZ, IEZ, SEZ and Gyre. Each zone has four demo profiles randomly picked in September of 2010. Profile from 2-layer is unavailable on the upper right plot. The horizontal and vertical dashed lines depict 26°C and the depth of 100 m, respectively. 125
Figure 4.1: The locations of Argo profiles used to validate REGWNP derived UOTS. Blue dots depict a total of 7,036 profiles collected from May to October of 2009 and 2010. Four validation zones, i.e., the Gyre, SEZ, IEZ and NEZ, are indicated. 126
Figure 4.2: Monthly scatter plots of D20 derived from REGWNP and Argo floats in the Gyre (upper-left section), SEZ (lower-left section), IEZ (upper-right section), and NEZ (lower-right section) during 2009-2010. The matching pairs are colored according to their corresponding SSHA values. 127
Figure 4.3: (a) Monthly RMSD, (b) error percentage, and (c) bias for REGWNP derived D20. The color code for each zone is shown in (a). 128
Figure 4.4: Monthly scatter plots of D26 derived from REGWNP and Argo floats in the Gyre (upper-left section), SEZ (lower-left section), IEZ (upper-right section), and NEZ (lower-right section) during 2009-2010. The matching pairs are colored according to their corresponding SSHA values. 129
Figure 4.5: (a) Monthly RMSD, (b) error percentage, and (c) bias for REGWNP derived D26. The color code for each zone is shown in (a). 130
Figure 4.6: Monthly scatter plots of UOHC derived from REGWNP and Argo floats in the Gyre (upper-left section), SEZ (lower-left section), IEZ (upper-right section), and NEZ (lower-right section) during 2009-2010. The matching pairs are colored according to their corresponding SSHA values. 131
Figure 4.7: (a) Monthly RMSD, (b) error percentage, and (c) bias for REGWNP derived UOHC.

The color code for each zone is shown in (a). 132
Figure 4.8: Monthly scatter plots of T100 derived from REGWNP and Argo floats in the Gyre (upper-left section), SEZ (lower-left section), IEZ (upper-right section), and NEZ (lower-right section) during 2009-2010. The matching pairs are colored according to their corresponding SSHA values. 133
Figure 4.9: (a) Monthly RMSD, (b) error percentage, and (c) bias for REGWNP derived T100. The color code for each zone is shown in (a). 134
Figure 4.10: Applicability chart for REGWNP derived D20, D26, UOHC and T100 for typhoon applications. From upper to lower rows are the NEZ, IEZ, SEZ and Gyre, respectively. The number in the pie charts represent the months from May to October. The applicability threshold for D20, D26 and UOHC is an error of 50%, for T100 is 2.5°C.135
Figure 4.11: The percentage of improvement on REGWNP with respect to 2-layer for D20, D26, UOHC and T100 in the four different zones, i.e., the Gyre, SEZ, IEZ and NEZ. A positive value represents that REGWNP is better than 2-alyer, and vice versa. Note that the scale of D20 improvement in the NEZ is different from the other three zones. 136
Figure 4.12: The maps of D20, D26, UOHC and T100 on 25 September 2010, derived from 2-layer (the first column), REGWNP (the second column) and REGWNP minus 2-layer (the third column). The color bars for the maps from 2-layer and REGWNP are the same and shown in the second column. The corresponding Argo profiles are superimposed on the maps and depicted by colored triangles according to the same color scheme. 137
Figure 4.13: *In situ* measurements during ITOP field experiment on August 28 (red), August 31 (green) and September 1 (blue), 2010. Circles represent the AXBTs deployed by US C130 aircraft, and triangles represent the Argo floats. 138
Figure 4.14: Inter-comparison of T100 from EASNFS, 2-layer and REGWNP with the AXBTs (red) and Argo floats (blue) on August 28 (first row), August 31 (second row), and September 1 (third row), 2010. The left column compares observations with EASNFS; the middle column compares with 2-layer; the right column compares with REGWNP. The RMS errors are shown in each plot. 139
Figure 4.15: May-October averaged (a) RMSD and (b) correlation of REGWNP estimated D26 to the isotherm at the base of the thermocline with respect to Argo *in situ* observations. Curves in green, blue, orange and red represents the Gyre, SEZ, IEZ and NEZ, respectively. The horizontal bars depict one standard deviation. 140
Figure 5.1: (a) The standard deviation of SSHA in the western North Pacific Ocean from October 14, 1992 to October 28, 2009, in which the red and blue boxes depict the SEZ and NEZ regions, respectively. (b) The corresponding SSHA field on September 3, 2003; the green boxes depict the SEZ and NEZ. 141
Figure 5.2: SSHA contour maps from September 2003. (a)-(d) Original weekly SSHA maps. (e) A monthly average SSHA map obtained by combining four weekly SSHA maps. The solid

and dashed contour lines depict positive and negative SSHAs, respectively; the contour interval is 2cm. 142
Figure 5.3: Five scenarios of eddy identification in the SEZ. The red contours indicate the eddies identified using the procedure. The green lines in (e) represent the boundary of the SEZ. The scenarios are explained in detail in the context. 143
Figure 5.4: Flow chart of the eddy identification procedure. The details of the procedure are described in the context. 144
Figure 5.5: Positive SSHA contour map from August 2004. The red contours indicate the eddies identified in the SEZ. Each circle depicts the size of the eddy; it is an estimation of the area enclosed by the 10 cm contour of the eddy. 13 warm eddies are identified on the map. 145
Figure 5.6: Histogram of the total numbers of warm (red bars) and cold (blue bars) eddies identified in the SEZ from May to October, 1993 to 2010. 146
Figure 5.7: Histogram of the monthly average numbers of warm (red bars) and cold (blue bars) eddies identified in the SEZ from May to October, averaged over 1993-2010. 147
Figure 5.8: Monthly average numbers of warm (red) and cold (blue) eddies from 1993 to 2010. The red and blue lines depict the trends of warm and cold eddies, respectively, calculated by the least square fitting. The rate enclosed by the dashed box indicates the trend is less than 95% significance. Otherwise, the trend shown is at 95% significance level. 148
Figure 5.9: The year-to-year changes in the numbers of warm and cold eddies from 1993 to 2010….. 149
Figure 5.10: Time series of the monthly average numbers of warm (red) and cold (blue) eddies from May (a) to October (f). The dashed lines depict the linear trends observed in the series. 150
Figure 5.11: The same as in Figure 5.7; the maximum and minimum numbers of eddies during each season are superimposed on the time series of the monthly average numbers of (a) warm and (b) cold eddies. The solid and dashed lines depict the trends in the maximum and minimum numbers of eddies during each season, respectively. The rate enclosed by the dashed box indicates the trend is less than 95% significant. Otherwise, the trend shown is at 95% significance level. 151
Figure 5.12: Monthly average amplitudes of warm (red) and cold (blue) eddies from 1993 to 2010. The red and blue lines depict the trends of warm and cold eddies, respectively, calculated by the least square fitting. Both trends are at 95% significance level. 152
Figure 5.13: The same as in Figure 5.7 with the eddies separated into three groups. (a) Eddies with amplitudes > 30cm; (b) eddies with amplitudes between 20 and 30cm; and (c) eddies with amplitudes < 20cm. 153
Figure 5.14: (a) The relationship between the contour area and SSHA for all eddies identified in August 1995. The solid dots depict the real contours recognized by the procedure, and the open dots depict the extrapolated values. (b) The scatter plots of the numbered

contours (from innermost to outermost) and their areas for each eddy identified in August from 1993 to 2007. 154
Figure 5.15: Monthly average radii of warm (red) and cold (blue) eddies from 1993 to 2010. The red and blue lines depict the trends of warm and cold eddies, respectively, calculated by the least square fitting. Both trends are at 95% significance level. 155
Figure 5.16: SSHA map of August 25, 2004. The yellow and purple dots depict the warm and cold eddies identified by Chelton et al. (2011). The green box is the region of the SEZ. The features labeled with "A" and "B" are discussed in the context. 156
Figure 5.17: A comparison between the time series of the number of eddies identified by Chelton et al. (2011) and that identified in the present study. Warm and cold eddies are depicted by red and blue curves, respectively. The dashed curves are the time series from Chelton et al. (2011), and the solid curves are from the present study. 157
Figure 5.18: (a) Time series of the monthly average D26 of warm (red curve and left-axis) and cold (blue curve and right-axis) eddies. (b) The same as in (a), but for UOHC. It should be noted that the intervals for left and right axes are the same. The dashed lines depict the trends observed in the series. 158
Figure 5.19: 18 years of typhoons with intensity $\geqq$64 knots (i.e., Category 1) occurring in the western North Pacific during May to October from 1993 to 2010. The best track data are from JTWC, and the green box depicts the region of the SEZ. 159
Figure 5.20: SSHA maps from (a) September 2000 and (b) September 2003 160
Figure 6.1: Geographical distribution of typhoon intensification in the western North Pacific Ocean. The map is calculated from the JTWC's 6-hour best track data from 1970-2008. Only the intensification segment (the first point of category 1 to peak) of the typhoon track is considered. The black box depicts the main typhoon intensification region, defined as 122-170°E, 10-26°N. 161
Figure 6.2: SSHA map from September 8, 2010 obtained from AVISO's DT Reference Series. The geographical locations of two sub-regions: Southern Eddy Zone (SEZ; 122-170°E, 19-26°N) and Gyre (122-170°E, 10-19°N) are depicted. The SSHA over +/-10 cm are shaded. The interval of the contour is 2 cm. 162
Figure 6.3: Time series of regional mean SST and SSHA. (a) Annual (June-October) regional mean SST for the SEZ (red dots) and Gyre (blue dots) between 1993 and 2010. The dashed lines are the linear trends calculated by the least squares fitting. The linear trend for the SEZ mean SST and Gyre mean SST are 0.004 and 0.01 °C yr^{-1}, respectively. (b) Same as (a), except for the SSHA. The linear trend for the SEZ mean SSHA and Gyre mean SSHA are 0.30 and 0.77 cm yr^{-1}, respectively. The horizontal line in (b) depicts the SSHA = 0 cm. The rate enclosed by the dashed box indicates the trend is less than 99% significant. Otherwise, the trend shown is at 99% significance level. 163
Figure 6.4: Ocean Niño Index (ONI) from NOAA Climate Prediction Center. The ONI is based on

the SST anomaly in the Niño 3.4 region. A minimum of five consecutive months with SST anomaly of +/-0.5°C is considered an El Niño/ La Niña. The three horizontal lines depict the SST anomaly of +0.5, 0 and -0.5 °C. 164
Figure 6.5: Time series of satellite-derived (a) D20, (b) D26, (c) UOHC, and (d) T100 during the 18-year (1993-2010) study period. All of the parameters are expressed by annual (June-October) regional means averaged over the SEZ (red dots) and Gyre (blue dots). The dashed lines show the linear trends calculated by the least squares fitting. The detailed changes in these four parameters are summarized in Tables 6.1 and 6.2..... 165
Figure 6.6: Percentage of total areas of oceanic features. Time series of annual percentage of total areas of positive (SSHA $\geqq$10 cm; red dots), negative (SSHA $\leqq$10 cm; blue dots) and no (SSHA within ±10 cm; green dots) features in the (a) SEZ and (b) Gyre during the 18-year (1993-2010) study period. The dashed lines represent the linear trends. The detailed changes in the percentage of total area of the ocean features are summarized in Tables 6.3 and 6.4. 166
Figure 6.7: Time series of annual EWT (red curve), SSHA (blue curve) and SSHA corrected by EWT (black curve). The domain for these time series is 122-150°E, 10-26°N. In addition, the rates of changes are also shown. 167
Figure 6.8: Time series of annual D26 (in red) and UOHC (in blue) with the mass correction for 1993-2010. The corresponding grey curves are the original D26 and UOHC without mass correction. The rates of changes are also shown..... 168
Figure 6.9: Three extra domains: 1) SEZ+Gyre, depicted by black box; 2) the western SEZ (WSEZ), depicted by green box; and 3) western Gyre (WGyre), depicted by blue box. 169
Figure 6.10: Comparison between results of SEZ (red), Gyre (blue) and SEZ+Gyre (black) for (a) SSHA, (b) SST, (c) D20, (d) D26, (e) UOHC, and (f) T100. 170
Figure 6.11: Comparison between results of SEZ (red), WSEZ (dark red), Gyre (blue) and WGyre (dark blue) for (a) SSHA, (b) SST, (c) D20, (d) D26, (e) UOHC, and (f) T100. 171
Figure 6.12: The regular ground tracks of TOPEX/Poseidon, Jason-1 and Jason-2. The pass numbers are shown; red and blue depict ascending and descending pass numbers, respectively. 172
Figure 6.13: Annual SSHA time series calculated from the 32 regular passes and from gridded SSHA field for (a) the SEZ and (b) Gyre. Black curve depicts the time series computed by gridded SSHA, red curve depicts by along track SSHA, and grey curves depict by the 32 individual passes. T/P's observation is from 1993 to 2002, J1's from 2002 to 2008, and J2's from 2008 to 2010..... 173

Chapter 1 Introduction

1.1 Background and motivation

Climatologically, the western North Pacific contains the highest number of tropical cyclones (i.e., typhoons) in the world annually, and their intensity is also greater with respect to other cyclone-rich basins (Webster et al. 2005; Lin et al. 2005, 2008, 2009b). Based on the best-track typhoon data between 1970 and 2008 from the U.S. Joint Typhoon Warning Center (JTWC), the average number of typhoons occurring each year in this basin is 16.5, of which 6.3, or 38%, are categorized as supertyphoons (Categories 4 and 5 based on Saffir-Simpson Tropical Cyclone Scale; Table 1.1). In fact, these typhoons threaten a half-billion people living in the coastal areas of East Asia and cause much loss of life and property damage every year. For this reason, a reliable typhoon prediction is necessity for carrying out an effective precaution and damage control against the coming typhoon. It is noteworthy that since the regular tropical cyclone forecasting became operational, there has been stable improvement on the typhoon track forecast; however, very little improvement has been made on the intensity forecast (Figure 1.1; Emanuel 1999; Bender and Ginis 2000; Emanuel et al. 2004). So, there is a pressing need to further understand the mechanism of typhoon intensification, thereby improve the intensity prediction.

1.1.1 Importance of upper ocean thermal structure

In the last decade, observational and numerical studies both show that not only the sea surface temperature (SST), but also the entire upper ocean thermal structure (UOTS) over which typhoons pass plays an extremely critical role in the intensification of typhoons (Schade and Emanuel 1999; Bender and Ginis 2000; Shay et al. 2000; Cione and Uhlhorn 2003; Goni and Trinanes 2003; Emanuel et al. 2004; Lin et al. 2005, 2008, 2009a, 2009b; Wu et al. 2007; Goni et al. 2009; Shay and Brewster 2010). This is because UOTS is in close relation to the energy supply from the ocean

to typhoons (Leipper and Volgenau 1972; Gray 1979; Holliday and Thompson 1979; Schade and Emanuel 1999; Shay et al. 2000; Goni and Trinanes 2003; Lin et al. 2005, 2008, 2009a, 2009b; Wu et al. 2007; Goni et al. 2009; Shay and Brewster 2010). From the typhoon perspective, here UOTS represents vertical depth-temperature distribution from the surface down to 200 m or so, within this layer the interaction between typhoons and the ocean takes place (Price 1981; Lin et al. 2005, 2008, 2009a, 2009b; D'Asaro et al. 2007; Price 2009). However, the lack of the UOTS information in the typhoon forecasting system is one of the major reasons causing the unrealistic intensity forecasts (Bender and Ginis 2000; Shay et al. 2000; Cione and Uhlhorn 2003; Goni and Trinanes 2003; Emanuel et al. 2004; Lin et al. 2005, 2008, 2009a).

During the typhoon-ocean interaction, typhoons continually draw the energy from the ocean; their strong winds in turn stir the upper ocean. According to the processes of the entrainment and/or upwelling, the relatively cold thermocline water will be pumped to the surface layer, causing a SST decrease beneath the typhoon's core (Price 1981). However, it is well-known that such storm-self-induced SST cooling is a negative feedback mechanism restraining the typhoon intensity (Emanuel 1999; Bender and Ginis 2000; Cinoe and Uhlhorn 2003; Emanuel et al. 2004; Lin et al. 2005, 2008, 2009a, 2009b). That is, only a few degree drops in SST can substantially reduce the enthalpy (i.e., sensible + latent heat) fluxes fueling up the typhoon (Gallacher et al. 1989; Bender et al. 1993; Emanuel 1999; Schade and Emanuel 1999; Bender and Ginis 2000; Hong et al. 2000, Cinoe and Uhlhorn 2003; Emanuel et al. 2004; Lin et al. 2005, 2008, 2009a, 2009b; Pun et al. 2007; Wu et al. 2007). Gallacher et al. (1989) and Emanuel (1999) suggested that merely 2.5°C of SST cooling may be sufficiently enough to cut off all the energy supply from the ocean and eventually terminate the intensification of the typhoon. As a result, SST cooling is a huge obstacle to typhoon intensification.

The extent to which SST is cooled by the typhoon is closely related to the underlying UOTS (Price 1981; Schade and Emanuel 1999; Emanuel et al. 2004; Lin et al. 2005, 2008, 2009a, 2009b;

Pun et al. 2007; Wu et al. 2007). For instance, if the warm water (> 26°C) layer of UOTS is thick extending sufficiently deep, the cold water will be pumped up less to the surface by the typhoon, resulting in a moderate SST cooling that allows the typhoon continuously gaining the energy from the ocean. By contrast, if the warm water layer is thin, a large amount of cold water will be brought up to the surface, producing a significant SST cooling that may compromise the intensification of the typhoon (Lin et al. 2005, 2008, 2009a, 2009b). Therefore, having the subsurface thermal conditions along the typhoon's passage is crucial for typhoon intensity research and forecasting.

1.1.2 Importance of ocean features

In practice, using climatological UOTS is not satisfactory, because it is substantially perturbed by many kinds of ocean features. It is evident in Figure 1.2, which compares the thicknesses of the warm water layer between the climatology and satellite estimation. Those ocean features can be associated with common ocean phenomena, such as currents (e.g., Kuroshio and Gulf Stream), fronts and mesoscale eddies (Leipper and Volgenau 1972; Qiu 1999; Shay et al. 2000; Roemmich and Gilson 2001; Goni and Trinanes 2003; Qiu and Chen 2004, 2010; Lin et al. 2005, 2008, 2009a; Goni et al. 2009; Shay and Brewster 2010; Chelton et al. 2007, 2011), and large-scale basin-wide variability related to climate events, such as El Niño and La Niña (Wyrtki 1979; Philander 1990; Johnson et al. 2000; Lin et al. 2008).

Among those features, ocean eddies are considered the primary ocean feature that play an important role in typhoon intensification (Shay et al. 2000; Goni and Trinanes 2003; Emanuel et al. 2004; Lin et al. 2005, 2008, 2009a, 2009b; Scharroo et al. 2005; Shay and Brewster 2010). More importantly, there are two types of eddies: warm associated with anticyclonic circulation and cold associated with cyclonic circulation (Figure 1.3a; Hwang et al. 2004; Chelton et al. 2007, 2011; Chaigneau et al. 2008). A warm (cold) eddy is characterized by thicker (thinner) warm water layer and higher (lower) sea surface height with respect to the climatology (Figure 1.3; Shay et al. 2000;

Hwang et al. 2004; Lin et al. 2005; Pun et al. 2007; Chaigneau et al. 2008). In some eddy-sensitive regions, the difference of the thickness of warm water layer inside and outside an eddy can be up to a factor of three (Lin et al. 2005, 2008). Consequently, the presence of warm eddies are considered a favorable condition for typhoon intensification, because it can enhance the thickness of the warm water layer and thus effectively restrain the SST cooling (Hong et al. 2000; Shay et al. 2000; Goni and Trinanes, 2003; Emanuel et al. 2004; Lin et al. 2005, 2008, 2009a, 2009b; Scharroo et al. 2005; Wu et al. 2007). Many events around the world, such as Supertyphoon Maemi (2003) in the western North Pacific (Lin et al. 2005), Hurricanes Opal (1995) and Katrina (2003) in the Atlantic (Shay et al. 2000; Scharroo et al. 2005), and Tropical Cyclone Nargis (2008) in the Indian Ocean (Lin et al. 2009a) were observed that experienced rapid intensification while they were passing over the warm ocean eddies. On the other hand, cold eddies are expected to have negative effect on typhoon intensification. This is demonstrating the importance of ocean eddies in typhoon intensification.

Figure 1.3 compares two *in situ* Argo temperature profiles that are obtained inside a cold eddy (blue curve in Figure 1.3a) and warm eddy (red curve in Figure 1.3b). It can be found that their UOTS are very different. Using the depth of 26°C isotherm (D26) as a proxy of the thickness of the warm water layer, the warm water can extend to ~80 m in the warm eddy, whereas only ~50 m in the cold eddy, equivalent to 60% difference. Such pronounced distinction in UOTS can have a significant impact on SST cooling (Lin et al. 2008). It is important to note that using SST alone is almost unable to distinguish such subsurface temperature differences. As in Figure 1.3, the SSTs of the two profiles are of similar value of ~29°C. This is especially true during the summer season when the western North Pacific Ocean is usually covered by a thin layer of warm SST (Figure 1.4a). Therefore, only using SST to represent the entire ocean is clearly insufficient for studying and forecasting the intensity evolution of the typhoon, because SST barely represents the temperature in the upper few tens of meters and is not able to reflect the temperature of the whole water column. In contrast, sea surface height anomaly (SSHA) measurements from satellite altimeters have ability to

effectively detect ocean eddies (Figure 1.4b).

Interestingly, the western North Pacific Ocean itself is highly dynamic with abundant ocean features and eddies (Qiu 1999). It has the two well-defined eddy-rich regions known as the north and south eddy zones (NEZ and SEZ, respectively), in which warm and cold eddies frequently occur all year round (Figure 1.4b; Yasuda et al. 1992; Qiu 1999; Roemmich and Gilson 2001; Hwang et al. 2004; Lin et al. 2005; Pun et al. 2007; Qiu and Chen 2010). It is noteworthy that the SEZ is a part of the main typhoon intensification area in the western North Pacific Ocean (Gray 1979; Holliday and Thompson 1979; Lin et al. 2005, 2008). Recent study conducted by Lin et al. (2008) demonstrated that warm eddies in the SEZ are playing an vital role for Category 5 typhoons because the climatological warm water layer there is relatively shallow, but it can be thickened considerably as a warm eddy exist. Therefore, taking account of the ocean features and associated changes in UOTS are also important in typhoon intensification research and forecasting.

1.1.3 Estimation of upper ocean thermal structure

Although there is a high demand for UOTS in typhoon intensity research and forecasting, the operational acquisition of the accurate UOTS with suitable spatial and temporal resolutions can be very difficult, especially in the vast ocean basin like the western North Pacific Ocean (Carnes et al. 1990; White and Tai 1995; Gilson et al. 1998; Shay et al. 2000; Goni and Trinanes 2003; Willis et al. 2004; Pun et al. 2007; Goni et al 2009; Shay and Brewster 2010). In the last decade, the quantity and techniques of ocean subsurface observations have remarkable improvement (Gould et al. 2004; Roemmich et al. 2004; Johnson et al. 2006; Lyman et al. 2006; Willis et al. 2007), such as the success of Argo profiling project (Gould et al. 2004; Roemmich et al. 2004), but the spatial and temporal resolutions are still far below the requirement for resolving the mesoscale ocean features (Carnes et al. 1990; White and Tai 1995; Gilson et al. 1998; Willis et al. 2004; Pun et al. 2007). Therefore, taking advantage of satellite observations is vital for obtaining UOTS with high spatial

and temporal resolutions.

Since the sea surface height is able to reflect the subsurface temperature, Goni et al. (1996) and Shay et al. (2000) proposed a simply two-layer reduced gravity model to estimate UOTS to a first order accuracy from the satellite SSHA filed. This approach has been widely used in many studies of typhoon-ocean interaction (Shay et al. 2000; Goni and Trinanes 2003; Pun et al. 2007; Lin et al. 2008; Mainelli et al. 2008; Goni et al. 2009; Shay and Brewster 2010), and was employed by the National Oceanic and Atmospheric Administration (NOAA)/ Atlantic Oceanographic and Meteorological Laboratory (AOML) to operationally provide global UOTS information for tropical cyclone intensity forecasts (Goni and Trinanes 2003). However, this method was mainly developed for the Atlantic basin. In order to further improve the accuracy of the two-layer-derived UOTS in the western North Pacific Ocean, in my M.S. dissertation (Pun 2005), I specifically modified the two-layer approach (hereafter refers to as "2-layer") for the western North Pacific Ocean and conducted a systematic validation to assess its quality. This work was already published in *IEEE Transactions on Geoscience and Remote Sensing* in 2007, i.e., Pun et al. (2007). We found that the 2-layer is only applicable in the southern part (i.e., 9° – 26°N) of the western North Pacific and has monthly dependence; however, it totally fails in the northern part (i.e., 26° – 40°N). In addition, the vertical resolution of the 2-layer-dervied profiles is rather coarse, which only consists of four depths: SST, mixed layer depth (MLD), D26 and the depth of 20°C isotherm (D20). This deficiency and limitation pose a constraint on its applications to typhoon research.

Nevertheless, with the advantage of fast computation, the 2-layer was used to operationally provide real-time daily UOTS estimates in the western North Pacific Ocean with 0.25° spatial resolution during the recent typhoon-ocean field experiment, Impact of Typhoons on the Ocean in the Pacific (ITOP) in 2010. The performance of the 2-layer was outstanding and noticeable with respect to other sophisticated operational ocean models.

In addition to the 2-layer approach, several studies demonstrated that UOTS can also be

estimated from SSHA by using a linear regression method (Cheney 1982; Carnes et al. 1990; White and Tai 1995; Gilson et al. 1998). The principle of this method is to construct a set of regressions of SSHA onto the variation in subsurface temperature. Once the regressions are developed, UOTS can be inversely retrieved by satellite SSHA. But, to establish meaningful regressions, a large number of *in situ* temperature profiles are required. In the past, the insufficient number of *in situ* data had caused a serious constraint on the quality and implementation of this technique. As a consequence, the regression method has been only applied to study large-scale subsurface variability related to some climate issues, such as the variability in global heat content (White and Tai 1995; Willis et al. 2003, 2004), and seldom used to produce the real-time UOTS for operational purposes. To date, with the revolution and enhancement in *in situ* observations (i.e., Argo floats; Gould et al. 2004; Roemmich et al. 2004) and satellite altimetry techniques (Fu et al. 1994), this method is becoming feasible for estimating UOTS operationally. Therefore, one of the purposes of this dissertation is to develop a regression method specifically for the western North Pacific Ocean, and assess whether it can improve the UOTS estimation.

1.1.4 Ocean conditions in the western North Pacific

As the rising concerns over the increasing trends in tropical cyclone frequency and intensity, most of studies have been merely focusing on the attribution of SST warming in the corresponding ocean basin (Emanuel 2005; Webster et al. 2005; Mann and Emanuel 2006; Elsner et al. 2008). However, the causal relationship between the increasing SST and increased tropical cyclone frequency is still under intense debate (Webster et al. 2005; Chan 2006, 2007). In fact, the ocean conditions for tropical cyclone intensification include not only SST, but also the entire UOTS and ocean eddies and/or features as mentioned previously. This is especially sure for the western North Pacific Ocean where contains a large number of ocean eddies and/or features.

Recently, with *in situ* and satellite observations, quite a number of studies have revealed that

the globally averaged ocean heat content exhibited a significantly increasing trend during the past few decades; meanwhile, a large part of the warming occurred in the upper ocean (0-700 m; Levitus et al. 2000, 2001, 2005, 2009, 2012; Willis et al. 2004; Gouretski and Koltermann 2007; Domingues et al. 2008; Lyman et al. 2008, 2010). Given the importance of UOTS and eddies in typhoon intensification, it is highly interesting to study the long-term variability and trends in UOTS and eddy activity in the western North Pacific Ocean. With almost two decades of high quality SSHA data since 1993 and the methods developed in this study, this study attempted to systematically investigate the long-term changes in the ocean conditions, i.e., UOTS and ocean eddies, in the western North Pacific typhoon intensification zone.

1.2 Objectives of the study

With the above background and the unique characteristic of satellite altimetry, this dissertation will cover several topics that are related to the estimation of UOTS from the satellite remote sensing data, the applications of the derived UOTS on typhoon intensity research, and the long-term changes in the western North Pacific Ocean conditions for typhoon intensification. The purpose of this dissertation is introduced as follows:

Objective 1: Use the satellite-estimated UOTS information to study the intensity change of the western North Pacific Supertyphoon Dianmu (2004), which is the most rapidly intensified (from Category 1 to 5 in 18 h) typhoon since 1960.

Objective 2: Present the operational application of satellite-estimated real-time UOTS on the typhoon-ocean interaction experiment in 2010, i.e., ITOP.

Objective 3: Investigate the relationship between SSHA and the corresponding changes in

subsurface isotherm depths in the western North Pacific Ocean.

Objective 4: Use *in situ* temperature profiles from Argo floats to develop the regression method to estimate the western North Pacific UOTS from the SSHA and SST fields. Then, carefully validate the regression-derived UOTS to assess the applicability of the regression method on typhoon research.

Objective 5: Compare the estimations between the regression and 2-layer methods to see whether the regression method developed in this study can improve the UOTS estimation in the western North Pacific.

Objective 6: Develop an automated eddy identification method that can objectively and systematically identify ocean eddies in the western North Pacific on satellite SSHA maps. With this method and nearly two decades of high-quality satellite SSHA data since 1993, systematically investigate the long-term variability of eddies (e.g. their number, size, intensity) in the southern eddy zone (SEZ), in which eddies are especially important in typhoon intensification.

Objective 7: Followed from objective 6, study the long-term changes and variability of ocean features and UOTS in the western North Pacific, which may provide some information on the changes of the ocean conditions for typhoon intensification.

Objectives 1 and 2 will be addressed in Chapter 2, Objectives 3-5 will be given in Chapter 3 and 4, Objective 6 will be presented in Chapter 5, and Objective 7 will be given in Chapter 6. Finally, the conclusion and future work will be given in Chapter 7.

Before going any further, it should be clarified that typhoon intensity change is a very complex

process involving multiple interactions between typhoon-own structure, atmosphere and ocean. The present study is from the ocean point of view to study typhoons. This is not meant to imply that the typhoon structure and atmospheric condition are not important. In fact, all three conditions are equally important in typhoon intensity research.

Chapter 2 Review of the two-layer reduced gravity model and its applications to typhoon research

This chapter will review the two-layer reduced gravity model that is commonly used to derive temperature profiles (i.e., UOTS) from satellite SSHA and SST data. In addition, its real applications on studying the intensification of Supertyphoon Dianmu (2004) and operationally providing real-time UOTS for the ITOP field experiment (2010) are presented. The contents of this chapter are within Pun et al. (2007, 2011).

2.1 Two-layer reduced gravity approach for the western North Pacific Ocean

Figure 2.1 shows the schematic diagram of derived temperature profile (i.e., UOTS) from satellite altimetry and SST data by using the two-layer reduced gravity model, which was originally proposed by Goni et al. (1996) and Shay et al. (2000). Basically, the two-layer-derived UOTS simply consists of four components that include D20, D26, SST, and MLD (Figure 2.1). The former two components are derived from the SSHA data. In the two-layer model, ocean is separated into two layers of fluid. The 20°C isotherm (usually lies in the center of the main thermocline in most tropical oceans; Shay et al. 2000; Goni and Trinanes 2003) serves as a border that separates the upper and lower layers. The distance from the sea surface to the 20°C isotherm (i.e., D20) is thus defined as the upper ocean thickness. D20 is estimated from the altimetry observed SSHA (η') data by the two-layer scheme as follows (Goni et al. 1996):

$$D20(x,y,t) = \overline{D20}(x,y,m) + \frac{\rho_2(x,y,m)}{\rho_2(x,y,m) - \rho_1(x,y,m)}\eta'(x,y,t), \qquad (2.1)$$

where $\overline{D20}$ is the climatological D20 from the 1/4° monthly temperature analysis from the World Ocean Atlas 2001 (WOA01; Stephens et al. 2002) of NOAA/National Ocean Data Center (NODC); ρ_1 and ρ_2 are the density of the upper (surface to D20) and lower layers (D20 to bottom), repectively; both are calculated from WOA01 temperature and salinity database (Millero et al. 1980;

Fofonoff and Millard 1983); and η' is satellite measured SSHA as functions of location (x, y) and time (t). After gaining D20, D26 is estimated based on the climatological ratio (θ) between D20 and D26 as follows:

$$D26(x, y, t) = D20(x, y, t) \times \theta(x, y, m), \qquad (2.2)$$

θ is also calculated from WOA01 temperature database. It is worth mentioning that all the climatological parameters (i.e., $\overline{D20}$, ρ_1, ρ_2, and θ) in equations (2.1) and (2.2) are functions of location (x, y) and month (m).

Next, SST can be obtained directly from the cloud-penetrating Tropical Rainfall Measuring Mission/Microwave Imager (TRMM/TMI) and the Advanced Microwave Sounding Radiometer for the Earth Observing System (AMSR-E) (Wentz et al., 2000) or from other SST analyses, depending on different purposes. Lastly, in order to derive more realistic temperature profiles, the climatological monthly MLD from the U.S. Naval Research Laboratory (NRL; Kara et al. 2002) is used to describe mixed layer, in which temperature is equal to SST. With this method, the upper ocean depth-temperature profile can be produced at 1/4º (~25km) spatial resolution on a daily basis (Figure 2.1). Hereafter, this method is referred to as the "2-layer" throughout this dissertation.

A rigorous validation for the 2-layer derived UOTS was presented in my M.S. dissertation (Pun 2005), so it is not going to be repeated here. Basically, the validation results indicate that for the western North Pacific Ocean, the 2-layer is generally applicable in the lower latitude areas, i.e. 9° – 26°N, but it totally break down in the higher latitude areas, i.e. 26° – 40°N.

2.2 Intensity change of Supertyphoon Dianmu (2004)

Using the 2-layer profiles, the intensity change of Supertyphoon Dianmu (2004) was studied, which was intensifying in the applicable region of the 2-layer (Figure 2.2). Dianmu, which means 'Mother of lighting' in Chinese and made landfall and damaged Japan, was the most

rapidly-intensified western North Pacific typhoon since 1960[1]. Within 18 h (0000 UTC – 1800 UTC 15 June), it rapidly intensified from Category 1 (70 kts) to the super, Category 5 scale (145 kts). This is equivalent to 100 kts intensification in 24 h, i.e., more than 3 times the usual 'rapid intensification' baseline of 30 kts in 24 h (Kaplan and DeMaria, 2003). In this work, the SSHA data is from the Jet Propulsion Laboratory's (JPL) delayed mode dataset from the TOPEX/Poseidon and Jason-1 satellite altimeters (Fu et al., 1994). With this product, SSHA is based on the difference between the observed sea surface height and the 6-year (1993-1998) mean of sea surface height data from multiple-altimetry missions including TOPEX/Poseidon, ERS-1, ERS-2, and GEOSAT (Picot et al., 2003). Observing the pre-Dianmu SSHA data, one can see that this happened as Dianmu entered a large warm ocean feature region characterising by positive SSHA ~20 cm (Figure 2.2a). From the 2-layer estimation, one can see that this warm feature caused further deepening of D26 by 10-30 m (Figure 2.2b) in that region. As a result, it can be seen that this rapid intensification took place at a region with extraordinarily thick layer of warm water, i.e., D26 reaching 150 m (Figure 2.2c). The corresponding pre-typhoon upper ocean heat content (UOHC[2]; Leipper and Volgenau 1972; Shay et al. 2000; Goni and Trinanes 2003) is around 120-150 kJ cm^{-2} (Figure 2.2d), higher than the well-known Hurricane Opal (1998) case of 80-120 kJ cm^{-2} (Shay et al., 2000; Goni and Trinanes, 2003). As it progressed into the interior of the warm feature at 0600 UTC 16 June,

[1] According to the 1-minute sustained wind best track data of the U.S. JTWC from 1960 till 2007, Dianmu (2004) and the #11 typhoon in 1983 are the most rapidly-intensified typhoon in the western North Pacific that both intensified by 75kts within 18h.

[2] UOHC, first proposed by Leipper and Volgenau (1972), is the heat content exceeding 26°C in the ocean. It can be calculated from a temperature profile via the equation:

$$UOHC(x, y, t) = c_p \rho \sum_{i=1}^{n} \Delta T(x, y, z_i, t) \Delta Z \text{ , (2.3)}$$

where c_p is the capacity heat of the water at constant pressure taken as 4178 J kg^{-1}°C^{-1}, ρ is the average density of the upper ocean taken as 1026 kg m^{-3}, and $\Delta T(x, y, z_i, t)$ is the difference between $T(z_i)$ and 26°C at depth z_i, and ΔZ is the depth interval. n is the total layers from the surface to D26. UOHC is a function of location (x, y) and time (t).

Dianmu reached its peak intensity at 155 kts (Figures 2.2a and 2.2c). This peak intensity sustained for 12 h till 1800 UTC 16 June and started to decline to the Category 4 120 kts at 1800 UTC 17 June as Dianmu moved into a region with shallower warm layer of 90 m (Figures 2.2c). This situation can also be seen from the 2-layer profiles where profiles from the intensification region (i.e., profiles 1-6) are depicted in red, from the intensity sustained region (profiles 7-8) in green and intensity declination region (profiles 9-12) in blue (Figure 2.3a). Here two *in situ* profiles (profile 6' and 9') from the NOAA/GTSPP (Global Temperature and Salinity Profile Program; Keeley et al. 2003) found prior to Dianmu's passing (from 10 and 12 June, 2004; one near profile 6 and one near profile 9) are depicted in black (Figure 2.3a, location depicted as stars in Figure 2.2), confirming acceptable quality of the 2-layer profiles. It can also be noted that with the satellite altimetry, profiles along the track can be obtained but with *in situ* profiles, such information is not available. As in the Dianmu case, only two *in situ* profiles are found. As reported by Lin et al. (2008), this lacking of *in situ* data along typhoon's tracks is common, especially before the deployment of Argo floats (Gould et al. 2004; Gould 2005) in 2003.

Thus, with the 2-layer profiles as initialisation together with wind forcing from the JTWC best track wind, an ocean mixed layer model (Mellor and Yamada 1982) was adopted to study ocean's dynamic response to typhoon and estimate the typhoon-induced cooling (Price, 1981; Emanuel, 1999; Bender and Ginis, 2000). From Figure 2.3b, one can see the progressive increase in mixing as typhoon intensifies (profiles 1-6) and reaching as deep as 120m, as confirmed by the *in situ* profile (black profile in Figure 2.3b, location depicted as triangle in Figure 2.2) acquired immediately after the intensification period on 17 June 2004. From Figure 2.4, one can also see the corresponding increase in self-induced cooling from the 0.6ºC during Category 1 (at 0000 UTC 15 June) to the 1.4 ºC at peak (i.e., Category 5, 0600 UTC 16 June). From 0600 UTC 16 June onwards, though Dianmu's intensity did not increase but cooling still enhanced to 2.1ºC as Dianmu moved into region with shallower warm water region (profiles 9-12 in Figures 2.3b, and Figure 2.4). This

situation can also be observed in the SST maps from TRMM and AMSR-E acquired before (on 13 June, Figure 2.5a) and after (on 18 June, Figure 2.5b) Dianmu's passing. From 0600 UTC 16 June onwards, one can see clear enhanced cooling at the right to typhoon's track (SST ~ 27 ºC in Figure 2.5b) (Chang and Anthes 1979; Price 1981; Bender and Ginis 2000; Wentz et al. 2000) as compared with the warm pre-typhoon SST of >29 ºC (Figure 2.5a). As in the earlier intensification period (i.e. before 0600 UTC 16 June), cooling is less pronounced (Figure 2.5b).

Finally, of much interest for future forecast reference is to identify parameters sensitive to typhoon's intensity change. As shown above, using the derived profiles to the mixed-layer model, self-induced cooling during typhoon along track can be estimated. Since upper ocean thermal profiles (i.e. Figure 2.3b) can also be obtained, it can be used to calculate the dynamic UOHC during typhoon (i.e. during typhoon UOHC). Therefore, two parameters which include ocean's dynamic response, i.e., the self-induced cooling and the dynamic UOHC during typhoon, can be calculated. It should be noted that without the derived profiles, these two parameters could not be calculated as it is impossible to have *in situ* profiles at each point of the track (Figure 2.2). Together with the other parameters, i.e., pre-typhoon SST (blue curve in Figure 2.4, 2-D map in Figure 2.5a), pre-typhoon UOHC (green curve in Figure 2.4, as from Figure 2.2d), and atmospheric vertical wind shear[3] data along the track (brown curve in Figure 2.4), the sensitivity of these 5 parameters to typhoon's intensity change during Dianmu's drastic intensity change period (i.e. covering the rapid intensification period from Category 1 to 5 and followed by the decay to Category 4, from 0000 UTC 15 June to 1800 UTC 17 June) was compared. From Figure 2.4, it can be seen that throughout the study period, there is little change in the vertical wind shear. With the rapid intensification and decay of Dianmu, shear was typically around 6 m s^{-1} and shows little variability. This is also true for

[3] Wind shear is estimated as the difference between the 200 and 850mb ECMWF (European Centre for Medium-Range Weather Forecasts) 1.25º resolution reanalysis wind data averaged over a 700 km×700 km box centered in typhoon at every 6 h interval.

the pre-typhoon SST. In comparison, the other 3 parameters, i.e., the pre-typhoon UOHC, the dynamic UOHC, and the self-induced cooling have more variability. As can also be seen in the relationship between 6 h intensity change against each of the 5 parameters (Figure 2.6), the two parameters which include ocean's dynamic responses, i.e., the self-induced cooling and the dynamic UOHC, have the highest correlation coefficient, with R^2=0.72 and 0.69, respectively (Figures 2.6a and 2.6b). This suggests that there seems to have a relation between the 6 h intensity change of Dianmu during this period with these 2 parameters. During this study period, the correlation coefficient with the pre-typhoon SST and the vertical wind shear is low, with R^2=0.07, and 0.10, respectively (Figures 2.6c and 2.6e). As for the pre-typhoon UOHC, the R^2=0.48 shows more sensitivity than pre-typhoon SST and shear, but still lower than the self-induced cooling and the dynamic UOHC.

It should be understood that typhoon's intensity is controlled by many necessary atmospheric and oceanic parameters as well as typhoon's own structure (Emanuel et al., 2004; Wang and Wu, 2004). It is still a current open question in identifying sensitive parameters in typhoon's intensity and identify roles each parameter plays (Goni and Trinanes, 2003; Wang and Wu, 2004; Emanuel et al., 2004; Emanuel, 2005). The above sensitivity comparison shows that pre-typhoon SST and vertical wind shear are less sensitive than other parameters. However, it does not imply that both parameters are not important. The very warm pre-typhoon SST of 29-30°C and the low wind shear of around 6 m s^{-1} (Gallina and Velden, 2002) are all very favorable for typhoon's intensification, but not sensitive to subsequent typhoon's intensity change when the value of the threshold of both parameters (i.e. pre-typhoon SST > 26 °C and wind shear < 10 m s^{-1}) are satisfactory. Unless the situation is close to threshold value, both parameters can be probably become sensitive to typhoon's intensity. In the Dianmu's case, both parameters were far beyond the threshold and experienced little change (blue and brown curves in Figure 2.4) during the study period thus pre-typhoon SST and vertical wind shear are not as sensitive as the other parameters. This study is the beginning of

investigation using the satellite derived profiles to systematically study these various parameters in the intensity change of western North Pacific typhoons. With the current analysis it can be found that at least for the Dianmu case, UOTS is highly critical and the two associated parameters, i.e., the self-induced cooling, and the dynamic UOHC during typhoon, are the most sensitive to the 6 h intensity change as compared with all other parameters.

2.3 Implementation of the 2-layer in the ITOP experiment in 2010

In the summer of 2010, a large typhoon-ocean field experiment named Impact of Typhoons on the Ocean in the Pacific (ITOP) was conducted by the Taiwan National Science Council (NSC) and the U.S. Office of Naval Research (ONR). The goals were to investigate the highly complex physical processes associated with the mechanism between typhoons and the ocean. Fortunately enough, I had an opportunity to participate in this field experiment; therefore, the satellite-derived UOTS was experimentally tested in real-time application.

During the ITOP intensive operational period (IOP; August-October 2010), the 2-layer was used to operationally produce the western North Pacific UOTS in near-real-time (one day delay) for identification of ocean features to be targeted for deployment of *in situ* instruments, and for planning strategic observations. In this application, the SSHA data used are the real-time (one day delay) 1/4° gridded and merged product from the AVISO (Archiving, Validation and Interpretation of Satellite Oceanographic data). The detailed introduction of the AVISO database will be given in Chapter 3, section 3.1.2. In this data set, SSHA from all available satellite altimeters are combined in order to maximize the spatial resolution and to enhance the accuracy of SSHA maps. During the experiment, four altimeter missions, i.e., ERS-2 (1995), Envisat (2002), Jason-1(2001) and Jason-2 (2008), are functionally operated providing high-quality SSHA observations. During the operation, a set of horizontal maps of SST, SSHA, D26, UOHC and the averaged temperature of the upper 100 m (T100; Price 2009) were generated on a daily basis. For example, Figure 2.7a-e shows the maps

of SST, SSHA, D26, UOHC and T100 on 24 September 2010, respectively. On these daily maps, all real-time accessible *in situ* data (including those observed by ITOP) are superimposed to provide additional information and quick comparisons with the estimated field. Such additional information includes all Argo floats within two days period (color-coded triangles), moorings (color-coded asterisks), drifters (black dots), air-deployed instruments and the typhoon tracks (observed and predicted) if available.

From the example maps in Figure 2.7, one can see that the satellite SST (Figure 2.7a) and estimated D26, UOHC and T100 (Figure 2.7c-e) show good agreement with the Argo and mooring *in situ* observations. The subsurface parameters, i.e., D26, UOHC and T100, give much more information than SST alone. Generally, subsurface temperature is higher in the south and lower in the north and varies associated with mesoscale features. For example, D26 in low latitude (10-15°N) is as high as 160 m, while it decreases to 20-30 m in higher latitude (30-35°N). In contrast, SST is rather homogeneous and around 29-30°C. Furthermore, it is noteworthy that a cold wake located around 20°N 142°E to the right of Typhoon Malakas (2010)'s passage can be clearly seen. The UOHC in this cold wake became very low (~10 kJ cm^{-2}) and even zero (Figure 2.7d). Note that the dense observations east of Taiwan around 23°N 127°E are the instruments deployed by the C-130 aircraft during ITOP from 12 to 21 September 2010 for Typhoon Fanapi (2010). In order to provide real-time comparison between *in situ* and derived temperature profiles, all Argo profiles on the daily maps are plotted individually with the satellite derived profile. Figure 2.8 shows a comparison between profiles from Agro #25 (depicted in Figure 2.7d) and the two-layer estimation. One can see that the estimated profile (red curve) is in a good agreement with the Argo profile (black curve), showing that the two-layer estimated UOTS is suitable for use with a reasonable accuracy although it only contains four depths. Besides the plan-view maps, the values of above five parameters as well as UOTS along the typhoon track were also provided operationally during the ITOP IOP (Figure 2.9).

These various daily products were used to provide a synoptic picture of what the ocean state was in the western North Pacific. It was proved that such satellite-derived UOTS was very useful for planning the reconnaissance flights and ship cruises during the IOP (D'Asaro et al. 2011; Pun et al. 2011), especially when we were attempting to observe specific and scientifically interesting features (e.g., eddies and oceanic fronts). Meanwhile, several sophisticated atmosphere-ocean coupled models were also operational during the experiment, but more often than not, these models generated diverse results. In this circumstance, satellite-derived UOTS was used to verify model performance. The detailed comparison between the 2-layer and a full-ocean model will be presented in Chapter 4.

Chapter 3 Linear regression technique

This chapter will investigate the relationship between SSHA and the corresponding displacement of subsurface isotherms, and then develop a linear regression method to derive UOTS in the western North Pacific Ocean during the typhoon season (i.e., May-October) from satellite altimetry SSHA and cloud-penetrating microwave SST data. The contents of this chapter and Chapter 4 are within Pun et al. (2012).

3.1 Data

3.1.1 In situ Argo temperature profiles

The *in situ* temperature profiles used in this study were obtained from the highly successful Argo project: the global array of temperature-salinity profiling floats (Gould et al. 2004; Roemmich et al. 2004). Argo is an autonomous float that continuously measures temperature and salinity profiles in the upper ocean (typically from the surface to 2000 m depth) every 10 days. The data is transferred in real-time as it emerges from the surface. To date, over 3,200 Argo floats have been deployed over the global oceans, providing an unprecedented number of real-time *in situ* subsurface measurements, especially in remote areas. In this study, 11 years of Argo temperature profiles from 2000-2010 were used. Profiles in the first nine years (i.e., 2000-2008) were adopted to build the linear regressions between SSHA and subsurface temperature variation, whereas profiles in the last two years (i.e., 2009 and 2010) were used for the validation of derived UOTS. The validation will be presented in Chapter 4. The locations of these profiles used to develop the linear regression method are shown in Figure 3.1.

Although the profiles provided by the Argo data center (www.argo.net) have already gone through a quality control (QC), additional procedure was made to ensure that the profiles used are in high quality and appropriate for the present study. Especially, Willis et al. (2007) reported that

there is cold bias in the profiles that were measured by SOLOs, one type of Argo floats made by Woods Hole Oceanographic Institution (WHOI) and deployed between mid-2003 and 2006. For this reason, the profiles from the problematic floats were signaled out and excluded in this study. All of the items and their thresholds for the additional QC are listed in Table 3.1. Therefore, profiles which only match one of the items in Table 3.1 were eliminated. On average, about 10% of profiles were ruled out by this additional QC.

3.1.2 Merged and gridded satellite altimetry SSHA data

Unlike the traditional sensors (such as scanning radiometers or scatterometers) that provide a swath of measurements on the ocean surface along a satellite's ground track, altimeters only measure the sea surface heights along their tracks, meaning that measurements from altimeters are concentrated on the footprint. Figure 3.2 shows the nominal 10-day ground tracks of TOPography EXperiment for ocean circulation (TOPEX)/Poseidon (Fu et al. 1994) and its follow-on mission Jason-1. The measurements are made only on these regular tracks. The spatial and temporal resolutions of the altimeter-derived SSHA field depend on the satellite's orbit configurations. Using TOPEX/Poseidon mission as an example, the orbit attitude is 1336 km with an inclination of 66°, thus it is able to observe sea surface height within +/- 66° latitudes covering 90% of the world oceans. The spacing between two of TOPEX/Poseidon's adjacent ground tracks (red lines in Figure 3.2) is ~316km over the equator, and the satellite exactly follows the ground track once every 9.9 days (Fu et al. 1994), after which a global measurement of SSHA is obtained. Table 3.2 summaries the main orbit configurations for TOPEX/Poseidon and ERS series missions. For the scientific application, it is usually necessary to have gridded SSHA field. However, even with sophisticated mapping methods available at this time, artificial features may appear in the gridded SSHA field. Therefore, careful attention needs to be paid to any features that are far away from the ground tracks or in the center of so-called diamond-shaped patterns, which are formed by four interleaved tracks

(Figure 3.2). Therefore, using single altimetric mission (e.g., TOPEX/Poseidon) alone is not sufficient to accurately recover mesoscale eddies. Furthermore, many studies have pointed out that at least two altimetric satellites are needed to resolve ocean eddies (Ducet et al. 2000; Le Traon and Morrow 2001; Le Traon and Dibarboure 2002). It is evident that, during tandem missions of TOPEX/Poseidon and Jason-1 from October 2002 to September 2005, the track-to-track space is reduced from ~316 to ~158 km at the equator (Figure 3.2; Fu et al. 2003; Le Traon and Dibarboure 2004), doubling the spatial resolution.

In this Chapter, the near real-time (NRT) daily and delay-time (DT) 7-day merged and gridded SSHA products were employed. Both products are in regular grid of quarter degree (1/4°) spatial resolution and operationally generated by the SSALTO/DUACS (Segment Sol multimissions d'ALTimétrie, d'Orbitographie et de localisation précise/Data Unification and Altimeter Combination System) and distributed by the AVISO (Archiving, Validation and Interpretation of Satellite Oceanographic data). In these merged and gridded products, SSHA measurements from multiple altimetry missions are blended together to enhance the spatial and temporal resolutions (Ducet et al. 2000). The past and current altimetry missions used by AVISO to produce merged SSHA dataset are listed in Table 3.3. Combining SSHA from multiple missions is critical in the use of SSHA data. Before the blending process, various necessary corrections have been applied to the altimeters' measurements to ensure the accuracy of the SSHA field. The corrections include orbit error, ionospheric effect, dry and wet tropospheres, tides, model-based dynamic atmospheric correction, etc. Table 3.4 lists the primary corrections for AVISO's SSHA products. In addition, all of the satellites used to create the AVISO dataset are rigorously intercalibrated to guarantee the consistency of data (SSALTO/DUACS User Handbook 2012). Therefore, the resolution and capability of AVISO's SSHA data are significantly improved that allow revealing the mesoscale features with high accuracy of 3-4 centimeters (Ducet et al. 2000; Pascual et al. 2006, 2009). It is important to note that AVISO's SSHA data are the residual height between the instantaneous

measurement and the 7-year (1993-1999) temporal mean of the sea surface height. This is in order to eliminate the uncertainty introduced by the earth's geoid and remove the permanent ocean current patterns.

Additionally, it is also important to note that the AVISO's merged SSHA products have two series. That is, Updated and Reference series. The Updated series is constructed using all of the altimeters that are available at any given time; the number of altimeters ranges from two to four flying simultaneously[4]. The Reference series, on the other hand, is produced always based on two ordinary-configured altimetric missions, one of which is a typical 10-day period mission (e.g., TOPEX/Poseidon) and the other a 35-day period mission (e.g., Envisat). The Updated series would provide better quality data at the periods when more altimeters are available, but the overall quality is not stable over time. However, although the Reference series only contains two altimeters, its quality is homogenous over the entire dataset. It should be emphasized that choosing the appropriate SSHA dataset is very critical for the altimetry applications and subsequent research. For the purpose of developing regressions and real-time application, Updated series is chosen in this chapter to maximize the accuracy.

Compared to the DT data, the NRT data is the primary choice in this study because they are released in real-time and on a daily basis, which fits with our operational purpose. Unfortunately, the NRT data only covers the period beginning from 5 July 2006. Therefore, the DT data was used as a substitution when the NRT data is not available. Using these two datasets, the SSHA data can cover the entire study period 2000-2010.

3.1.3 Satellite microwave SST data

For the SST, the version-3 fusion SST from TRMM/TMI and AMSR-E was used in this study.

[4] During the period from October 2002 to September 2005, spanning almost 3 years, four altimeters (i.e., TOPEX/Poseidon, Jason-1, Envisat and GFO) were flying simultaneously. Most of the time, the number of overlapping altimeter missions was less than four and usually two.

This SST data are operationally provided by Remote Sensing Systems (RSS; www.ssmi.com) with an error of less than 0.5°C (Wentz et al. 2000). The spatial and temporal resolutions are 1/4° and on a daily basis, respectively.

3.2 Hydrographic characteristics in the western North Pacific Ocean

In this study, the western North Pacific is defined as the region of 120-170°E and 0-40°N (Figure 3.3), which is a region with the most frequent occurrence of tropical cyclones (i.e., typhoons) among the world oceans (Gray 1979; Webster et al. 2005; Pun et al. 2011). More importantly, the western North Pacific Ocean itself is very complex and dynamic involving several current systems and associated features. In addition, it is also sensitive to climatic events, such as El Niño-Southern Oscillation (ENSO; Wyrtki 1979; Philander 1990; Johnson et al. 2000). The complex nature of the western North Pacific Ocean makes the UOTS estimation difficult.

Figure 3.3 roughly delineates the hydrographic systems in the western North Pacific Ocean. Basically, a wind-driven subtropical circulation dominates the western North Pacific Ocean. The south rim of the circulation is the broad and energetic westward-flowing North Equatorial Current (NEC). It splits into two western boundary currents when it reaches the western coast of the Pacific. The northward-flowing branch forms the well-known Kuroshio Current, flowing along the east coast of Taiwan and then turns to the north-east direction along the south coast of Japan. Finally, the Kuroshio moves eastward to the open Pacific Ocean at the southeast of Japan. The final section of the Kuroshio is usually called the Kuroshio extension region, where obvious meander occurs (Qiu 2001). The meander of the Kuroshio generates a large number of warm and cold eddies with anticyclonic and cyclonic circulations, respectively. As a result, the Kuroshio extension is also named the Northern Eddy-Rich Zone (NEZ; Yasuda et al. 1992; Qiu 1999), which is one of the two well-recognized enhanced eddy zones in the western North Pacific. Another is the Southern Eddy-Rich Zone (SEZ), which is located east of Taiwan in the latitudinal band of 21-26°N (Qiu

1999; Roemmich and Gilson 2001; Hwang et al., 2004). In the SEZ, the surface current is dominated by the weak eastward-flowing Subtropical Countercurrent (STCC) while the interior is still dominated by the periphery of the NEC (Qiu 1999; Qiu and Chen 2010). The strong baroclinic instability resulted from the shear of these opposite flowing currents generates numerous warm and cold eddies. The typical sizes of eddies are about 50-500 km in diameter and they slowly propagate westward with a speed of 8-12 km day^{-1} (Hwang et al. 2004; Lin et al. 2005). It is noteworthy that the SEZ is collocated with the typhoon intensification zone, thus the existence of eddies highly influences the intensification of typhoons (Goni and Trinanes 2003; Lin et al., 2005, 2008, 2009b). The southward-flowing branch of the NEC forms the Mindanao Current, and the eastward-flowing Equatorial Countercurrent dominates near the equator.

Based on the current regimes and associated eddy zones, this work separates the western North Pacific Ocean into four hydrographic regions, including the Gyre, SEZ, Intermediate Eddy-Rich Zone (IEZ) and NEZ (Figures 3.1 and 3.3). The Gyre (125-170°E and 10-21°N) is the region where the NEC dominates. The common features of UOTS in this region are the basin-wide variations associated with ENSO (Wyrtki 1979; Philander 1990; Johnson et al. 2000). In the SEZ (127-170°E and 21-26°N) and NEZ (140-170°E and 30-40°N), warm and cold eddies occur all year round. Lastly, the IEZ (135-170°E and 26-30°N) is defined as the region in-between the two eddy zones (Pun et al. 2007). The validations and comparisons of the developed method are mainly based on these four regions.

Figure 3.4 shows all of the Argo temperature profiles (gray curves) in September from 2000-2008 in the Gyre, SEZ, IEZ, and NEZ. Superimposed in Figure 3.4, the blue curves depict the mean profiles and the solid circles depict the mean depths of the isotherms from 28°C to 4°C (D28-D4). Clearly, one can see that UOTS are different among these zones. Two pronounced thermoclines exist at the high latitude areas, i.e., the IEZ and NEZ (Figures 3.4c, d); this is because of the strong solar insolation in the summer heating up the surface layer. As a result, a seasonal

thermocline forms near the surface and leaves the permanent thermocline in the deeper ocean.

From the typhoon perspective, the warm water layer thickness (i.e., D26) has distinctive differences among these zones. One can see that the mean D26 is deepest in the Gyre with the value of ~100 m (Figure 3.4a). However, it decreases sharply by 35% to ~65 m in the SEZ (Figure 3.4b), and merely remains 40 m in the IEZ and NEZ (Figures 3.4c, d). Furthermore, the most varying portion of temperature profiles is found in the upper 1000 m, except in the NEZ where the variation is greater and extends deeper. This demonstrates that UOTS has large spatial variation.

3.3 Relationship between SSHA and depth variation of isotherms

It is well-known that there is a close physical relationship between the changes in sea surface height and the variations in subsurface properties such as temperature and salinity. In the tropical and subtropical oceans, the changes in sea surface height are largely dominated by temperature changes in a water column because of thermal expansion (White and Tai 1995; Gilson et al. 1998; Willis et al. 2003). Thus, a positive SSHA can generally reflect the subsurface temperature that is warmer than the climatology. In this relatively warm condition, the isotherms within the thermocline are expected to be deeper than usual. In contrast, a negative SSHA represents the thermocline isotherms that are shoaling with respect to their climatological depth, resulting in a relatively cold situation. Based on this characteristic, the changes in the depth of the isotherms can theoretically be estimated from the SSHA field. However, not all the isotherms of which depth changes are corresponding to SSHA. Instead, their relationships are expected to have regional and/or temporal variation, especially in the vast and dynamical western North Pacific Ocean (Figure 3.3; Gilson et al. 1998; Qiu 1999; Willis et al. 2003). Therefore, before developing regressions to estimate ocean subsurface temperature from the SSHA field, it is interesting to investigate what the SSHA actually means in the western North Pacific.

In this investigation, only the isotherms in the thermocline are considered. Figure 3.5 shows

the monthly correlation coefficients between SSHA and depth variation in each isotherm from D26 to the base of the thermocline for the Gyre, SEZ, IEZ and NEZ. The base of the thermocline in each zone is depicted in Figure 3.4. The variation of the isotherm depth is calculated from the isotherm displacement between *in situ* and climatology. The detailed information about how to obtain this quantity will be presented in next section. Nevertheless, the isotherm-correlation profiles exhibit unique structures with respect to the different regions. It can be found that the correlation varies from isotherm to isotherm, region to region and month to month.

In the Gyre (Figure 3.5a), the strongest correlation (>0.75) is found in the layer between D22 and D18, and gradually decrease upward and downward. This implies that SSHA primarily represents the variation of D22 to D18 in this region. Moreover, one can see that the correlation also varies with months, with relatively low correlation in May/June and high correlation in October.

In the SEZ (Figure 3.5b), the correlation is >0.6 throughout the whole column of the isotherms (i.e., D26-D6). The maximum correlation is found at D23 to D19. Frequent occurrence of eddies in this zone may be responsible for the high correlation with SSHA. Interestingly, almost in an entire typhoon season, the local minimum is found at D17. This may be due to the fact that D17 is located in the transition layer between the seasonal and permanent thermoclines (Figure 3.4b). This layer, however, is expected to be less related to SSHA. The monthly variation of the correlation is greater in the lower isotherms (i.e., D17-D5) than in the upper isotherms (i.e., D26-D18).

Moving northward, the correlation in the IEZ appears a little complex; the isotherms with high correlation are generally located below D17 (Figure 3.5c). The correlation tends to increase with depth. It should be noted that these high correlated isotherms are all within the permanent thermocline (Figure 3.4c). In contrast, the isotherms above D17 belong to the seasonal thermocline, thus this part of isotherms have relatively low correlation with SSHA. Moreover, the correlation in this layer has obvious monthly dependence with the highest correlation in August/September. Similar to the SEZ, the local minimum in the IEZ is also found at D17, indicating that the transition

layer is also around this isotherm.

Finally, in the NEZ (Figure 3.5d), the isotherms with high correlation (~0.8) are found below D17. These isotherms are located in the layer of the permanent thermocline (Figure 3.4d). On average, the highest correlation appears at D16 and then gradually decreases with depth. Moreover, the correlation drops rapidly from D17 up to D26. This is due to D26-D18 that usually lies in the mixed layer, where the isotherms are rarely relevant to SSHA. It is noteworthy that some of upper isotherms, such as D26, do not even exist during some months because SST is already lower than these isothermal temperatures. For example, there is no D26-D21 in May due to the water in the NEZ is generally lower than 20°C. The low correlation at D20-D18 in May is due to insufficient data points in these isotherms.

In order to summarize the meaning of SSHA in the western North Pacific Ocean, a seasonally (May-October) averaged correlation coefficient of 0.6 is taken as a threshold guide to determine whether the isotherm depths of which variations can be implied by SSHA. Figure 3.6 is a schematic that demonstrates which isotherms can effectively be described by SSHA for the Gyre, SEZ, IEZ and NEZ. Clearly, the meaning of SSHA has regional dependence. In general, SSHA can reflect the variations in D26-D12 in the Gyre, D26-D6 in the SEZ, D18-D7 in the IEZ and NEZ. Therefore, extra attention needs to be paid when using SSHA to retrieve subsurface temperature because SSHA describes the variation in different layers in different areas and months.

It should be clarified that the threshold of the correlation of 0.6 in Figure 3.6 is an experimental value demonstrating the high related section of UOTS to the SSHA. Undoubtedly, the higher the correlation, the higher the accuracy of SSHA-derived isotherm depth will be. As shown in Figure 3.6, the correlation with SSHA is generally >0.6 in most of the isotherms lying in the thermocline during typhoon season, representing that over 36% of the variance of the variations of these isotherms can be explained by SSHA.

3.4 Linear regression technique

Collected from 2000 to 2008 during typhoon season May to October, a total of 38,556 Argo *in situ* temperature profiles (Figure 3.1) were used to develop the regressions between SSHA and subsurface isotherm variation. As mentioned in section 3.2, the western North Pacific Ocean is a highly dynamic ocean basin. Although it can roughly be divided into four regions with distinct hydrographic features, a single regional regression may not be enough to account for the spatial variation. In other words, one regression for one specific region is not adequate to produce accurate UOTS estimates. The regional regressions will also generate discontinuity of UOTS field. Therefore, it is particularly important to have a set of representative regressions that is able to account for the variations in space and time.

Therefore, this work attempted to construct a regression at every 0.25°×0.25° grid mesh and on a monthly basis. Besides, vertical resolution of the regressions is also vital for the estimation of the UOTS because the covariance between SSHA and isotherm varies from isotherm to isotherm (Figure 3.6). In addition, the vertical resolution of a derived profile is determined by the number of available regressions for the subsurface. The more the vertical depth, the more accurate the estimated profile is expected. In vertical, this study attempted to develop monthly regressions from D26 down to the base of the thermocline with an interval of 1°C. Two reasons for choosing D26 for the upper bound of the regression set. First, the isotherms warmer than 26°C (e.g., D27, D28, and so on) are probably in the mixed layer, in which the isotherm variation is expected to have less correlation with SSHA. Second, it is due to the fact that D26 represents the thickness of warm water layer that is critical for typhoon intensification (Shay et al. 2000; Goni and Trinanes 2003; Pun et al. 2007; Lin et al. 2008; 2009b). Extending to the base of the thermocline is because the isotherms within this layer are physically related to the variation in SSHA (Figure 3.4).

3.4.1 Procedure of developing regressions

To have a robust and representative regression, a large number of *in situ* profiles are required. However, in such a fine resolution grid point (0.25°) designed in this study, it is unlikely to have sufficient *in situ* profiles within 0.25° grid box. To solve this problem, the profile searching area is enlarged for each grid node. It should be noted that although the number of available profiles increases with large searching box, the derived regressions may loss the spatial variation. In this study, profiles within a box of 10° longitude by 5° latitude were binned to calculate the regressions for each isotherm at each grid point. Using the rectangle box is because the relationship between SSHA and subsurface temperature is expected to be less various in longitude. The searching box is centered at a grid point where the regressions are constructed.

The regressions were constructed by linearly regressing the isotherm displacements onto their collocated and coincident SSHA values. The displacement, as such, means the isotherm depth difference between *in situ* and climatological profiles, representing the deviation from the climatology. In this study, the high resolution (1/4°) monthly temperature analysis of the WOA01 (Stephens et al. 2002) provided by the U.S. NOAA/NODC were adopted as a climatological temperature field. Note that this work employ the WOA01 instead of the one made of the present data set. This is because the WOA01 uses an objective analysis with all the available historical *in situ* data other than Argo to generate the optimal and high resolution climatological temperature field (Stephens et al. 2002). On the other hand, the number of *in situ* profiles used in this study may not be large enough to produce realistic climatological field. To evaluate the displacements of *in situ* isotherms, all of *in situ* profiles were paired up with the nearest location of monthly WOA01 profiles. The isotherm displacement (ΔD) in each *in situ* profile is derived as:

$$\Delta Di = Di - \overline{Di}, i = 26,25,... \qquad (3.1)$$

where D and $\overline{D}$ are the *in situ* and climatological depths of isotherm, respectively; and i is the isotherm from 26°C to the temperature at the base of the thermocline.

After that, each *in situ* profile was paired up with the collocated and coincident SSHA values. As mentioned in section 3.1.2, AVISO's DT 7-day SSHA was used when the NRT daily SSHA product is not available. In the situation of using 7-day SSHA, the closest SSHA map to the time of *in situ* profile was chosen as the coincident SSHA map. The collocated SSHA value is taken from the nearest grid point of the daily or 7-day map. Figure 3.7 compares SSHA that are obtained from NRT and DT products for all of the Argo profiles in 2009 season. Apparently, for all four zones, SSHA from both data sets are very similar with an averaged correlation coefficient of ~0.98, indicating that using these two data sets together does not pose a serious problem on the quality of the regressions.

Next, the displacements in each isotherm of the *in situ* profiles were linearly regressed onto their collocated and coincident SSHA by using least squares fitting. Therefore, the monthly regression equation for each isotherm from 26°C to the temperature at the base of the thermocline at each grid node is obtained:

$$\Delta Di = a_{(x,y,m,i)} \times \eta_{(x,y,t)} + b_{(x.y,m,i)} \qquad (3.2)$$

where η is the satellite observed SSHA, which is a function of location (x, y) and time (t); a and b are the linear regression coefficients representing the slope and offset, respectively; both coefficients are a function of location (x, y; 0.25°), isotherm (i; D26-isoherm at the thermocline base), and month (m; May-October). With this set of regression equations, the displacement of an isotherm (ΔDi) can be estimated from the SSHA observations. The actual depth of isotherm (Di) is then retrieved by adding back the corresponding climatological depth to the SSHA-derived ΔDi.

3.4.2 The spatial pattern of the regressions

Figures 3.8a, b show the regression coefficients of equation (3.2) for D20 in September. One can see that the slope (a) of the regressions varies over the entire western North Pacific Ocean, verifying the concern about the regressions that have regional dependence. The steepest slope is

found in a band of 15°-25°N, which is the location of the SEZ and the northern part of the Gyre. In this area, the slope is about 2.5 m cm^{-1}, meaning that 1 cm of SSHA can produce 2.5 m variation in D20. However, the slope flattens out in the NEZ. As seen in Figure 3.8a, the slope patterns roughly follow the four hydrographic zones. However, the zonal variation is still significant in some areas such as at low latitudes (0°-15°N). The offset (b) is generally negative, except some areas in the NEZ (Figure 3.8b). This reflects the difference between the WOA01 and the "real" climatological field. Recall that such coefficients are also varies from month to month and isotherm to isotherm.

Figures 8c, d show the spatial distributions of the correlation and the number of profiles used to calculate the D20 regressions in September. Basically, the correlation between SSHA and D20 variation is quite high (~0.7) over the western North Pacific Ocean. However, significantly low correlation areas can still be found. Such as the Kuroshio extension, the correlation drops to ~0.3. The energetic motions associated with the Kuroshio meander might be the reason for the low relationship. As shown in Figure 3.8d, the number of profiles used for calculating the regression is spatially inhomogeneous. Nevertheless, each grid point contains at least 50 profiles for calculating the regressions. In the western boundary region, however, >300 profiles are available for each grid point. Although the number of Argo profiles grows rapidly, the relatively scarce area still exists, such as the areas around 155°E 13°N and 170°E 13°N, where the available profiles decreases to ~40 (Figure 3.8d). Interestingly, in the profile-sparse areas, the correlation is still high and statistically significant (Figure 3.8c).

Figure 3.9a shows the isotherm-SSHA-correlation transect from the equator to 40°N along 145°E in September. It can be found that the correlation pattern varies significantly with isotherm and latitude. Basically, the correlation pattern is roughly consistent with the four hydrographic zones (Figure 3.6), but the small-scale spatial variations still exist. As in the Gyre, a local minimum appears at around 13°N, where the correlation is <0.6 for all isotherms (Figure 3.9a). It is probably because it is where the main axis of the North Equatorial Current (NEC) is located (Figure 3.3). In

addition, one can also see that there is high correlation extending from D26 to D10 around 5-10°N, where is the region between two energetic currents of westward-flowing NEC and eastward-flowing Equatorial Countercurrent (Figure 3.3).

Figure 3.9b shows the corresponding cross section for the slope of the regression. It can be found that the pattern of the slope is somewhat similar to that of the correlation (Figure 3.9a). The steepest slope is found in the lower isotherms (i.e., D17 downward) in the IEZ and NEZ (26-40°E), in which the slope is up to ~5 m cm^{-1} corresponding to the high correlation area (Figure 3.9a). In the northern part of the Gyre and SEZ, the slope is greater in the upper isotherms D25-D19 of ~2.5 m cm^{-1} and gradually decreases with depth. Furthermore, a relatively steep slope occurs around D15-D14 at the equator.

According to Figure 3.9, the relationship between SSHA and subsurface isotherms varies remarkably in latitude. However, it is not implying that the variation in longitude is unimportant. As in Figure 3.8a, the variation in longitude is also significant. In addition, this relationship also varies with months. Therefore, the quality of the regression-derived UOTS is directly related to whether the regression is allowed to change in space and time.

It is especially important to note that although the correlation does not exceed the threshold criterion of correlation of 0.6 (Figures 3.8c and 3.9a), the regression equation is employed when it is over 99% significance. As shown in Figure 3.9b, the slope is less than 99% significance level is masked in grey. Consequently, the regressions with low correlation like D26-D18 in the NEZ (Figure 3.9) are still being used. Applying this criterion is in order to maximize the capability of the regression method and provide an enhanced temperature profile.

3.4.3 Treatment for mixed layer

In reality, the linear regressions only provide most of the components (i.e., D26-isoherm at the thermocline base) consisting of UOTS. However, they are usually constrained below the mixed

layer. Thus, additional information about the sea surface and mixed layer are required to complete the UOTS estimation. The temperature of the sea surface (depth = 0) is directly using satellite SST observation. Unfortunately, it is very difficult to parameterize the mixed layer depth (MLD), owning to MLD is fairly dynamical and highly influenced by many factors, such as winds, waves and even the stratification of the upper ocean (Price et al. 1981). According to the 2-layer method (Pun et al. 2007) in Chapter 2, two components were taken into account for this part of UOTS. They include the satellite SST and climatological monthly MLD from U.S. NRL (Kara et al. 2002). In this study, this approach is adopted to complete the UOTS estimation.

With this technique, UOTS from the surface to the depth of ~600 m can be estimated by the combination of satellite SSHA and SST data. Hereafter in this paper, the regression method is referred to as “REGWNP” (regression for the western North Pacific Ocean). Figure 3.10 displays some profiles in September of 2010 that were obtained from REGWNP (green curves), Argos (black curves) and 2-layer (red curves). It is worth mentioning that those profiles were randomly selected from the Gyre, SEZ, IEZ and NEZ. From Figure 3.10, one can see that REGWNP’s profiles are in a good agreement with *in situ* profiles. Additionally, it can be found that the combination of the satellite SST and climatological MLD gives a reasonable approximation of the mixed layer structure. The rigorous validations of REGWNP will be carried out in Chapter 4.

3.5 Summary

Based on the hydrographic characteristic, four difference zones (i.e., the Gyre, SEZ, IEZ and NEZ) are defined in the western North Pacific Ocean. The relationship between SSHA and the subsurface isotherm displacement are examined with respect to these zones. It is found that the meaning of SSHA is region dependent in the western North Pacific. SSHA typically reflects the variations of D26-D12 in the Gyre, D26-D6 in the SEZ, D18-D7 in the IEZ and NEZ. The correlation between SSHA and those isotherms is > 0.6.

Based on this close relationship and using >38,000 Argo *in situ* temperature profiles from 2000 to 2008 during typhoon season (May to October), a linear regression method (i.e., REGWNP) was developed to estimate upper ocean temperature profiles in the western North Pacific with satellite SSHA and SST observations. In REGWNP, the monthly regressions were made in every 0.25° grid mash to account for the spatial and temporal variations. For the mixed layer temperature, satellite SST and NRL's climatological MLD were used. Combining the isothermal depths estimated from SSHA and mixed layer temperature, a temperature profile from the surface to ~600 m is obtained. With this technique, UOTS in the western North Pacific Ocean with high spatial (0.25°) and temporal (daily) resolutions can be estimated on an operational basis.

Chapter 4 Validation of regression-derived altimetry-based upper ocean thermal structure in the western North Pacific Ocean

This chapter will conduct a rigorous validation for the regression-derived UOTS to access the accuracy of REGWNP developed in Chapter 3 and determine whether it is suitable for typhoon research. In addition, an inter-comparison with the 2-layer, a full ocean model, and ITOP observations will also be made.

4.1 Validation

An independent set, containing 7,036 Argo profiles from 2009 and 2010 during May to October were used to validate the regression-derived UOTS. The locations of these profiles are shown in Figure 4.1 with blue dots. Using this independent set of profiles for the validation is in order to examine whether the regressions, conducted from the profiles between 2000 and 2008 in Chapter 3, have an ability to estimate UOTS in other years.

The validation was made for four distinct zones, i.e., Gyre, SEZ, IEZ and NEZ (Figure 3.3; see Chapter 3, section 3.2). Since this regression technique is developed mainly for typhoon application, thus, isotherms and associated parameters that are related to typhoon intensification were selected for the validation. They include two major isotherms in the two-layer model: D20 and D26 (Shay et al. 2000; Goni and Trinanes 2003; Pun et al. 2007) as well as two parameters used to characterize the upper ocean temperature for typhoon intensity forecasts: UOHC (Leipper and Volgenau 1972; Shay et al. 2000; Goni and Trinanes 2003) and averaged temperature of upper 100 m (T100; Price 2009). At each zone, the monthly root-mean-square difference (RMSD), error[5], and bias between the estimated and *in situ* values were calculated.

[5] $Error = \frac{RMSD}{Mean_{obs}} \times 100\%$, representing the percentage of RMSD in the observed mean.

4.1.1 Validation for D20

In the two-layer model, D20 serves as a boundary separating the ocean into the upper and lower layers of the fluid. Also, it is the primary parameter calculated by the two-layer model from SSHA. Therefore, it is interesting to test the performance of REGWNP in producing D20. Figure 4.2 shows the monthly scatter plots comparing D20 derived from REGWNP and Argo floats. In general, the derived D20 is quite reasonable as compared with observations. Most of the pairs fall near around the 1:1 line. Especially in the Gyre and SEZ, derived D20 is highly consistent with the observations throughout May to October. However, the accuracy of D20 gradually degrades northward. This is consistent with the correlation pattern in Figure 3.8c, in which the correlation of D20 reaches the minimum of ~0.3. It is also noteworthy that in the IEZ and NEZ, underestimations are found when the D20 is deeper than 100 m, and usually occur in positive features (SSHA > 0). However, one can see that the D20 estimation in the NEZ is relatively accurate in October, indicating that the regression has time dependence.

Figure 4.3 shows the monthly accuracy analyses of RMSD, error and bias for the REGWNP estimated D20. From Figure 4.3a, one can see that the monthly RMSD of derived D20 is usually <30 m for all zones. In addition, it can be found that in the Gyre (green curve), RMSD is relative low (~15 m) and exhibits stable over the entire season as compared with the other zones. However, in the SEZ (blue curve), RMSD slightly increases to ~20 m and peaked in August. In the IEZ (orange curve), RMSD has a tendency that is higher in early summer (i.e., May/June) to ~27 m and then gradually decreases through October to ~15 m. In the NEZ (red curve), RMSD is a little bit higher in May to ~28 m, and slowly reduces to ~20 m in October. Figure 4.3b shows the corresponding error percentage of derived D20. It can be found that the error in the Gyre and SEZ is rather small which are ~8% and ~15%, respectively. However, in the IEZ, the error increases noticeably to ~35% during the early season, although it gradually decreases through October to

~16%. Lastly, in the NEZ, the error of the derived D20 is higher than any other zones, reaching ~53% in May/June and then gently dropping to ~25% in October. It is noteworthy that the monthly RMSD of the derived D20 for all four zones are at similar level of 15-30 m (Figure 4.3a). However, the monthly error increases obviously from the Gyre to NEZ. This is because the observed mean D20 decreases significantly from south to north in the western North Pacific Ocean (Figure 3.6). As a result, the error will increase northward. In addition, no apparent bias is observed in the derived D20 (Figure 4.3c). In general, the bias is within ±10 m.

4.1.2 Validation for D26 (i.e. warm water thickness)

Figure 4.4 shows the monthly scatter plots between the derived and *in situ* D26. Basically, in the Gyre and SEZ (two left panels), REGWNP performs fairly well that is highly consistent with the Argo measurements. The range of D26 is about 50-150 m. However, in the SEZ, D26 is somewhat underestimated in May for positive SSHA points. In the IEZ and NEZ (two right panels), the variation of D26 becomes small that ranges only from 0 to ~50 m. It is noteworthy that in these two regions, less D26 data appears in early season, such as May/June. This is because at this time of the year, D26 does not exist. Even though D26 appears, it is usually shallow and near the surface. In such shallow depth, D26 is affected by other external forcing from the atmosphere. It is evident from Figure 3.9a, the correlation between D26 and SSHA is relatively weak in the IEZ and NEZ. As a result, the accuracy of REGWNP derived D26 becomes less accurate in these two regions.

Figure 4.5 summarize the accuracy analysis for REGWNP derived D26. It can be found that the monthly RMSD is about 10-20 m for all zones. Interestingly, RMSD in the Gyre and SEZ is even greater than that in the IEZ and NEZ. However, it is not meant that the accuracy of derived D26 is better in the IEZ and NEZ. However, this is because the variation in D26 in the Gyre and SEZ is much larger than that in the IEZ and NEZ (Figure 4.4). In terms of the error, the derived D26 is usually less than 20% in the Gyre, representing it is of high accuracy. In the other three zones, the

error ranges from ~20% to ~50%, depending on months. Generally, the higher error usually occurs in early summer when D26 is close to the surface. The bias of derived D26 is small within ±10 m.

4.1.3 Validation for UOHC and T100

Many recent studies, e.g., Shay et al. (2000), Goni and Trinanes (2003), Price (2009), and Lin et al. (2009b), have been attempting to find a proxy that is able to effectively quantify the upper ocean energy for typhoon intensity research and forecasting. As early as 1970s, Leipper and Volgenau (1972) had proposed a concept of UOHC to evaluate the available energy from the ocean for typhoons. Since the past decade, this parameter has been widely used in typhoon intensification studies (Shay et al. 2000; Goni and Trinanes 2003; Pun et al. 2007; Lin et al. 2008; 2009b; Goni et al. 2009; Shay and Brewster 2010). Furthermore, UOHC started to be considered into an operational typhoon forecast system, and a notable improvement was made (Mainelli et al. 2008). More recently, a new concept of T100 was proposed by Price (2009) to approximate the SST cooling induced by typhoons. Therefore, it is interesting to evaluate the accuracy of these two parameters which are calculated from REGWNP derived temperature profiles.

Figure 4.6 shows the scatter plots comparing UOHC calculated from REGWNP and Argo floats. In general, one can see that the derived UOHC is highly consistent with the observations in all validation regions. Surprisingly, the estimated UOHC are also in a good agreement with the observations in the IEZ and NEZ where the derived D26 exhibits relatively less accurate (Figure 4.4). The possible reason is that although D26 is important in the calculation of UOHC, the MLD and SST are also critical. As demonstrated in Figure 3.10, the mixed layer structure is reasonably approximated by SST and climatological MLD. As a result, REGWNP's UOHC shows a better result than its D26. In the IEZ and NEZ, Again, a few and even no data point in early summer, because SST is already lower than 26°C. Figure 4.7 presents the accuracy analysis of derived UOHC. One can see that RMSD is quite small of <20 kJ cm^{-2}. And similar to D26, the lowest

RMSD is found in the NEZ. This is because the variation of UOHC in the NEZ is relatively small. The smallest error of ~20% is found in the Gyre. In the other zones, the error varies from 25% to 70% depending on different months. It should be noted that the error for UOHC in the IEZ and NEZ is higher than that of D26 (Figure 4.5b), although UOHC is more consistent with the observations (Figure 4.6). It is because the observed mean UOHC is relatively smaller compared to the mean D26, resulting in higher error in UOHC. Furthermore, the bias for the derived UOHC is rather small of ± 5 kJ cm^{-2} (Figure 4.7c).

Figure 4.8 shows the scatter plots of T100. Surprisingly, one can see that the T100 calculated from REGWNP-derived profiles is highly consistent with the observed T100 in all zones and months, demonstrating the high performance of REGWNP in estimating T100 in the western North Pacific Ocean. RMSD for T100 is generally less than 1°C, except in the NEZ, in which RMSD is 1-1.4°C (Figure 4.9a). Moreover, no obvious bias is found for the derived T100 (Figure 4.9b). It should be noted that there is no error analysis for T100 because the mean T100 is too large (typically > 20°C) comparing with the variation in T100 (few degrees). Therefore, it is inadequate for comparing this quantity for T100.

4.1.4 Applicability of regression-derived D20, D26, UOHC and T100 for typhoon research

According to the above validations, REGWNP is proved to have a capability to estimate the typhoon-related ocean parameters: D20, D26, UOHC and T100 in the western North Pacific Ocean. The accuracy of these four REGWNP-derived parameters was quantified. As for its application in typhoon intensity research and forecasting, this study experimentally took 50% error as a threshold guide to determine whether the estimations from REGWNP are applicable. For T100, however, a threshold of RMSD of 2.5°C was used because it is a critical value of SST cooling in typhoon intensification (Gallacher et al. 1989; Emanuel 1999). Figure 4.10 is an applicabilty chart showing the applicable zones and months of REGWNP for each validated parameter. For D20, it is almost

applicable in all four zones during the entire season, except May in the NEZ. For D26, it is not applicable in the IEZ and NEZ during May and June. For UOHC, it is not applicable in the NEZ during May-July and October, IEZ during May and June, and SEZ during May. For T100, it is all applicable for the entire western North Pacific Ocean.

Although D20, D26 and UOHC derived by REGWNP do not pass the threshold (50% error) in the northern zones during the early season, it does not mean the failure of REGWNP. In fact, during the early summer, the values of these three parameters are quite low in the northern area. As a result, a relatively large error appears in REGWNP. In contract, REGWNP is able to provide T100 in a reasonable accuracy over the entire western North Pacific over the whole season. In fact, the quality of T100 is directly related to the thermal structure of the upper 100 m. This indicates that UOTS derived by REGWNP is rather reliable. Moreover, if we consider the western North Pacific Ocean as a whole, REGWNP is deemed to have ability to provide synoptic estimations of D20, D26, UOHC, and especially T100 for typhoon research and forecasting.

4.2 Comparison with the 2-layer, EASNFS full ocean model and AXBT data from ITOP field experiment (2010)

4.2.1 Comparison with the 2-layer

The validation results suggest that UOTS estimated by REGWNP is of reasonable accuracy in the western North Pacific Ocean. However, it is also interesting to compare with the traditional two-layer approach to see if there are improvements in UOTS estimation. As shown in Figure 3.10, REGWNP can provide more detailed and realistic profiles than the 2-layer. Basically, REGWNP derives a profile with up to 25 depths from the surface to the base of the thermocline, whereas the 2-layer only provides four depths. To further quantify their differences, the inter-comparison was conducted by using the same set of *in situ* data used in the validation section. Due to 2-layer cannot derive profiles at some *in situ* points, thus, those points were ruled out from the comparison.

Based on the four hydrographic zones, Figure 4.11 shows the percentage of improvement on REGWNP with respect to 2-layer for D20, D26, UOHC and T100. A positive value means that REGWNP outperforms the 2-layer, and vice versa. As seen in Figure 4.11, significant improvement is found for D20. It has ~25% improvement in the Gyre (except October in which no obvious improvement is found), ~20% in the SEZ, ~27% in the IEZ, and remarkably ~70% in the NEZ. Noted that no comparison for the NEZ in May is because the 2-layer is not available and/or D20 does not exist. For D26, the improvement becomes less obvious in the Gyre, in which only ~3% improvement is made and it even turns to a negative value in August. However, it should be noted that in the 2-layer, D26 is computed from the estimated D20 by multiplying a climatological ratio (θ; see Chapter 2). And one can see that D20 estimated from REGWNP has significant improvement with respect to the 2-layer. This indicates that the 2-layer-derived D26 is calculated from less accurate D20, but somewhat compensated by the ratio. In the other three zones, a noticeable improvement on D26 is made by REGWNP. The improvements for the SEZ, IEZ and NEZ are ~13%, ~27% and ~32%, respectively.

For UOHC, one can see that the improvement is less significant. It is because mixed layer structure plays a role in UOHC. And both methods are using the same approximation for the mixed layer (Figure 3.10). As a result, the improvement from REGWNP on UOHC is limited. Finally for T100, substantial improvement is found in the REGWNP for the SEZ, IEZ and NEZ, in which the improvement is ~20%, ~44% and ~40%, respectively. Moreover, it is also noteworthy that no T100 comparison for the IEZ in May-June and NEZ in May-July and October. This is because the 2-layer-derived UOTS is shallower than 100 m depth. In the Gyre, the improvement is relatively less of ~8%, and even no improvement in September and October. This is due to the 2-layer generates reasonab thermal structure in the upper 100 m in the Gyre (Figure 3.10).

Figure 4.12 shows the maps of D20, D26, UOHC and T100 on 25 September 2010, derived from REGWNP and the 2-layer. On these maps, concurrent Argo measurements (triangles) are

superimposed. One can see that apparent overestimations are found in the north of 25°N in the 2-layer's D20. In contract, REGWNP's D20 matches the observations very well. Inspecting the difference maps, it can be found that the 2-layer overestimated (underestimated) D20 in positive (negative) SSHA areas. Similar result is found in D26. Such as in a warm eddy at 147°E 34°N, in which D26 is ~50 m from the Argo, whereas nearly 100 m from the 2-layer. Again, D26 from REGWNP agrees with the Argo observations. In terms of UOHC, the patterns from both methods are comparable. Finally, for T100, it can be found that REGWNP is able to provide T100 estimates over the entire western North Pacific Ocean with high accuracy, whereas the 2-layer overestimated T100 in the north of 25°N. In addition, the 2-layer is not able to derive T100 in the north of 35°N as well as in cold eddy areas at the belt of 30°-35°N. It is due to the maximum depth that the 2-layer can estimate depends on D20. Consequently, when D20 is shallower than 100 m, T100 cannot be calculated (Figure 3.10). As a result, REGWNP has not only better accuracy, but less spatial constraint with respect to the 2-layer.

4.2.2 Inter-comparison with EASNFS full ocean model and AXBT data from ITOP experiment

During ITOP field experiment, a number of Airborne Expendable Bathythermographs (AXBTs) were deployed ahead of the passages of typhoons in order to obtain the pre-conditions of the subsurface temperature (D'Asaro et al. 2011; Pun et al. 2011). Meanwhile, along with other sophisticated ocean prediction models, the 2-layer was used to operationally generate synoptic UOTS field for the experiment. It revealed that the 2-layer is of acceptable performance (see Chapter 2).

This valuable AXBT data set provides a unique opportunity to further examine whether REGWNP is suitable for the operational purposes and typhoon applications. In addition, the temperature field generated by NRL's East Asian Seas Ocean Nowcast/Forecast System (EASNFS; Ko et al. 2008, 2009), one of the sophisticated full ocean models operated during the experiment, is

also compared. With a spatial resolution of ~1/16° and 41 sigma levels, EASNFS assimilates *in situ* and historical temperature/salinity profiles, satellite SSHA and SST, providing a real-time analysis of UOTS.

As showing in Figure 4.13, AXBT profiles (circles) compared were obtained from the three US C130 flights on August 28 (in red), August 31 (in green), and September 1 (in blue), 2010. In addition, concurrent Argo profiles (triangles) were also included for the comparison. Figure 4.14 compares T100 from EASNFS, 2-layer and REGWNP with the AXBTs (red) and Argos (blue). It can be found that T100 from Argo profiles shows wider range of T100 than that from AXBTs, particularly on August 31 and September 1. This is because the Argo data scattered over the entire basin, whereas AXBTs concentrated at low latitude, south of 20°N, on these two days (Figure 4.13). Basically, EASNFS and 2-layer both produced reasonable estimates of T100. The root-mean-square (rms) errors with respect to AXBTs and Argos are shown in Tables 4.1 and 4.2, respectively. Compared with AXBTs, the averaged errors in EASNFS and 2-layer are 0.5°C. Compared with Argos, EASNFS has an error of 0.94°C while the 2-layer is slight higher to have an error of 1.1°C. Taking a closer look at the Figure 4.14, we found an obvious warm bias in the 2-layer estimation when T100 is lower than 27°C (middle column of Figure 4.14). In fact, those warm bias points are all located at the north of 19°N, where the 2-layer obviously overestimates T100 (Figure 4.12). Interestingly, EASNFS also overestimated T100 at most of AXBT points on August 28. Nevertheless, it is found that the warm biases associated with the 2-layer are significantly improved by REGWNP. The averaged error in REGWNP-derived T100 is 0.47°C and 0.77°C for AXBT and Argo data, respectively. Clearly, REGWNP is better than the 2-layer and even comparable to EASNFS full ocean model from the UOTS point of view, indicating the high performance of REGWNP. It should be clarified that this comparison result does not imply that REGWNP can replace full ocean models. Models such as EASNFS can produce many other different fields (e.g., three dimensional current velocity and wave fields) and has dynamical considerations. In addition,

full ocean models are able to provide much high temporal resolution (number of outputs a day) and prediction. However, this work merely emphasizes the performance of REGWNP in producing real-time daily UOTS that is comparable to full ocean models.

4.3 Accuracy in other isotherm depths

According to the rigorous validation and comparison, it is found that typhoon-related parameters (i.e., D20, D26, UOHC and T100) derived from REGWNP are of reasonable accuracy. Unlike the two-layer method, the regression method does not limit in producing above parameters. Rather, it is able to estimates UOTS of the whole layer above the base of the thermocline. Figure 4.15 shows the May-October averaged RMSD and correlation between REGWNP and Argo *in situ* observations for D26 to the isotherm at the base of the thermocline. One can see that RMSD for all isotherms is ~20 m in the Gyre, SEZ, and IEZ. In the NEZ, however, the RMSD increases from ~10 m for D26 to ~80 m for the deeper isotherms (Figure 4.15a). As seen in Figure 3.4d, the variation in the depth of isotherms below D17 in the NEZ is typically in a magnitude of ~200 m. Therefore, although RMSD in the NEZ is relatively high, it is deemed to be of reasonable level. It is also noteworthy that the monthly deviation of RMSD is rather small. Even in the NEZ, the monthly derivation is less than 10 m.

The correlation confirms the excellent performance of REGWNP (Figure 4.15b). The depth of most of the isotherms estimated by REGWNP is highly consistent with the observations. Their correlation is generally > 0.8. One can see that the correlation below D18 in the NEZ is fairly high of ~0.9, showing that they are in a good agreement with the observation although RMSD is relatively high (red curve in Figure 4.15a). Low correlations are found for D26-D20 in the IEZ and NEZ. It is because these isotherms are near the surface.

Apparently, using regression method is a promising way for obtaining higher quality UOTS in the western North Pacific Ocean. Like the traditional two-layer method, it is time efficient and

requires less computation power as compared to other sophisticated full ocean models. Therefore, this method is highly appropriate for real-time applications. Indeed, REGWNP has shown a high performance as compared with AXBTs from ITOP. As the continuous growth of Argo floats, the regression coefficients are expected to be improved in the future. Moreover, REGWNP can also be extended to include other months to cover the whole year. Thus, it is believed that this will increase the accuracy and applicability of REGWNP.

4.4 Summary

REGWNP was systematically validated with > 7,000 Argo profiles from 2009 and 2010. The results show that the regression-derived UOTS is of reasonable accuracy. During the typhoon season (May-October), RMSD for D20, D26, UOHC and T100 over the entire basin is less than 30 m, 20 m, 20 kJ cm^{-2}, and 1.5°C, respectively. In addition, no obvious bias is found in the estimations. However, the error varies somewhat considerably with respect to the different zones that increases northward from the Gyre to the NEZ but decreases from May to October. For the use in typhoon research, the applicable zones/months of these derived parameters were identified based on the error of 50%. It is found that applicability of derived D20, D26 and UOHC depends on zones/months. However, T100 is applicable for over the entire western North Pacific, indicating that UOTS estimated from REGWNP is rather reliable. From D26 to the base of the thermocline, the averaged RMSD is ~20 m in the Gyre, SEZ and IEZ, and ~40 m in the NEZ, respectively. The estimated and observed isotherm depths are highly consistent with a correlation of ~0.8.

As compared with the traditional two-layer method (i.e., 2-layer), REGWNP is able to provide more detailed and completed temperature profiles. REGWNP can generate profiles with up to 25 depths, whereas 2-layer only provides four depths. According to the comparison, REGWNP has 20-70% improvement in D20 estimation, 2-32% in D26, and 8-44% in T100. However, the improvement is relatively moderate in UOHC. In addition, REGWNP has less spatial limitation for

UOTS estimation. Further compared REGWNP with AXBTs from ITOP experiment (2010), it is found that REGWNP-derived UOTS is in an excellent agreement with AXBT data, and even comparable to sophisticated EASNFS full ocean model. These results suggest that REGWNP is a useful tool for deriving accurate UOTS in the western North Pacific for typhoon research or other potential applications.

Chapter 5 Eddy identification and variability in the South Eddy Zone of the western North Pacific Ocean

This chapter will develop an automated eddy identification method to objectively identify ocean eddies on SSHA maps. With this method, the variability of warm and cold eddies in the western North Pacific SEZ is investigated.

5.1 Overview of existing eddy identification techniques

Since the success of the satellite altimetric mission TOPEX/Poseidon launched in 1992 (Fu et al. 1994), ocean eddies have been widely observed. This is because sea surface height contains ocean subsurface thermal and dynamical information, which is valuable for studying ocean dynamics and mesoscale (50-500km) variability (Fu et al. 1994; Shay et al. 2000; Le Traon and Morrow 2001; Goni and Trinanes 2003; Lin et al. 2005, 2008, 2009a; Pun et al. 2007). As mentioned in Chapter 1, warm eddies are associated with a warm and anticyclonic flow that leads water to expand and converge, thus forming a higher sea surface height (i.e., positive SSHA) relative to the outer lying water. Conversely, cold eddies are associated with a cold and cyclonic flow that causes water to contract and diverge, resulting in a lower sea surface height (i.e., negative SSHA). Based on these characteristics, satellite SSHA measurements are able to efficiently detect ocean eddies in ice-free oceans. In traditional SST images, however, the warm SSTs (> 29°C) cover nearly the entire western North Pacific Ocean in the summer due to strong solar insolation. Thus, compared with SST, SSHA is considered a much better parameter for identifying and monitoring eddies (Figure 1.4).

Many studies have shown that eddies can be effectively observed and recognized on SSHA maps by visual intuition (Shay et al. 2000; Hwang et al. 2004; Lin et al. 2005, 2008, 2009a); however, this eddy identification approach can be subjective and less accurate, and only suitable for

case studies. For the purpose of studying eddy variability over a long period of time as in the present study, an objective and consistent identification method is needed. However, systematically and objectively determining the properties of ocean eddies, such as their number, size and intensity, in a statistical manner is far more complex than visually detecting them on SSHA maps. In order to have consistency in eddy identification, some criteria for defining eddies on SSHA maps are required. It should be noted that these criteria mainly depend on the features which are to be investigated. Some visual approaches involve identifying eddies using pre-determined criteria (Gründlingh 1995; Siegel et al. 1999; Puillat et al. 2002; Wang et al. 2003; Chow et al. 2008). Wang et al. (2003), for example, studied the South China Sea's Mesoscale eddies using five criteria for eddy identification. In some circumstances, however, eddy patterns in SSHA maps can be highly variable and ambiguous. For this reason, researchers may have to make some subjective adjustments that do not follow their pre-defined rules in order to identify eddies with reasonable accuracy. In addition, some eddy properties, such as size and location, cannot be obtained precisely by visual inspection. These deficiencies of visual methods may affect the quality of research findings, and the results are not likely to be re-examined by other researchers. As a result, the visual methods described here are regarded as less efficient and less objective approaches to eddy identification and are not suitable for long-term variation studies. For this reason, it is particularly important to have a method which is able to automatically and systematically identify eddies.

Isern-Fontanet et al. (2003 and 2006) developed an automated eddy-identification technique by using the Okubo-Weiss (OW) parameter, which is calculated from the SSHA field. This parameter determines the dominant component between the deformation (strain) and rotation (vorticity) of the feature (Isern-Fontanet et al. 2003, 2006; Morrow et al. 2004, Chelton et al. 2007). An SSHA feature is considered to be an eddy only if the rotation component dominates when the OW parameter passes a pre-defined threshold value. Chelton et al. (2007) applied this parameter to automatically identify eddies in global oceans from the SSHA field. However, the occasional

inconsistency between the OW and SSHA fields might introduce some ambiguity into the eddy identification process. For this reason, additional criteria for the SSHA field are also needed to complete the identification process (Morrow et al. 2004). The threshold value of the OW parameter is also critical for eddy identification. However, a constant threshold value is usually used in a global study (Chelton et al. 2007). A recent study conducted by Chelton et al. (2011) utilized the SSHA field solely instead of the OW parameter to develop a more sophisticated approach to automatically identifying eddies in global oceans. Surprisingly, the results obtained using the SSHA-based and OW-based methods showed a very large discrepancy in the number of eddies identified. The SSHA-based method appears to identify up to five-fold more eddies than the OW method (Chelton et al. 2007, 2011). This demonstrates that eddy identification is difficult, and that different approaches may produce different results. In addition, eddy characteristics are highly region dependent (Le Traon and Morrow 2001; Morrow et al. 2004; Chelton et al. 2007, 2011), yet the methods mentioned above usually apply a single algorithm (or a single set of criteria) to global oceans, which may not be suitable for identifying eddies in specific regions like the SEZ.

Therefore, this work attempted to develop a specific method for eddy identification in the SEZ using the satellite SSHA field. Of interest to the typhoon community, the SEZ domain in this chapter is defined as the area of 19°-26°N, 120°-170°N as shown in Figure 5.1, and only the typhoon season (i.e., May-October) are considered.

5.2 Satellite altimetry data

The AVISO's DT merged and gridded SSHA dataset is used in this chapter. The detailed introduction of the AVISO's SSHA data is given in Chapter 3, section 3.1.2. Since this study is focusing on the long-term variability, the homogeneity of dataset is particularly important. For this reason, AVISO's Reference series dataset was adopted for the present analysis. Likewise, this SSHA dataset has quarter degree (1/4°) spatial resolution and on a weekly basis.

Eighteen years of SSHA data spanning the period 1993 to 2010 was used in this study to investigate the eddy variability. In addition, weekly gridded SSHA data were combined to create monthly data so as to minimize the mapping noise and smooth the features, thus facilitating eddy identification and reducing the possibility of misidentification. To do this, weekly SSHA data belonging to the same month were simply averaged to create a monthly gridded SSHA field (Figure 5.2). The eddy identification procedure and subsequent statistical analysis were conducted based upon this monthly dataset.

5.3 Automated eddy identification procedure

As Figure 5.2e shows, numerous eddy-like features can be visually recognized on SSHA contour maps of the SEZ. In such maps, independent groups of closed contour lines reveal eddies. Our automated eddy identification technique was developed based on this characteristic.

5.3.1 Contour lines of SSHA

The contour lines in Figure 5.2 with 2 cm intervals were directly generated by using the contour-drawing function in the Generic Mapping Tools (GMT; Wessel and Smith 1998). This function is based on a triangulation method proposed by Shewchuk (1996) for computing contour lines in the gridded SSHA field without the need for further smoothing and gridding. It is noteworthy that, with this approach, almost all of the primitive features in AVISO's SSHA maps are preserved in the contour field. In other words, the contour field is able to entirely show the SSHA field without distortions.

In this study, the contour lines were created in digital format using 2 cm intervals beginning at a threshold height of ±10 cm SSHA. In fact, many different SSHA thresholds have been employed in previous studies to identify eddies on SSHA maps, but their thresholds were somewhat arbitrary, depending on the authors' purposes and the features of interest. In this study, a threshold of ±10 cm

was chosen in order to minimize the possible noise in the gridded SSHA field. Furthermore, small eddies with minor amplitudes are considered to have little impact on typhoon intensity; thus, using a high threshold (i.e., 10 cm) is appropriate for studying eddy variation in typhoon intensity research.

5.3.2 Criteria for the eddy identification procedure

In this research, the automated eddy identification process was carried out using closed contour lines in SSHA maps. Some specific criteria were designed based on five possible scenarios that commonly occur in the SEZ. For the sake of brevity, the criteria and scenarios introduced below are for warm eddies (i.e., positive SSHA features). To obtain corresponding criteria and scenarios for cold eddies (i.e., negative SSHA features), the signs simply need to be reversed.

Basically, two criteria are required throughout the entire procedure: (1) contour lines must be closed, and (2) SSHA must $\geqq$ 10 cm. The five scenarios are described below and illustrated in Figure 5.3:

Scenario #1: Individual eddy

This type of eddy is identified when at least 3 closed contour lines exist within the same feature and are enclosed by an outermost contour line of 10 cm. Figure 5.3a shows an example of an isolated eddy, whose outermost contour line is 10 cm and innermost contour line is 16 cm.

Scenario #2: Merged eddies

Consistent with previous findings (e.g., Lin et al. 2008; Qiu and Chen 2010), Figures 5.2 show that the SEZ eddy field is rather dynamic: eddies merge and interact with one another, causing them to become interconnected. It is also noteworthy that individual eddies (i.e., Scenario #1) are comparatively less frequent in the SEZ. Instead, more complex features are formed due to interaction among eddies. As a consequence, the threshold contour (10

cm) is not able to separate adjoining eddies located within compound features (Figure 5.2e and 5.3b). For this reason, an additional criterion is included in our procedure to handle merged eddies. When two or more contour groups are located within the same larger feature, which is enclosed by a closed 10 cm contour line, each contour group containing at least 2 closed contour lines is recognized as an isolated eddy (Figure 5.3b).

Scenario #3: One contour eddy

This is a special case of Scenario #2 where only one independently closed contour line exists inside a complex feature. In Figure 5.3c, there are two smaller features within the same complex feature, but one of them consists of only one closed contour line. According to the Scenario #2 criterion explained above, this sub-feature would not be recognized as an eddy. Rather, the entire complex feature would be treated as one single eddy. Apparently, the smaller features ought to be counted as two separate eddies because they manifest eddy-like patterns. To fix this problem, eddies consisting of only one closed contour line are counted only if the SSHA of the contour is equal to or greater than 16 cm and the area enclosed by the contour is greater than 7,850 km^2, which is equivalent to a radius of 50 km.

Scenario #4: Double-core eddy

Occasionally, fine features appear near the center of eddies, a circumstance that complicates the eddy identification process. Figure 5.3d shows an eddy with two cores (i.e., two individual innermost contours). To help the eddy identification procedure determine whether this type of feature is a single eddy or multiple eddies, one criterion is proposed: the minimum distance between the innermost contours. In this study, the threshold of the minimum distance was taken as 150 km. Thus, two situations need to be considered: (1) if the minimum distance is less than 150 km, then the contour with the smaller area is ignored, and the entire feature is considered to be a single eddy; (2) if the minimum distance is equal to or greater than 150 km, then an additional criterion, the area within the smaller

contour, is required. When this area is greater than 7,850 km^2 (i.e., radius = 50 km), each innermost contour is considered to be an individual eddy. But when the area within the smaller contour does not meet this standard, then the smaller contour is omitted, and the whole feature is viewed as a single eddy. An example is shown in Figure 5.3d, where the minimum distance between the two innermost contours does not satisfy the criterion; thus, the whole feature is identified as a single eddy.

Scenario #5: Cross-boundary eddy

As eddies travel across the western North Pacific, they move in and out of the SEZ. At times, an eddy straddles one of the boundaries of the SEZ. To decide whether such an eddy lies within the SEZ, a clear criterion is needed. If more than half of the area within the outermost contour lies within the domain of the SEZ and part of the innermost contour is in contact with the SEZ, then the entire eddy is considered to belong to the SEZ. Two contrasting examples are shown in Figure 5.3e.

Figure 5.4 shows the flow chart of the eddy identification procedure. The criteria for the above five scenarios were coded to create a computer procedure, which is able to automatically identify eddies on SSHA contour maps. There are two advantages of using this procedure: (1) ambiguity is avoided throughout the entire study, and (2) the efficiency of the eddy identification process is increased. Figure 5.5 shows an example of multiple eddies identified on the SSHA map from August 2004. On this map, the eddies indicated by red contour groups were recognized by the automated procedure as individual eddies. It can be found that the procedure performed fairly well in that 13 warm eddies were objectively identified on this SSHA contour map. Although the procedure is automatic, all of the eddies identified in this study were double-checked manually to ensure the accuracy of identification.

Because the present procedure does not require any manual adjustments, the results are objective, coherent, and systematic. Furthermore, additional information about eddies, i.e., their

number, amplitude, and size, is also yielded by this automated procedure.

5.4 Results of eddy variability in the SEZ

5.4.1 Eddy number

Based on the automated eddy identification procedure, a total of 1,758 eddies were identified in the SEZ from the 108 monthly SSHA contour maps available for the summer months (May-October) of 1993 to 2010. Figure 5.6 shows the total number of eddies identified in each year. It should be noted that this annual number is the sum of the eddies that identified in monthly maps from May to October. On average, about 98 eddies ±13 were identified each summer (a total of 6 monthly SSHA maps) in the SEZ. It can be found that there was interannual variability over the whole period. During the first 5 years (1993-1997), the annual number of eddies steadily increased with a rate of ~4 eddies per year. During the remaining years (1998-2010), the total number fluctuated significantly: the year-to-year difference was as high as 39 eddies, which occurred between 2001 and 2002. Notably, no significant overall trend in the total number of eddies in the SEZ was detected (Figure 5.6).

As shown in Figure 5.6, the number of warm eddies was significantly greater than that of cold eddies. The total numbers of warm and cold eddies identified were 1,067 and 691, respectively. Thus, warm eddies outnumbered cold eddies by about 50%. This tendency of warm eddies to outnumber cold eddies in the SEZ is in a good agreement with the findings of Hwang et al. (2004), who observed that warm eddies were dominant in the STCC region. Chelton et al. (2011), on the other hand, reported that the global numbers of warm and cold eddies did not show substantial polarity; their numbers were almost equal. This inconsistency was likely due to the fact that the study by Chelton et al. (2011) was a global census that may not have reflected regional variability. Therefore, our results imply that the numbers of warm and cold eddies have a strong geographical dependence. In addition, Figure 5.7 shows that on a monthly basis, the number of eddies peaked in

early summer (i.e., May and June) and gradually decreased through October. This finding is consistent with those of Qiu (1999) and Qiu and Chen (2010), who showed that the dynamic field in the SEZ clearly exhibits a seasonal cycle, with the eddy kinetic energy (EKE) being higher in summer and lower in winter. A closer examination of Figure 5.7 reveals that the number of cold eddies decreased from May to October, while that of warm eddies remained relatively steady but with slightly lower numbers in early and late summer (Figure 5.7). Detailed statistics for the number of warm and cold eddies for each month of each year are shown in Table 5.1.

It should be pointed out, however, that some eddies in Figure 5.6 were likely counted more than once as they propagated westward since eddies can normally last up to several months (Hwang et al. 2004; Chelton et al. 2011; Qiu and Chen 2010). To avoid this problem, this work adopted the monthly average number of eddies, which indicated how many eddies actually occurred on a monthly basis. Figure 5.8 shows the time series of the monthly average numbers of warm and cold eddies. Compared with Figure 5.6, it gives more insights into the variability of warm and cold eddies. It is interesting to note that the numbers of warm and cold eddies exhibited not only interannual variation but also trends over the whole study period, which are not visible in Figure 5.6. Between 1993 and 2010, the numbers of warm and cold eddies exhibited opposite trends. The number of cold eddies decreased significantly by 51% from 8.6 to 4.2 at a rate of -0.26 per year. Meanwhile, the number of warm eddies increased by 19% from 9 to 10.7 at a modest rate of 0.09 per year, which is less than 95% statistically significance. It is worth mentioning that the calculation of the trends in this dissertation is based on the least squares fitting and the significance level is based on the t-test[6]. In addition, El Nino signals, such as the 1994/1995, 1997/1998 and 2002/2003 events, are also captured in both time series. During El Nino years, the number of warm eddies in

[6] $t = r\sqrt{\frac{n-2}{1-r^2}}$, where t is t-value, r is correlation coefficient, and n is sample size. The significance level can be obtained via the t distribution table by given t-value. In this study regarding 18-year annual time series, the trend is at 95% significance when the t-value is $\geqq$ 2.12.

the SEZ tended to grow, while the number of cold eddies fell. Furthermore, the numbers of warm and cold eddies were similar at the beginning of the time series but started to diverge in 1997, after which the numbers of both types of eddies became substantially different. Between 1993 and 2010, there were, on average, 40% more warm eddies per month than cold eddies, and the monthly average numbers of warm and cold eddies were approximately 10 and 6, respectively. It is also worth noting that the degree of annual variation of both types of eddies was higher after 1997. This transition in 1997 may have been caused by a large scale regime shift or mean sea level rise.

Over the entire study period, a negative correlation of -0.36 was found between the numbers of warm and cold eddies, indicating that the numbers of warm and cold eddies in the SEZ tended to vary in opposite directions. In general, when the number of warm eddies increased, the number of cold eddies decreased and vice versa. Thus, the increase in the number of warm eddies compensated for the decrease in the number of cold eddies, causing the total number of eddies (i.e., warm + cold) to remain relatively steady. To further demonstrate this tendency, Figure 5.9 shows the year-to-year changes in the numbers of warm and cold eddies. For instance, in 1994, the number of warm eddies increased by 2.5 compared with 1993, whereas the number of cold eddies decreased by 1.2. Although the numbers of warm and cold eddies moved in opposite directions in most years, exceptions existed. As shown in Figure 5.9, in 2002, 2005 and 2009, the numbers of both types of eddies decreased concurrently, and in 2006, they both increased. These changes resulted in three local minima and one local maximum in the total number of eddies (Figure 5.6). This may imply that the ocean conditions in the SEZ were unfavorable for both warm and cold eddies in 2002, 2005 and 2009, but favorable for them in 2006.

Figure 5.10 compares the time series of warm and cold eddies in each month from May to October. It is interesting to note that the number of warm eddies (red curves) increased more significantly in May than in the other months, demonstrating that the overall warm eddy trend shown in Figure 5.8 was mainly due to the increased number of warm eddies in May. In the other

months, the number of warm eddies increased gently. In comparison, the number of cold eddies (blue curves in Figure 5.10) declined considerably during all of the summer months. However, it should be noted that the steepest decrease in the number of cold eddies was also found in May. Nevertheless, May was the month when the number of cold eddies peaked and even exceeded that of warm eddies (Figure 5.7). The number of cold eddies throughout the summer months showed a decreasing trend, which is the reason for the more significant overall trend in the monthly average number of cold eddies shown in Figure 5.8.

Figure 5.11 shows the time series of the monthly average numbers of warm and cold eddies superimposed on time series showing the maximum and minimum monthly numbers of warm and cold eddies during each typhoon season. It can be found that the minimum number of warm eddies increased significantly during the study period, while the maximum number remained steady (Figure 5.11a). The rate of increase in the minimum number of warm eddies was 0.2 per year, which was more significant than the overall trend (red line in Figure 5.8). This implies that the increase in the monthly average number of warm eddies was largely due to the increase in the minimum number during each summer season. Interestingly, the behavior of cold eddies was nearly opposite to that of warm eddies. As shown in Figure 5.11b, the maximum number of cold eddies dropped dramatically at a rate of -0.38 per year. In contrast to warm eddies, the minimum number of cold eddies exhibited a decreasing trend but with a rate of -0.19 per year.

5.4.2 Eddy amplitude

Figure 5.12 compares the variation in the amplitude of warm and cold eddies during the study period. Here, amplitude means the absolute maximum SSHA (i.e., the inner core SSHA) of each eddy; thus, the amplitudes of cold eddies are positive. It can be found that the amplitude of warm eddies enhanced dramatically at a rate of 0.2 cm yr^{-1} and exhibited rather large interannual oscillation with a peak amplitude of 26.5 cm in 2003. During the study period, the interannual

difference was as much as approximately 8 cm, which occurred between 2000 and 2003, and was equivalent to about 37% of the average amplitude of warm eddies. Compared with warm eddies, the overall trend and interannual variation in the amplitude of cold eddies were relatively moderate. The amplitude of cold eddies decreased at a rate of -0.15 cm yr^{-1}. However, the degree of amplitude variation tended to relax after 2002.

Because the above trends in the eddy amplitude were observed, it was worthwhile to further investigate the variation in the number of eddies with different amplitudes. Therefore, the eddies discussed in the previous section were split into three groups based on their amplitudes. Group 1 consisted of eddies with amplitudes greater than 30 cm; Group 2, amplitudes between 20 and 30 cm; and Group 3, amplitudes less than 20 cm. Figure 5.13 shows the numbers of both warm and cold eddies in these three groups. In Group 1, warm eddies were more numerous than cold eddies. In addition, the number of warm eddies tended to increase, whereas that of cold eddies tended to decrease although the change was less pronounced. In the early 1990s, there were some cold eddies in Group 1, but after 2002, there were very few (Figure 5.13a). In Group 2, there were slightly more cold eddies than warm eddies before 1997. However, this trend reversed after 1997, when the number of warm eddies was three times greater than that of cold eddies. Finally, in Group 3, the numbers of warm and cold eddies were comparable and relatively stable; except in 2010, warm eddies were much more than cold eddies. These findings imply that the number of warm eddies with higher amplitude (> 20cm) increased, while that of cold eddies decreased.

5.4.3 Eddy size

It is also interesting to investigate how the size of warm and cold eddies varies in the SEZ since their size is one of the factors that determine the area and duration of interaction between eddies and typhoons. However, comparing the sizes of warm and cold eddies is difficult because the bases (i.e., the outermost contours) of identified eddies are not often in the same level. In Figure 5.5,

only the independent eddies have a complete set of contours, in which, as defined previously, the amplitude progresses from 10 cm at the outermost contour to the peak amplitude at the core. In fact, most of the observed eddies are merged with others. In each case of merged eddies, the amplitude of the outermost indentified contour of each eddy is higher than 10 cm (Figure 5.3).

It is not possible to compare the sizes of eddies if different base amplitudes are employed. To conquer this problem, in the case of merged eddies, the base amplitude of each eddy was adjusted to 10 cm. Figure 5.14a presents the relationship between the area enclosed by each contour and its SSHA value for all of the eddies identified in August 1995, consisting of five independent eddies and four merged eddies. In Figure 5.14a, each curve represents one eddy. The solid dots in each curve denote the real contours of that eddy. Therefore, one can see that the five solid dots at 10 cm represent the outmost contours of the five independent eddies. It is important to note that the relationship between the contour area and SSHA value exhibits negative linear correlation; i.e., the higher the SSHA value, the smaller the area (except for one eddy that has two different slopes (the pink curve) due to irregular features in its 10- and 12-cm contours). Based on this correlation, it was able to extrapolate the areas enclosed by the contours of each merged eddy back to 10 cm as indicated by the open dots in Figure 5.14a. Apparently, the results are reasonable as shown in Figure 5.14a. However, as pointed out in section 5.3.2, there is a scenario in which an identified eddy only contains one contour. In this situation, extrapolation cannot be applied; thus, an average slope between the contours and their enclosed areas was used. The scatter plots shown in Figure 5.14b demonstrate the relationship between the location of each contour (from innermost to outermost) and its enclosed area for each eddy identified in August from 1993 to 2007. For this purpose, numbers to the contours of each eddy were assigned, beginning with 1 for the innermost contour. Based on the 1993 to 2007 subset, an empirical formula for estimating the area (A) enclosed by a 10 cm contour in the one-contour situation was obtained:

$$A = 9471.1x - 878.66 \qquad (5.1)$$

where x is the total number of contours, which consists of the original contour plus contours extrapolated out to 10 cm at 2 cm intervals. For example, if an eddy consists of only one contour at 20 cm, then x will be 6 (including the 10 cm contour); therefore, the estimated size of this eddy will be 55,948 km^2. Consequently, the size of a one-contour eddy based on the 10 cm contour standard can be obtained by using equation (5.1). The circles shown in Figure 5.5 indicate the sizes of the identified eddies, in which the area of each circle is equivalent to the area enclosed by the 10 cm contour. One can see that they match the original SSHA pattern very well, indicating that the size estimation is reasonable. For scientific intuition for eddy size, the area of eddy was converted to radius by assuming that the eddy is round as shown in Figure 5.5.

Figure 5.15 shows the time series of the annual averaged radii of warm and cold eddies. It can be found that the radius of warm eddies increased by 19% from 140 to 166 km at a rate of 1.5 km yr^{-1}, whereas the radius of cold eddies decreased by 21% from 140 to 111 km a rate of -1.7 km yr^{-1} during the study period; simultaneously, there were explicit interannual variations. It is noteworthy that interannual oscillations of warm and cold eddies were completely out of phase at the time prior to 2006, but they turned to in phase afterward (Figure 5.15). Table 5.2 summarizes the trends and changes in the properties of warm and cold eddies in the SEZ from 1993 to 2010.

5.5 Discussion

5.5.1 Issue of the eddy identification method

In this chapter, the procedure for automated identification of eddies in the SEZ was developed. For this procedure, the criteria for identification were established based on the monthly SSHA features in the SEZ. Furthermore, the criteria themselves were examined multiple times in order to obtain the correct features of eddies. In addition, all of the eddies identified in the present study were double-checked manually in order to reduce the possibility of misidentification of eddies and to ensure high quality identification. Therefore, it is believed that the identification procedure is

reliable.

However, given the realities of the sea level rise and background warming, it is extremely difficult to differentiate the signals between the warming and eddies from the SSHA observations. In this situation, the eddy trends found in this study may be somewhat overestimated due to the contamination of the mean sea level change. On the other hand, it cannot be ruled out that the changes in eddy field in turn alter the mean sea level. This complexity makes it nearly impossible to extract pure eddy signals from now available observations. As a result, the trends in warm and cold eddies showed in section 5.4 is more suitable to be treated as the upper-bound rates.

In addition, the monthly SSHA was used in this analysis. However, an eddy cannot be tracked using monthly data since the temporal resolution is too large and the amplitudes of eddies are unavoidably weakened by monthly smoothing (Figure 5.2e). The contour interval and the SSHA threshold for eddy identification were 2 cm and 10 cm, respectively. The former is used to reduce the complexity and computation time, and the latter has two purposes: (1) to increase the signal to noise ratio, and (2) to limit the identified eddies to those which are large enough to have a significant impact on typhoon intensification. Both settings can be modified and tested for different purposes.

5.5.2 Comparison with the results obtained using another eddy identification procedure

Chelton et al. (2011) also developed an automated eddy identification procedure for globally identifying ocean eddies from AVISO's weekly SSHA field. Their method also contains sophisticated criteria for detecting eddies on SSHA maps, but no threshold is needed. Instead, when the procedure encounters closed SSHA contours, it begins to diagnose the features. The details of this procedure are referred to Chelton et al. (2011). However, it is interesting to compare the results from Chelton et al. (2011) and from the present study.

The global mesoscale eddy dataset of Chelton et al. (2011) spinning over the 16-year period

from October 1992 through December 2008 is available at http://cioss.coas.oregonstate.edu/eddies/. The information contained in the dataset includes locations, amplitudes, radii, translation speeds, etc. of eddies. Figure 5.16 shows an SSHA map with eddy locations on August 25, 2004 as identified by Chelton et al. (2011). It should be noted that the SSHA data they used were filtered using a spatial high-pass filter to remove the seasonal signals; thus, some features may have been lost from the original SSHA data. Nevertheless, their global approach was able to capture most of the eddies in the SEZ (the eddies identified by Chelton et al. (2011) are depicted using yellow and pink dots). However, a warm eddy like the feature at location "A" in Figure 5.16 could not be recognized, perhaps due to the use of spatial filtering and their global criteria. Interestingly, some relatively small eddies, such as the one at location "B" in Figure 5.16, were identified. The possible reason is that their method does not employ a threshold. However, such small scale eddies that are less important to typhoon intensification are filtered in the present study by using a threshold of 10 cm in the identification procedure.

Figure 5.17 compares the time series of warm and cold eddies identified by Chelton et al. (2011) with that obtained in the present study. Because the spatial high-pass filter was applied by Chelton et al. (2011), no overall trend is preserved in their time series (dashed curves). In order to make a comparison, the time series from this study was detrended (solid curves). One can see that the numbers of warm and cold eddies identified by Chelton et al. (2011) are generally greater than those obtained in the present study, probably because no SSHA threshold was employed in their eddy identification procedure. However, the eddy variations observed using both methods are similar with R=0.5 for warm eddies and R=0.4 for cold eddies. This suggests that these two methods are qualitatively comparable, and the trends in warm and cold eddies observed in the present study may be partially caused by the background warming.

5.5.3 Issue of eddy variability and typhoon intensification in the SEZ

As shown in section 5.4, the variations of warm eddies and cold eddies in the SEZ are significantly different. Over time, all three main properties of warm eddies (i.e., their number, amplitude, and size) tend to enhance, implying that warm eddies in the SEZ store more heat and the chance of typhoon encountering increases. In addition, the increase in the size of the warm eddies suggests that both the area and time of interaction between warm eddies and typhoons also increased. The behavior of cold eddies in the SEZ, however, was nearly opposite to that of warm eddies. It is expected that the influence of cold eddies on typhoons would reduce.

In order to further quantify these changes in typhoon related quantities, the corresponding changes in D26 (i.e., warm water layer) and UOHC were evaluated by using a two-layer reduced gravity model, i.e., the equations (2.1) and (2.2) in Chapter 2. In this evaluation, $\overline{D20}$, $\frac{\rho_2}{\rho_2 - \rho_1}$, θ, SST and MLD were prescribed by the seasonal (May-October) average of the SEZ mean. The values and sources of these parameters are summarized in Table 5.3.

Figure 5.18 shows the corresponding D26 and UOHC with respect to the variation in the monthly average amplitude of warm and cold eddies. It can be found that both D26 and UOHC in warm and cold eddies exhibit increasing tendency. During the study period, the average D26 increased by 4 m from 76 to 80 m in warm eddies, and 2 m from 38 to 40 m in cold eddies. This is equivalent to ~5% of D26 increases in both types of eddies (Figure 5.18a). Meanwhile, average UOHC increased 2 and 1 kJ cm^{-2} in warm and cold eddies, respectively, equivalent to ~3% increases (Figure 5.18b). It should be noted that these are very rough estimations computed with fixed parameters (Table 5.3). Especially in the calculation of UOHC, the variations in SST and MLD are also important. In fact, SST in the western North Pacific has been warming in the past few decades (Rayner et al. 2006; Emanuel 2005; Webster et al. 2005). Therefore, more UOHC increase is expected in eddies. As in Figure 5.18, one can see that the differences of D26 and UOHC between warm and cold eddies can be ~50 and ~40%, respectively. This demonstrates that the

presence of warm and cold eddies in the SEZ is fairly critical in typhoon intensification.

These findings suggest that there is a greater tendency for warm eddies to form in the SEZ than cold eddies. Simultaneously, warm eddies become warmer and larger. It can be expected that the variations of warm and cold eddies causes the ocean conditions in the SEZ to be more favorable to typhoon intensification. Figure 5.19 illustrates 18 years of typhoons with intensity $\geqq$64 kts (i.e., Category 1) in the western North Pacific during May to October from 1993 to 2010. The high density of typhoon tracks clearly indicates the immense typhoon activity in this basin, threatening the surrounding areas. It is extremely important that over 80% of typhoons in the western North Pacific pass through the SEZ (green box) during their lifetimes. This large number of typhoons would benefit from the enhancement of warm eddies as they travel over the SEZ. Therefore, it is expected that both typhoon intensity and the possibility of the occurrence of rapid intensification will increase in the future.

On the other hand, the activity of warm and cold eddies in the SEZ also apparently exhibits interannual variations. These variations might also affect typhoon intensity changes interannually. Figure 5.20 compares the eddy fields during September in 2000 and 2003. Distinct differences between the activities of warm and cold eddies are found. Warm eddies were much larger and warmer in 2003 than in 2000. It appears, however, that cold eddies were more active in 2000 than in 2003. It is anticipated that such manifest changes in the eddy field substantially alter the upper ocean conditions in the SEZ and eventually influence typhoon intensification. Further investigation of eddy variations and typhoon intensification is needed to confirm this speculation.

As mentioned in section 5.4.1, the eddy variability in the SEZ contains some signals from interannual oscillation such as ENSO. However, the results show that eddy variability cannot be fully explained by just one single climate event. The intricate climate variations at different times and on different spatial scales should also play important roles in eddy variability. For instance, Qiu and Chan (2010) indicated that the SEZ's eddy activity may, in part, correspond to the negative

western Pacific (WP) index. Interestingly, there was an obvious abrupt change in eddy variability around 1997 (e.g., Figure 5.8) that might correspond to longer climate variability or a large scale regime shift. Given the limited amount of data available at this time, it is not yet possible to fully explore the link between decadal and eddy variability. However, this is worthwhile to investigate in the future.

5.6 Summary

Objectively identifying eddies on SSHA maps is rather difficult. In this chapter, an automated eddy identification procedure has been developed exclusively for typhoon intensification research in the SEZ of the western North Pacific. This automated procedure provides an objective, systematic, and effective way of identifying mesoscale ocean eddies on SSHA maps. The results prove that the procedure is able to identify eddies in the SEZ with high degree of reliability. In addition, it also enables separate investigation of the long-term variability of warm and cold eddies, which have opposite effects on typhoon intensification.

A total of 1,758 eddies were identified in the SEZ from 18 years (1993-2010) of merged SSHA data during the summer months from May to October. Among them, warm eddies totaled 1,067 and cold eddies 691, and both types showed long-term trends and interannual variation. Careful analysis of their properties, i.e., their numbers, amplitudes, and sizes, was conducted. During the 18 years, warm eddies increase 19% in number, 17% in amplitude (equal to 4.5% and 3% increases in D26 and UOHC), and 19% in radius. In contrast, cold eddies decrease 51% in number, 13% in amplitude (equal to 6.6% and 3% increases in D26 and UOHC) and 21% in radius.

Because D26 and UOHC in the SEZ is very sensitive to the occurrence of eddies, the variations of eddies may directly be linked to typhoon intensity. However, this study shows that the activity of warm eddies in the SEZ tends to strengthen over time, while that of cold eddies weakens. Moreover, these shifts are believed to affect UOTS. As a result, the ocean conditions in the SEZ are

becoming more favorable for typhoons. In addition, significant interannual variability has been detected in the SEZ's eddy field. This alters the ocean conditions from year to year and might also affect typhoon intensification interannually.

Chapter 6 Changes in ocean conditions in the western North Pacific typhoon intensification region

Chapter 5 has already investigated the eddy variability in the SEZ, which is only a part of the main typhoon intensification region of the western North Pacific. Meanwhile, there may be some uncertainties in the eddy variability because the signals are likely to be mixed with the possible background warming. From the typhoon perspective, however, either the background or eddies changes would eventually impact on typhoon intensity. Therefore, this chapter will explore the long-term variability in UOTS and ocean features regardless of eddies or not in the western North Pacific typhoon intensification region. The study period is from 1993 to 2010, and only focuses on the main typhoon season, June to October, of the western North Pacific.

6.1 Typhoon intensification zone of the western North Pacific Ocean

Figure 6.1 illustrates the geographical distribution of typhoon intensification in the western North Pacific Ocean. This map was counted by 1° x 1° bins from the JTWC's 6-hour best track data from 1970-2008. For each typhoon track, only the intensification segment from the first point of Category 1 of Saffir-Simpson Scale (Table 1.1) to the peak intensity is considered. Clearly, it can be found that the intensification of typhoons commonly takes place in the area enclosed by 122-170°E, 10-26°N. Based on this statistic, we defined this region as the main typhoon intensification region of the western North Pacific and it is the primary focus of the present study.

From the ocean point of view, the main typhoon intensification region covers two distinct hydrographical regions in the western North Pacific Ocean. Figure 6.2 shows the SSHA map from September 8, 2010. The northern part within a latitudinal band of 19-26°N is the well-known SEZ, in which energetic mesoscale eddies exist all year round (see Chapter 3, section 3.2). The southern part of the typhoon intensification zone (10-19°N) belongs to the regime of the western subtropical

gyre (Gyre; Lin et al. 2008). The common features in this region are large-scale variations associated with basin-wide climate events, such as El Niño and La Niña. As shown in Figure 6.2, the large area of positive SSHA (>10 cm) dominates in the Gyre. This is because 2010 is a classical La Niña year (Johnson et al. 2011), during which abnormal warm water gathers in the western part of the Pacific Ocean, resulting in the higher sea surface height. It is worth mentioning that the areas of the SEZ (122-170°E, 19-26°N) and Gyre (122-170°E, 10-19°N) defined here are slightly different than that in the previous chapters. The purpose of this analysis is to investigate the UOTS and ocean feature variability in these two regions.

6.2 Methodology and Data

Assuming that the changes in SSHA are purely due to the thermal expansion effect in the water column, the UOTS data used in this analysis is derived on a weekly basis from satellite altimetry SSHA and optimum interpolation (OI) SST data by using the 2-layer method that has been introduced in details in Chapter 2. For purpose of studying the long-term variability, the AVSIO's Reference series DT weekly SSHA data is used. See Chapter 3 for the detailed information about this dataset.

For the SST, 1° weekly OI SST analysis version 2.0 (Reynolds et al. 2002) from NOAA/ National Centers for Environmental Prediction (NCEP) is used. Two reasons are considered for choosing this OI SST dataset. First, the record length of this dataset, i.e., 1981-present, is long enough to cover the period of SSHA data starting at the end of 1992. Second, this OI SST dataset is primarily designed for climate research and long-term applications (Reynolds et al. 2002), which fits the purpose of the present analysis. In fact, the OI SST is based mainly on the satellite infrared SST observations from the Advanced Very High Resolution Radiometer (AVHRR). However, the satellite SST is carefully calibrated with *in situ* measurements from ships, drifting and moored buoys. The combination of satellite and *in situ* data can substantially reduce the satellite bias.

According to Reynolds et al. (2002), the globally averaged bias is about -0.03°C in the OI SST dataset. Therefore, the NCEP OI SST is considered a high-accuracy and stable SST product that suits for long-term analyses. Both weekly data of SSHA and SST are centered on Wednesday; hence no further effort is needed to fit these two data sets in the same temporal basis. As the OI SST is on 1° resolution, the SST data are linearly interpolated into 0.25° grid to match the SSHA data.

For studying the variability in ocean features, the areas of the positive (usually representing a warm situation) and negative (usually representing a cold situation) features on the SSHA maps are directly calculated regardless if the features are recognized as eddies or not. Following the threshold in the eddy identification procedure in Chapter 5, positive, negative and no features are defined as SSHA $\geqq$10 cm, SSHA $\leqq$10 cm, and SSHA between -10 and 10 cm, respectively.

6.3 Results

This section will present the 18-year (1993-2010) variations in ocean conditions in the typhoons intensification zone of the western North Pacific based on the satellite-based observations.

6.3.1 Variability in SST and SSHA

Figure 6.3 shows the timer series of annual (June-October) regional mean SST and SSHA for the SEZ and Gyre between 1993 and 2010. One sees that both SST series (Figure 6.3a) display noticeable interannual variability as well as slightly warming trends, although the trends are not statistically significant (< 95%). This is probably due to the relatively short time period of 18 years. Nevertheless, the linear trends of mean SST are 0.004 and 0.01°C yr^{-1} for the SEZ and Gyre, respectively. Both trends generally agree with the global SST warming trend (Rayner et al. 2006). Again, the trends are based on the least squares fitting and the significance level is based on the t-test. In addition, it is found that the interannual variability of both SSTs is likely to be dominated by El Niño events; the correlation between Oceanic Niño Index (ONI; Figure 6.4) and SST is -0.66

for the SEZ and -0.42 for the Gyre. The negative correlation comes out with the fact that the ONI is computed based on the SST anomalies in the Niño 3.4 region (5°N-5°S, 120°-170°W). However, the behavior of the western Pacific is virtually opposite to the Niño 3.4 during the El Niño (Wyrtki 1979; Philander 1990; Johnson et al. 2000). Similarly, SSHA (Figure 6.3b) also exhibits apparent interannual variability but with more significant upward trends. Over the 18 years, the mean SSHA has increased by 5 cm at a rate of 0.30 cm yr^{-1} in the SEZ. However, the increasing rate is more than double in the Gyre to 0.77 cm yr^{-1}, increasing by 13 cm. Both SSHA trends are at 99% significance level and consistent with the global mean SSHA rising rate of 0.33 cm yr^{-1} (Cazenave et al. 2011). Because SSHA is linked to the temperature variations in the subsurface, especially in the upper ocean (White and Tai 1995; Willis et al. 2003), thus the increase in SSHA implies that the upper ocean has also undergone warming. In addition, it is found that the amplitude of the interannual variability of the mean SSHA is greater in the Gyre than in the SEZ. In contrast to the SST, only the Gyre mean SSHA has a close relation with the El Niño (R ~ -0.65), suggesting that the variations in the sea surface and subsurface are generally consistent in the Gyre, but not the case in the SEZ. This is also implying that the SSHA (subsurface temperature) variations in these two regions are controlled by different mechanisms. For the SEZ, the enhanced eddy activity may be the cause for the SSHA variation on interannual time scale.

6.3.2 Variability in UOTS

Figure 6.5 illustrates the 18-year time series of four satellite-derived upper ocean thermal parameters that are commonly used to characterize the ocean conditions for typhoon intensification for the SEZ and Gyre. These parameters include the D20 used to represent the thermocline depth (Figure 6.5a), D26 used as a proxy for the thickness of warm water layer (Figure 6.5b), UOHC (Leipper and Volgenau 1972) which is the heat content exceeding 26°C integrated from the surface to D26 (Figure 6.5c), and the averaged temperature of upper 100 m (T100; Price 2009) used to

approximate the typhoon-induced SST cooling (Figure 6.5d). Apparently, all of these parameters exhibit increasing trends and year-to-year variability in the typhoon intensification region. The values of the subsurface parameters are usually higher in the Gyre than in the SEZ. This is mainly due to their geographic locations. In addition, the trends of these parameters are also greater in the Gyre as well. During the 18-year study period, in the SEZ, D20 and D26 have deepened significantly by 15 and 5 m at rates of 0.9 and 0.3 m yr^{-1} (with 99% significance level), respectively. Meanwhile, UOHC and T100 have increased by 5 kJ cm^{-2} and 0.16°C at rates of 0.3 kJ cm^{-2} yr^{-1} and 0.01°C yr^{-1}, respectively, although they are less statistically significant. It is worth noting that the trends of UOHC in the SEZ is about 50% greater than that in the Gulf of Mexico (0.2 kJ cm^{-2} yr^{-1}; Goni et al. 2009), where is also the well-known eddy-enhanced region in the Atlantic basin. In the Gyre, D20, D26, UOHC and T100 have undergone significant trends of 1.7 m yr^{-1}, 1 m yr^{-1}, 1.1 kJ cm^{-2} yr^{-1}, and 0.02°C yr^{-1}, respectively. All of the trends in the Gyre are at 99% significance level, except T100, which is at 98% significance level. Over the whole period, the Gyre mean D20 increased by 30 m, D26 by 17 m, UOHC by 19 kJ cm^{-2}, and T100 by 0.35°C. The detailed changes in these four parameters in the SEZ and Gyre are summarized in the Tables 6.1 and 6.2, respectively. It is interesting to note that, in both regions, the trends of T100 are nearly twice as high as that of SST, implying that subsurface undergone greater warming.

6.3.3 Variability in ocean features

Figure 6.6 illustrates the time series of the annual percentages of total areas of positive, negative and no features in the SEZ and Gyre. The positive, negative and no features are defined as SSHA $\geqq$10 cm, SSHA $\leqq$10 cm, and SSHA between -10 and 10 cm, respectively. In the SEZ over the study period (Figure 6.6a), the total area of positive features increased at a rate of 0.7% yr^{-1}, while the total area of cold features decreased at a rate of -0.8% yr^{-1} and the total area of no feature remains no change. This result suggests that warm eddies occur more frequently in the SEZ,

consistent with the results of Chapter 5. In the Gyre (Figure 6.6b), the total area of positive features increased sharply from 7 to 65% at a rate of 3.4% yr^{-1}. At the same time, the total area of no features decreased substantially from 81 to 35% at a rate of -2.7% yr^{-1}, whereas the total area of negative features decreased at a relatively gentle rate of -0.7% yr^{-1}. We found that during the recent years in the Gyre, the negative features nearly vanish while the positive features become more dominant, suggesting that ocean conditions in the Gyre is shifting to the La Niña-like condition. The rapid increase in positive features also explains the higher rate of the subsurface warming in the Gyre in Figure 6.5. Tables 6.3 and 6.4 summarize the changes in the percentage of the total area of the ocean features over 1993-2010 for the SEZ and Gyre, respectively.

6.4 Discussion

6.4.1 Issue on satellite-estimated UOTS trends

In this analysis, UOTS was estimated from high-quality satellite altimetric data. The estimation, however, is based on the assumption that variations in sea surface height are due purely to thermal expansion. In practice, the changes in sea surface height can be contributed by several other factors, such as salinity and mass redistribution (Cabanes et al. 2001; Willis et al. 2003; Wunch et al. 2007). Which component is dominant is still under an intense debate (Cabanes et al. 2001; Miller and Douglas 2004; Nerem et al. 2006; Ishii et al. 2006; Wunch et al. 2007; Cazenave et al. 2009). In particular, the importance of each component probably changes with time and has large regional variability. Notwithstanding, due to the near-global coverage and almost unbiased sampling, satellite altimetry is considered one of the effective ways to assess the variations in subsurface temperature (White and Tai 1995; Gilson et al 1998; Willis et al. 2003). In addition, the correlation between SSHA and subsurface temperature variation, especially in the upper ocean, are rather strong in this study domain as indicated by Gilson et al. (1998) and Willis et al. (2003). This is implying that the temperature variation is primarily responsible for the change in sea surface height

at least in this region.

In order to assess the mass contribution to the change in sea surface height, this study attempted to use the monthly equivalent water thickness (EWT) data derived from the Gravity Recovery and Climate Experiment (GRACE) satellite (Chambers 2006) to eliminate the mass effect from the altimetry derived SSHA field. The monthly EWT used this study is the Release 04 processed and distributed by the Center for Space Research (CSR) of University of Texas (Chamber 2006). The EWT data are available from 2003 onward. Figure 6.7 compares the annul time series of EWT (red curve), SSHA (blue curve) and SSHA corrected by GRACE's EWT (black curve). The domain of this assessment is 122-150°E, 10-26°N. The SSHA time series is corrected by directly subtracting the annual EWT. Since the EWT data is started from 2003, the correction for 1993-2002 is subtracting the average percentage of EWT with respect to SSHA, which is ~11.9%. One can see that the variation in mass-corrected SSHA (black curve) is similar to that in the original SSHA (blue curve), while the former trend appears a bit smaller at a rate of 0.43 cm yr^{-1} as compared to the original SSHA rate of 0.55 cm yr^{-1}. Figure 6.8 shows the annual time series of the D26 and UOHC with the mass correction for 1993-2010. Clearly, the mass effect appears to be relatively moderate. The 18-year trends for the corrected D26 and UOHC are 0.52 m yr^{-1} and 0.50 kJ cm^{-2} yr^{-1}, respectively. According to this evaluation, the mass contribution accounts for 18-20% of the original D26 and UOHC signals. However, it is worth noting that the uncertainty of the GRACE's EWT solution is still quite large, thus the mass assessment presented here is a rough estimate. Nevertheless, this result suggests that using satellite altimetry to evaluate the UOTS variability and trends in the western North Pacific is reliable for the present analysis.

Table 6.5 compares the trend estimates of the heat content in the upper ocean provided by recent studies. All of these estimates were global averages of upper 700 or 750 m and based mainly on *in situ* observations. In order to compare with our results, a unit of W m^{-2}, which is commonly used by the climate community, was converted to a unit of kJ cm^{-2} yr^{-1}. Nevertheless, it can be

found that the trends in UOHC in the SEZ and Gyre estimated by this study are consistent with the trends in global heat content of upper 700 m found by other studies. Since the integrated depth of UOHC is not fixed and dependent on D26, cautious have to be paid when compare with fixed integrated depth quantities. In the SEZ, the mean D26 is about 58.4 m, which is less than 10% of thickness (700 m) employed in other studies. However, the trend in UOHC accounts for 11-36% of rates in globally averaged heat content of upper 700 m. Similarly, D26 in the Gyre is about 112.8 m equivalent to ~16% of 700 m thickness, but the UOHC trend appears to be 40-133% of global trends in upper 700 m. The potential reasons are that most of the heat content anomalies are usually stored in the upper ocean (Levitus et al. 2005, 2012; Domingues et al. 2008), and the heat content trend indeed varies considerably over the global oceans (Willies et al. 2004; Wunch et al 2007; Levitus et al. 2009, 2012).

6.4.2 Issue on the study domain

This study has focused mainly on the typhoon intensification region of the western North Pacific and discussed the changes in SEZ and Gyre separately (Figures 6.1 and 6.2). It is interesting to evaluate the impact of the different domain definitions on the above results. For this reason, the changes in ocean conditions are recomputed for three extra domains and then compare with the original results. These three domains include the whole typhoon intensification region, i.e., SEZ+Gyre, and two sub regions as indicated in Figure 6.9. The two sub regions are the western SEZ (WSEZ) and western Gyre (WGyre), in which the most typhoon intensification frequency is found (Figure 6.1).

Figure 6.10 compares the ocean condition changes for the entire typhoon intensification region (black curve) and for the SEZ (red curve) and Gyre (blue curve). Clearly, the variations and trends among these three regions are similar. The values of SSHA, SST, D20, D26, UOHC and T100 in the big domain are in between that in the SEZ and Gyre. Similarly, the results of WSEZ and WGyre are

almost identical to the results of SEZ and Gyre (Figure 6.11). These comparisons suggest that using different domain definition does not affect the conclusion.

6.4.3 Issue on SSHA gridded data

The results of the ocean condition changes provided by this chapter are primarily based on the AVISO's 1/4° gridded SSHA field. Therefore, it is worthwhile to examine whether the results are robust by using different kind of SSHA data. For the reason, the along track non-gridded SSHA data are used to investigate the impact of using different SSHA data. In this work, the along track data with standard configuration (immovable ground track and 10-day cycle) from TOPEX/Poseidon series (i.e., plus Jason-1 and Jason-2) observed from 1993 to 2010 are employed. Figure 6.12 shows the regular ground tracks flied by TOPEX/Poseidon series missions. Recall that these tracks do not change over time. It can be found that there are 32 passes within the SEZ and Gyre. Their identification numbers are shown in Figure 6.12. It should be noted that these along track data are also provided by AVISO, and have gone through all the necessary corrections as what was done for gridded data.

Figure 6.13 shows the annual SSHA time series calculated from the 32 regular passes and from gridded SSHA field for the SEZ and Gyre. Apparently, either using 32 tracks data or gridded SSHA data, the results are very consistent. However, the deviation of the individual track results (grey curves) is greater in the SEZ than in the Gyre. It is due to there are many mesoscale features (e.g., eddies) existing in the SEZ, whereas the main features in the Gyre are basin-wide changes. As a consequence, the track by track changes are greater in the SEZ. Nevertheless, this results suggest that using different kinds of SSHA products (i.e., along track and gridded) does not substantially affect the main results found in the present study.

6.5 Summary

It is known that upper ocean thermal conditions (e.g. 0-200 m) and eddies play a critical role in typhoon intensity change. With the advancement in remote sensing, especially the satellite altimetry since 1993, this work carefully investigated the variations in UOTS and ocean features in the typhoon intensification zone of the western North Pacific during the typhoon season (June-October) of 1993-2010. In this study, UOTS was estimated from the satellite SSHA field by the well-developed two-layer reduced gravity approach (i.e. 2-layer). It is found that UOTS exhibited a long-term trend and interannual variability over the entire study period. From 1993 to 2010, the averaged D26, D20 and UOHC increased in the typhoon intensification region (i.e., Gyre and SEZ). These trends resulted in the averaged T100 warming by ~0.35°C in the Gyre and ~0.16°C in the SEZ, suggesting the reduction in the typhoon-induced SST cooling. Interestingly, the rate of UOHC increasing in the SEZ is 50% higher than that in the Gulf of Mexico.

The trends in the percentages of the total areas of ocean features in the SEZ and Gyre over 1993-2010 are found. Basically, the area of positive features increased, whereas the area of negative features shrunk. In addition, the rates of changes are more significant in the Gyre. The results imply that the ocean condition in the western North Pacific main typhoon intensification region is becoming more favorable to typhoon intensification.

Chapter 7 Conclusion and future work

With the advantage of containing the ocean subsurface thermal information, sea surface height anomaly (SSHA) measurements from satellite altimetry was used to estimate the upper ocean thermal structure (UOTS) in the western North Pacific Ocean for typhoon research. Traditionally, UOTS can be derived to a first order from the SSHA field by using the two-layer reduced gravity model (i.e., 2-layer). The results and applications of using 2-layer in typhoon research are summarized as follows:

1. 2-layer-dervied temperature profiles were used to study the intensity change of the Supertyphoon Dianmu (2004). Five parameters including pre-typhoon SST, pre-typhoon UOHC, SST cooing, dynamic UOHC and vertical wind shear were examined. It is found that the two parameters, i.e., the typhoon's self-induced SST cooling and the dynamic UOHC during the typhoon, are the most sensitive parameters ($R^2 \sim 0.7$) to the 6-h intensity change of Dianmu's rapid intensification period.
2. During the ITOP field experiment in 2010, the 2-layer method was used to provide daily UOTS in the western North Pacific from the satellite SSHA and SST fields for the operational purpose. The satellite-derived UOTS is proved to be valuable for the experiment to identify the ocean features and to plan the observing routes of the C-130 aircraft as well as the deployment of the *in situ* instruments.

Since 2-layer provides relatively simple UOTS (only four vertically depths) and has some obvious limitations in the western North Pacific Ocean, this work intended to develop an enhanced method, i.e., the regression method, in order to improve the UOTS estimation in the western North Pacific Ocean for typhoon intensity research and forecasting. The results of this part are summarized as follows:

1. The relationship between SSHA and the subsurface isotherm displacement were investigated. It is found that the meaning of SSHA on subsurface temperature has regional dependence in the western North Pacific. SSHA typically reflects the variations of D26 to D12 in the Gyre (10-21°N), D26 to D6 in the SEZ (21-26°N), D18 to D7 in the IEZ (26-30°N) and NEZ (30-40°N).
2. >38,000 *in situ* Argo temperature profiles from 2000 to 2008 were used to develop a linear regression method (i.e., REGWNP). In REGWNP, the monthly regressions were made for D26 to the isotherm at the base of the thermocline in every 0.25° grid mash to account for the spatial and temporal variations. Typically, REGWNP is able to provide temperature profiles from the surface to ~600 m.
3. REGWNP was systematically validated with an independent set of > 7,000 Argo profiles from 2009 and 2010. The results show that the regression-derived UOTS is of reasonable accuracy. During the western North Pacific typhoon season (May-October), RMSD for D20, D26, UOHC and T100 over the entire basin is less than 30 m, 20 m, 20 kJ cm^{-2}, and 1.5°C, respectively. In addition, the averaged RMSD from D26 to the base of the thermocline is ~20 m in the Gyre, SEZ and IEZ, and ~40 m in the NEZ. The estimated isotherm depths are highly consistent with the Argo observations with a correlation of ~0.8, indicating that UOTS estimated from REGWNP is rather reliable.
4. Compared with 2-layer, REGWNP is able to provide more detailed and completed temperature profiles. Quantitatively, REGWNP has 20-70% improvement in D20 estimation, 2-32% in D26, and 8-44% in T100 with respect to the traditional 2-layer.
5. Compared with AXBTs from ITOP experiment in 2010, REGWNP-derived UOTS is in an excellent agreement with AXBT observation. Encouragingly, the accuracy of REGWNP is also comparable to the sophisticated EASNFS full ocean model to produce real-time UOTS field. This suggests that REGWNP-derived UOTS is appropriate to be used for typhoon intensity

research and forecast.

Finally, with 2-layer method and 18 years of high-quality SSHA data since 1993 when the TOPEX/Poseidon satellite altimeter was launched, the long-term variability of ocean conditions (i.e. eddies, features, and UOTS) in the western North Pacific typhoon intensification region over the period of 1993-2010 is investigated. The results of this analysis are summarized as follows:

1. In order to identify ocean eddies on SSHA maps in an objective and consistent way, an automated eddy identification procedure was developed exclusively for the western North Pacific southern eddy zone (SEZ). The results prove that the procedure is able to identify eddies in the SEZ with high degree of reliability.
2. With the eddy identification method, a total of 1,758 eddies were identified in the SEZ from 18 years of merged SSHA data during the summer months (May-October). During the study period, warm eddies increased by 19% in number, 17% in amplitude (equal to 4.5% and 3% increases in D26 and UOHC), and 19% in radius. In contrast, cold eddies decreased by 51% in number, 13% in amplitude (equal to 6.6% and 3% increases in D26 and UOHC) and 21% in radius.
3. For the UOTS variability, the averaged D26, D20 and UOHC increased in the Gyre and in the SEZ from 1993 to 2010. In addition, the averaged T100 increased by ~0.35°C in the Gyre and ~0.16°C in the SEZ, suggesting the warming in the upper ocean of the western North Pacific typhoon intensification region.
4. For the ocean feature variability, the percentage of the total area of positive features (SSHA $\geqq$ 10 cm) increased (0.7% yr^{-1}) while that of negative features (SSHA $\leqq$ -10 cm) decreased (-0.8% yr^{-1}) in the SEZ. In the Gyre, the total area of positive features increased (3.4% yr^{-1}), whereas the total areas of no features and negative features both exhibit decreasing trends (-2.7% yr^{-1} and -0.7% yr^{-1}, respectively). This indicates that the overall ocean condition in the western North Pacific is becoming more favorable to typhoon intensification.

In short, satellite remote sensing, especially altimetry, provides a unique way for estimating UOTS in the vast western North Pacific Ocean with relatively high spatial and temporal resolutions. This study has proved that the satellite-derived UOTS is playing a crucial role in typhoon intensity research and real-time applications. Also, the UOTS estimation is further improved by using the regression method developed in this study. In addition, using the satellite SSHA data and derived UOTS, it is found that the western North Pacific Ocean conditions are getting more favorable for typhoon intensification.

For the future, the subjects of continuing investigation are as follows:

1. As growing concern and demand for UOTS in the typhoon intensity research and forecasting, it is useful to develop a webpage to operationally provide real-time satellite-derived UOTS in the western North Pacific for researchers and modelers who need the UOTS information.
2. Regression-derived UOTS has been proved to be able to provide reliable UOTS for the pre-typhoon condition. However, during and after typhoon UOTS are also important for understanding the typhoon-ocean interaction. With the unique dataset from ITOP experiment (2010), the assessment of the accuracy of satellite-derived UOTS for during and after typhoon conditions will be conducted.
3. Although the subsurface temperature profiles estimation has significantly improved by using the regression method, there is no improvement in the mixed layer. Undoubtedly, improving the MLD estimation will substantially increase the accuracy of satellite-derived temperature profiles, especially for during and after typhoon situations when the upper ocean is mixed. Given the unique dataset, i.e., pairs of AXBTs and dropsondes, from ITOP experiment (2010), it is extremely useful to develop a parameterization scheme to derive more accurate MLD from satellite observations, such as SST, sea surface salinity (SSS), and sea surface wind, thus further

improve the accuracy and applicability of the satellite-derived UOTS

4. For the eddy identification, it is worthwhile to recalculate the eddies with daily SSHA maps, which is now available from AVISO. Based on the daily data, the accuracy of eddy identification is expected to be enhanced.
5. This study presents the change of ocean condition, i.e., oceanic eddies/features and subsurface thermal structure, from the observation point of view. Therefore, it is worthwhile to investigate the scientific causes of this change in the future.
6. This study suggests that the ocean conditions of the western North Pacific are becoming more favorable for typhoon intensification. A systematic study of the impact of variability of ocean conditions on the western North Pacific typhoons should be conducted.
7. In addition to the ocean conditions, it is worthwhile to examine the changes in the atmospheric and typhoon structure conditions in the western North Pacific. It will clarify the overall changes in the western North Pacific conditions for typhoon intensification.

References

Bender, M. A., I. Ginis, and Y. Kurihara, 1993: Numerical Simulations of Tropical Cyclone-Ocean Interaction with a High-Resolution Coupled Model. *J Geophys Res-Atmos*, **98,** 23245-23263.

Bender, M. A., and I. Ginis, 2000: Real-case simulations of hurricane-ocean interaction using a high-resolution coupled model: Effects on hurricane intensity. *Mon Weather Rev*, **128,** 917-946.

Cabanes, C., A. Cazenave, and C. Le Provost, 2001: Sea level rise during past 40 years determined from satellite and in situ observations. *Science*, **294,** 840-842.

Carnes, M. R., J. L. Mitchell, and P. W. Dewitt, 1990: Synthetic Temperature Profiles Derived from Geosat Altimetry - Comparison with Air-Dropped Expendable Bathythermograph Profiles. *J Geophys Res-Oceans*, **95,** 17979-17992.

Cazenave, A., and F. Remy, 2011: Sea level and climate: measurements and causes of changes. *Wires Clim Change*, **2,** 647-662.

Cazenave, A., and Coauthors, 2009: Sea level budget over 2003-2008: A reevaluation from GRACE space gravimetry, satellite altimetry and Argo. *Global Planet Change*, **65,** 83-88.

Chaigneau, A., A. Gizolme, and C. Grados, 2008: Mesoscale eddies off Peru in altimeter records: Identification algorithms and eddy spatio-temporal patterns. *Prog Oceanogr*, **79,** 106-119.

Chambers, D. P., 2006: Observing seasonal steric sea level variations with GRACE and satellite altimetry, *J Geophys Res*, **111**.

Chan, J. C. L., 2006: Comment on "Changes in tropical cyclone number, duration, and intensity in a warming environment". *Science*, **311**.

Chan, J. C. L., 2007: Interannual variations of intense typhoon activity. *Tellus A*, **59,** 455-460.

Chang, S. W., and R. A. Anthes, 1979: Mutual Response of the Tropical Cyclone and the Ocean. *J Phys Oceanogr*, **9,** 128-135.

Chelton, D. B., M. G. Schlax, R. M. Samelson, and R. A. de Szoeke, 2007: Global observations of

large oceanic eddies. *Geophys Res Lett*, **34**.

Chelton, D. B., M. G. Schlax, and R. M. Samelson, 2011: Global observations of nonlinear mesoscale eddies. *Prog Oceanogr*, **91,** 167-216.

Cheney, R. E., 1982: Comparison Data for Seasat Altimetry in the Western North-Atlantic. *J Geophys Res-Oc Atm*, **87,** 3247-3253.

Chow, C. H., J. H. Hu, L. R. Centurioni, and P. P. Niiler, 2008: Mesoscale Dongsha Cyclonic Eddy in the northern Asouth China Sea by drifter and satellite observations. *J Geophys Res-Oceans*, **113**.

Cione, J. J., and E. W. Uhlhorn, 2003: Sea surface temperature variability in hurricanes: Implications with respect to intensity change. *Mon Weather Rev*, **131,** 1783-1796.

D'Asaro, E. A., T. B. Sanford, P. P. Niiler, and E. J. Terrill, 2007: Cold wake of Hurricane Frances. *Geophys Res Lett*, **34**.

D'Asaro, E., and Coauthors, 2011: Typhoon-ocean interaction in the western North Pacific: Part 1. *Oceanography*, **24,** 24-31.

Domingues, C. M., J. A. Church, N. J. White, P. J. Gleckler, S. E. Wijffels, P. M. Barker, and J. R. Dunn, 2008: Improved estimates of upper-ocean warming and multi-decadal sea-level rise. *Nature*, **453,** 1090-U1096.

Ducet, N., P. Y. Le Traon, and G. Reverdin, 2000: Global high-resolution mapping of ocean circulation from TOPEX/Poseidon and ERS-1 and-2. *J Geophys Res-Oceans*, **105,** 19477-19498.

Elsner, J. B., J. P. Kossin, and T. H. Jagger, 2008: The increasing intensity of the strongest tropical cyclones. *Nature*, **455,** 92-95.

Emanuel, K. A., 1999: Thermodynamic control of hurricane intensity. *Nature*, **401,** 665-669.

Emanuel, K., C. DesAutels, C. Holloway, and R. Korty, 2004: Environmental control of tropical cyclone intensity. *J Atmos Sci*, **61,** 843-858.

Emanuel, K., 2005: Increasing destructiveness of tropical cyclones over the past 30 years. *Nature*, **436,** 686-688.

Fofonoff, N. P., and R. C. Millard, 1983: Algorithms for computation of fundamental properties of seawater. *UNESCO technical paper in marine science 44, UNESCO*.

Fu, L. L., E. J. Christensen, C. A. Yamarone, M. Lefebvre, Y. Menard, M. Dorrer, and P. Escudier, 1994: Topex/Poseidon Mission Overview. *J Geophys Res-Oceans*, **99,** 24369-24381.

Fu, L.L., D. Stammer, B. B. Leben, and D. B. Chelton, 2003. Improved spatial resolution of ocean surface topography from the TOPEX/Poseidon – Jason-1 tandem altimeter mission, *EOS, Trans. Amer. Geophys. Union*, **84**, 247-248.

Gallacher, P. C., R. Rotunno, and K. A. Emanuel, 1989: Tropical cyclogenesis in a coupled ocean-atmosphere model. *18th Conference on Hurricanes and Tropical Meteorology*, American Meteorological Society.

Gallina G. M., and C. S. Velden, 2002: Environmental wind shear and tropical cyclone intensity change using enhanced satellite derived wind information. *Preprints, 25th Conference Hurricanes and Tropical Meteorology*, San Diego, CA, *Amer. Meteor. Soc.*, 172-173.

Gilson, J., D. Roemmich, B. Cornuelle, and L. L. Fu, 1998: Relationship of TOPEX/Poseidon altimetric height to steric height and circulation in the North Pacific. *J Geophys Res-Oceans*, **103,** 27947-27965.

Goni, G., S. Kamholz, S. Garzoli, and D. Olson, 1996: Dynamics of the Brazil-Malvinas Confluence based on inverted echo sounders and altimetry. *J Geophys Res-Oceans*, **101,** 16273-16289.

Goni, G. J., and J. A. Trinanes, 2003: Ocean thermal structure monitoring could aid in the intensity forecast of tropical cyclones. *EOS, Trans. Amer. Geophys. Union*, **84,** 573-580.

Goni, G., and Coauthors, 2009: Applications of Satellite-Derived Ocean Measurements to Tropical Cyclone Intensity Forecasting. *Oceanography*, **22,** 190-197.

Gould, J., and Coauthors, 2004: Argo Profiling Floats Bring New Era of In Situ Ocean Observations. *EOS, Trans. Amer. Geophys. Union*, **84,** 179,190-191.

Gould, W. J., 2005: From Swallow floats to Argo - the development of neutrally buoyant floats. *Deep-Sea Res Pt Ii*, **52,** 529-543.

Gouretski, V., and K. P. Koltermann, 2007: How much is the ocean really warming? *Geophys Res Lett*, **34**.

Gray, W. M., 1979: Hurricanes: Their formation, structure and likely role in the tropical circulation. *Meteorology over the Tropical Oceans*, D. B. Shaw, Ed., Royal Meteorological Society, 155-218.

Gründlingh, M. L., 1995: Tracking eddies in the southeast Atlantic and southwest Indian oceans with TOPEX/POSEIDON. *J Geophys Res-Oceans*, **100,** 24977-24986.

Holliday, C. R., and A. H. Thompson, 1979: Climatological Characteristics of Rapidly Intensifying Typhoons. *Mon Weather Rev*, **107,** 1022-1034.

Hong, X. D., S. W. Chang, S. Raman, L. K. Shay, and R. Hodur, 2000: The interaction between Hurricane Opal (1995) and a warm core ring in the Gulf of Mexico. *Mon Weather Rev*, **128,** 1347-1365.

Hwang, C., C. R. Wu, and R. Kao, 2004: TOPEX/Poseidon observations of mesoscale eddies over the Subtropical Countercurrent: Kinematic characteristics of an anticyclonic eddy and a cyclonic eddy. *J Geophys Res-Oceans*, **109**.

Isern-Fontanet, J., E. Garcia-Ladona, and J. Font, 2003: Identification of marine eddies from altimetric maps. *J Atmos Ocean Tech*, **20,** 772-778.

Isern-Fontanet, J., 2006: Vortices of the Mediterranean Sea: An altimetric perspective. *J Phys Oceanogr*, **36,** 87-103.

Ishii, M., M. Kimoto, K. Sakamoto, and S. I. Iwasaki, 2006: Steric sea level changes estimated from historical ocean subsurface temperature and salinity analyses. *J Oceanogr*, **62,** 155-170.

Johnson, G. C., M. J. McPhaden, G. D. Rowe, and K. E. McTaggart, 2000: Upper equatorial Pacific Ocean current and salinity variability during the 1996-1998 El Nino-La Nina cycle. *J Geophys Res-Oceans*, **105,** 1037-1053.

Johnson, G. C., and S. C. Doney, 2006: Recent western south Atlantic bottom water warming (vol 33, art no L21604, 2006). *Geophys Res Lett*, **33**.

Johnson, G. C., J. M. Lyman, J. K. Willis, S. Levitus, T. Boyer, J. Antonov, and S. A. Good, 2011: Ocean heat content. *In "State of the Climate in 2010"*, Bull. Amer. Meteor. Soc., S81-S84.

Kaplan, J., and M. DeMaria, 2003: Large-scale characteristics of rapidly intensifying tropical cyclones in the North Atlantic basin. *Weather Forecast*, **18,** 1093-1108.

Kara, A. B., P. A. Rochford, and H. E. Hurlburt, 2002: Naval Research Laboratory Mixed Layer Depth (NMLD) Climatologies.

Keeley, B., C. Sun, and L. P. Villeon, 2003: Global Temperature and Salinity Profile Program Annual Report.

Ko, D. S., P. J. Martin, C. D. Rowley, and R. H. Preller, 2008: A real-time coastal ocean prediction experiment for MREA04. *Journal of Marine Systems*, 69, 17-28.

Ko, D. S., S. Y. Chao, P. Huang, and S. F. Lin, 2009: Anomalous Upwelling in Nan Wan: July 2008. *Terr Atmos Ocean Sci*, **20,** 839-852.

Le Traon, P. Y., and R. A. Morrow, 2001: Ocean currents and mesoscale eddies. *Satellite Altimetry and Earth Sciences. A Handbook of Techniques and Applications*, Academic Press, 171-215.

Le Traon, P. Y., and G. Dibarboure, 2002: Velocity mapping capabilities of present and future altimeter missions: The role of high-frequency signals. *J Atmos Ocean Tech*, **19,** 2077-2087.

Le Traon, P.Y. and G. Dibarboure, 2004. Illustration of the contribution of the tandem mission to mesoscale studies . *Marine Geodesy*, 27, 3-13

Leipper, D. F., and D. Volgenau, 1972: Hurricane Heat Potential of the Gulf of Mexico. *J. Phys. Oceanogr.*, **2,** 218-224.

Levitus, S., J. I. Antonov, T. P. Boyer, and C. Stephens, 2000: Warming of the world ocean. *Science*, **287,** 2225-2229.

Levitus, S., J. I. Antonov, J. L. Wang, T. L. Delworth, K. W. Dixon, and A. J. Broccoli, 2001: Anthropogenic warming of Earth's climate system. *Science*, **292,** 267-270.

Levitus, S., J. Antonov, and T. Boyer, 2005: Warming of the world ocean, 1955-2003. *Geophys Res Lett*, **32**.

Levitus, S., J. I. Antonov, T. P. Boyer, R. A. Locarnini, H. E. Garcia, and A. V. Mishonov, 2009: Global ocean heat content 1955-2008 in light of recently revealed instrumentation problems. *Geophys Res Lett*, **36**.

Levitus, S., J. I. Antonov, T. P. Boyer, O. K. Baranova, H. E. Garcia, R. A. Locarnini, A. V. Mishonov, J. R. Reagan, D. Seidov, E. S. Yarosh, and M. M. Zweng, 2012: World ocean heat content and thermosteric sea level change (0–2000 m), 1955–2010, *Geophys Res Lett*, **39**.

Lin, I. I., C. C. Wu, K. A. Emanuel, I. H. Lee, C. R. Wu, and I. F. Pun, 2005: The interaction of Supertyphoon Maemi (2003) with a warm ocean eddy. *Mon Weather Rev*, **133,** 2635-2649.

Lin, I. I., C. C. Wu, I. F. Pun, and D. S. Ko, 2008: Upper-ocean thermal structure and the western North Pacific category 5 typhoons. Part I: Ocean features and the category 5 typhoons' intensification. *Mon Weather Rev*, **136,** 3288-3306.

Lin, I. I., C. H. Chen, I. F. Pun, W. T. Liu, and C. C. Wu, 2009a: Warm ocean anomaly, air sea fluxes, and the rapid intensification of tropical cyclone Nargis (2008). *Geophys Res Lett*, **36**.

Lin, I. I., I. F. Pun, and C. C. Wu, 2009b: Upper-Ocean Thermal Structure and the Western North Pacific Category 5 Typhoons. Part II: Dependence on Translation Speed. *Mon Weather Rev*, **137,** 3744-3757.

Lyman, J. M., J. K. Willis, and G. C. Johnson, 2006: Recent cooling of the upper ocean. *Geophys Res Lett*, **33**.

Lyman, J. M., and G. C. Johnson, 2008: Estimating Annual Global Upper-Ocean Heat Content

Anomalies despite Irregular In Situ Ocean Sampling. *J Climate*, **21,** 5629-5641.

Lyman, J. M., and Coauthors, 2010: Robust warming of the global upper ocean. *Nature*, **465,** 334-337.

Mainelli, M., M. DeMaria, L. K. Shay, and G. Goni, 2008: Application of oceanic heat content estimation to operational forecasting of recent Atlantic category 5 hurricanes. *Weather Forecast*, **23,** 3-16.

Mann, M. E., and K. A. Emanuel, 2006: Atlantic Hurricance Trends Linked to Climate Change. *EOS, Trans. Amer. Geophys. Union*, **87,** 233,238,241.

Mellor, G. L., and T. Yamada, 1982: Development of a Turbulence Closure-Model for Geophysical Fluid Problems. *Rev Geophys*, **20,** 851-875.

Miller, L., and B. C. Douglas, 2004: Mass and volume contributions to twentieth-century global sea level rise. *Nature*, **428,** 406-409.

Millero, F. J., C. T. Chen, K. Schleicher, and A. Bradshaw, 1980: A New High-Pressure Equation of State for Seawater. *Deep-Sea Res*, **27,** 255-264.

Morrow, R., F. Birol, D. Griffin, and J. Sudre, 2004: Divergent pathways of cyclonic and anti-cyclonic ocean eddies. *Geophys Res Lett*, **31**.

Nerem, R. S., E. Leuliette, and A. Cazenave, 2006: Present-day sea-level change: A review. *Cr Geosci*, **338,** 1077-1083.

Pascual, A., Y. Faugere, G. Larnicol, and P. Y. Le Traon, 2006: Improved description of the ocean mesoscale variability by combining four satellite altimeters. *Geophys Res Lett*, **33**.

Pascual, A., C. Boone, G. Larnicol, and P. Y. Le Traon, 2009: On the Quality of Real-Time Altimeter Gridded Fields: Comparison with In Situ Data. *J Atmos Ocean Tech*, **26,** 556-569.

Philander, S. G. H., 1990: *El Niño, La Niña and the Southern Oscillation.* Academic Press, 293 pp.

Picot, N., K. Case, S. Desai and P. Vincent, 2003: AVISO and PODAAC User Handbook. IGRDR and GRD Jason Products. SMM-MU-M5-OP-13184-CN (*AVISO*), JPL D-21352 (*PODAAC*).

Price, J. F., 1981: Upper Ocean Response to a Hurricane. *J Phys Oceanogr*, **11,** 153-175.

Price, J. F., 2009: Metrics of hurricane-ocean interaction: vertically-integrated or vertically-averaged ocean temperature? *Ocean Sci*, **5,** 351-368.

Puillat, L., L. Taupier-Letage, and C. Millot, 2002: Algerian Eddies lifetime can near 3 years. *J Marine Syst*, **31,** 245-259.

Pun, I. F., 2005: Estimation of upper-ocean thermal structure in the North West Pacific Ocean by satellite remote sensing and its application to typhoon intensity change, Earth Sciences, National Taiwan Normal University.

Pun, I. F., I. I. Lin, C. R. Wu, D. H. Ko, and W. T. Liu, 2007: Validation and application of altimetry-derived upper ocean thermal structure in the western North Pacific Ocean for typhoon-intensity forecast. *Ieee T Geosci Remote*, **45,** 1616-1630.

Pun, I. F., Y. T. Chang, I. I. Lin, T. Y. Tang, and R. C. Lien, 2011: Typhoon-ocean interaction in the western North Pacific: Part 2. *Oceanography*, **24,** 32-41.

Pun, I. F., I. I. Lin, P. G. Black, and D. S. Ko, 2012: Regression-derived satellite-based upper ocean thermal structure for the Western North Pacific Typhoon Research. *Prog Oceanogr*. (in revision)

Qiu, B., 1999: Seasonal eddy field modulation of the North Pacific subtropical countercurrent: TOPEX/Poseidon observations and theory. *J Phys Oceanogr*, **29,** 2471-2486.

Qiu, B., 2001: Kuroshio and Oyashio Currents. *Encyclopedia of Ocean Sciences*, Academic Press, 1413-1425.

Qiu, B., and S. M. Chen, 2004: Seasonal modulations in the eddy field of the South Pacific Ocean. *J Phys Oceanogr*, **34,** 1515-1527.

Qiu, B., 2010: Interannual Variability of the North Pacific Subtropical Countercurrent and Its Associated Mesoscale Eddy Field. *J Phys Oceanogr*, **40,** 213-225.

Rayner, N. A., and Coauthors, 2006: Improved analyses of changes and uncertainties in sea surface

temperature measured in situ sice the mid-nineteenth century: The HadSST2 dataset. *J Climate,* **19,** 446-469.

Reynolds, R. W., N. A. Rayner, T. M. Smith, D. C. Stokes, and W. Q. Wang, 2002: An improved in situ and satellite SST analysis for climate. *J Climate,* **15,** 1609-1625.

Roemmich, D., and J. Gilson, 2001: Eddy transport of heat and thermocline waters in the North Pacific: A key to interannual/decadal climate variability? *J Phys Oceanogr,* **31,** 675-687.

Roemmich, D., S. Riser, R. Davis, and Y. Desaubies, 2004: Autonomous profiling floats: Workhorse for broad-scale ocean observations. *Mar Technol Soc J,* **38,** 21-29.

Schade, L. R., and K. A. Emanuel, 1999: The ocean's effect on the intensity of tropical cyclones: Results from a simple coupled atmosphere-ocean model. *J Atmos Sci,* **56,** 642-651.

Scharroo, R., W. H. F. Smith, and J. L. Lillibridge, 2005: Satellite Altimetry and the Intensification of Hurricane Katrina. *EOS, Trans. Amer. Geophys. Union,* **86,** 366-367.

Shay, L. K., G. J. Goni, and P. G. Black, 2000: Effects of a warm oceanic feature on Hurricane Opal. *Mon Weather Rev,* **128,** 1366-1383.

Shay, L. K., and J. K. Brewster, 2010: Oceanic Heat Content Variability in the Eastern Pacific Ocean for Hurricane Intensity Forecasting. *Mon Weather Rev,* **138,** 2110-2131.

Shewchuk, J. R., 1996: Triangle: Engineering a 2D Quality Mesh Generator and Delaunay Triangulator. *First Workshop on Applied Computational Geometry,* 124-133.

Siegel, D. A., D. J. McGillicuddy, and E. A. Fields, 1999: Mesoscale eddies, satellite altimetry, and new production in the Sargasso Sea. *J Geophys Res-Oceans,* **104,** 13359-13379.

SSALTO/DUACS User Handbook, 2012: (M)SLA and (M)ADT Near-Real Time and Delayed Time Products. *SALP-MU-P-EA-21065-CLS,* edition 3.1, pp. 59.

Stephens, C., J. I. Antonov, T. P. Boyer, M. E. Conkright, R. A. Locarnini, T. D. O'Brien, and H. E. Carcia, 2002: World Ocean Atlas 2001 Volume 1: Temperature. *NOAA Altas NESDIS 49,* S. Levitus, Ed., U.S. Government Printing Office.

Wang, Y., and C. C. Wu, 2004: Current understanding of tropical cyclone structure and intensity changes - a review. *Meteorol Atmos Phys*, **87,** 257-278.

Wang, G. H., J. L. Su, and P. C. Chu, 2003: Mesoscale eddies in the South China Sea observed with altimeter data. *Geophys Res Lett*, **30**.

Webster, P. J., G. J. Holland, J. A. Curry, and H. R. Chang, 2005: Changes in tropical cyclone number, duration, and intensity in a warming environment. *Science*, **309,** 1844-1846.

Wentz, F. J., C. Gentemann, D. Smith, and D. Chelton, 2000: Satellite measurements of sea surface temperature through clouds. *Science*, **288,** 847-850.

Wessel, P., and W. H. F. Smith, 1998: New, improved version of the Generic Mapping Tools Released. *EOS, Trans. Amer. Geophys. Union*, **79,** 579.

White, W. B., and C. K. Tai, 1995: Inferring interannual changes in global upper ocean heat storage from TOPEX altimetry. *J Geophys Res-Oceans*, **100,** 24943-24954.

Willis, J. K., D. Roemmich, and B. Cornuelle, 2003: Combining altimetric height with broadscale profile data to estimate steric height, heat storage, subsurface temperature, and sea-surface temperature variability. *J Geophys Res-Oceans*, **108**.

Willis, J. K., 2004: Interannual variability in upper ocean heat content, temperature, and thermosteric expansion on global scales. *J Geophys Res-Oceans*, **109**.

Willis, J. K., J. M. Lyman, G. C. Johnson, and J. Gilson, 2007: Recent cooling of the upper ocean (vol 33, artn no. L18604, 2006). *Geophys Res Lett*, **34**.

Wu, C. C., C. Y. Lee, and I. I. Lin, 2007: The effect of the ocean eddy on tropical cyclone intensity. *J Atmos Sci*, **64,** 3562-3578.

Wunsch, C., R. M. Ponte, and P. Heimbach, 2007: Decadal trends in sea level patterns: 1993-2004. *J Climate*, **20,** 5889-5911.

Wyrtki, K., 1979: Response of Sea-Surface Topography to the 1976-El-Nino. *J Phys Oceanogr*, **9,** 1223-1231.

Yasuda, I., K. Okuda, and M. Hirai, 1992: Evolution of a Kuroshio Warm-Core Ring - Variability of the Hydrographic Structure. *Deep-Sea Res*, **39,** S131-&.

Table 1.1: Saffir-Simpson tropical cyclone scale based on 1-min maximum sustained wind speeds.

Category	Winds (m s^{-1})	Winds (knots)
1	33-42	64-82
2	43-48	83-95
3	49-58	96-113
4	59-69	114-135
5	>69	>135

Table 3.1: Additional quality control for Argo profiles. [1] WMO: World Meteorological Organization.

Items	**Threshold**
Problematic floats	WMO[1] instrument type 852
1st points of temperature	< 0 °C or > 35 °C
Temperature jump	> 1 °C
Maximum depth	< 200 m
Depth jump	> 300 m
Valid points	< 10 points

Table 3.2: Orbit parameters for T/P series and ERS series missions.

	T/P, J1, and J2	**ERS-1/2, and Envisat**
Attitude	1336 km	785 km
Inclination	66°	98.5°
Repeat cycle	9.9 days	35 days
Ground track separation at Equator	316 km	80 km

Table 3.3: The past and current altimetry missions used by AVISO to produce merged SSHA products.

Missions	Start date	End date
ERS-1 (European Remote Sensing)	1991/7/17	2000/3/31
TOPEX/Poseidon	1992/8/10	2006/1/18
ERS-2	1995/4/21	2011/7/6
GFO (Geosat Follow-On)	1998/2/10	2008/11/26
Jason-1	2001/7/12	-
Envisat	2002/3/1	2012/4/8
Jason-2	2008/6/20	-

Table 3.4: Correction applied to AVISO SSHA products.

	Applied correction
1	Orbit
2	Ionosphere
3	Dry troposphere
4	Wet troposphere
5	Dynamic atmospheric correction
6	Ocean tide
7	Pole tide
8	Solid earth tide
9	Loading tide
10	Sea state bias
11	Long wavelength errors

Table 4.1: Root-mean-square error (°C) of T100 from EASNFS, 2-layer and REGWNP as compared with AXBTs on August 28, August 31 and September 1, 2010.

	8/28	8/31	9/1	Average
EASNFS	**1.02**	**0.23**	**0.25**	**0.5**
2-layer	**0.95**	**0.27**	**0.28**	**0.5**
REGWNP	**0.81**	**0.27**	**0.32**	**0.47**

Table 4.2: Root-mean-square error (°C) of T100 from EASNFS, 2-layer and REGWNP as compared with Argos on August 28, August 31 and September 1, 2010.

	8/28	8/31	9/1	Average
EASNFS	**0.71**	**1.02**	**1.1**	**0.94**
2-layer	**0.87**	**1.27**	**1.16**	**1.1**
REGWNP	**0.65**	**0.76**	**0.9**	**0.77**

Table 5.1: The number of warm (cold) eddies identified in each monthly SSHA contour map during May to October from 1993 to 2010. The months in which cold eddies outnumbered warm eddies are highlighted with **bold** text.

	May	Jun.	Jul.	Aug.	Sep.	Oct.
1993	**3 (14)**	**6 (10)**	10 (8)	10 (7)	7 (7)	**5 (7)**
1994	**7 (12)**	10 (9)	11 (8)	13 (4)	10 (7)	**5 (6)**
1995	**5 (14)**	**7 (10)**	**6 (9)**	9 (7)	12 (9)	8 (7)
1996	**5 (13)**	**8 (13)**	**9 (10)**	12 (8)	10 (7)	9 (5)
1997	**11 (12)**	13 (12)	9 (7)	10 (6)	11 (4)	11 (5)
1998	11 (5)	14 (6)	12 (8)	9 (3)	8 (1)	15 (2)
1999	**9 (11)**	11 (5)	9 (4)	12 (3)	8 (3)	9 (3)
2000	**3 (12)**	**12 (13)**	14 (10)	9 (4)	11 (4)	8 (5)
2001	13 (9)	15 (8)	11 (7)	14 (6)	13 (9)	7 (7)
2002	8 (8)	9 (9)	8 (3)	7 (5)	9 (4)	8 (2)
2003	10 (6)	10 (7)	12 (4)	14 (4)	16 (3)	11 (3)
2004	**11 (12)**	10 (8)	14 (9)	13 (6)	10 (6)	11 (5)
2005	**9 (10)**	9 (7)	11 (7)	9 (3)	7 (3)	10 (4)
2006	13 (9)	13 (11)	8 (7)	8 (7)	9 (6)	9 (6)
2007	11 (7)	11 (7)	11 (5)	11 (5)	11 (3)	9 (3)
2008	10 (7)	12 (7)	12 (7)	12 (5)	9 (5)	9 (3)
2009	**9 (10)**	**7 (8)**	6 (2)	7 (1)	10 (2)	6 (3)
2010	7 (4)	10 (3)	13 (1)	15 (1)	12 (2)	12 (1)

Table 5.2: Trends and changes in the numbers, amplitudes and radii of warm and cold eddies in the SEZ from 1993 to 2010. The trends are based on least squares fitting and the significance level is based on the t-test.

Eddy types	Property	Trend (per year)	Change in linear trend	Beginning of trend (1993)	End of trend (2010)	Change in percentage (%)	Level of significance (%)
Warm	Number	0.09	1.7	9.0	10.7	19	80
	Amplitude (cm)	0.2	3.4	20.1	23.5	17	95
	Radius (km)	1.5	26	140	166	19	99
Cold	Number	-0.26	-4.4	8.6	4.2	-51	99
	Amplitude (cm)	-0.15	-2.6	19.4	16.8	-13	99
	Radius (km)	-1.7	-29	140	111	-21	99

Table 5.3: Parameters used in the two-layer reduced gravity model, i.e., equations (2.1) and (2.2), for calculating D26 and associated UOHC. Each value is a seasonal (May-October) average of the SEZ mean.

Parameter	Value	Source
$\overline{D20}$	161.6 m	WOA01
$\frac{\rho_2}{\rho_2 - \rho_1}$	280	WOA01
θ	0.35	WOA01
SST	28.3 °C	WOA01
MLD	34.1 m	NRL

Table 6.1: Linear trends and changes in D26, D20, UOHC and T100 in the SEZ over 1993-2010. The trends are based on least squares fitting and the significance level is based on the t-test.

	Trend (per year)	Beginning of trend (1993)	End of trend (2010)	Change in linear trend	Change in percentage (%)	Significance level (%)
D20 (m)	0.9	158	173	15	9	99
D26(m)	0.3	56	61	5	9	99
UOHC (kJ cm^{-2})	0.3	54	59	5	9	80
T100 (°C)	0.01	26.72	26.88	0.16	0.6	80

Table 6.2: Linear trends and changes in D26, D20, UOHC and T100 in the Gyre over 1993-2010. The trends are based on least squares fitting and the significance level is based on the t-test.

	Trend (per year)	Beginning of trend (1993)	End of trend (2010)	Change in linear trend	Change in percentage (%)	Significance level (%)
D20 (m)	1.7	189	219	30	16	99
D26(m)	1.0	104	121	17	16	99
UOHC (kJ cm^{-2})	1.1	109	127	19	17	99
T100 (°C)	0.02	28.44	28.79	0.35	1.2	98

Table 6.3: Linear trends and changes in the percentage of total area of warm, no and cold features in the SEZ over 1993-2010. The unit is %. The trends are based on least squares fitting and the significance level is based on the t-test.

	Trend (per year)	**Beginning of trend (1993)**	**End of trend (2010)**	**Change in linear trend**	**Change in percentage**	**Significance level**
Warm features	0.7	24	35	11	46	99
No features	0.1	56	58	2	4	<50
Cold features	-0.8	20	7	-13	-65	99

Table 6.4: Linear trends and changes in the percentage of total area of warm, no and cold features in the Gyre over 1993-2010. The unit is %. The trends are based on least squares fitting and the significance level is based on the t-test.

	Trend (per year)	**Beginning of trend (1993)**	**End of trend (2010)**	**Change in linear trend**	**Change in percentage**	**Significance level**
Warm features	3.4	7	65	58	829	99
No features	-2.7	81	35	-46	-57	99
Cold features	-0.7	12	0	-12	-100	80

Table 6.5: Comparison of recent estimates of heat content in the upper ocean. Heat storage is per unit area of ocean surface.

Study	Integrated depth (m)	Heat storage ($W\ m^{-2}$)	Trend ($kJ\ cm^{-2}\ yr^{-1}$)	Period	Region	Dataset
Willis et al. (2004)	750	0.86	2.17	1993-2003	Global	Satellite + *in situ*
Levitus et al. (2012)	700	0.27	0.83	1955-2010	Global	*In situ*
Lyman et al. (2010)	700	0.64*	2.84	1993-2008	Global	*In situ*
Levitus et al. (2009)	700	0.36	1.1	1969-2008	Global	*In situ*
Domingues et al. (2008)	700	0.36	1.1	1961-2003	Global	*In situ*
Present analysis	58.4 (Mean D26 in SEZ)	-	0.3	1993-2010	SEZ	Satellite
Present analysis	112.8 (Mean D26 in Gyre)	-	1.1	1993-2010	Gyre	Satellite

* per unit area of Earth's surface

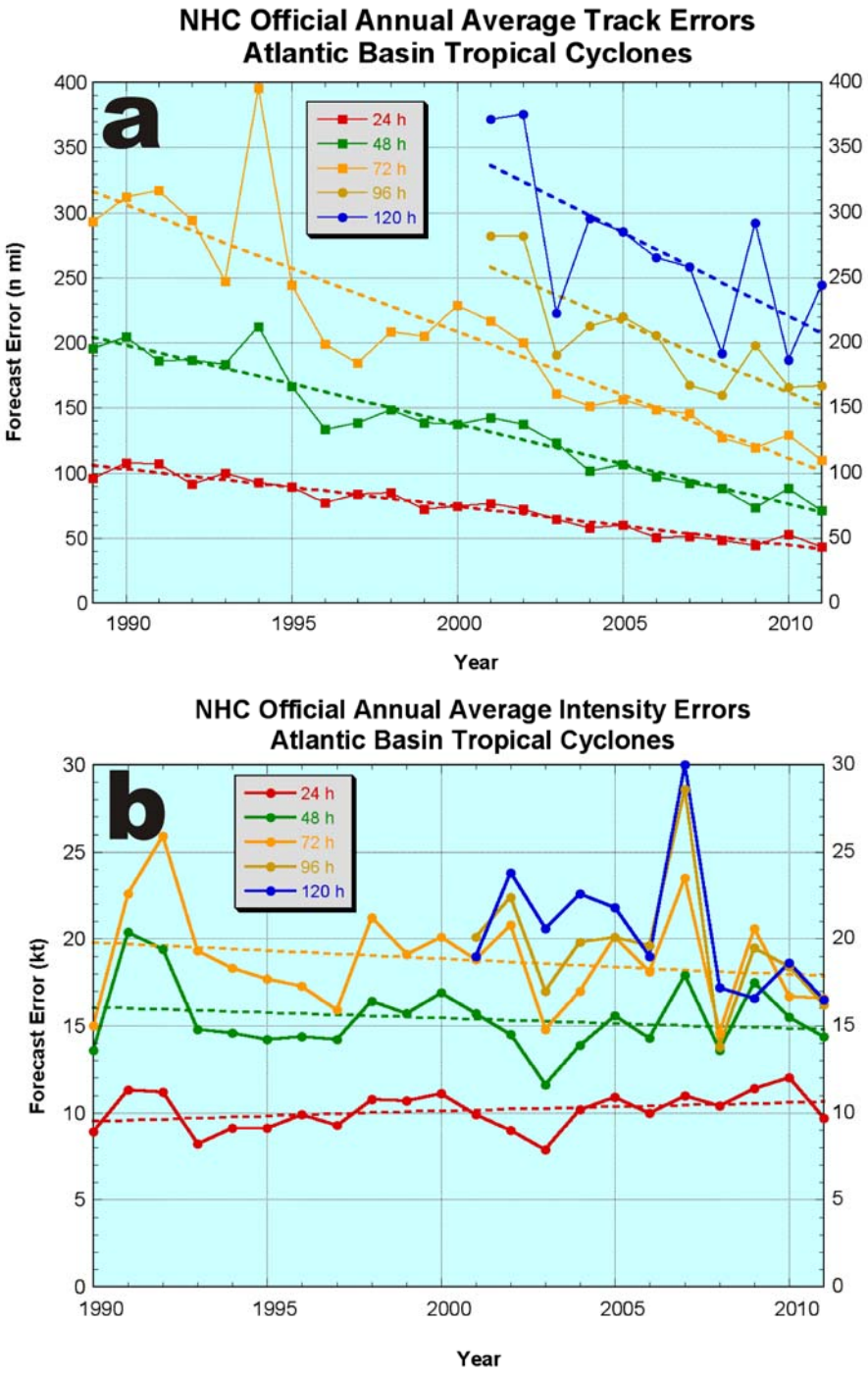

Figure 1.1: Average errors of tropical cyclone forecast in (a) track for the period 1989-2011 and (b) intensity for the period 1990-2011 for the Atlantic basin. [Courtesy of NOAA/National Hurricane Center (NHC), http://www.nhc.noaa.gov/verification/verify5.shtml]

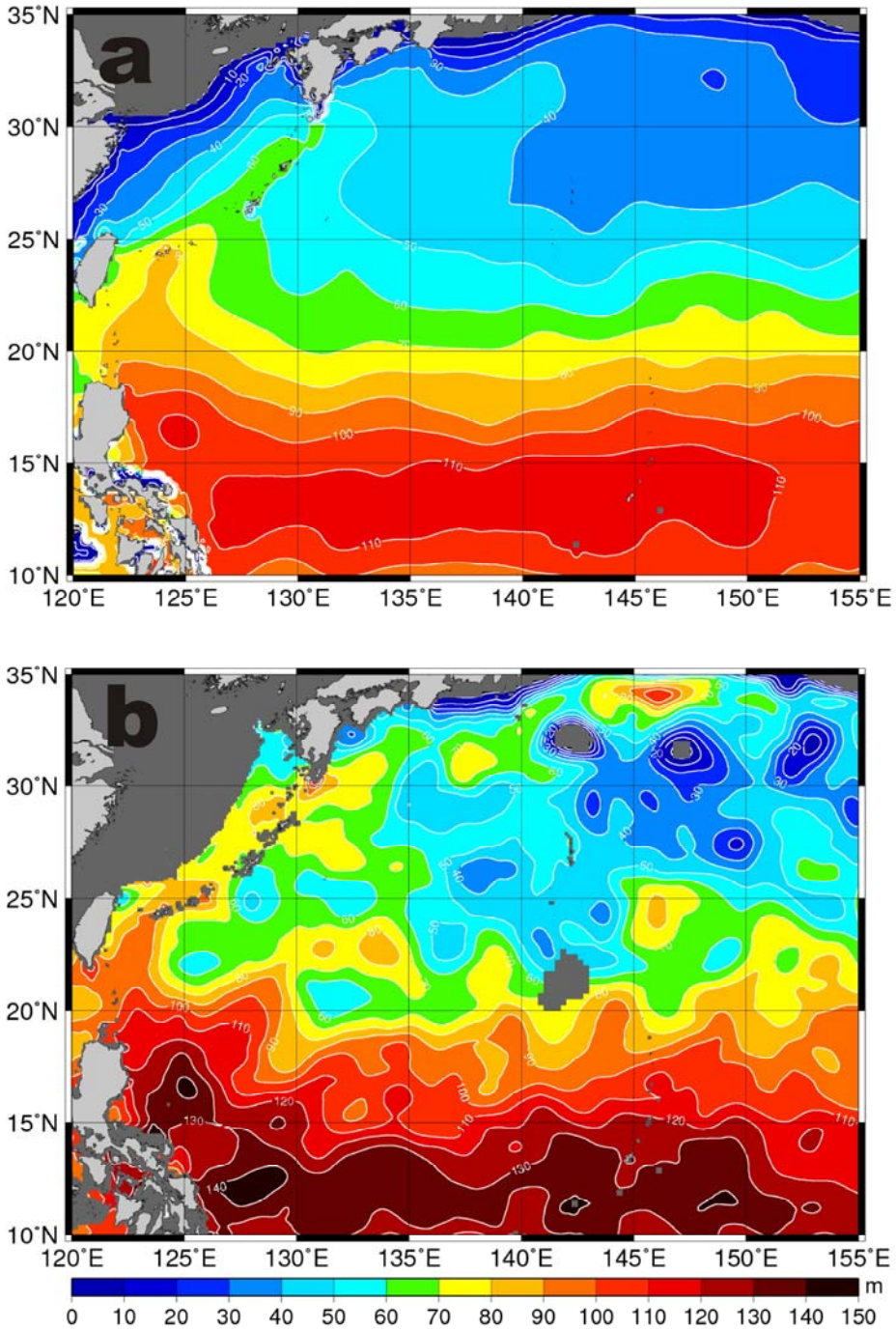

Figure 1.2: A comparison of the thicknesses of the warm water layer (> 26°C) between (a) the climatology for September from the World Ocean Atlas 2001 (WOA01, Stephens et al. 2002), and (b) the satellite estimation on 24 September 2010 from the two-layer model (Pun et al. 2007).

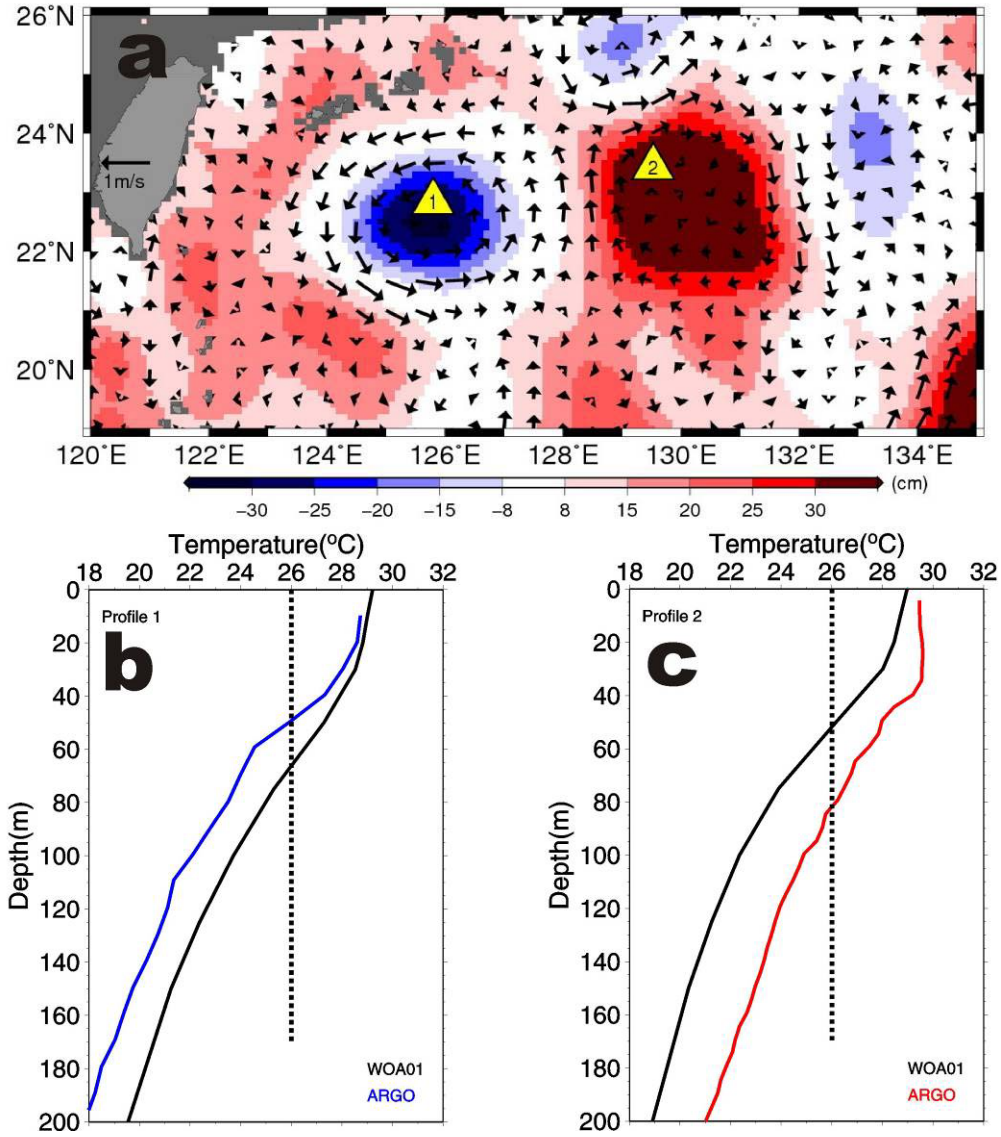

Figure 1.3: (a) Relative geostrophic currents superimposed on an SSHA map from August 20, 2008. One can see that there are two distinct warm and cold eddies east of Taiwan. The warm eddy is associated with positive SSHA and anticyclonic flow, whereas the cold eddy is associated with negative SSHA and cyclonic flow. (b) A comparison of an *in situ* depth-temperature profile-1 of August 16, 2008 from Argo float and a profile of August from the World Ocean Atlas 2001 (WOA01, Stephens et al. 2002). The two profiles are depicted by blue and black curves, respectively. (c) the same as in (b), but the red curve depicts the Argo profile-2 of August 20, 2008. The locations of the profiles are indicated by yellow triangles in (a).

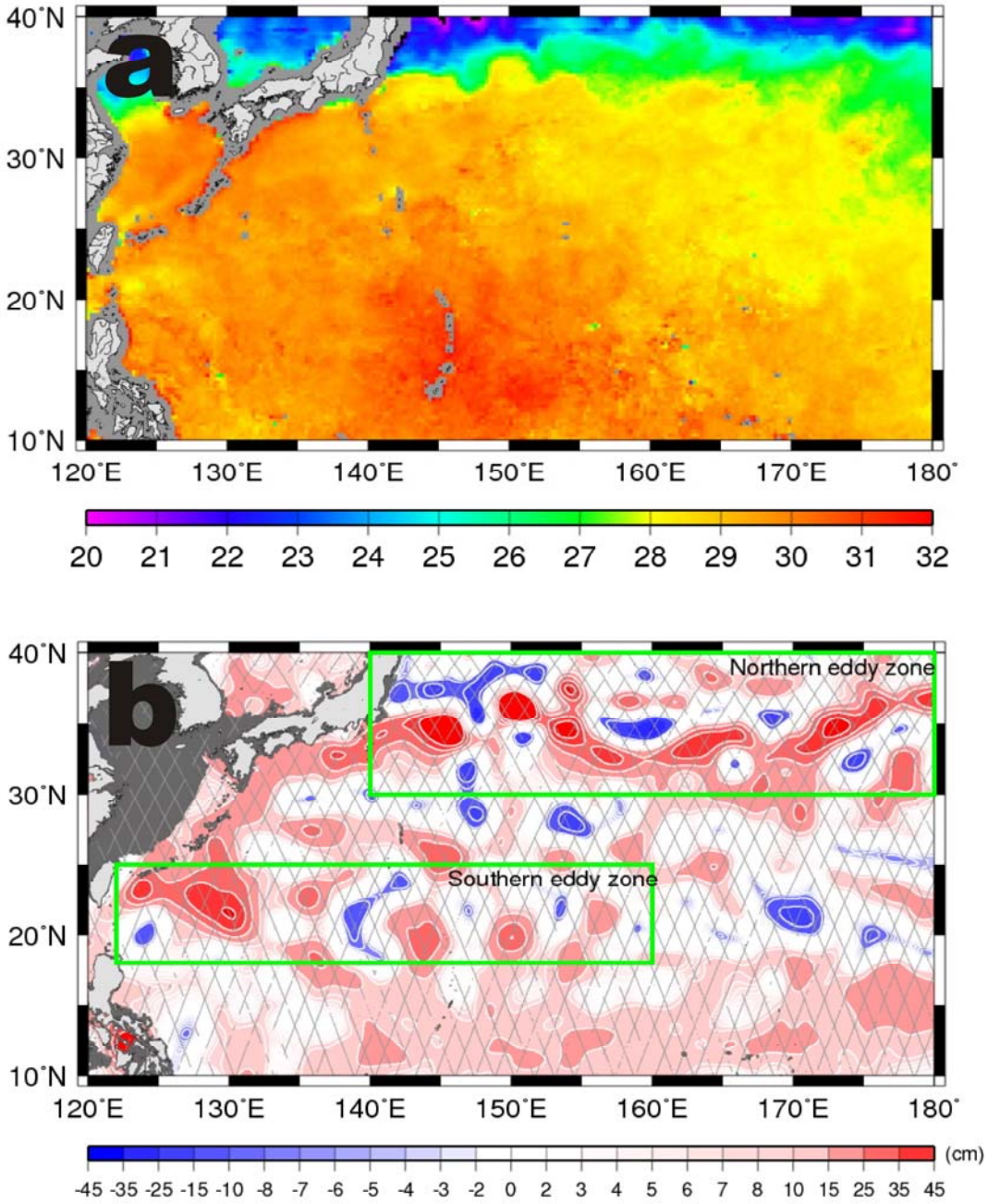

Figure 1.4: (a) 3-day averaged SST from 4-6 September 2003 from Tropical Rainfall Measuring Mission/Microwave Imager (TRMM/TMI). (b) Composite of SSHA measurements from TOPEX/Poseidon and Jason-1 for one 10-day cycle between 27 August and 5 September 2003. Their ground tracks are shown in light grey lines. The southern and northern eddy zones are indicated by green boxes.

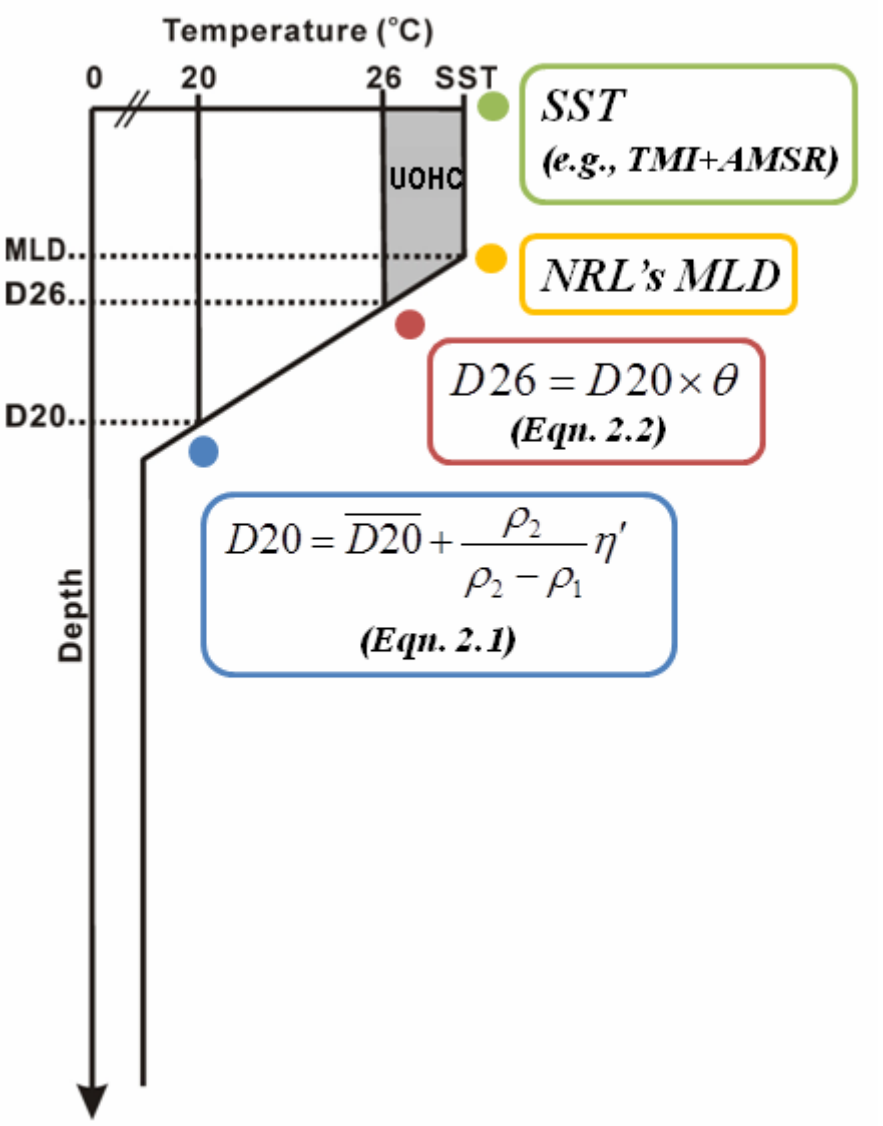

Figure 2.1: The schematic of satellite-derived upper ocean temperature profiles (i.e., UOTS) consisting of SST, MLD (mixed-layer depth), D26 (the depth of the 26°C isotherm, above which the water is regarded as warm), and D20 (the depth of the 20°C isotherm).

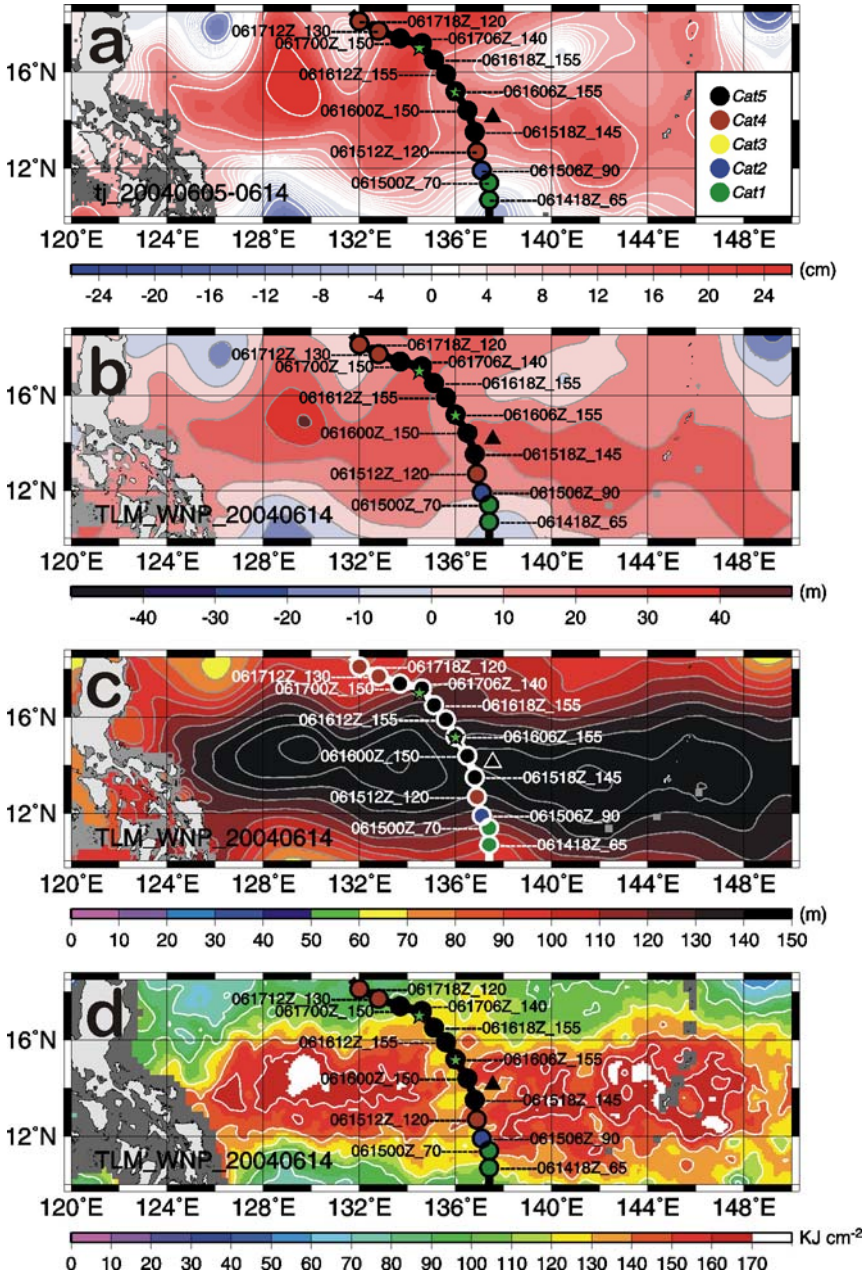

Figure 2.2: (a) Composite of TOPEX/Poseidon and Jason-1 altimetry measurements for one cycle (10 days) between 5 and 14 Jun 2004 showing the pre-Dianmu SSHA. (b) △D26 (2-layer-derived D26 minus climatological D26), (c) 2-layer-derived D26, and (d) UOHC estimated from the 2-layer-derived profiles. Green stars and black triangle depict the *in situ* profiles found before and during the Dianmu's passage. Typhoon's intensity in Saffir-Simpson scale is shown in the legend of (a).

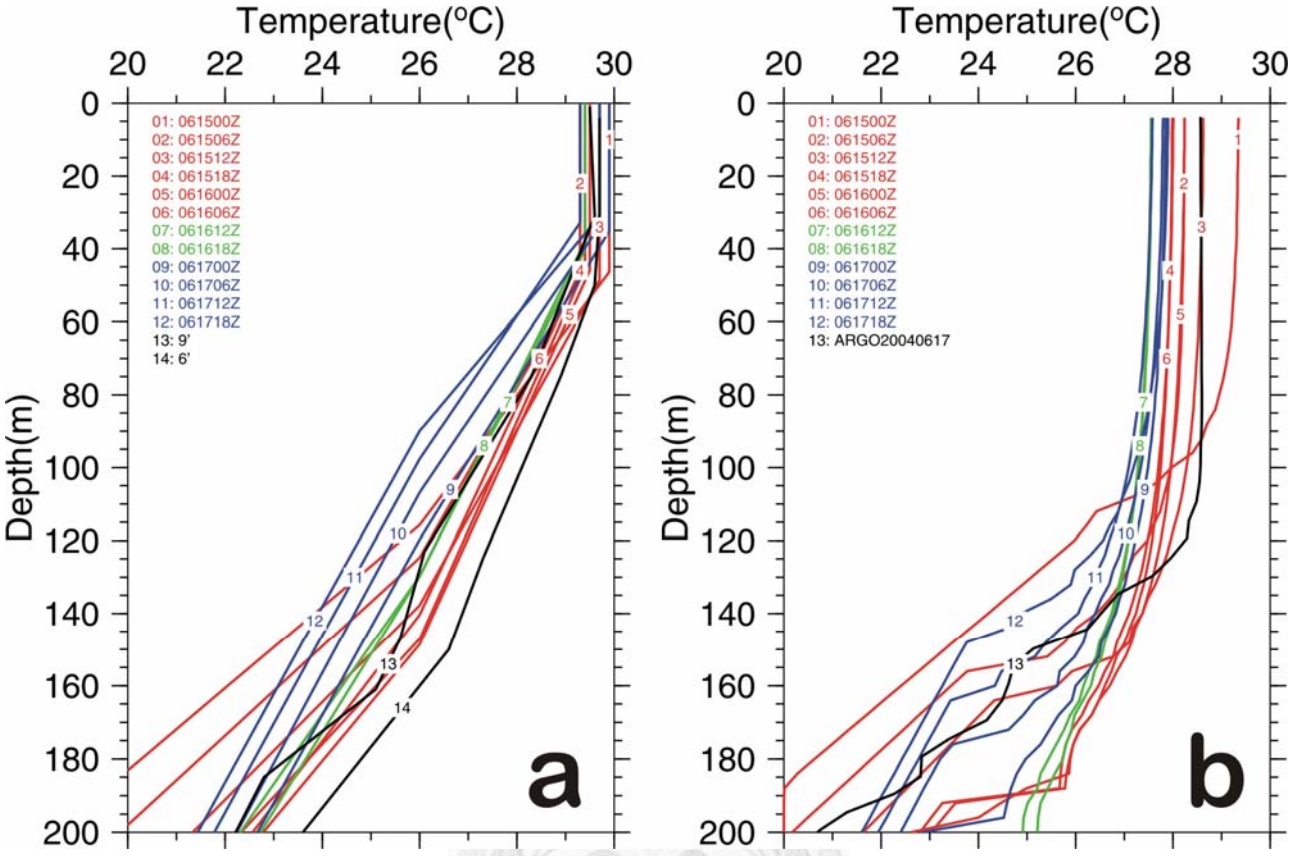

Figure 2.3: (a) Initial profiles along Dianmu's track used in the mixed-layer model experiment where *in situ* profiles are depicted in black, profiles along Dianmu's intensification location in red, along Dianmu's intensity maintenance location in green, along Dianmu's intensity decay location in blue.

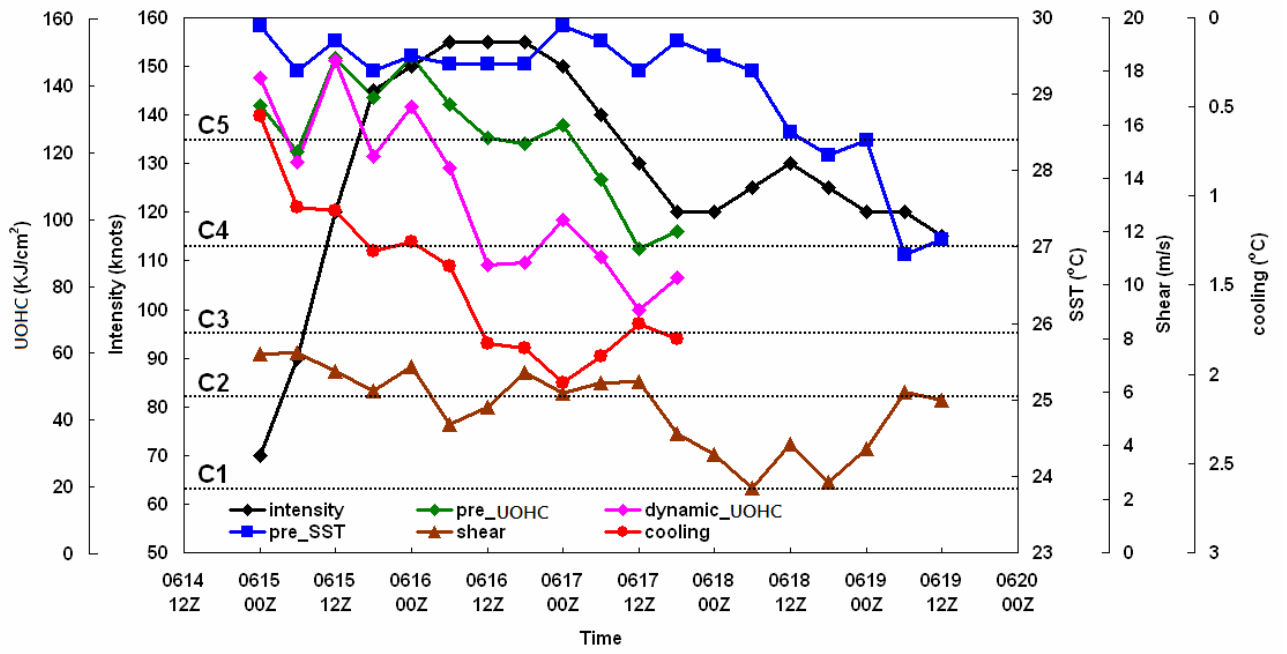

Figure 2.4: The relationship between 5 parameters (self-induced SST cooling, dynamic UOHC, pre-typhoon SST, pre-typhoon UOHC and vertical wind shear) and typhoon's intensity.

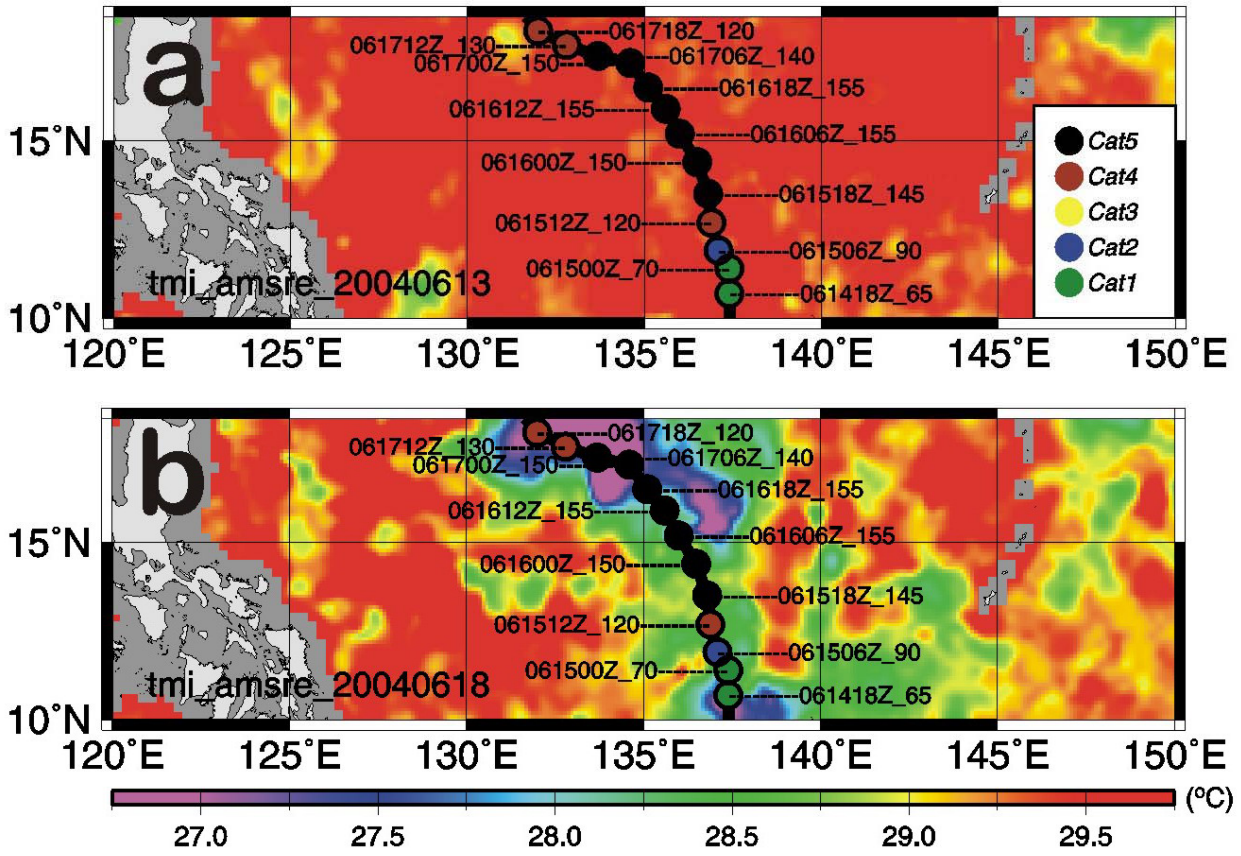

Figure 2.5: Composite of SST from the TMI and AMSR-E passes in (a) 13 Jun 2004 for Pre-Dianmu and in (b) 18 Jun 2004 for after-Dianmu's passage.

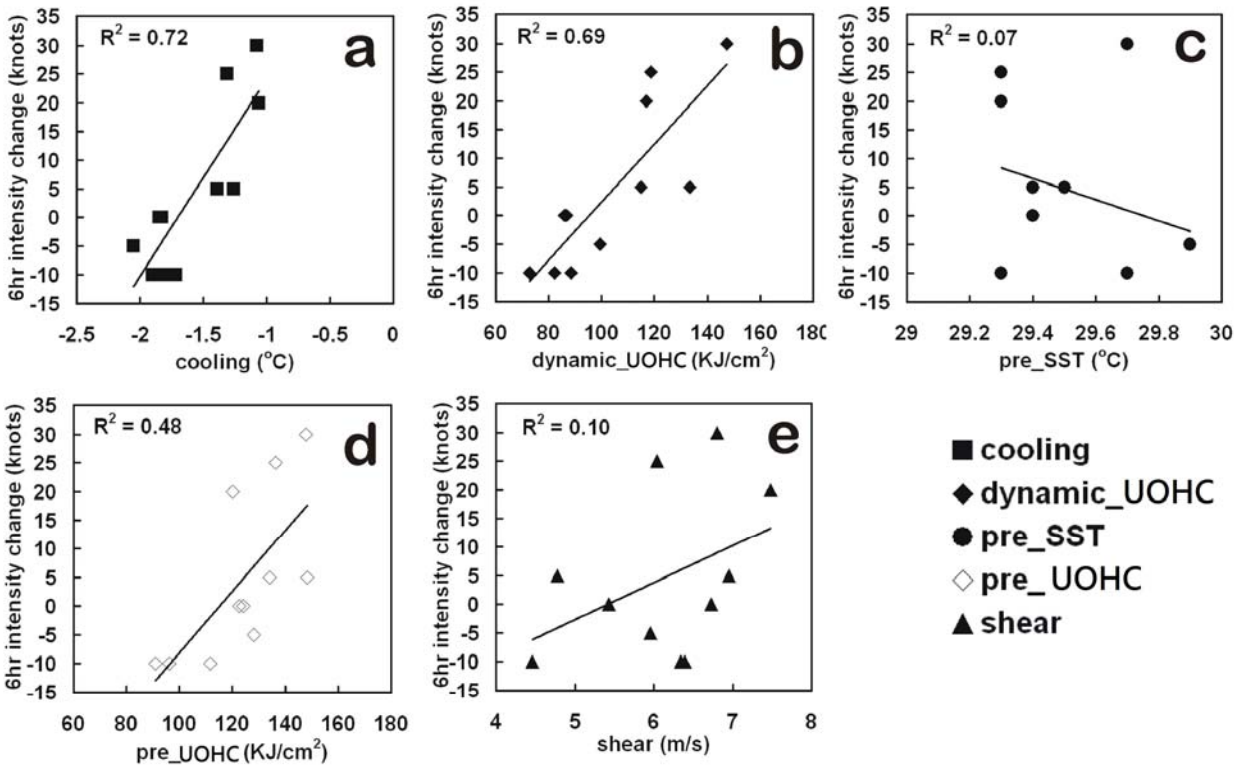

Figure 2.6: The 6 h intensity change of Dianmu with the 5 parameters, i.e., (a) self-induced SST cooling, (b) dynamic UOHC, (c) pre-typhoon SST, (d) pre-typhoon UOHC, and (e) vertical wind shear.

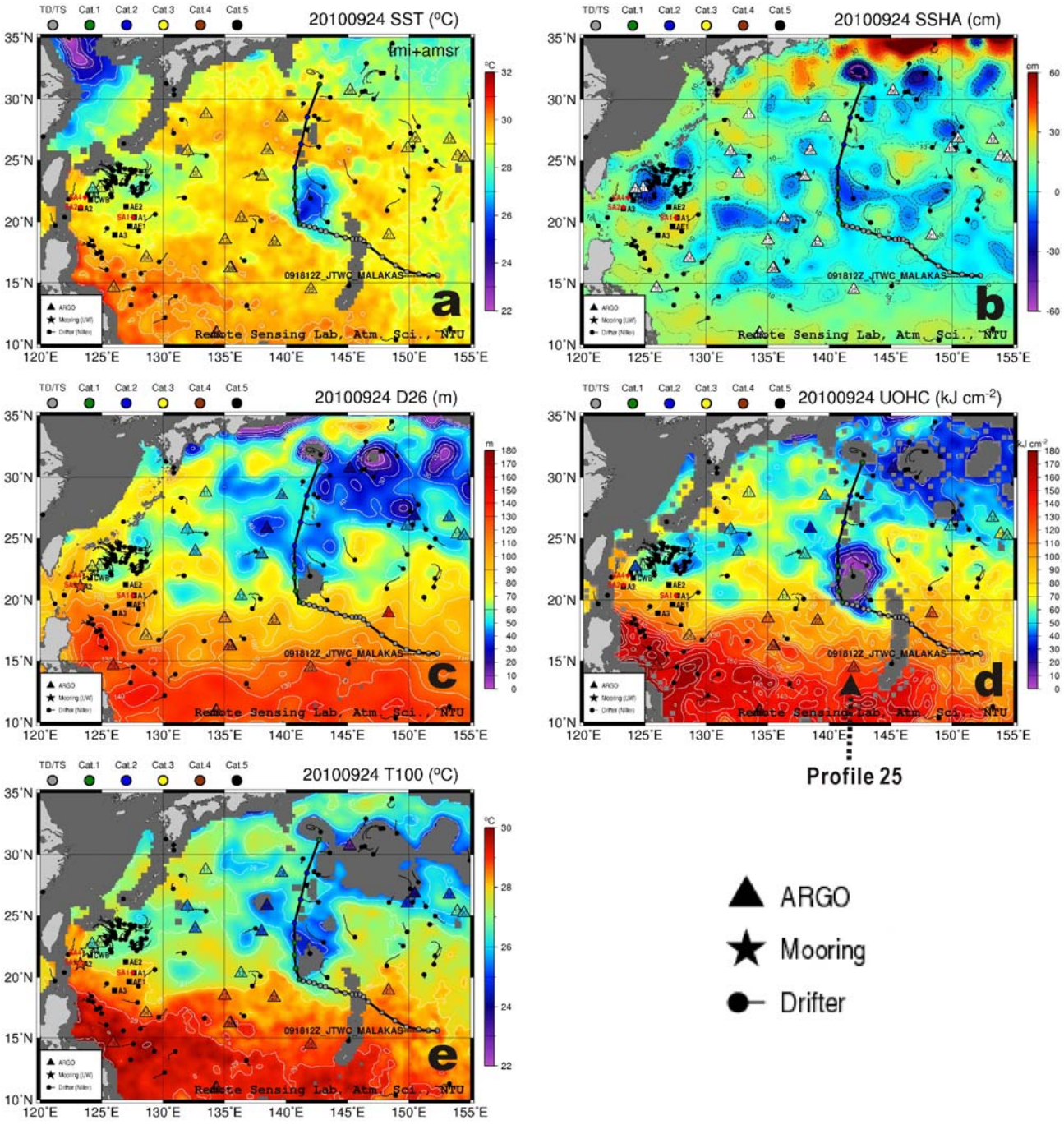

Figure 2.7: Operational daily two-dimensional maps of (a) SST, (b) SSHA, (c) D26, (d) UOHC, and (e) T100 on 24 September 2010. On the maps, color-coded triangles represent Argos searched within 2 days period; color-coded asterisks in (c) and (e) represent mooring measurements; black dots represent drifters and floats; and black curve with color-coded dots represents typhoon Malakas (2010)' track and intensity from the JTWC.

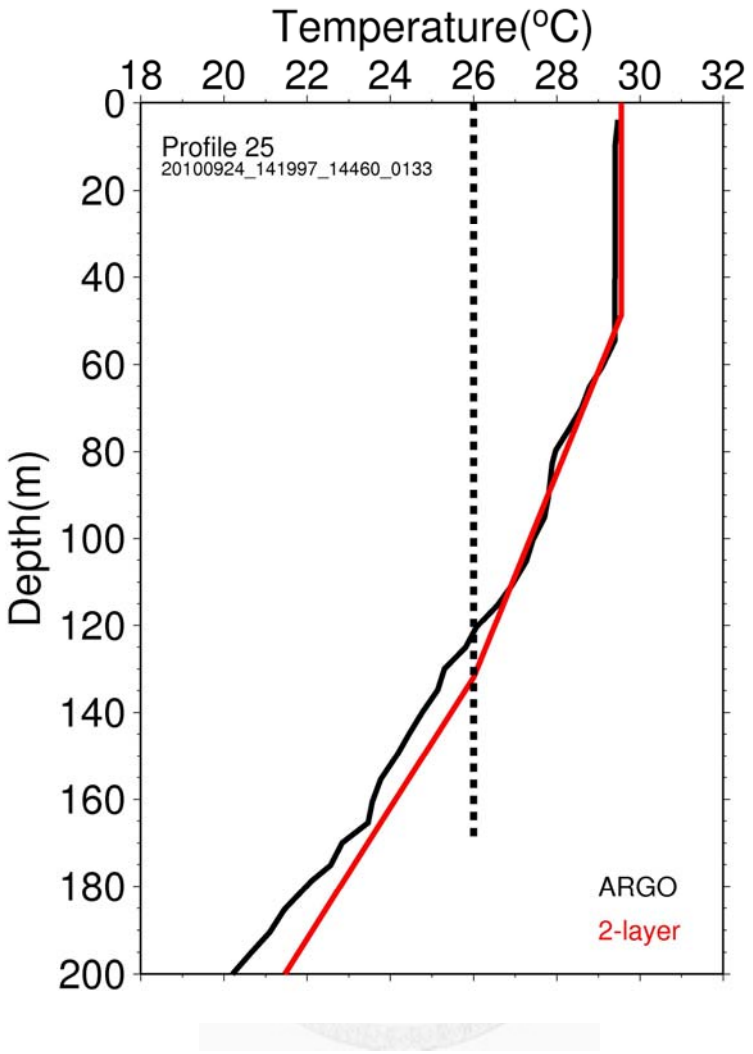

Figure 2.8: Comparison of Argo float (black) and satellite-derived (red) temperature profiles. See Figure 2.7 for the profile's location (Profile 25).

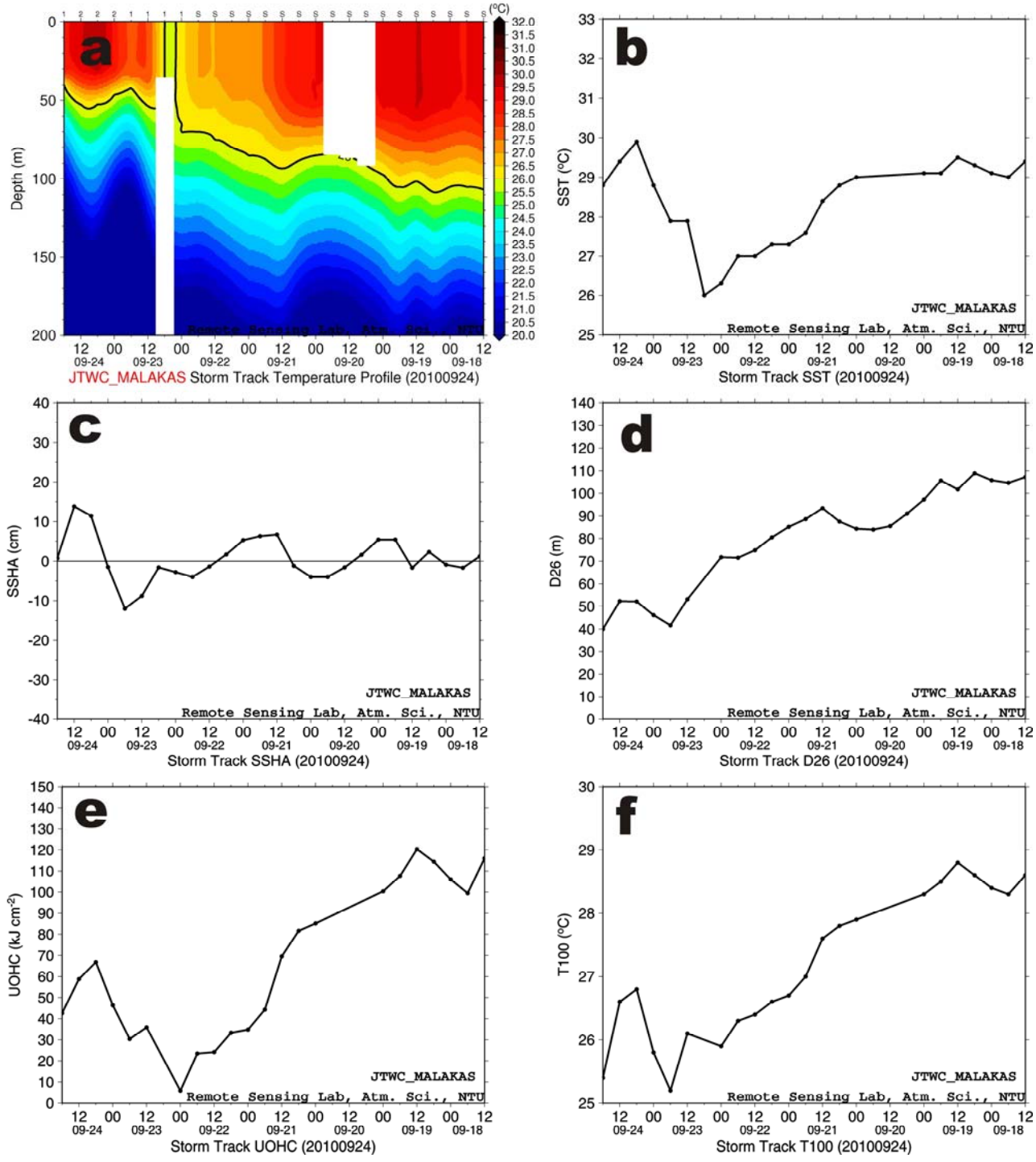

Figure 2.9: Operational products of along the typhoon Malakas (2010) track: (a) UOTS, (b) SST, (c) SSHA, (d) D26, (e) UOHC, and (f) T100 on 24 September 2010 during the ITOP experiment.

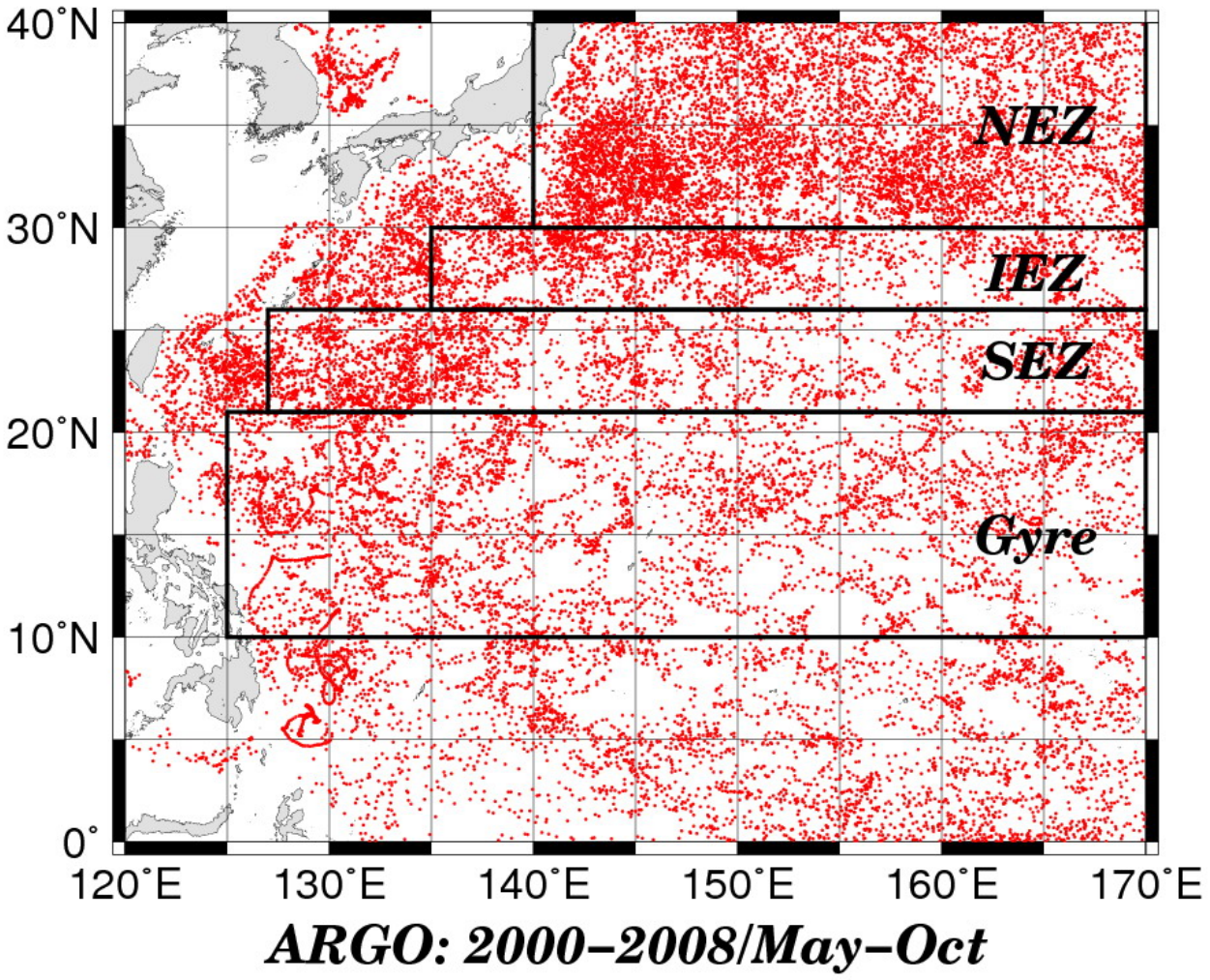

Figure 3.1: The locations of Argo profiles in the western North Pacific used to establish the linear regressions of SSHA onto displacement of subsurface isotherms. Red dots depict a total of 38,556 profiles collected from May to October of 2000-2008. Four hydrographic zones, i.e., the Gyre, SEZ, IEZ and NEZ, are indicated.

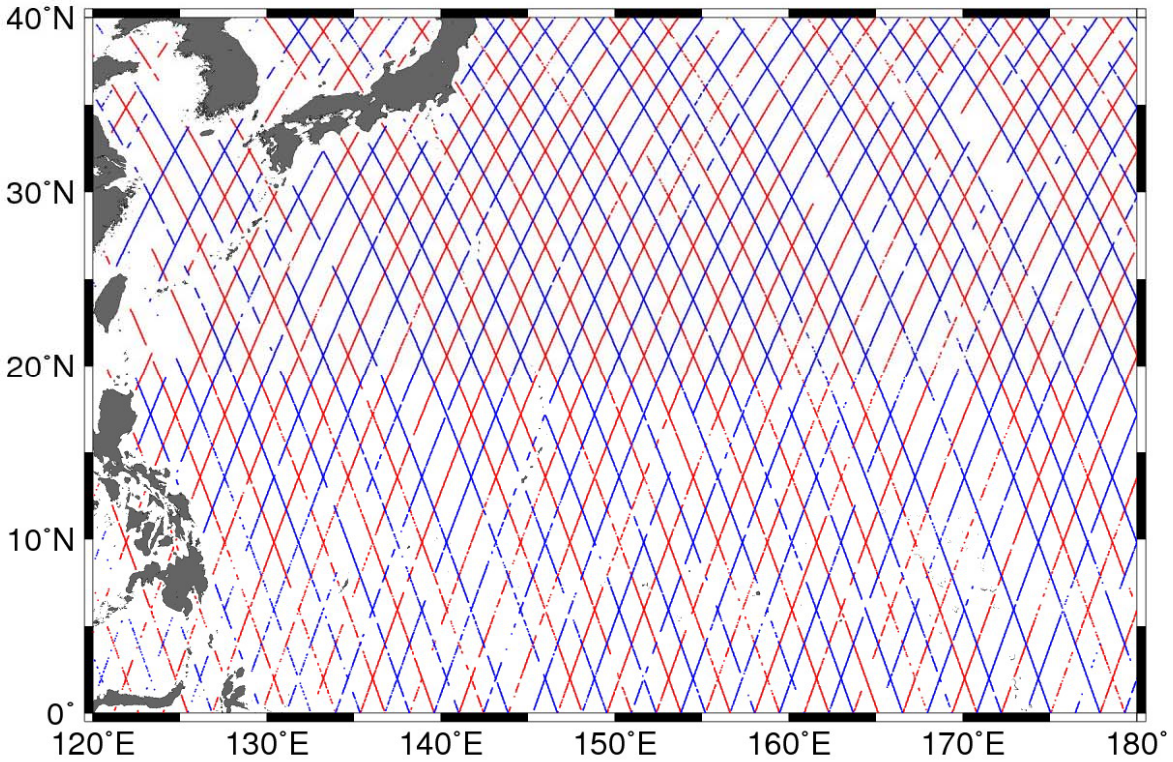

Figure 3.2: 10-day ground tracks of TOPEX/Poseidon (red) and Jason-1 (blue) in the western North Pacific.

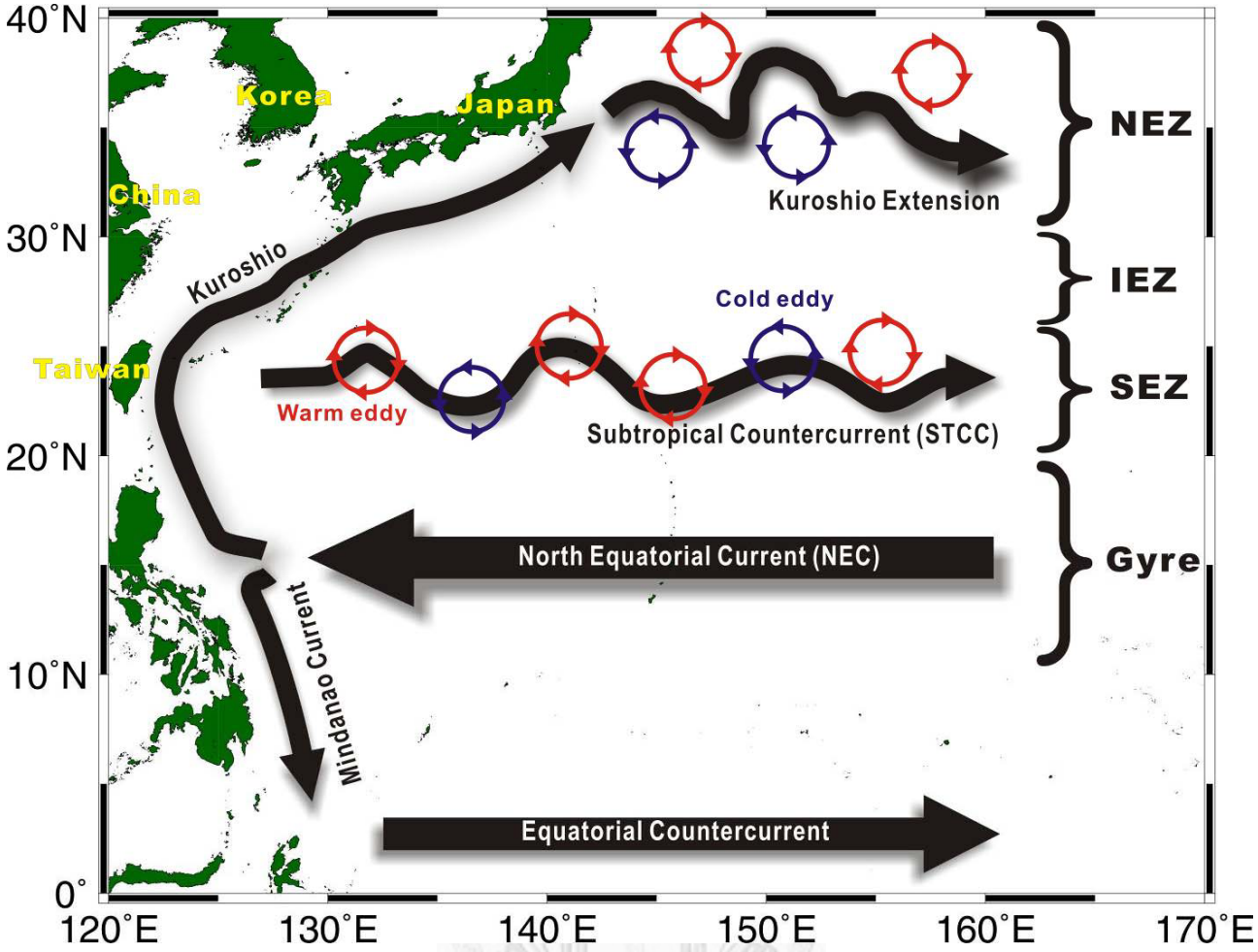

Figure 3.3: Schematic of current systems and associated eddy fields in the western North Pacific. Red and blue rings depict anti-cyclonically circulated warm eddies and cyclonically circulated cold eddies, respectively. The latitudinal band of the Gyre, SEZ, IEZ and NEZ are denoted. The current systems refer mainly to Qiu (2001).

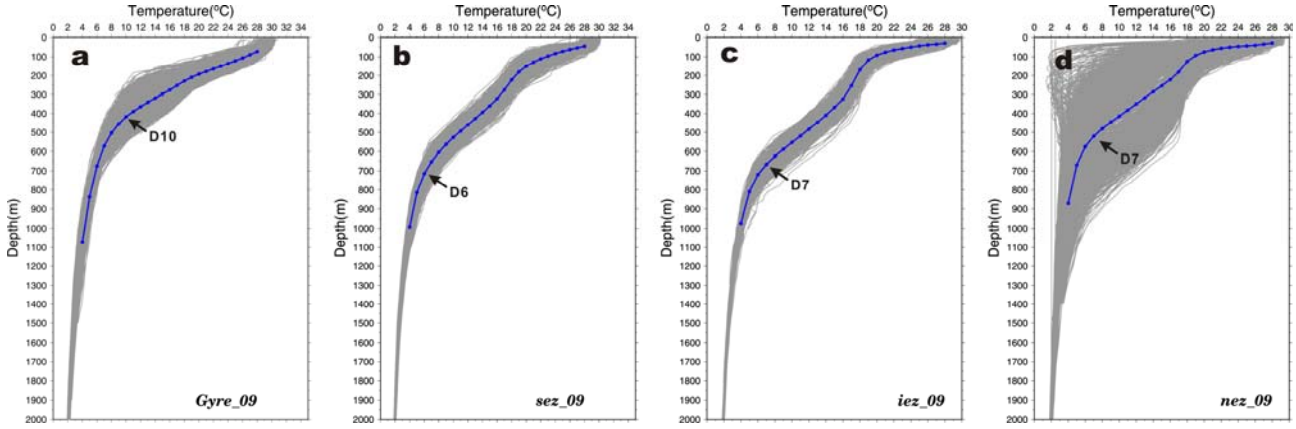

Figure 3.4: All of the Argo profiles (grey curves) in September from 2000 to 2008 in (a) the Gyre, (b) the SEZ, (c) the IEZ and (d) the NEZ. The blue curves depict the mean profiles and the blue dots depict the mean depths of isotherms from D28 to D4. The arrows depict the base of thermocline, which is located at D10 in Gyre, D6 in SEZ and D7 in IEZ and NEZ.

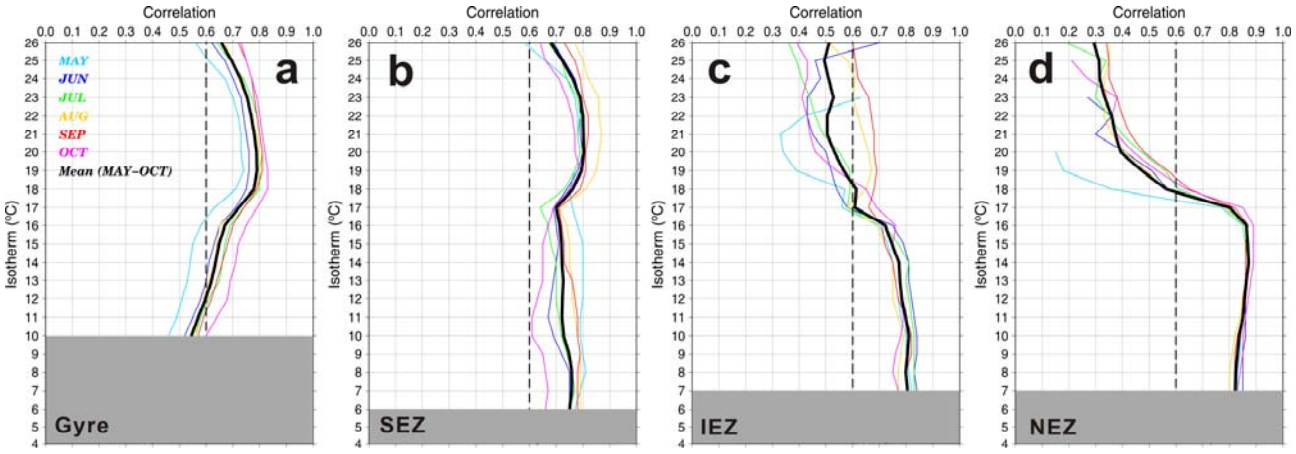

Figure 3.5: The monthly correlation coefficients between SSHA and displacements of the isotherms from 26°C to 4°C in (a) the Gyre, (b) the SEZ, (c) the IEZ and (d) the NEZ. The color code for each curves are shown in (a). The dashed line depicts the correlation of 0.6. Grey area masks the isotherms which are below the base of the thermocline.

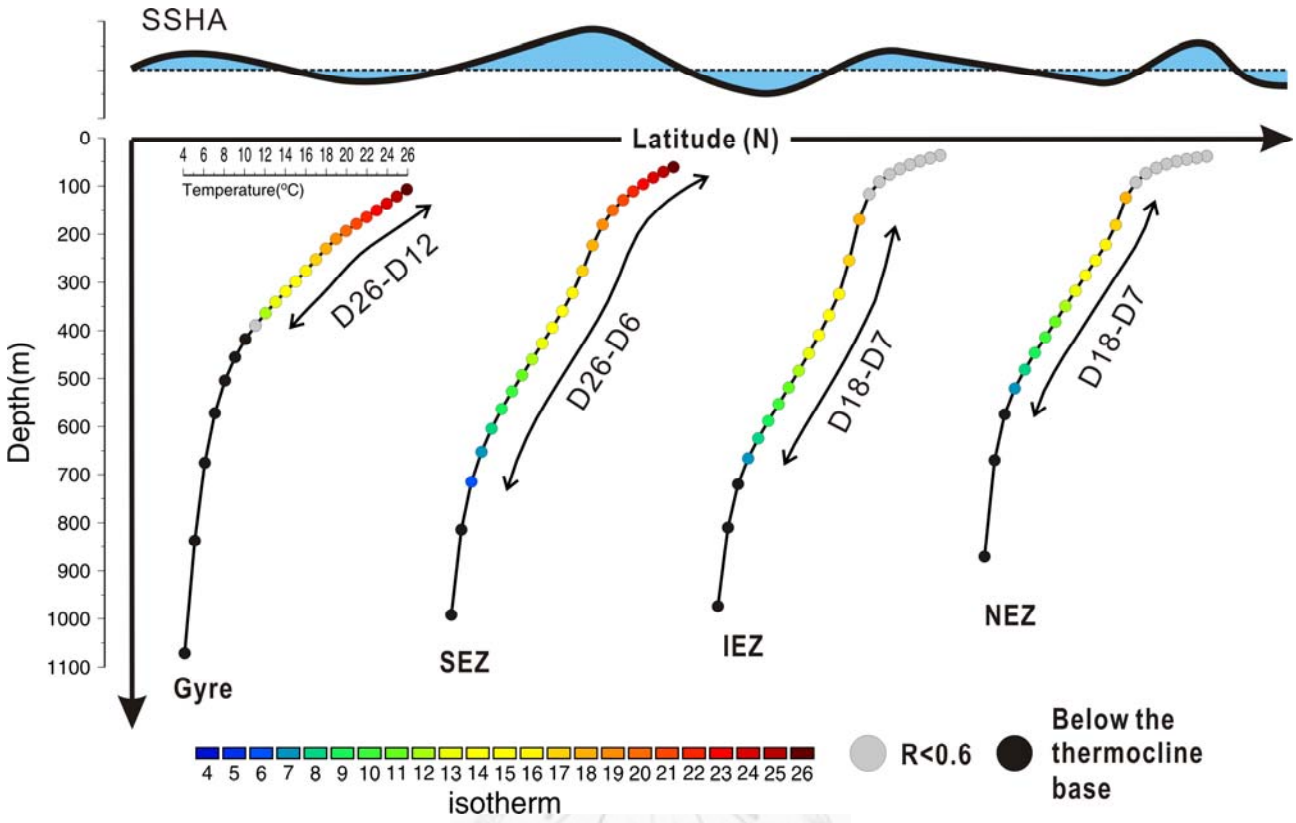

Figure 3.6: the schematic demonstrates the meaning of SSHA for the Gyre, SEZ, IEZ and NEZ. The profile of each zone is the mean profile averaged from 2000-2008 during May-October. The isotherms of which the variation can be described by SSHA are colored, whereas the correlation with SSHA is <0.6 are masked with grey, representing that they cannot be expressed by SSHA effectively, and the isotherms below the base of the thermocline are masked in black. Generally, SSHA can reflect the variation in D26-D12 in the Gyre, D26-D6 in the SEZ, D18-D7 in the IEZ and NEZ.

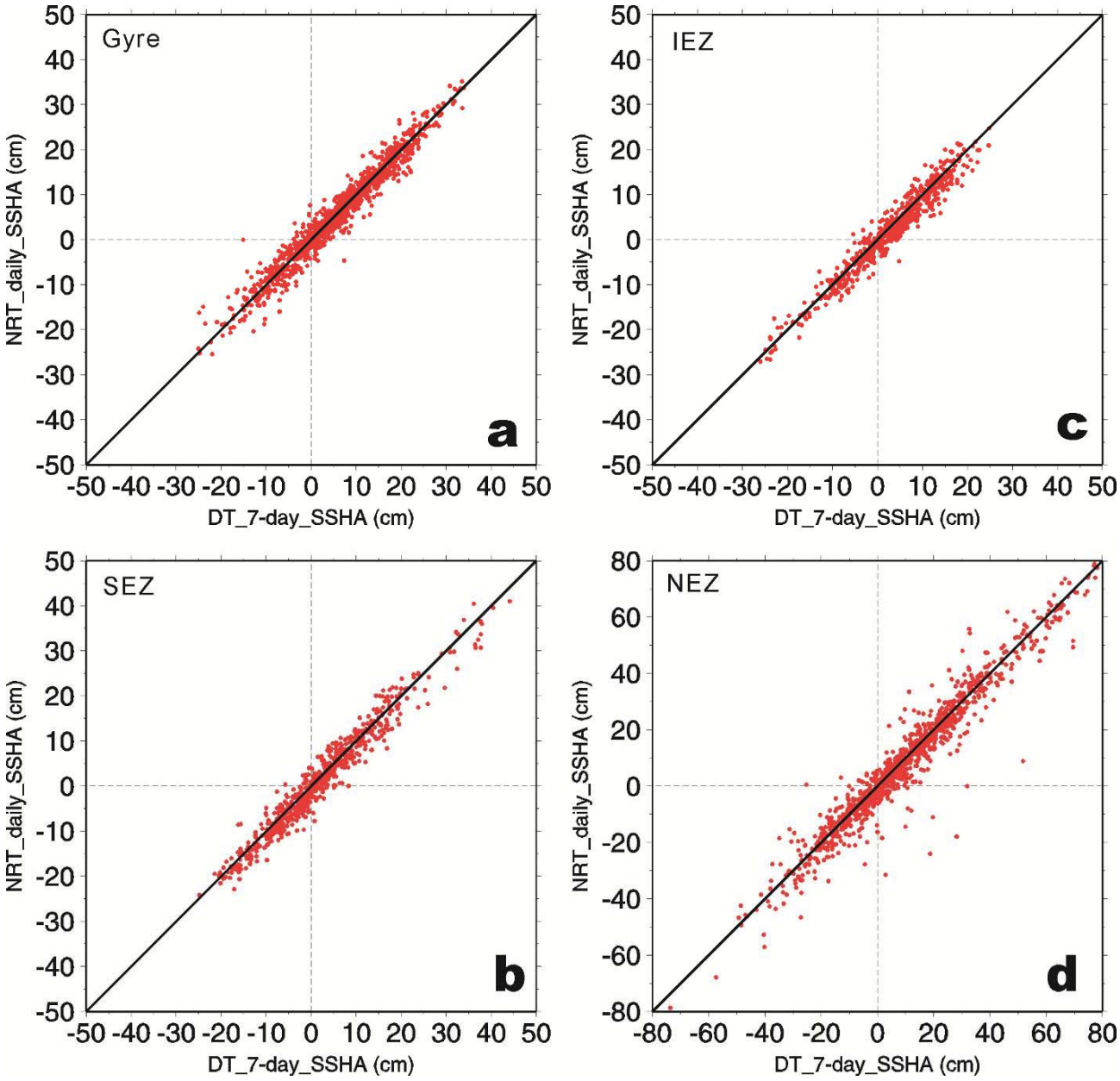

Figure 3.7: Comparison of the near real-time (daily) and delay time (7-day) SSHA, which paired with Argo profiles in 2009 /May-October in (a) the Gyre, (b) the SEZ, (c) the IEZ and (d) the NEZ.

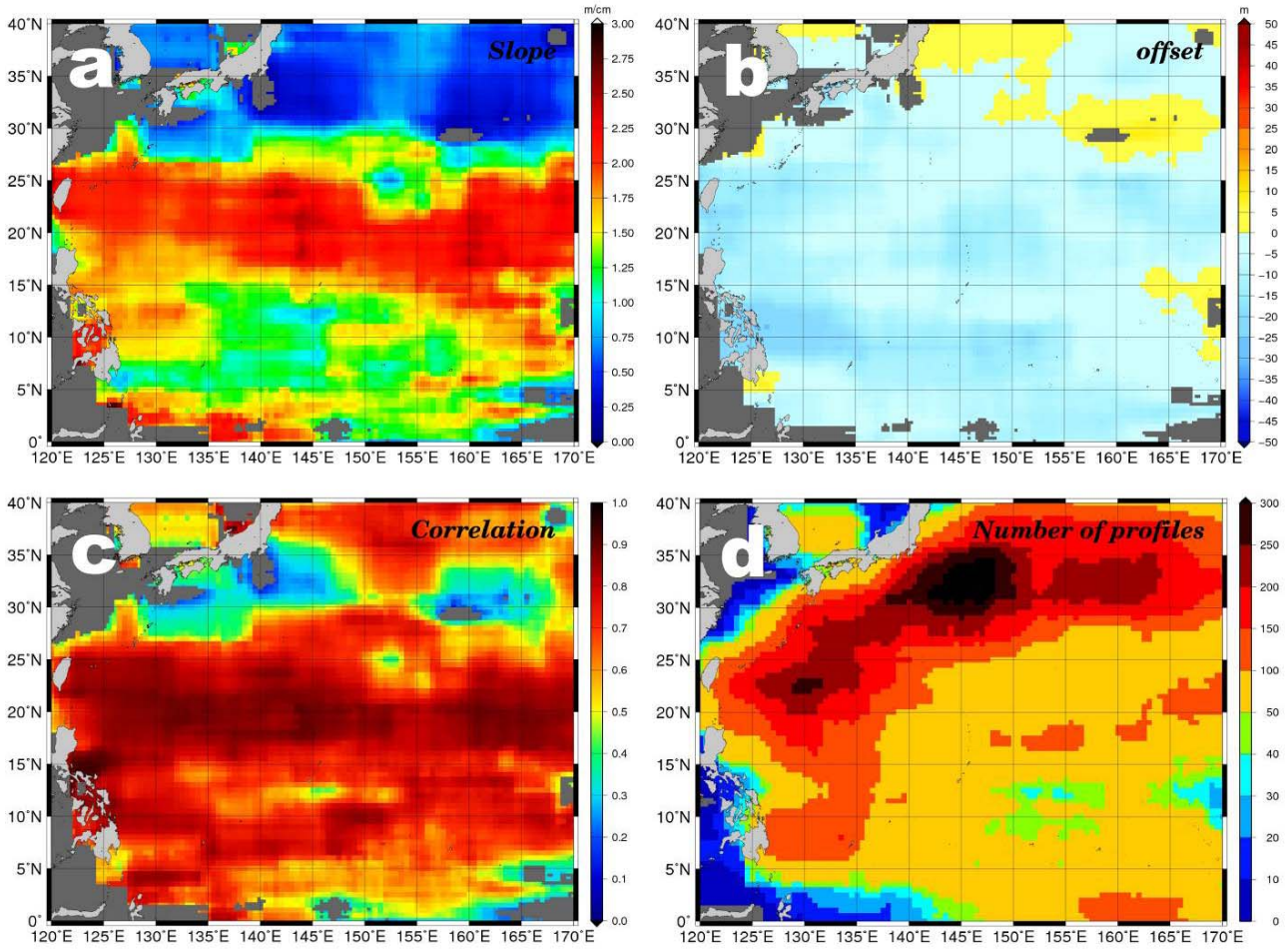

Figure 3.8: (a) and (b) show the slope and offset, respectively, in the eqn. (3.2) for D20 in September. (c) the corresponding correlation coefficient between the variation of D20 and SSHA, and (d) the number of profiles used to calculate the regressions. Grey areas in (a)-(c) represent the significance level that is less than 99%.

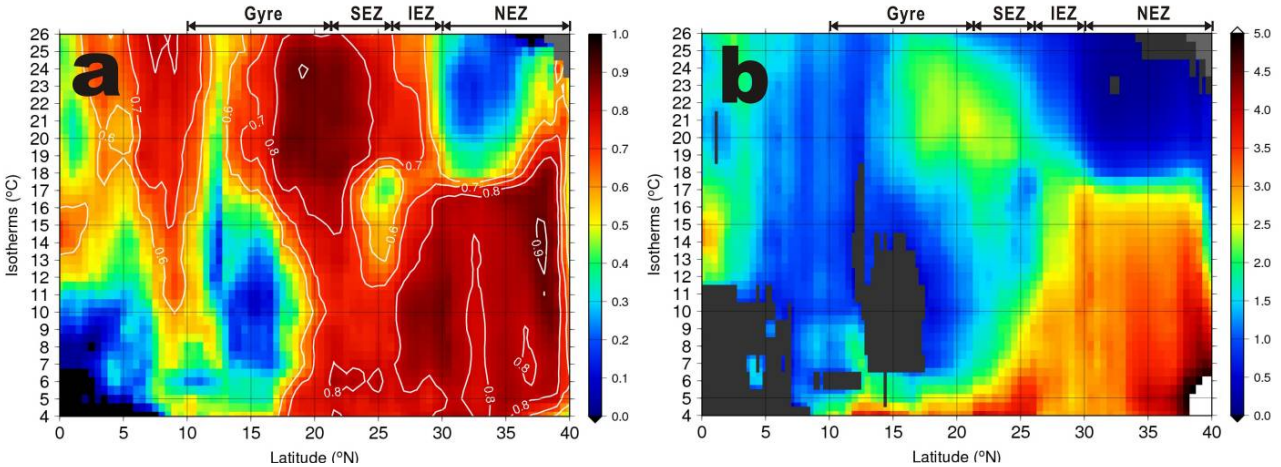

Figure 3.9: (a) The correlation cross section from the equator to 40°N along 145°E in September from D26 down to D4. (b) Same as in (a), but for the slope. In (b), the slope less than 99% significance is marked in grey.

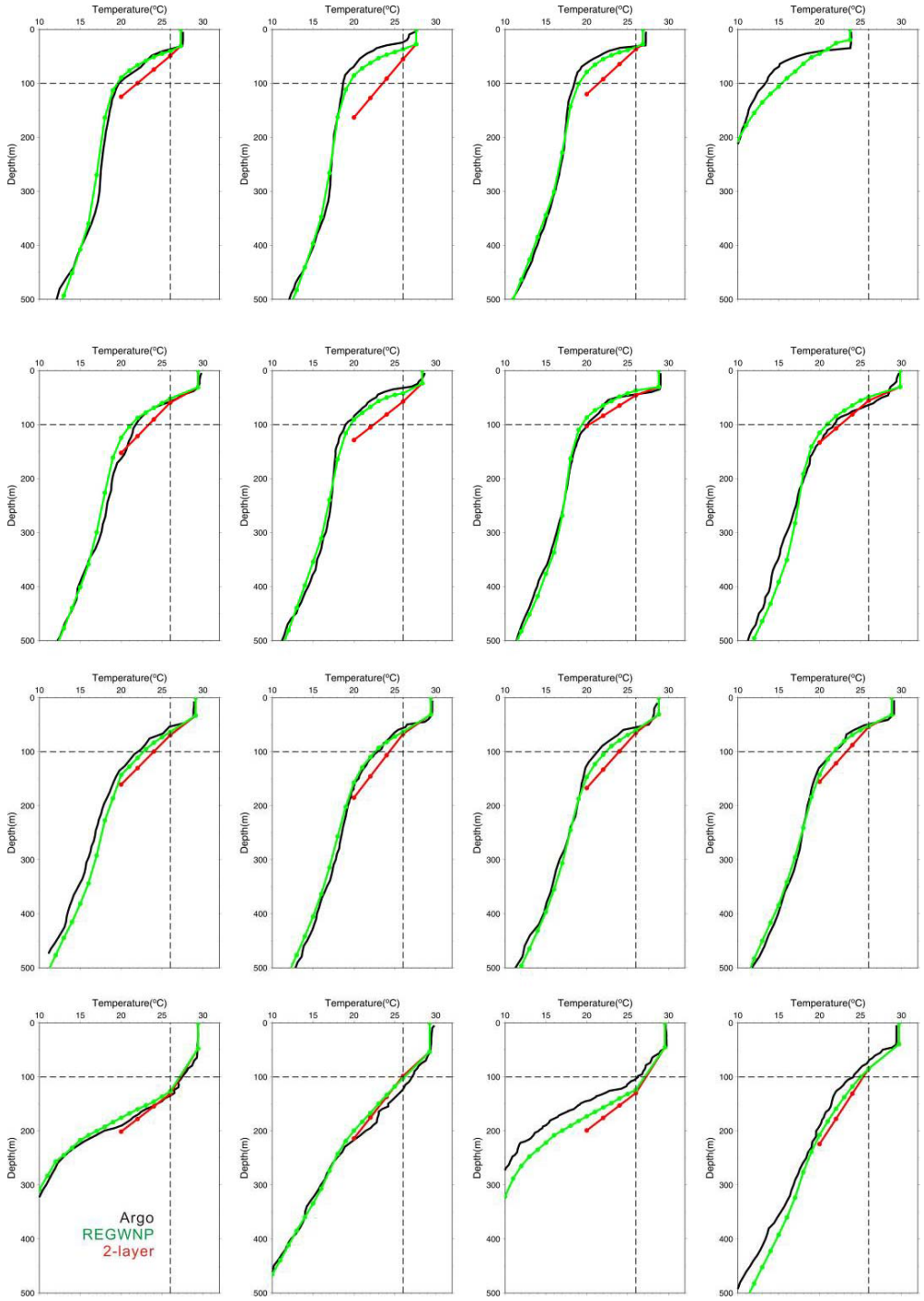

Figure 3.10: Comparison between the profiles from REGWNP (green), 2-layer (red) and Argo (black). The legend is also shown on the lower left plot. From the upper to lower rows represent the profiles from the NEZ, IEZ, SEZ and Gyre. Each zone has four demo profiles randomly picked in September of 2010. Profile from 2-layer is unavailable on the upper right plot. The horizontal and vertical dashed lines depict 26°C and the depth of 100 m, respectively.

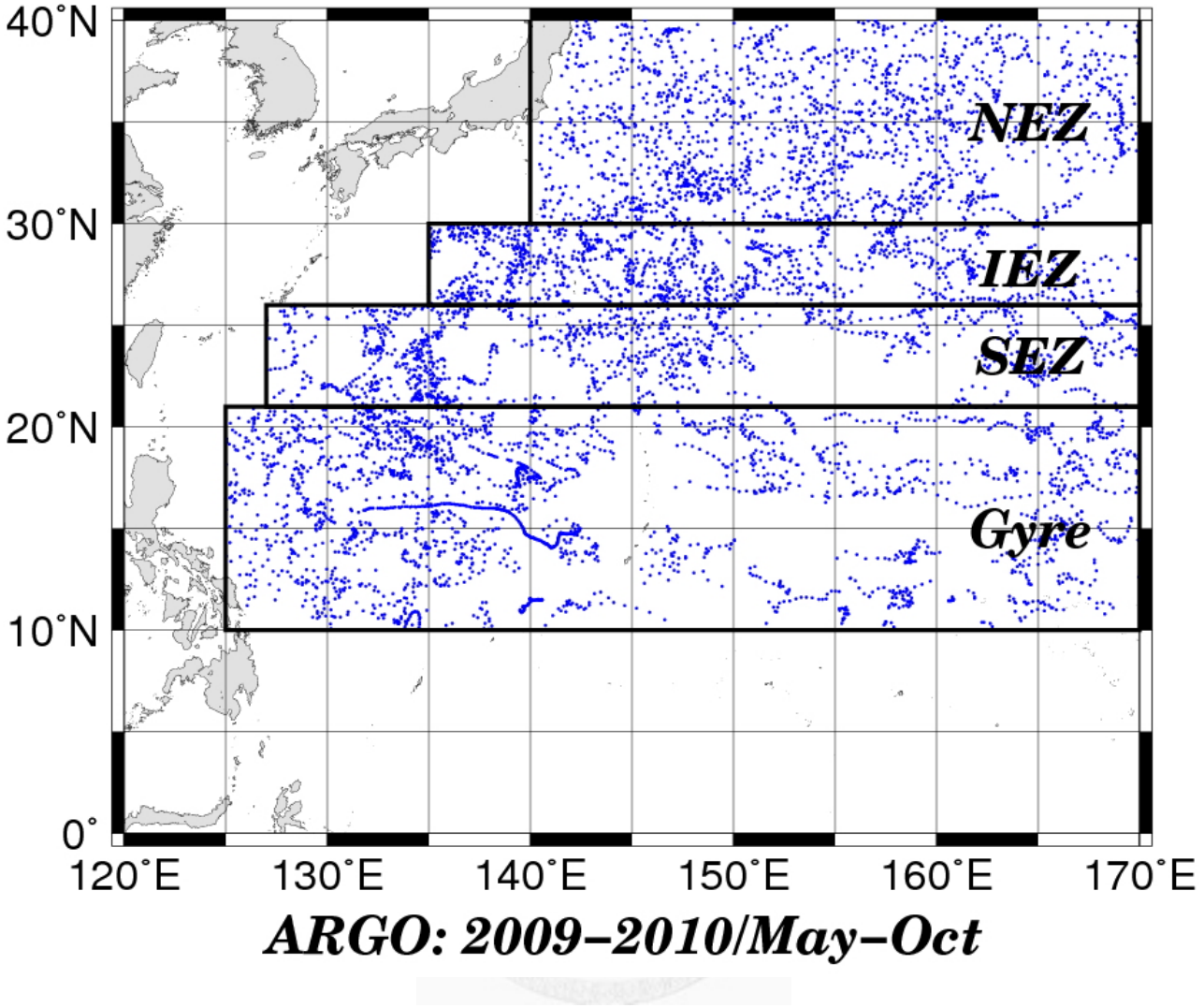

Figure 4.1: The locations of Argo profiles used to validate REGWNP derived UOTS. Blue dots depict a total of 7,036 profiles collected from May to October of 2009 and 2010. Four validation zones, i.e., the Gyre, SEZ, IEZ and NEZ, are indicated.

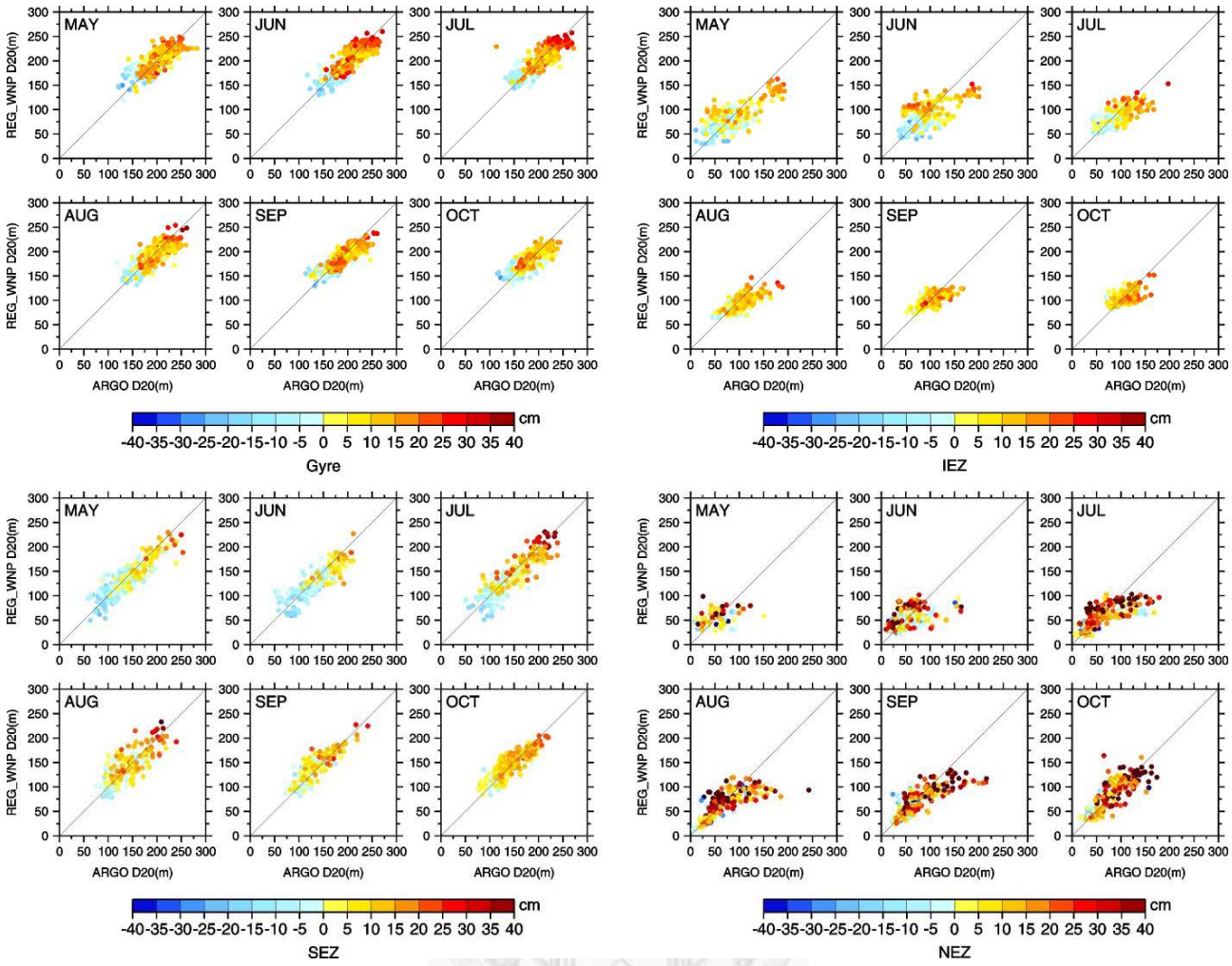

Figure 4.2: Monthly scatter plots of D20 derived from REGWNP and Argo floats in the Gyre (upper-left section), SEZ (lower-left section), IEZ (upper-right section), and NEZ (lower-right section) during 2009-2010. The matching pairs are colored according to their corresponding SSHA values.

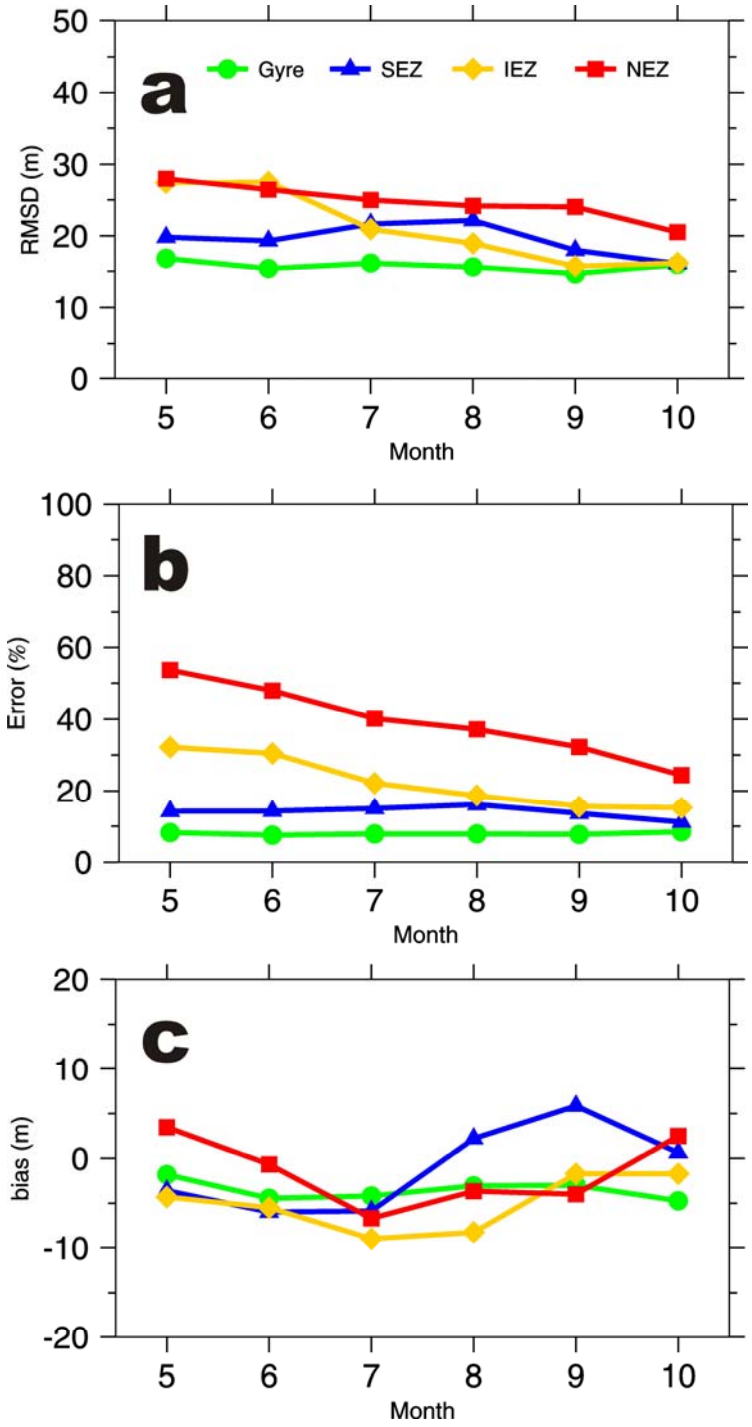

Figure 4.3: (a) Monthly RMSD, (b) error percentage, and (c) bias for REGWNP derived D20. The color code for each zone is shown in (a).

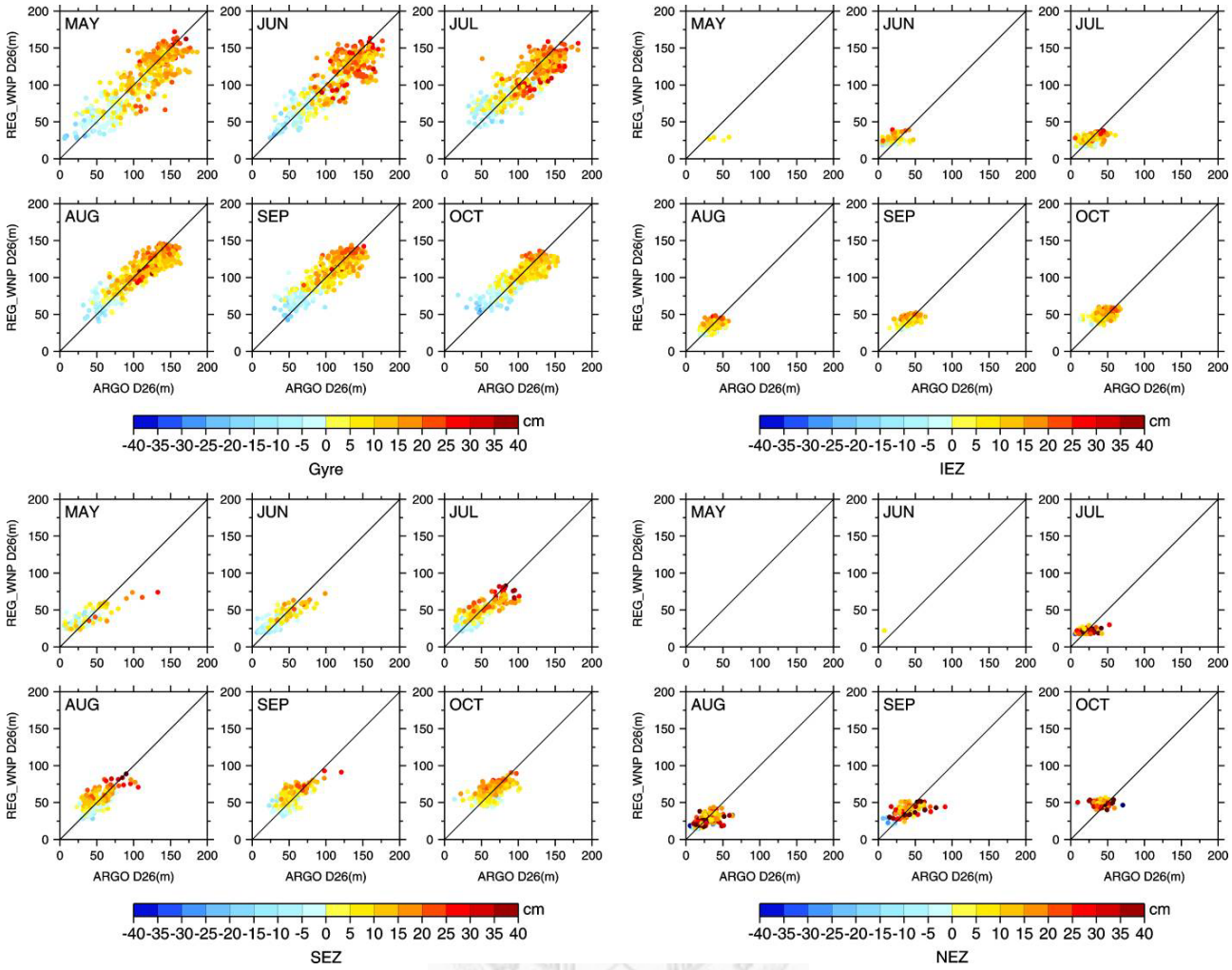

Figure 4.4: Monthly scatter plots of D26 derived from REGWNP and Argo floats in the Gyre (upper-left section), SEZ (lower-left section), IEZ (upper-right section), and NEZ (lower-right section) during 2009-2010. The matching pairs are colored according to their corresponding SSHA values.

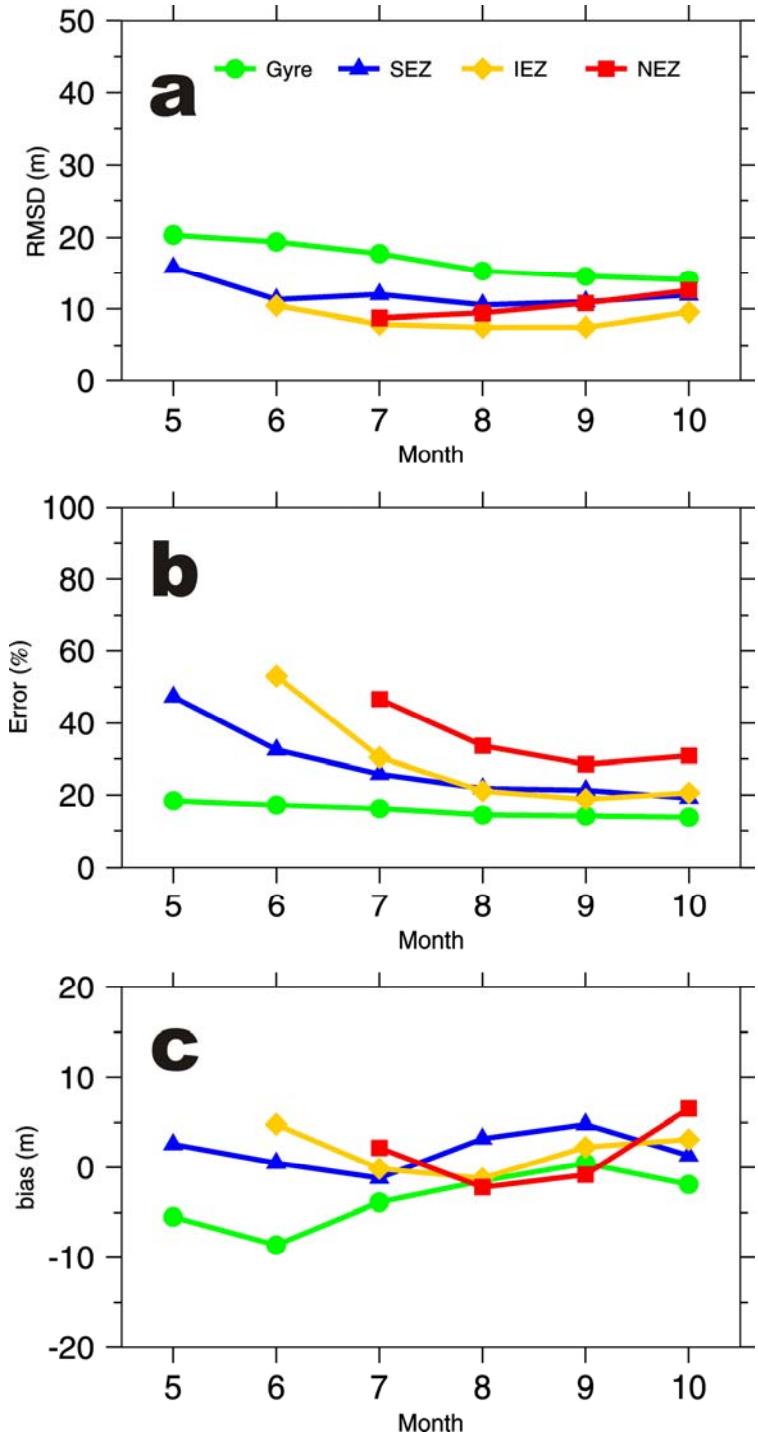

Figure 4.5: (a) Monthly RMSD, (b) error percentage, and (c) bias for REGWNP derived D26. The color code for each zone is shown in (a).

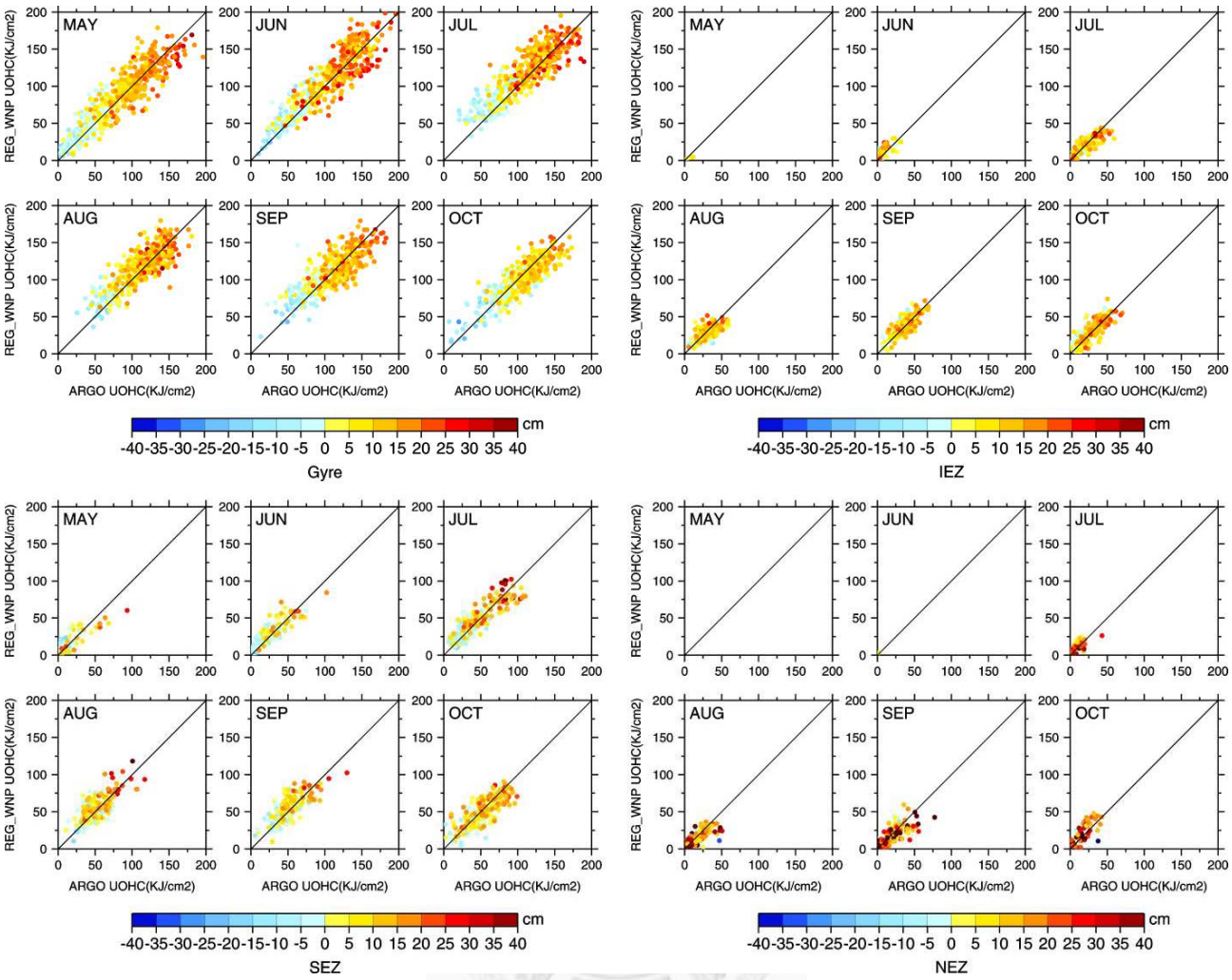

Figure 4.6: Monthly scatter plots of UOHC derived from REGWNP and Argo floats in the Gyre (upper-left section), SEZ (lower-left section), IEZ (upper-right section), and NEZ (lower-right section) during 2009-2010. The matching pairs are colored according to their corresponding SSHA values.

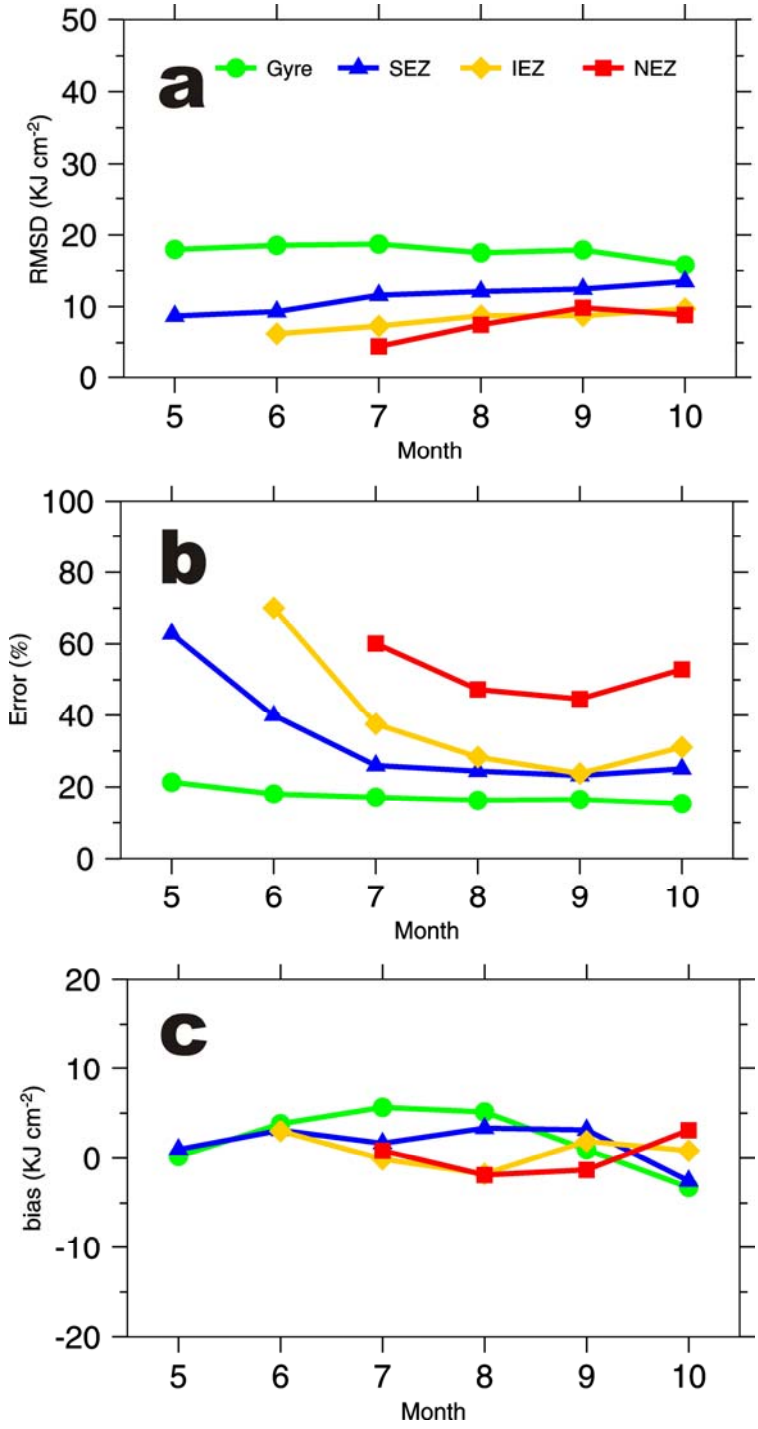

Figure 4.7: (a) Monthly RMSD, (b) error percentage, and (c) bias for REGWNP derived UOHC. The color code for each zone is shown in (a).

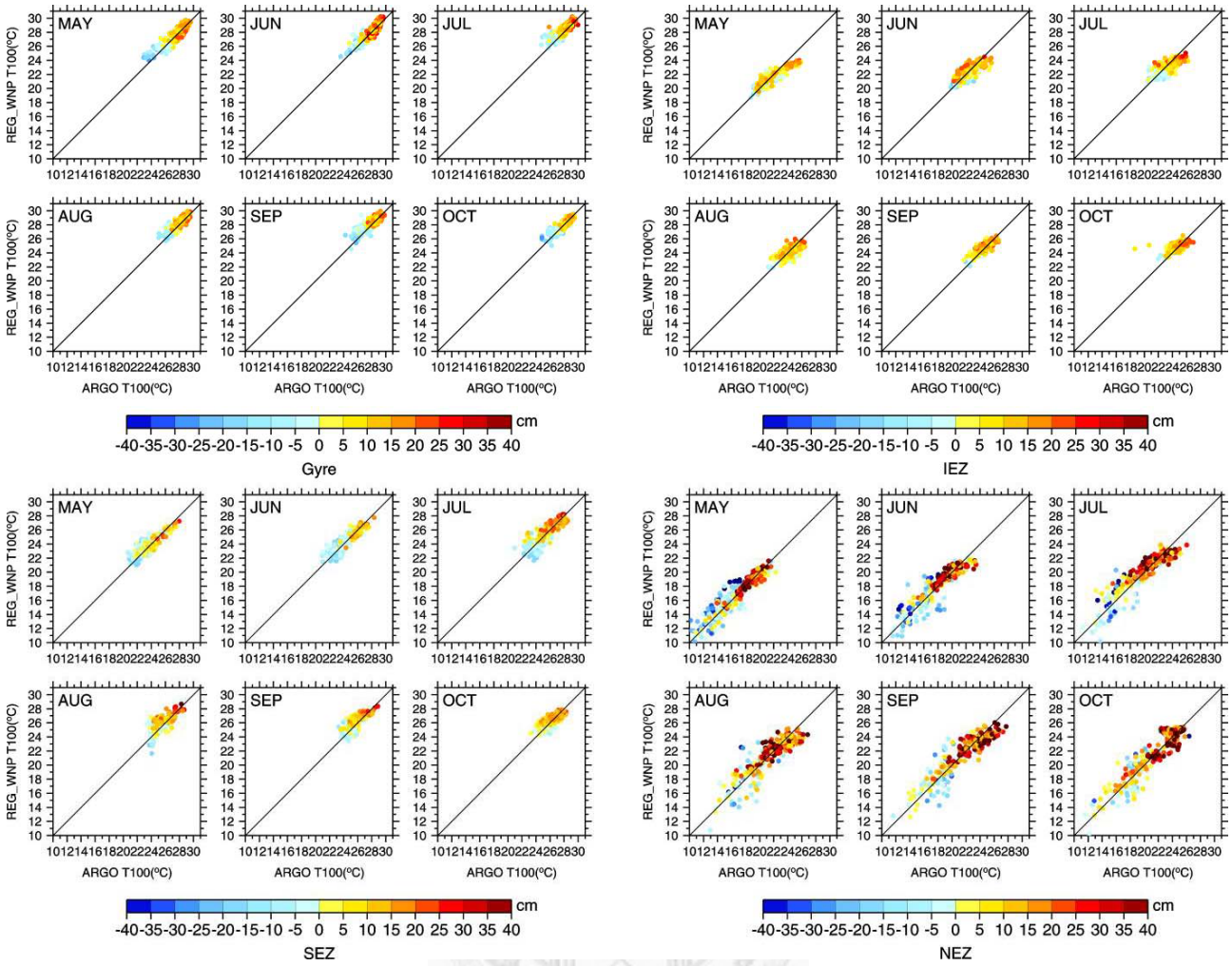

Figure 4.8: Monthly scatter plots of T100 derived from REGWNP and Argo floats in the Gyre (upper-left section), SEZ (lower-left section), IEZ (upper-right section), and NEZ (lower-right section) during 2009-2010. The matching pairs are colored according to their corresponding SSHA values.

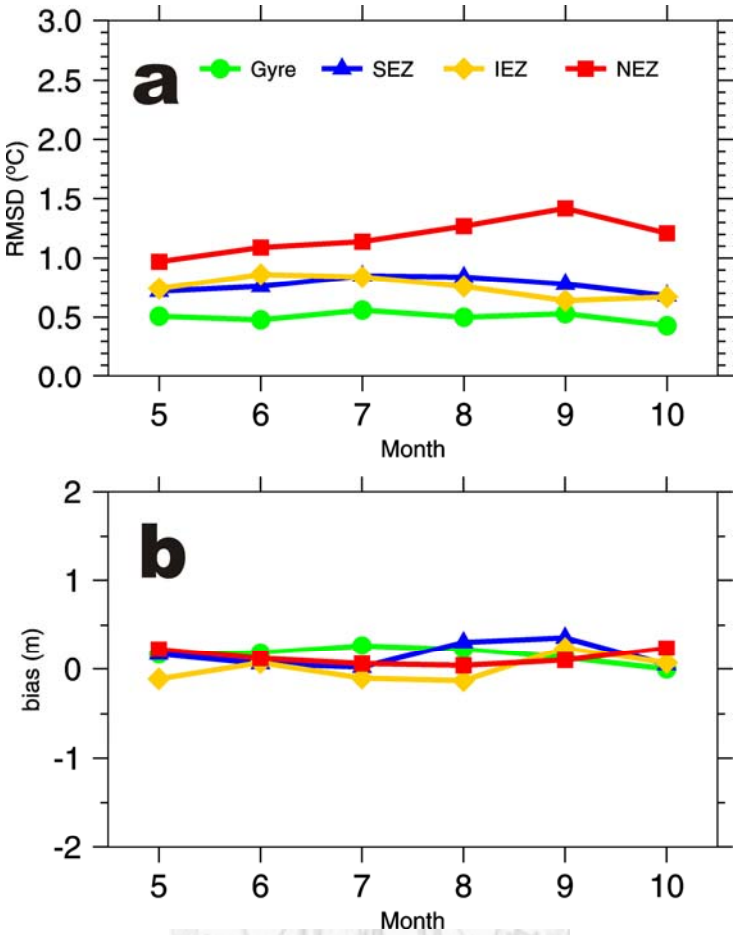

Figure 4.9: (a) Monthly RMSD, (b) error percentage, and (c) bias for REGWNP derived T100. The color code for each zone is shown in (a).

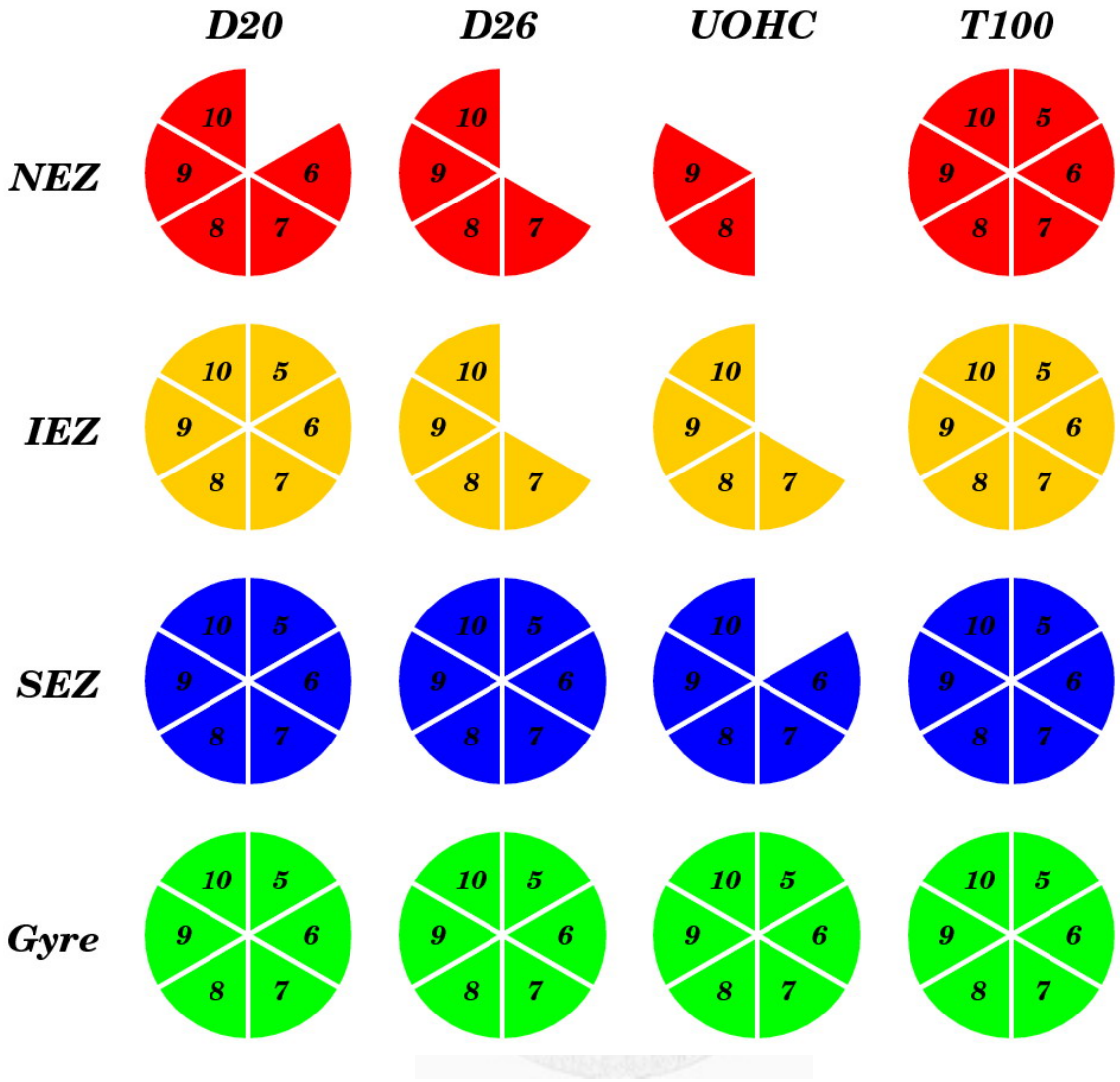

Figure 4.10: Applicability chart for REGWNP derived D20, D26, UOHC and T100 for typhoon applications. From upper to lower rows are the NEZ, IEZ, SEZ and Gyre, respectively. The number in the pie charts represent the months from May to October. The applicability threshold for D20, D26 and UOHC is an error of 50%, for T100 is 2.5°C.

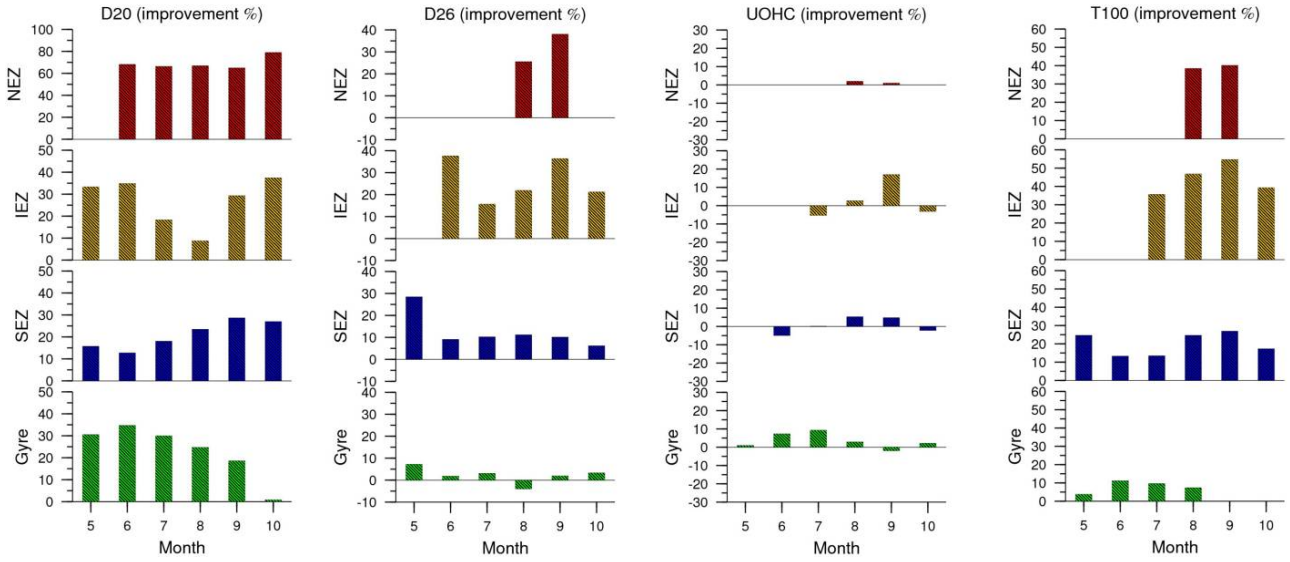

Figure 4.11: The percentage of improvement on REGWNP with respect to 2-layer for D20, D26, UOHC and T100 in the four different zones, i.e., the Gyre, SEZ, IEZ and NEZ. A positive value represents that REGWNP is better than 2-alyer, and vice versa. Note that the scale of D20 improvement in the NEZ is different from the other three zones.

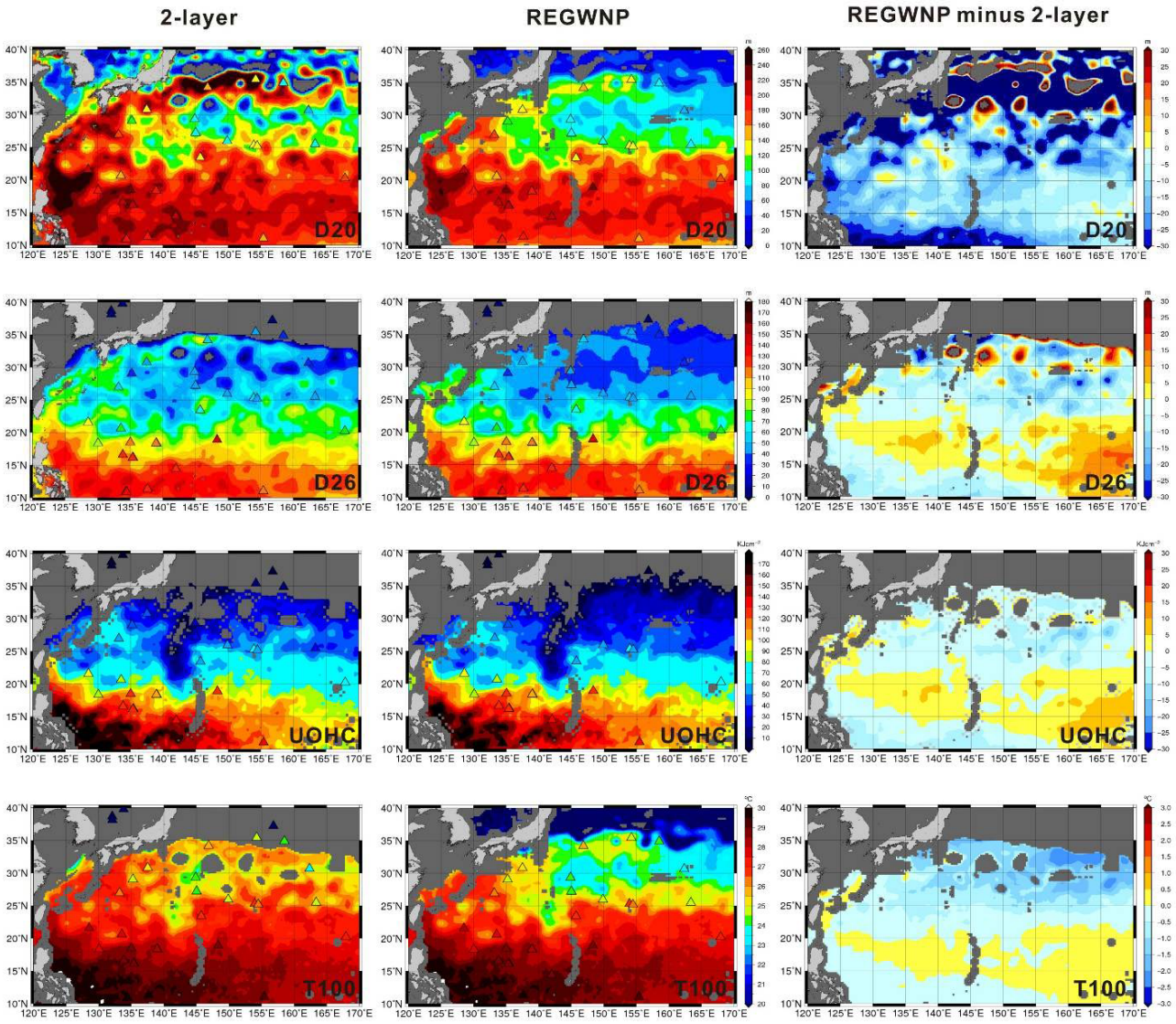

Figure 4.12: The maps of D20, D26, UOHC and T100 on 25 September 2010, derived from 2-layer (the first column), REGWNP (the second column) and REGWNP minus 2-layer (the third column). The color bars for the maps from 2-layer and REGWNP are the same and shown in the second column. The corresponding Argo profiles are superimposed on the maps and depicted by colored triangles according to the same color scheme.

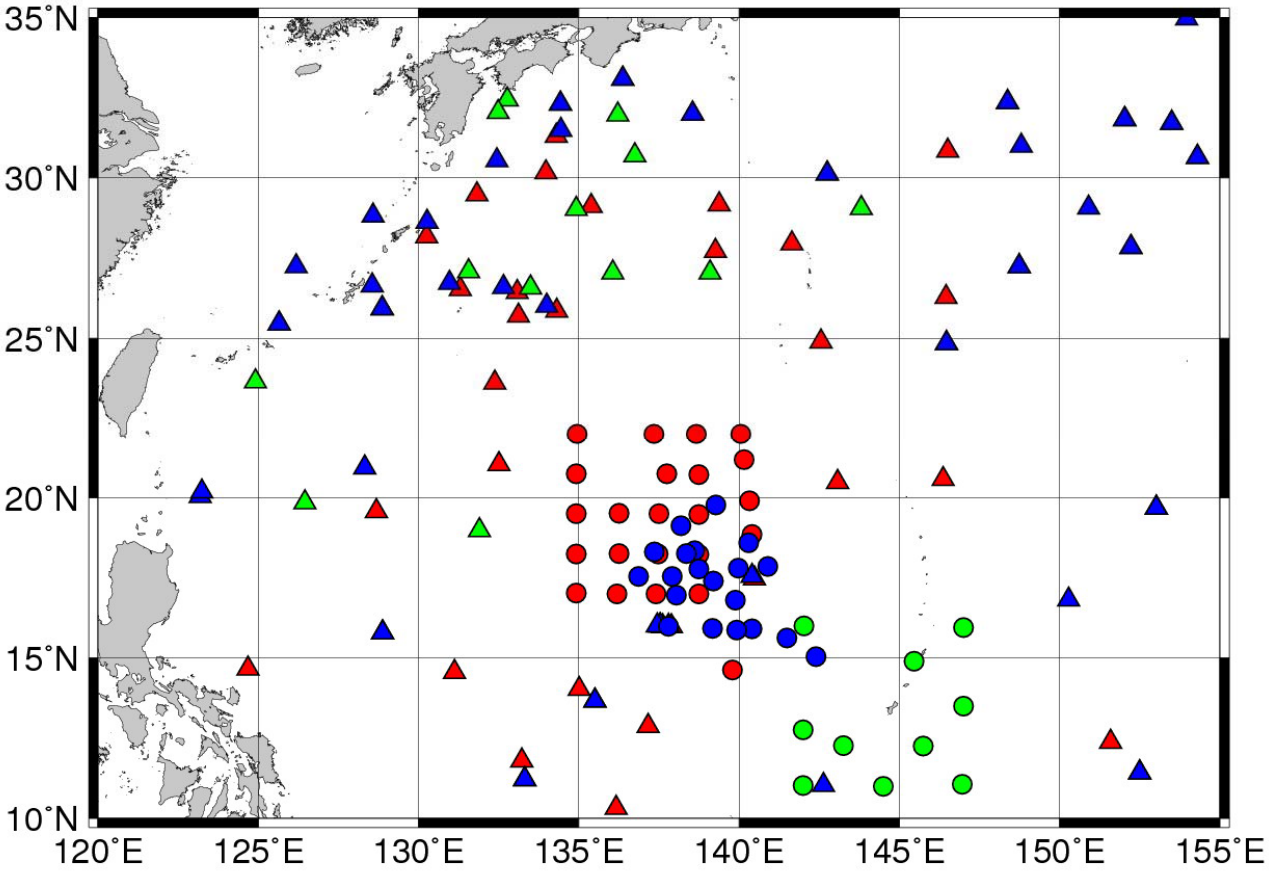

Figure 4.13: *In situ* measurements during ITOP field experiment on August 28 (red), August 31 (green) and September 1 (blue), 2010. Circles represent the AXBTs deployed by US C130 aircraft, and triangles represent the Argo floats.

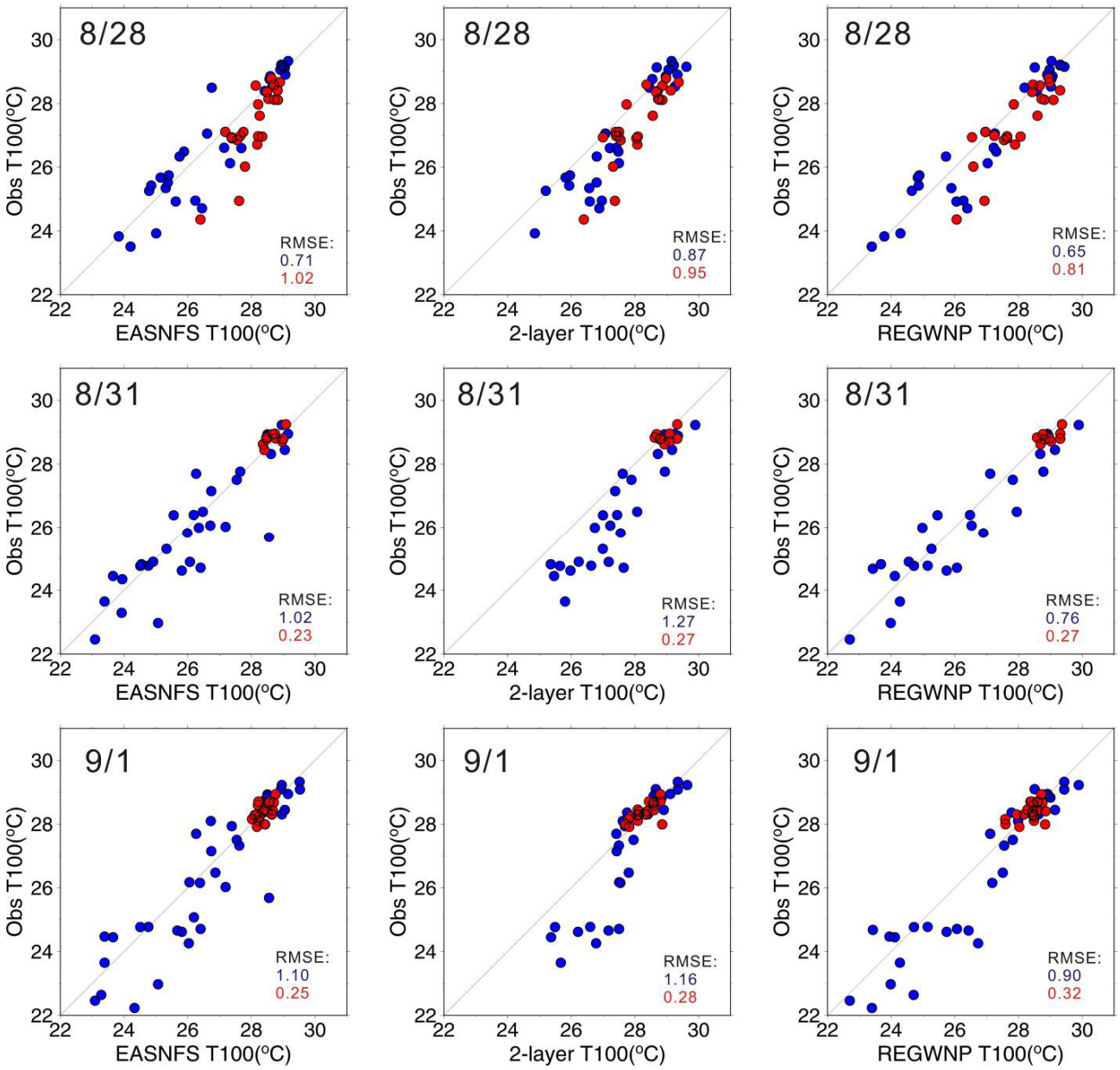

Figure 4.14: Inter-comparison of T100 from EASNFS, 2-layer and REGWNP with the AXBTs (red) and Argo floats (blue) on August 28 (first row), August 31 (second row), and September 1 (third row), 2010. The left column compares observations with EASNFS; the middle column compares with 2-layer; the right column compares with REGWNP. The RMS errors are shown in each plot.

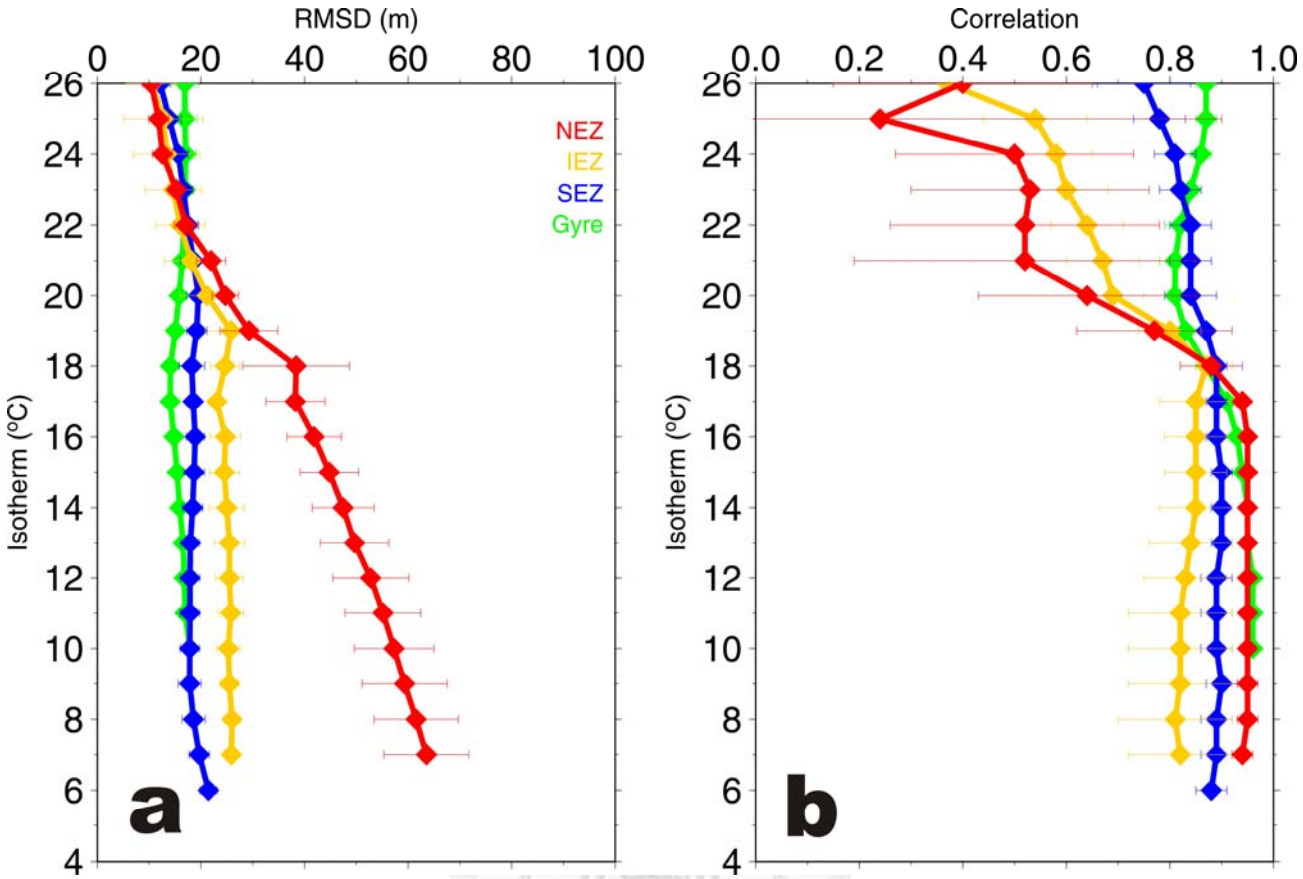

Figure 4.15: May-October averaged (a) RMSD and (b) correlation of REGWNP estimated D26 to the isotherm at the base of the thermocline with respect to Argo *in situ* observations. Curves in green, blue, orange and red represents the Gyre, SEZ, IEZ and NEZ, respectively. The horizontal bars depict one standard deviation.

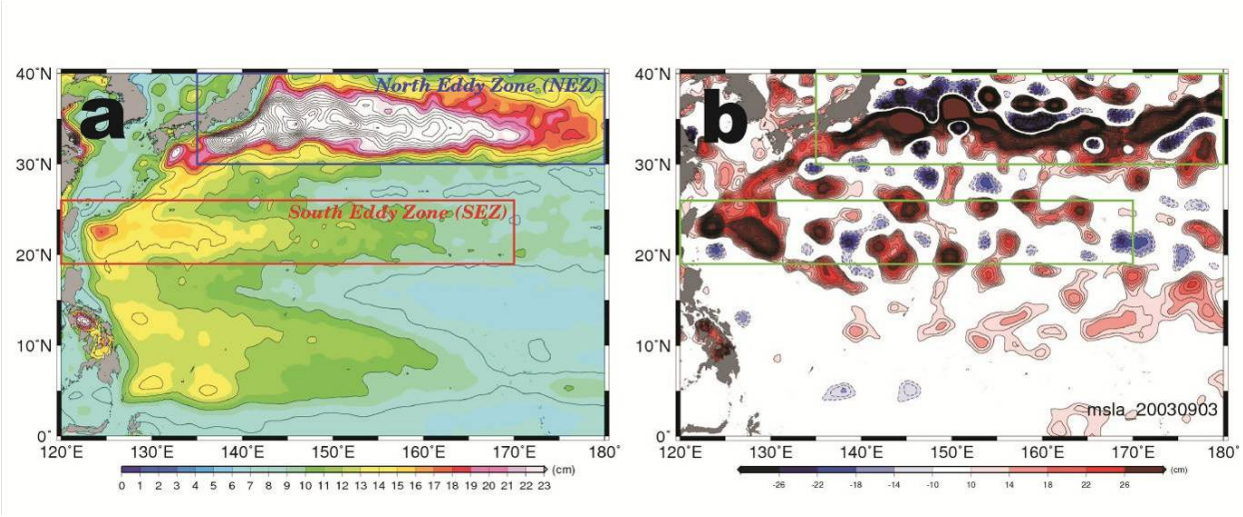

Figure 5.1: (a) The standard deviation of SSHA in the western North Pacific Ocean from October 14, 1992 to October 28, 2009, in which the red and blue boxes depict the SEZ and NEZ regions, respectively. (b) The corresponding SSHA field on September 3, 2003; the green boxes depict the SEZ and NEZ.

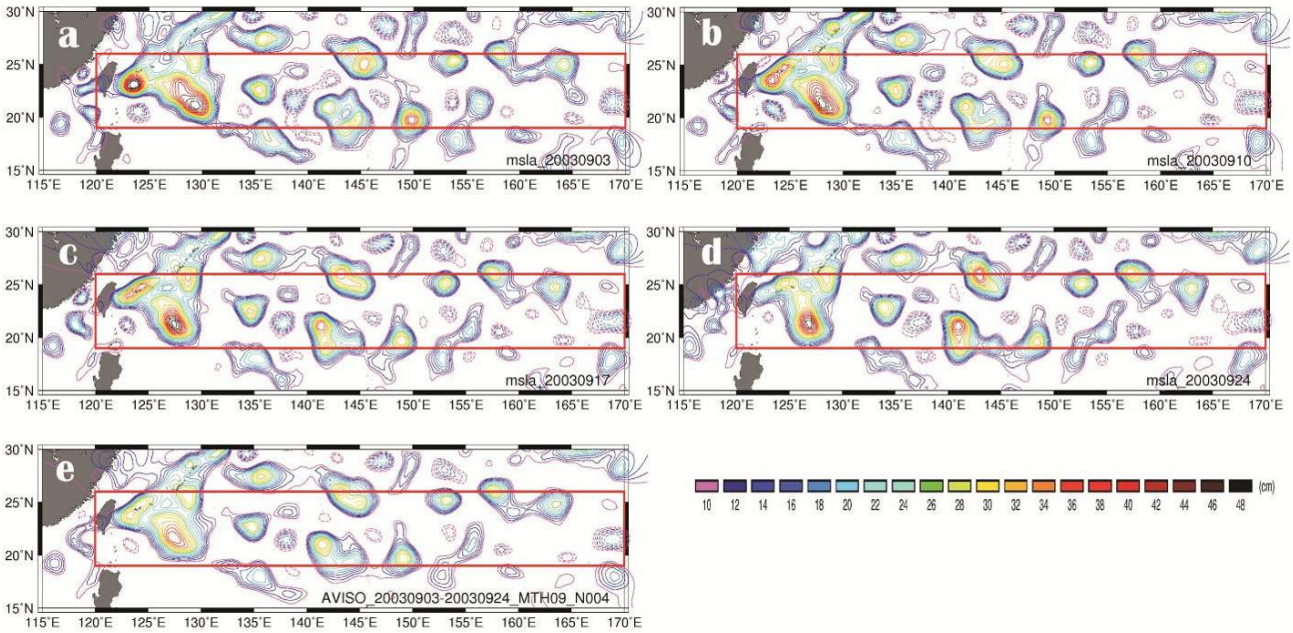

Figure 5.2: SSHA contour maps from September 2003. (a)-(d) Original weekly SSHA maps. (e) A monthly average SSHA map obtained by combining four weekly SSHA maps. The solid and dashed contour lines depict positive and negative SSHAs, respectively; the contour interval is 2cm.

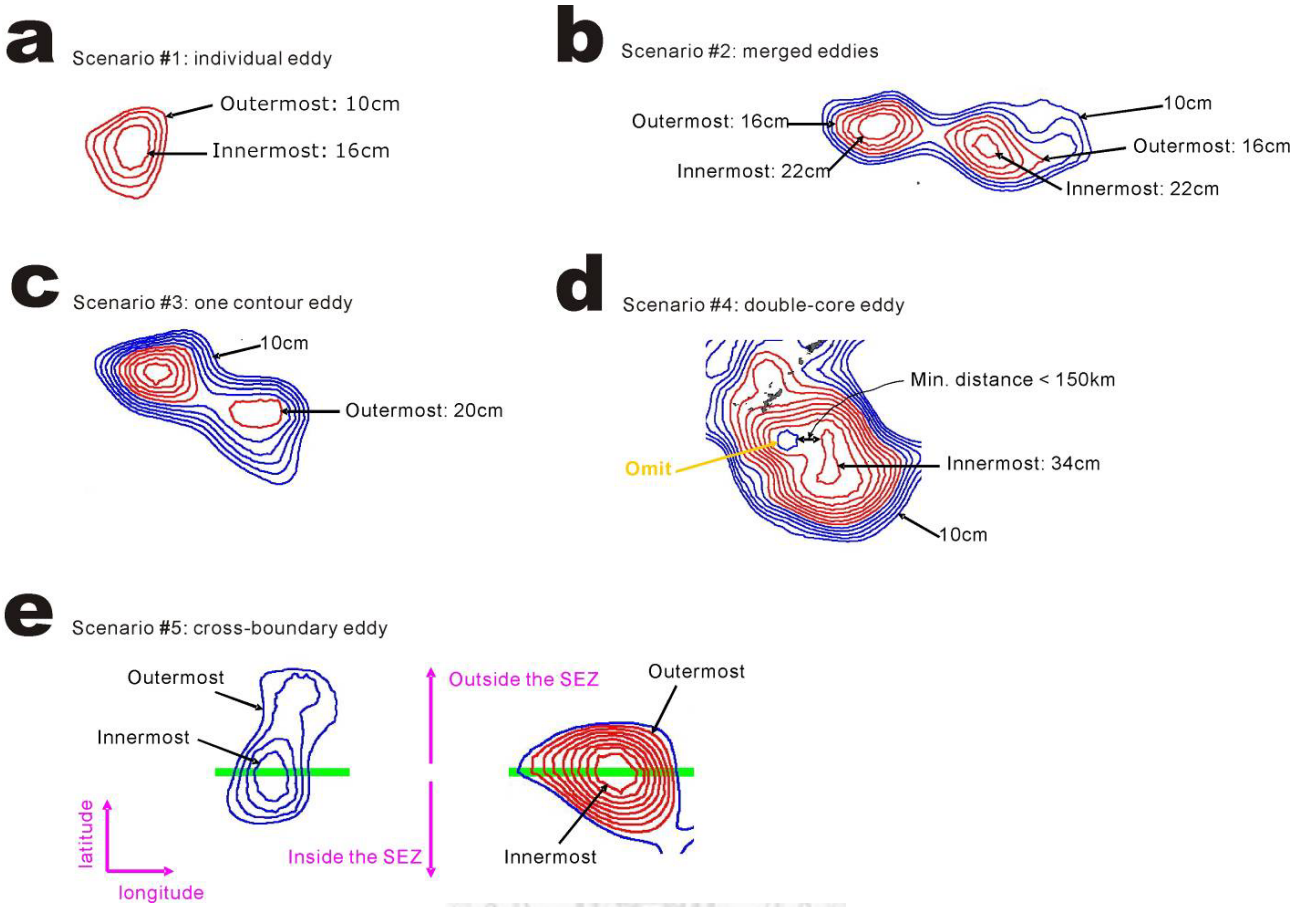

Figure 5.3: Five scenarios of eddy identification in the SEZ. The red contours indicate the eddies identified using the procedure. The green lines in (e) represent the boundary of the SEZ. The scenarios are explained in detail in the context.

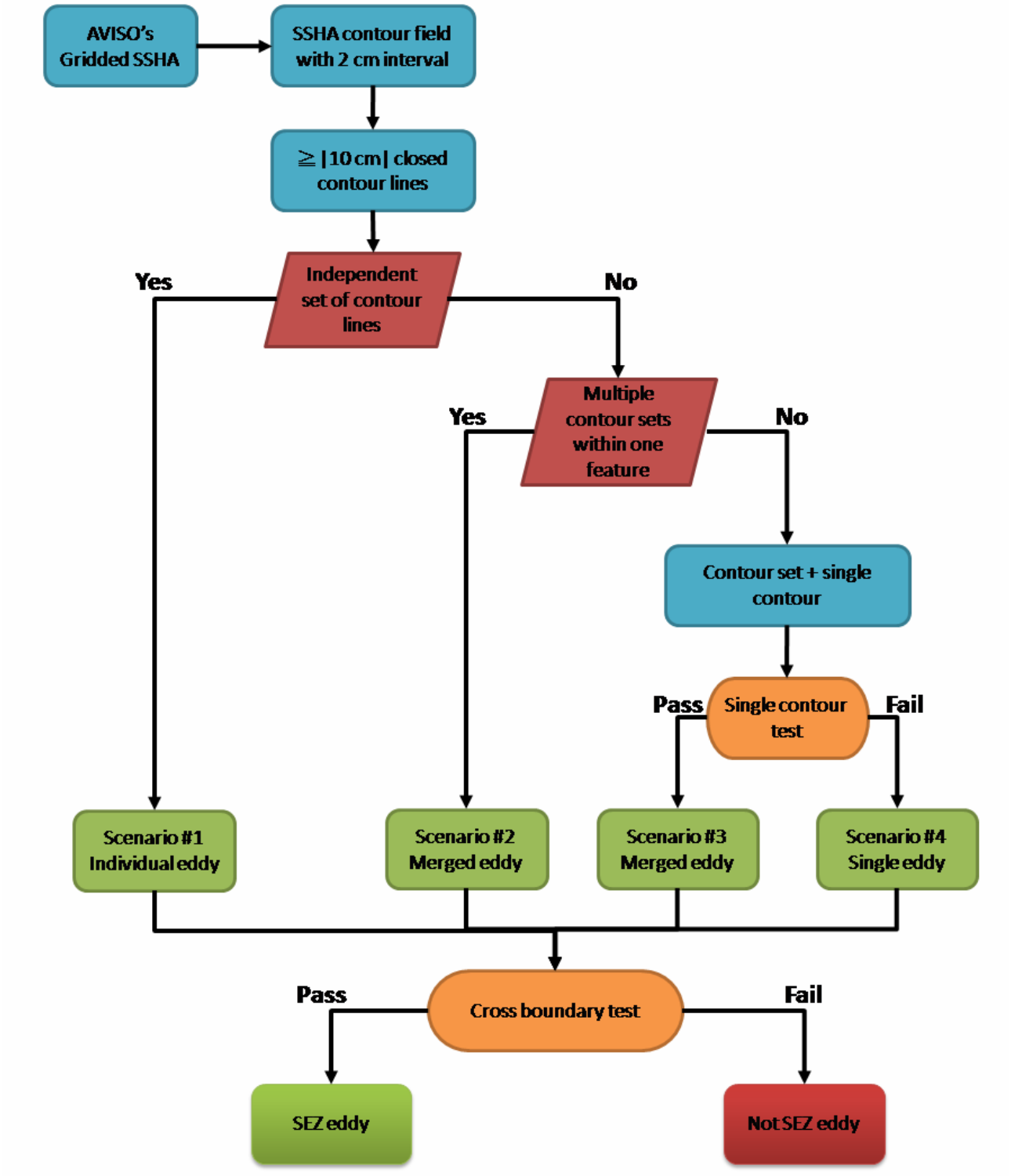

Figure 5.4: Flow chart of the eddy identification procedure. The details of the procedure are described in the context.

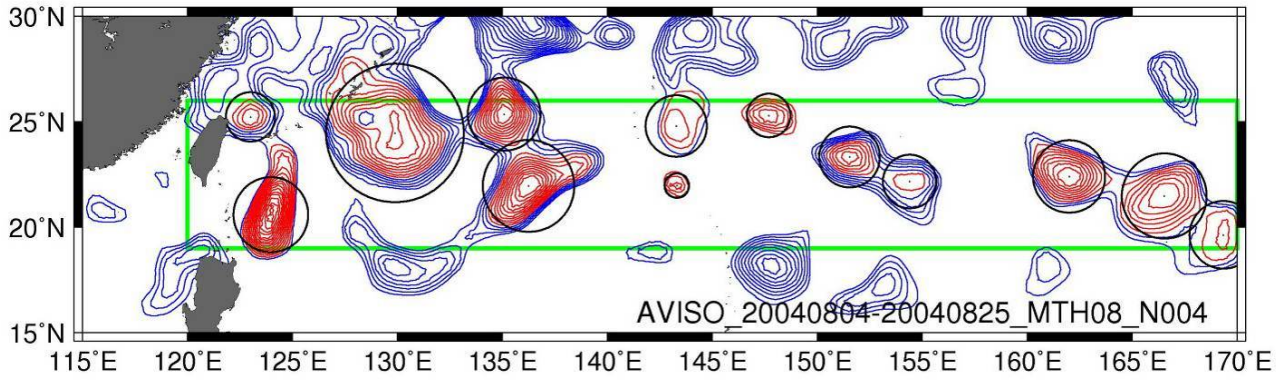

Figure 5.5: Positive SSHA contour map from August 2004. The red contours indicate the eddies identified in the SEZ. Each circle depicts the size of the eddy; it is an estimation of the area enclosed by the 10 cm contour of the eddy. 13 warm eddies are identified on the map.

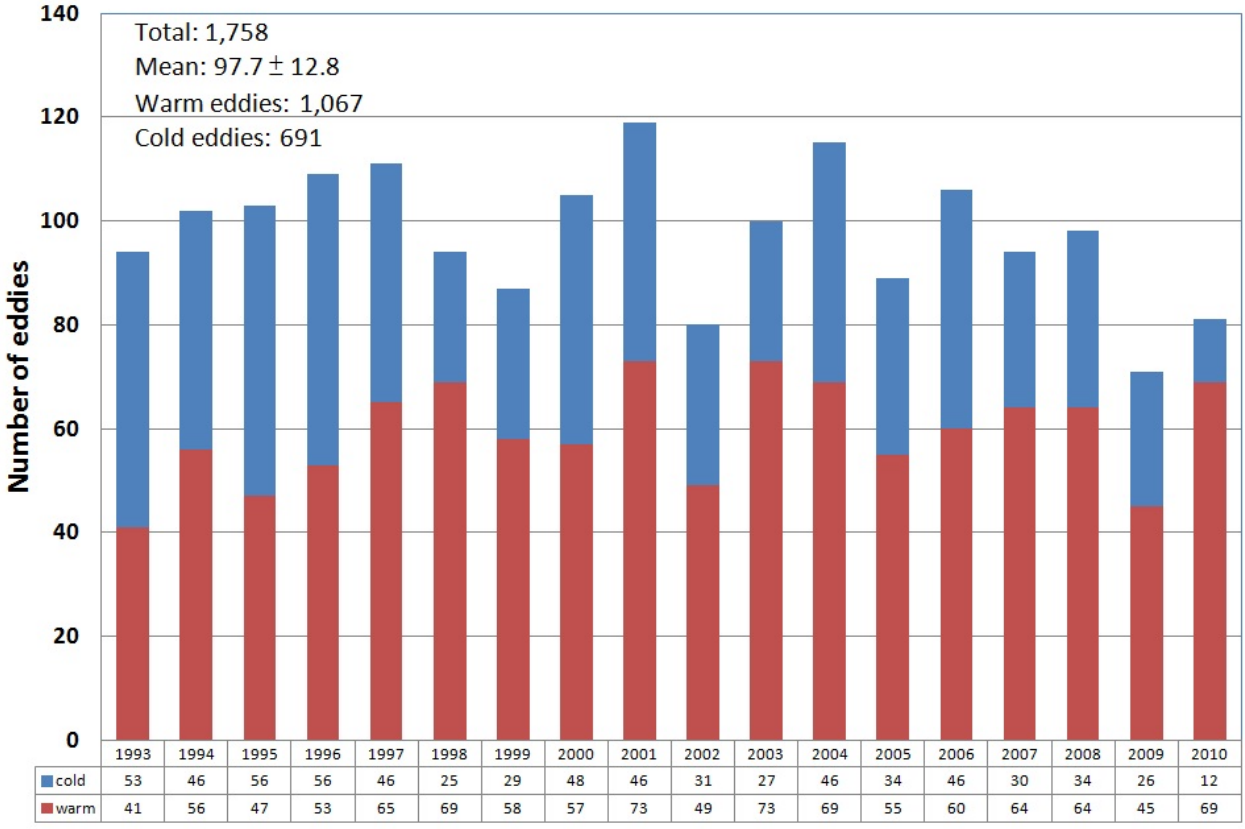

	1993	1994	1995	1996	1997	1998	1999	2000	2001	2002	2003	2004	2005	2006	2007	2008	2009	2010
cold	53	46	56	56	46	25	29	48	46	31	27	46	34	46	30	34	26	12
warm	41	56	47	53	65	69	58	57	73	49	73	69	55	60	64	64	45	69

Figure 5.6: Histogram of the total numbers of warm (red bars) and cold (blue bars) eddies identified in the SEZ from May to October, 1993 to 2010.

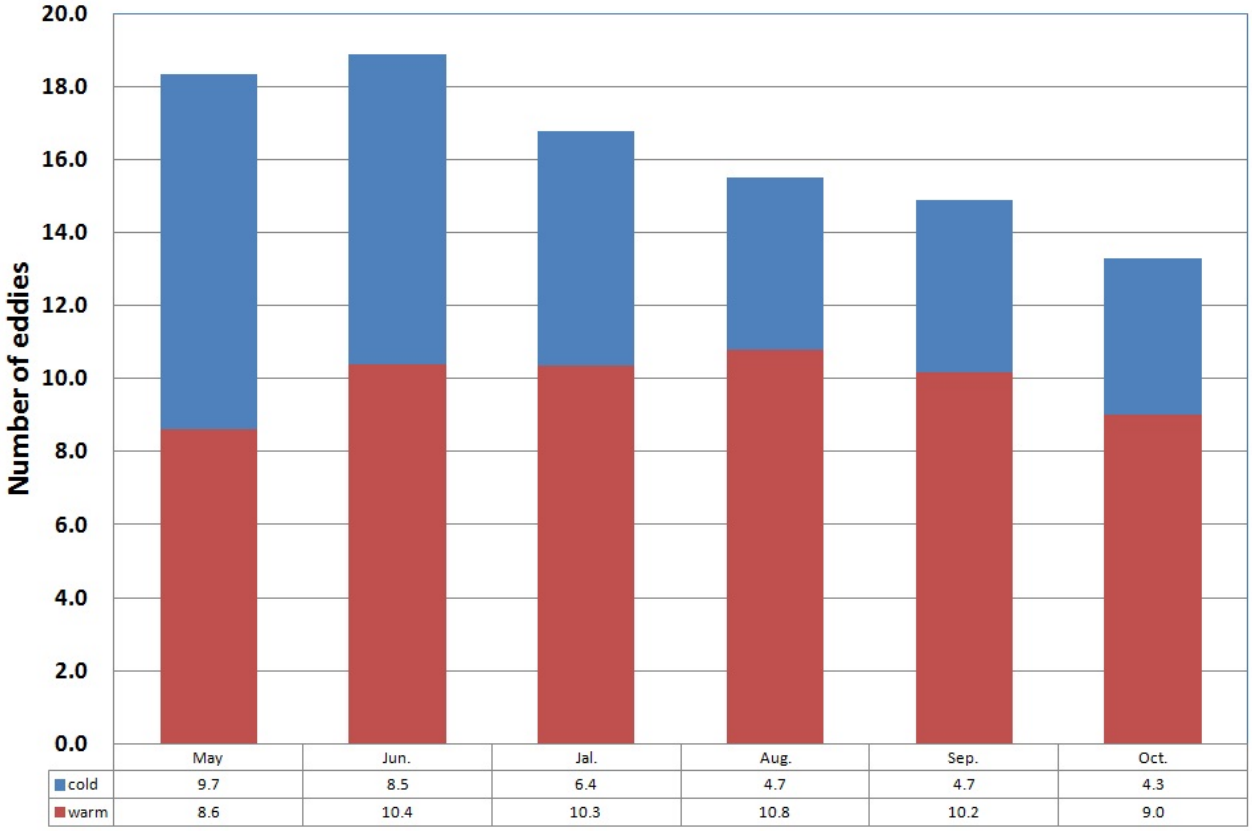

	May	Jun.	Jal.	Aug.	Sep.	Oct.
cold	9.7	8.5	6.4	4.7	4.7	4.3
warm	8.6	10.4	10.3	10.8	10.2	9.0

Figure 5.7: Histogram of the monthly average numbers of warm (red bars) and cold (blue bars) eddies identified in the SEZ from May to October, averaged over 1993-2010.

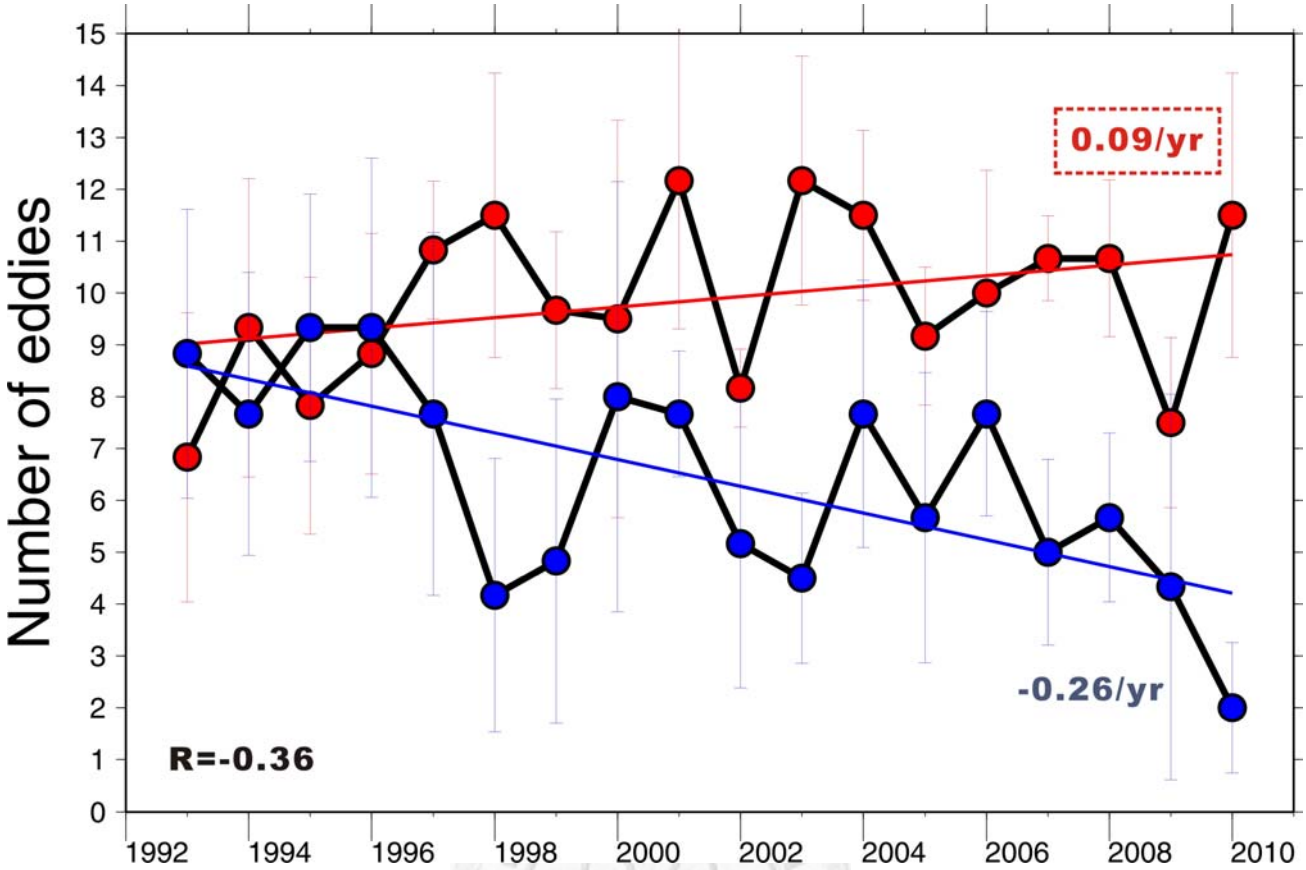

Figure 5.8: Monthly average numbers of warm (red) and cold (blue) eddies from 1993 to 2010. The red and blue lines depict the trends of warm and cold eddies, respectively, calculated by the least square fitting. The rate enclosed by the dashed box indicates the trend is less than 95% significance. Otherwise, the trend shown is at 95% significance level.

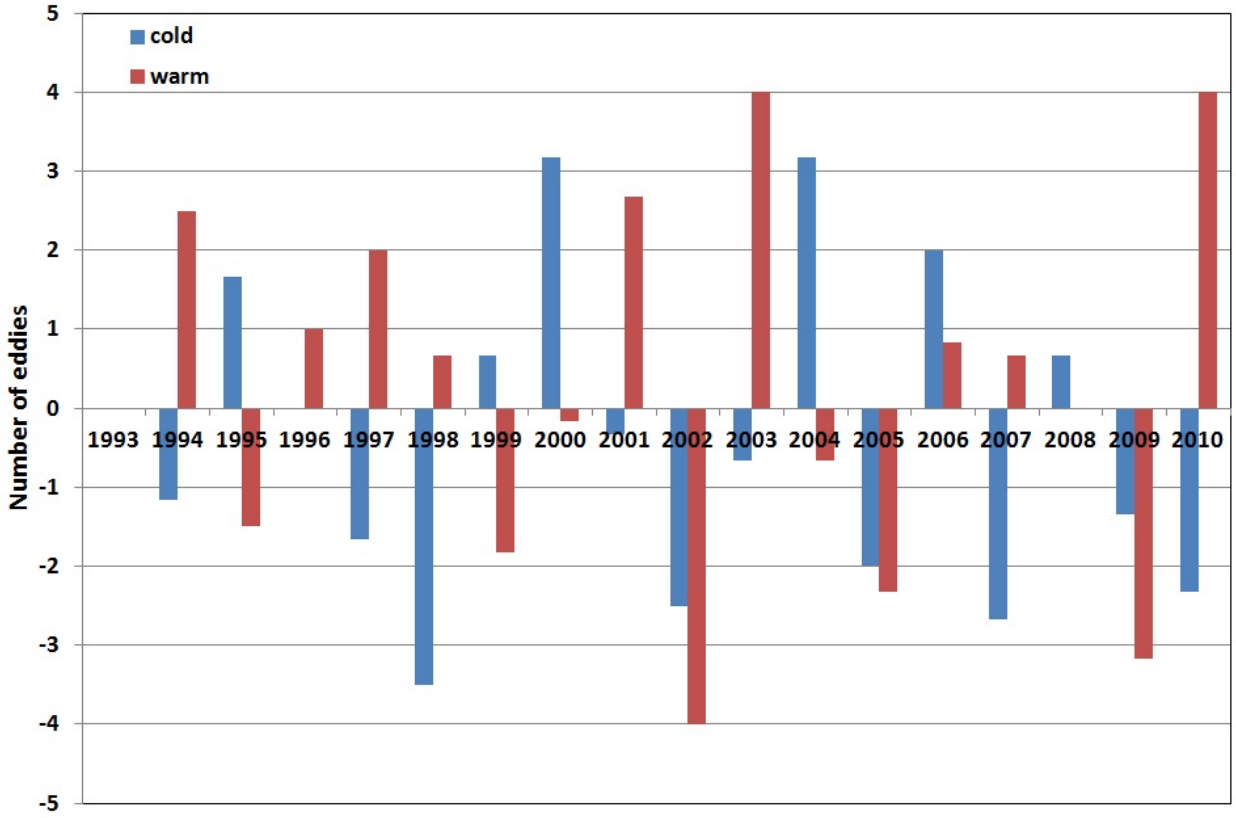

Figure 5.9: The year-to-year changes in the numbers of warm and cold eddies from 1993 to 2010.

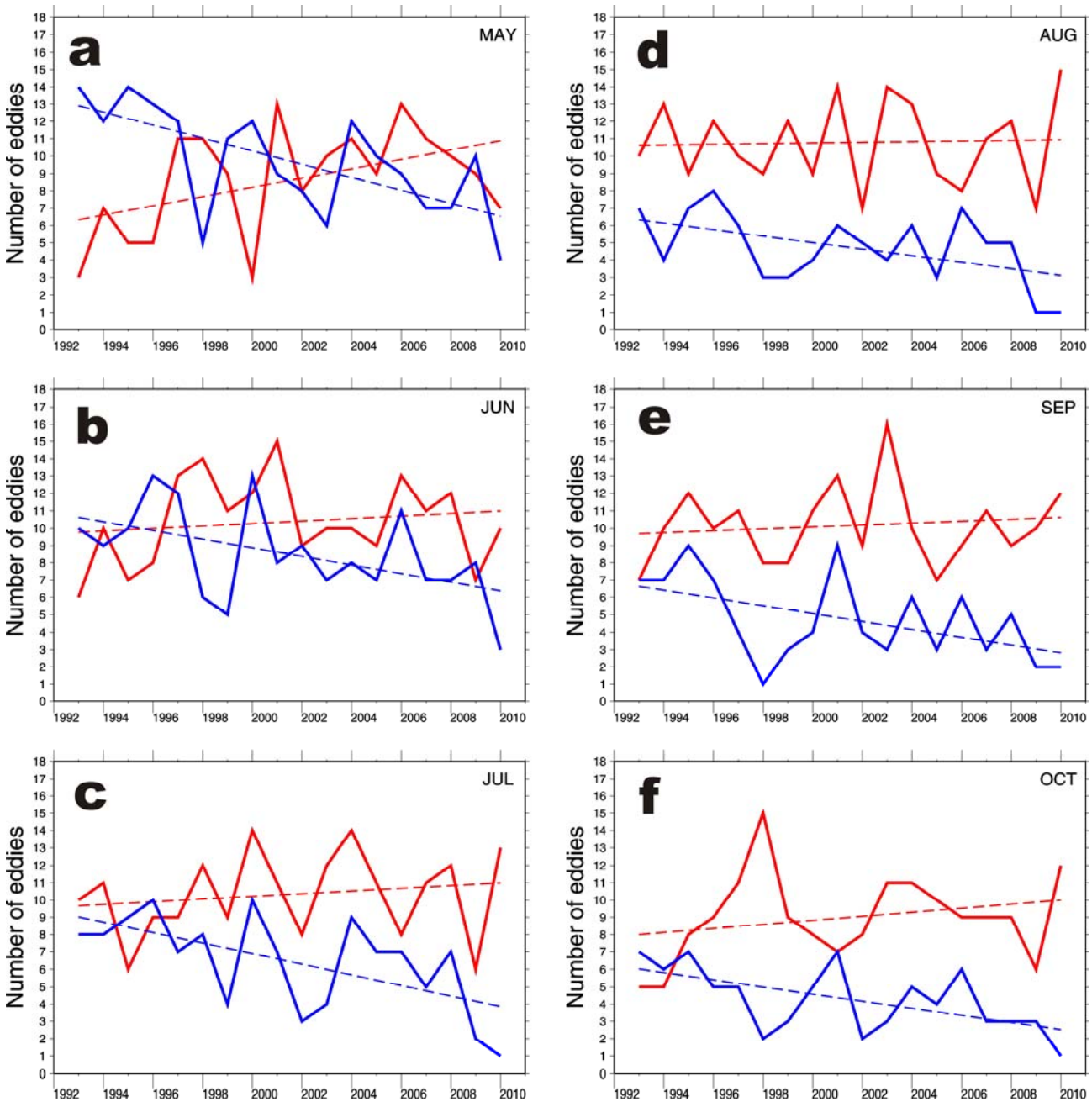

Figure 5.10: Time series of the monthly average numbers of warm (red) and cold (blue) eddies from May (a) to October (f). The dashed lines depict the linear trends observed in the series.

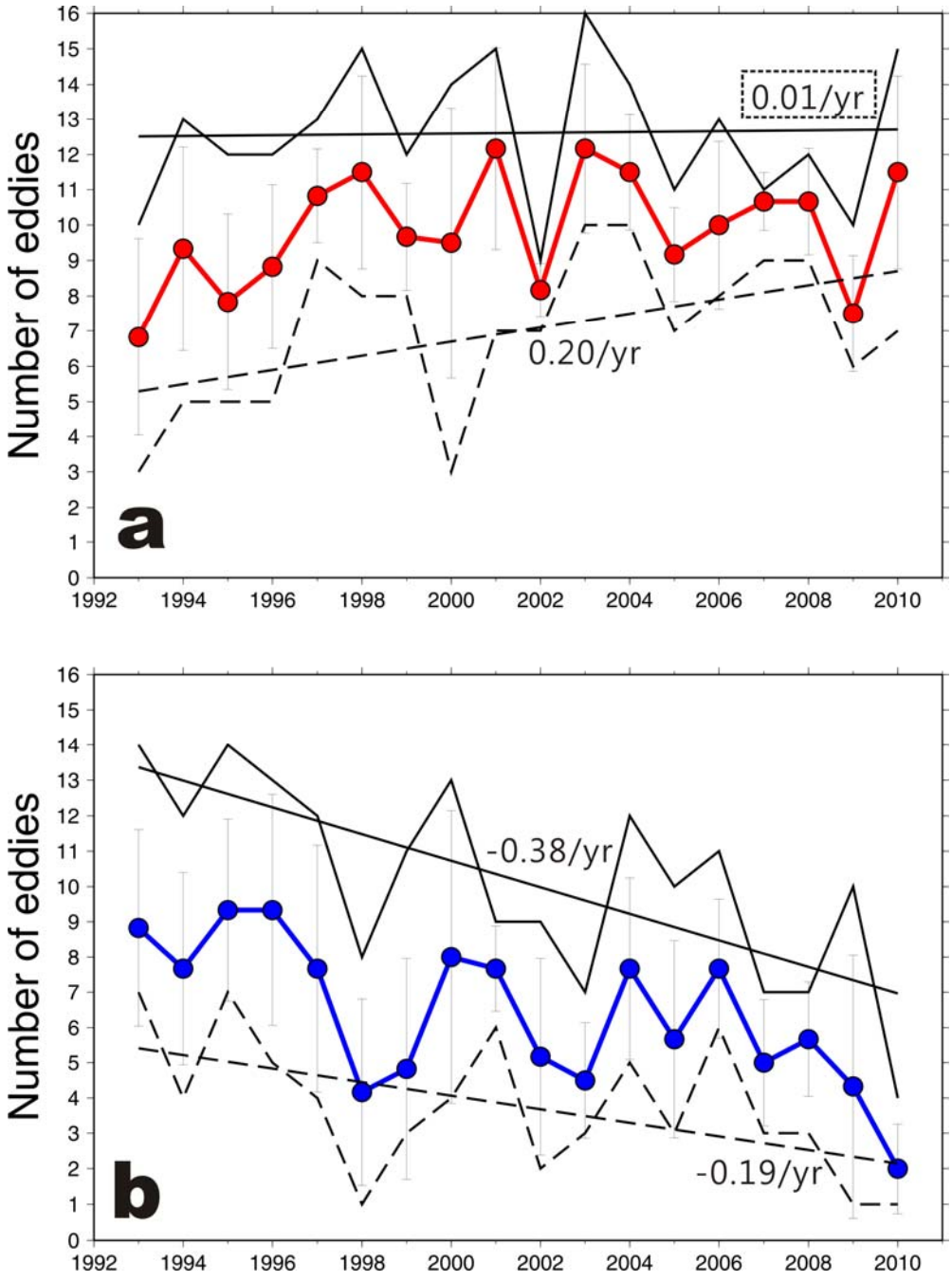

Figure 5.11: The same as in Figure 5.7; the maximum and minimum numbers of eddies during each season are superimposed on the time series of the monthly average numbers of (a) warm and (b) cold eddies. The solid and dashed lines depict the trends in the maximum and minimum numbers of eddies during each season, respectively. The rate enclosed by the dashed box indicates the trend is less than 95% significant. Otherwise, the trend shown is at 95% significance level.

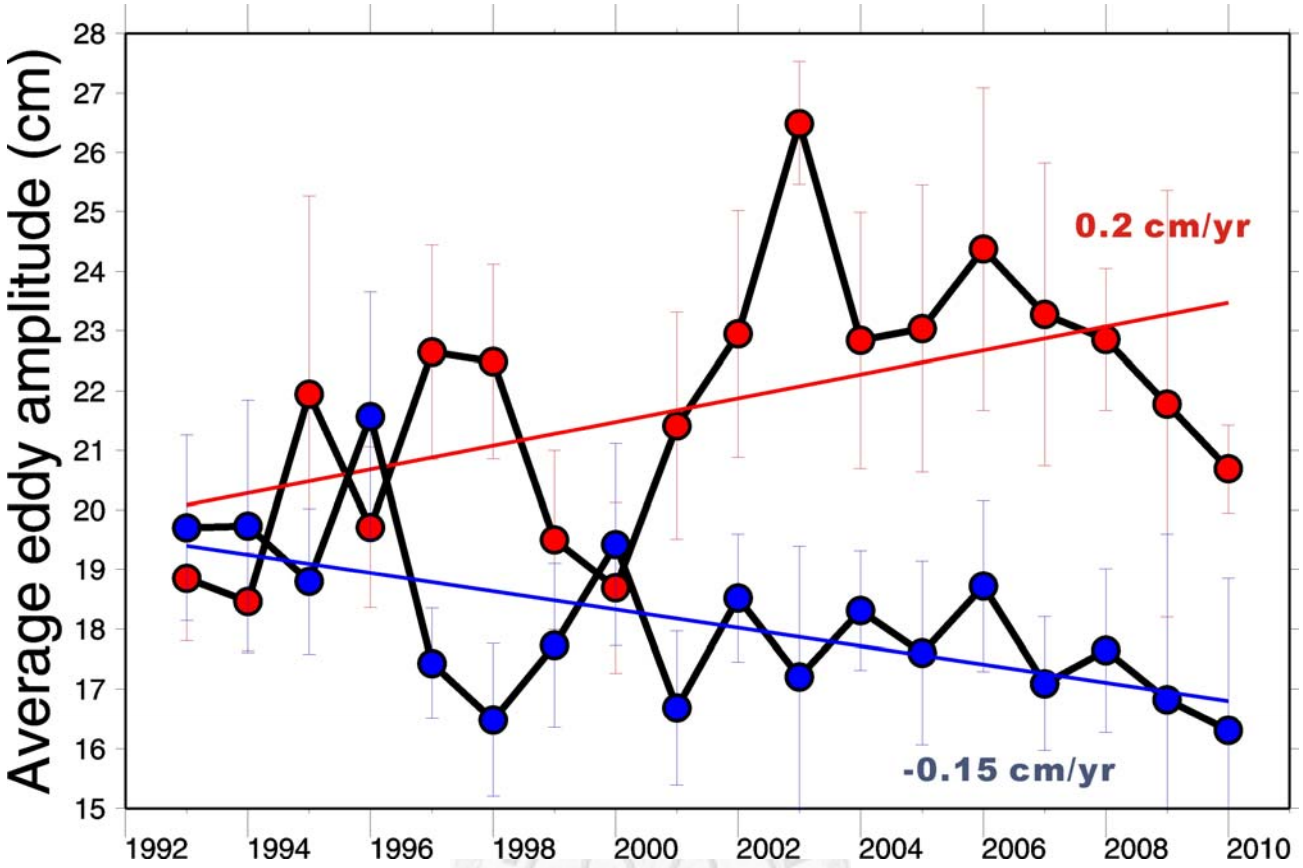

Figure 5.12: Monthly average amplitudes of warm (red) and cold (blue) eddies from 1993 to 2010. The red and blue lines depict the trends of warm and cold eddies, respectively, calculated by the least square fitting. Both trends are at 95% significance level.

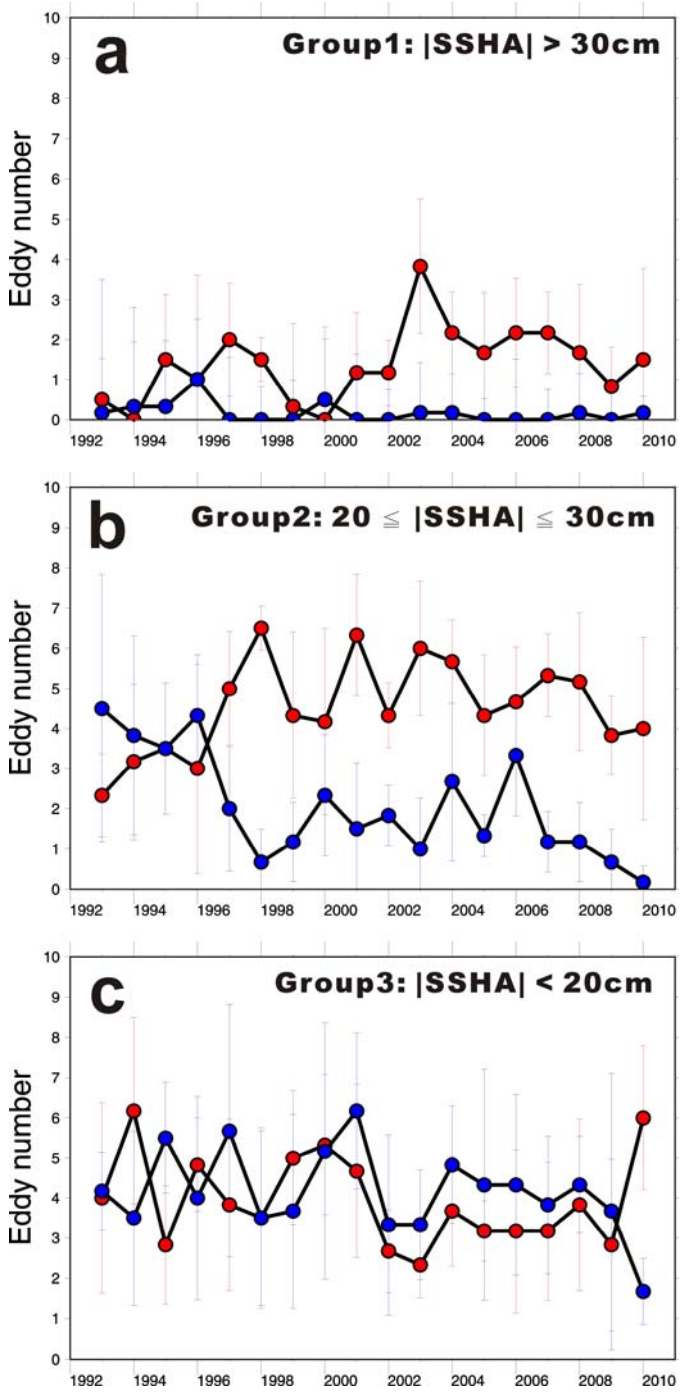

Figure 5.13: The same as in Figure 5.7 with the eddies separated into three groups. (a) Eddies with amplitudes > 30cm; (b) eddies with amplitudes between 20 and 30cm; and (c) eddies with amplitudes < 20cm.

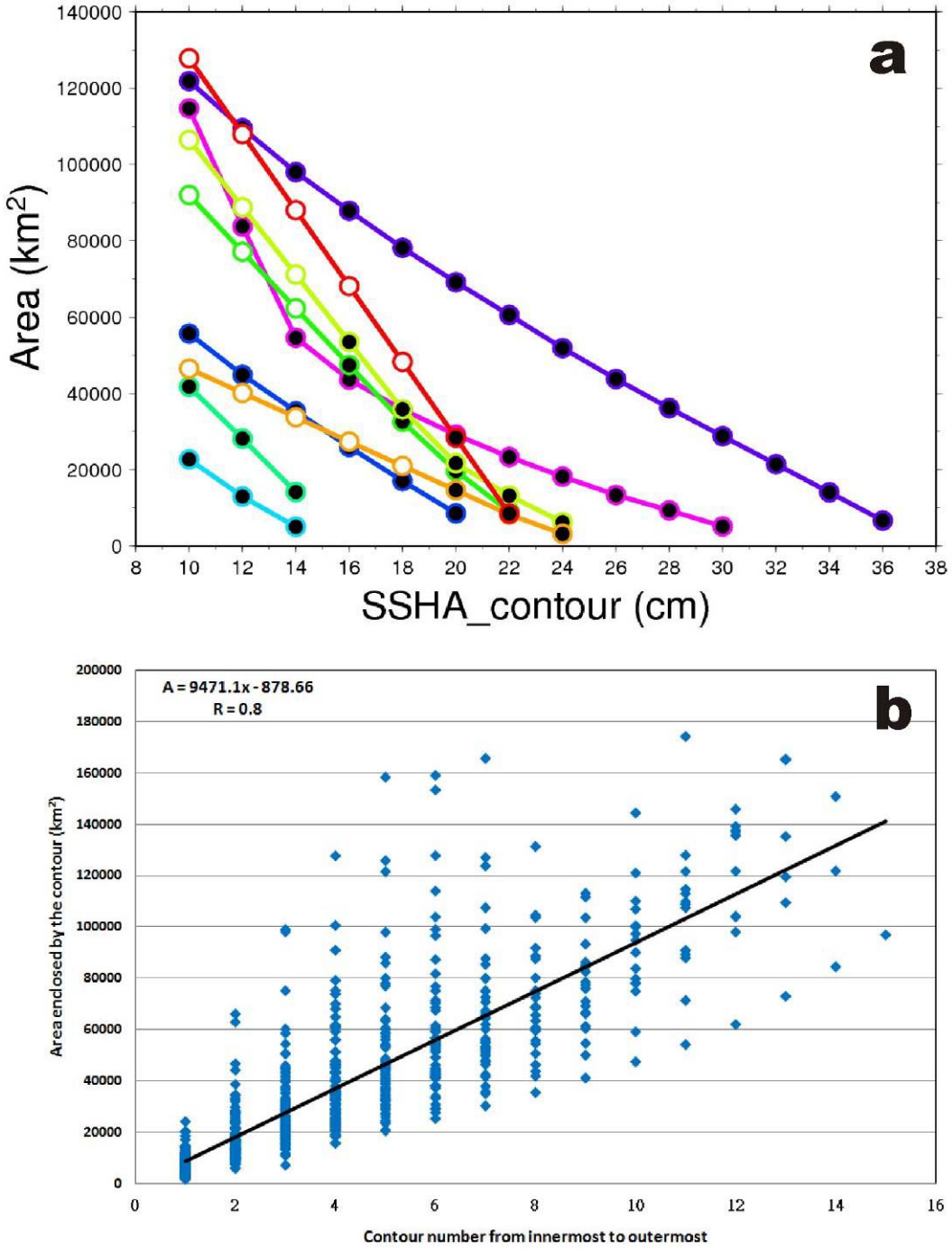

Figure 5.14: (a) The relationship between the contour area and SSHA for all eddies identified in August 1995. The solid dots depict the real contours recognized by the procedure, and the open dots depict the extrapolated values. (b) The scatter plots of the numbered contours (from innermost to outermost) and their areas for each eddy identified in August from 1993 to 2007.

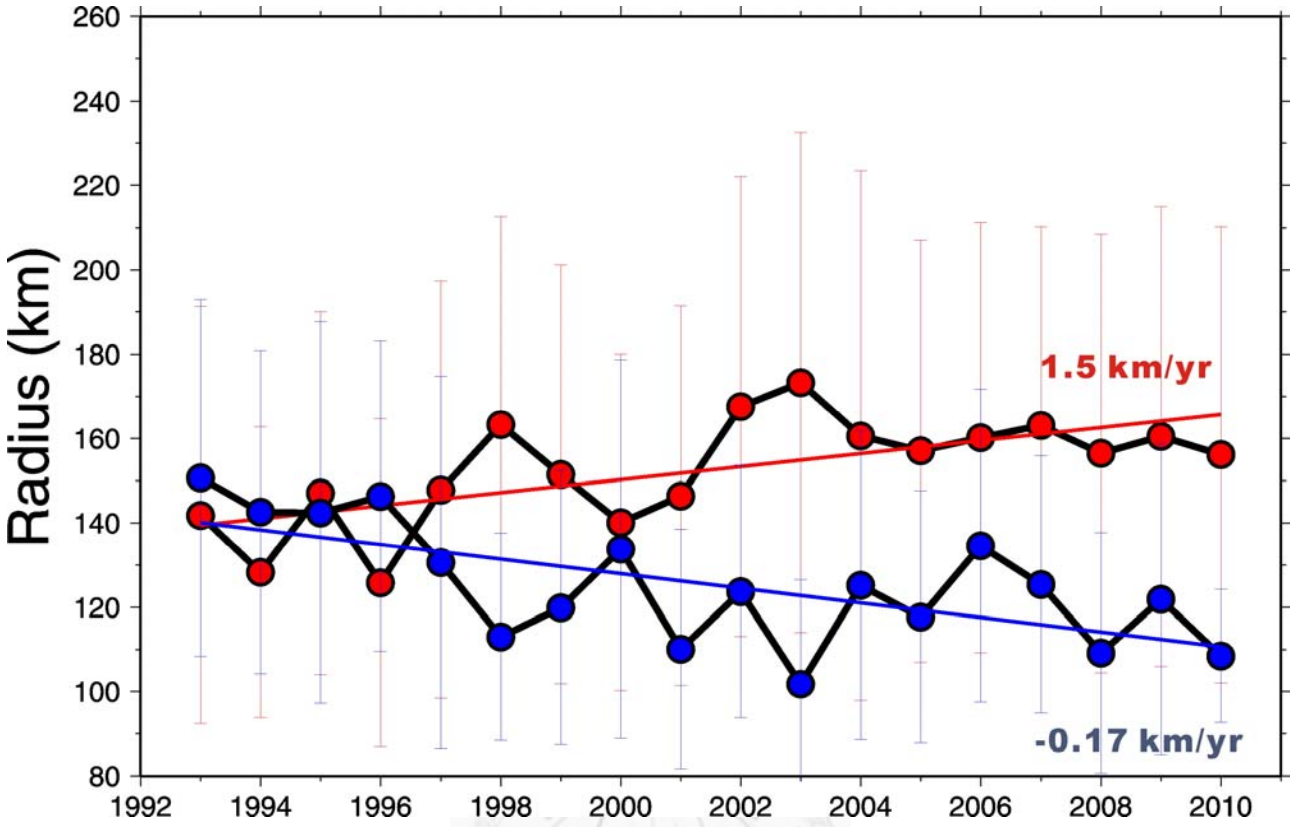

Figure 5.15: Monthly average radii of warm (red) and cold (blue) eddies from 1993 to 2010. The red and blue lines depict the trends of warm and cold eddies, respectively, calculated by the least square fitting. Both trends are at 95% significance level.

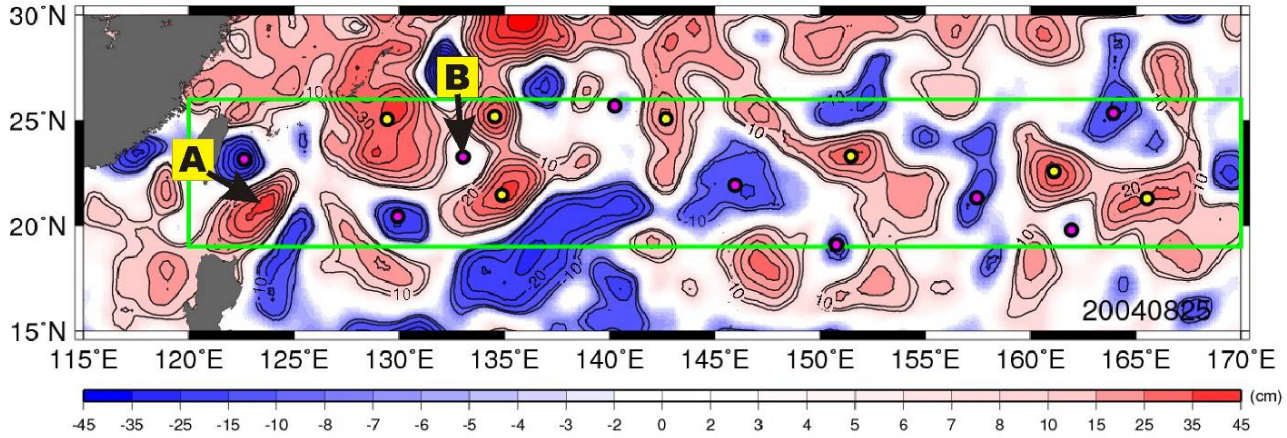

Figure 5.16: SSHA map of August 25, 2004. The yellow and purple dots depict the warm and cold eddies identified by Chelton et al. (2011). The green box is the region of the SEZ. The features labeled with “A” and “B” are discussed in the context.

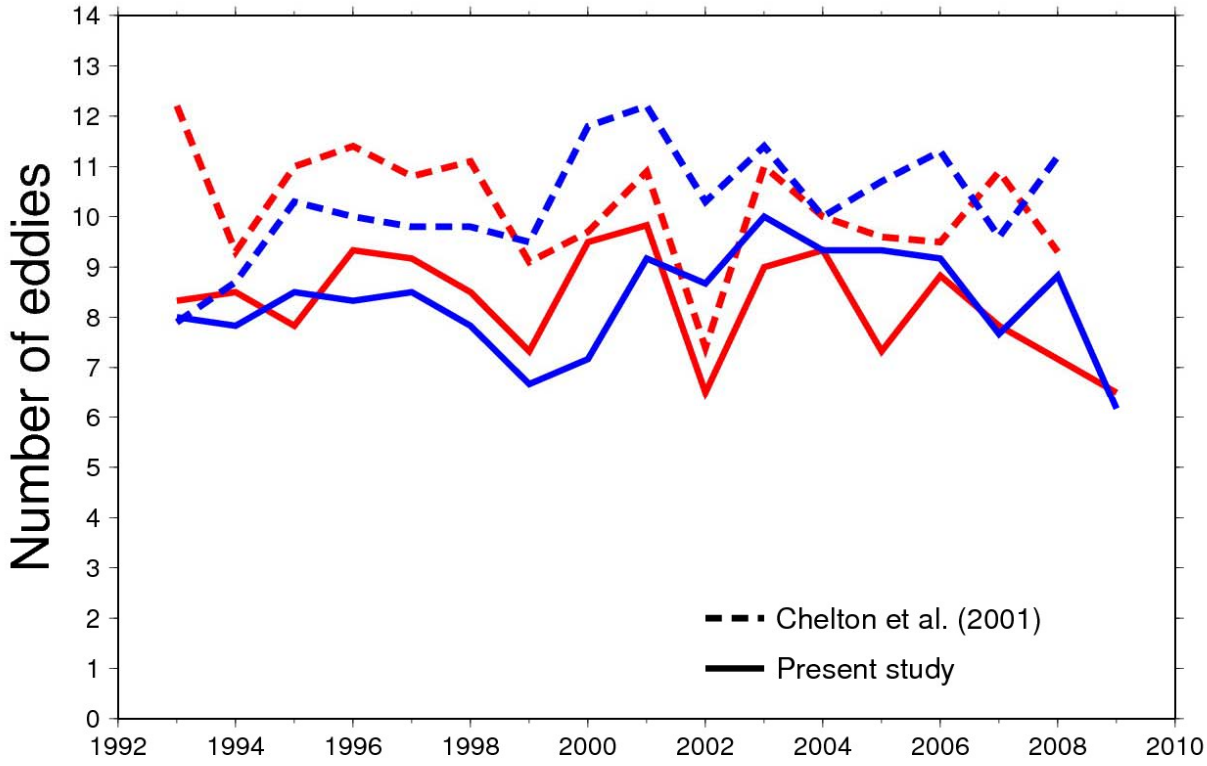

Figure 5.17: A comparison between the time series of the number of eddies identified by Chelton et al. (2011) and that identified in the present study. Warm and cold eddies are depicted by red and blue curves, respectively. The dashed curves are the time series from Chelton et al. (2011), and the solid curves are from the present study.

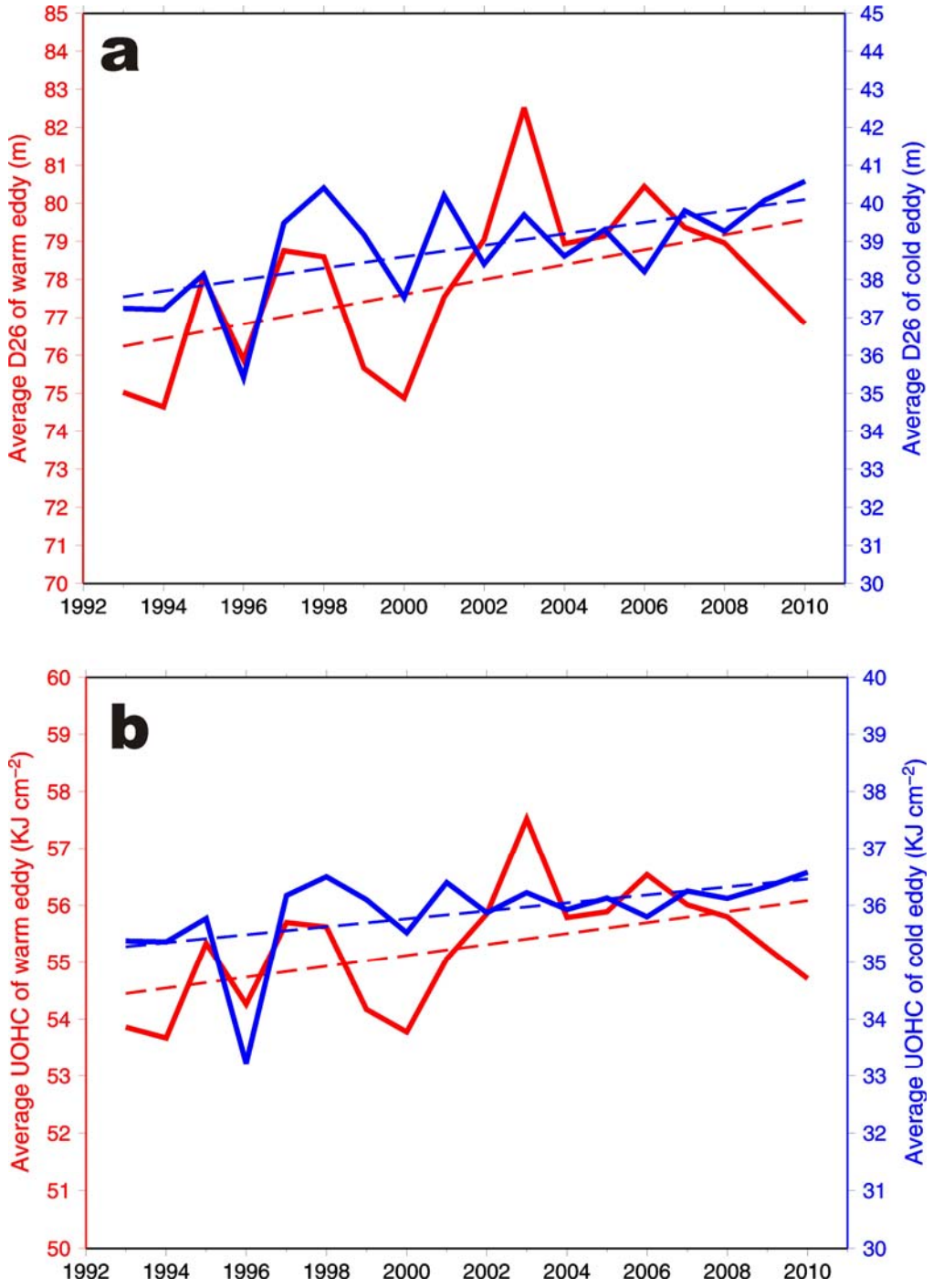

Figure 5.18: (a) Time series of the monthly average D26 of warm (red curve and left-axis) and cold (blue curve and right-axis) eddies. (b) The same as in (a), but for UOHC. It should be noted that the intervals for left and right axes are the same. The dashed lines depict the trends observed in the series.

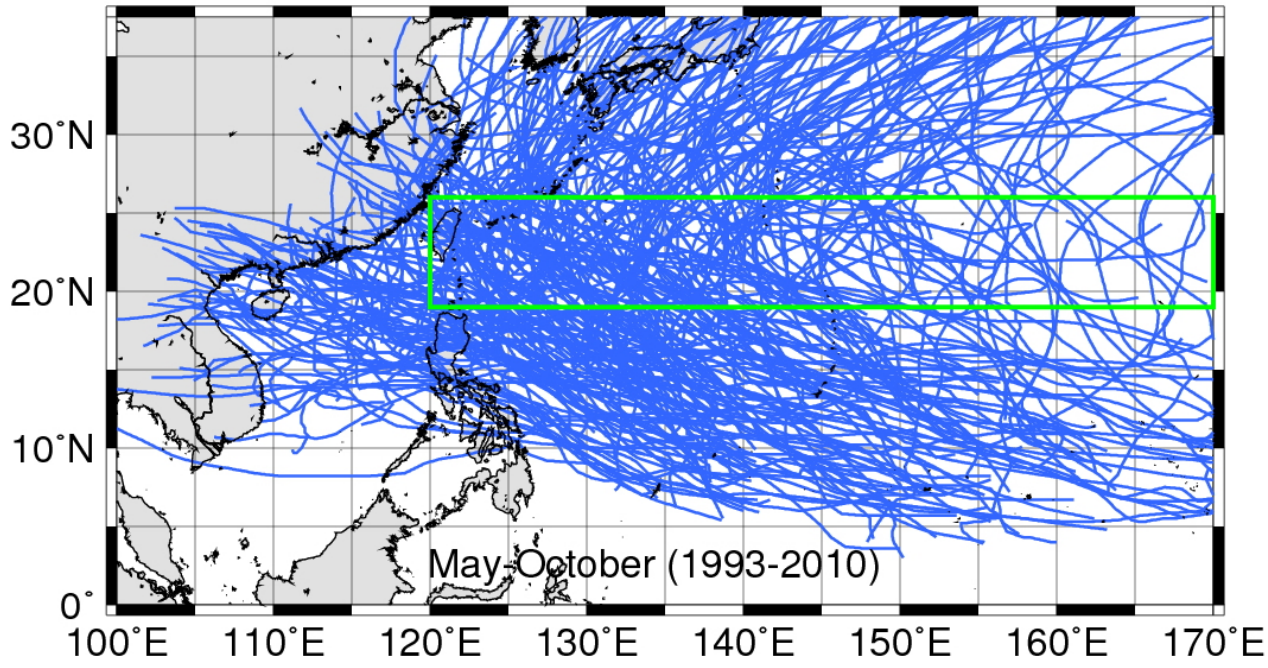

Figure 5.19: 18 years of typhoons with intensity ≧64 knots (i.e., Category 1) occurring in the western North Pacific during May to October from 1993 to 2010. The best track data are from JTWC, and the green box depicts the region of the SEZ.

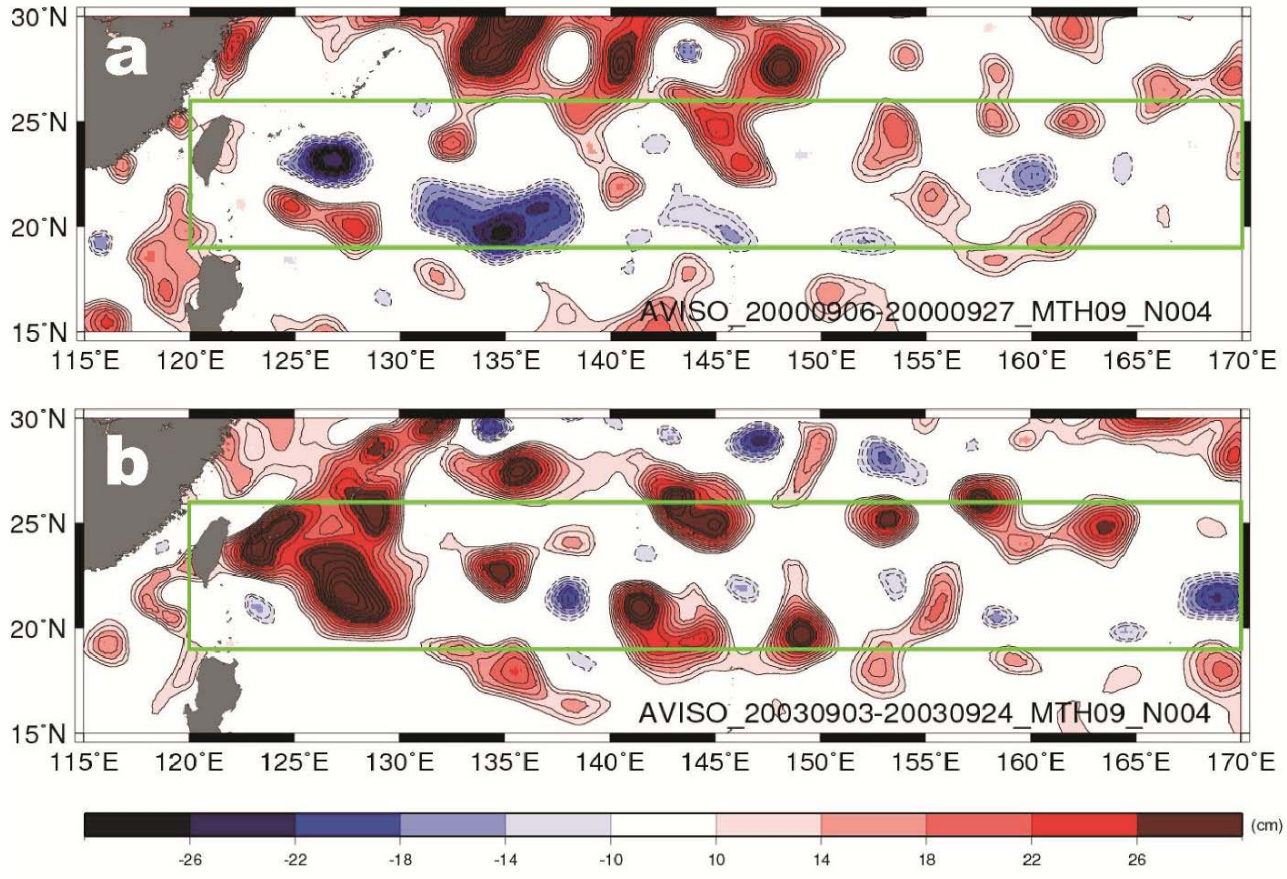

Figure 5.20: SSHA maps from (a) September 2000 and (b) September 2003.

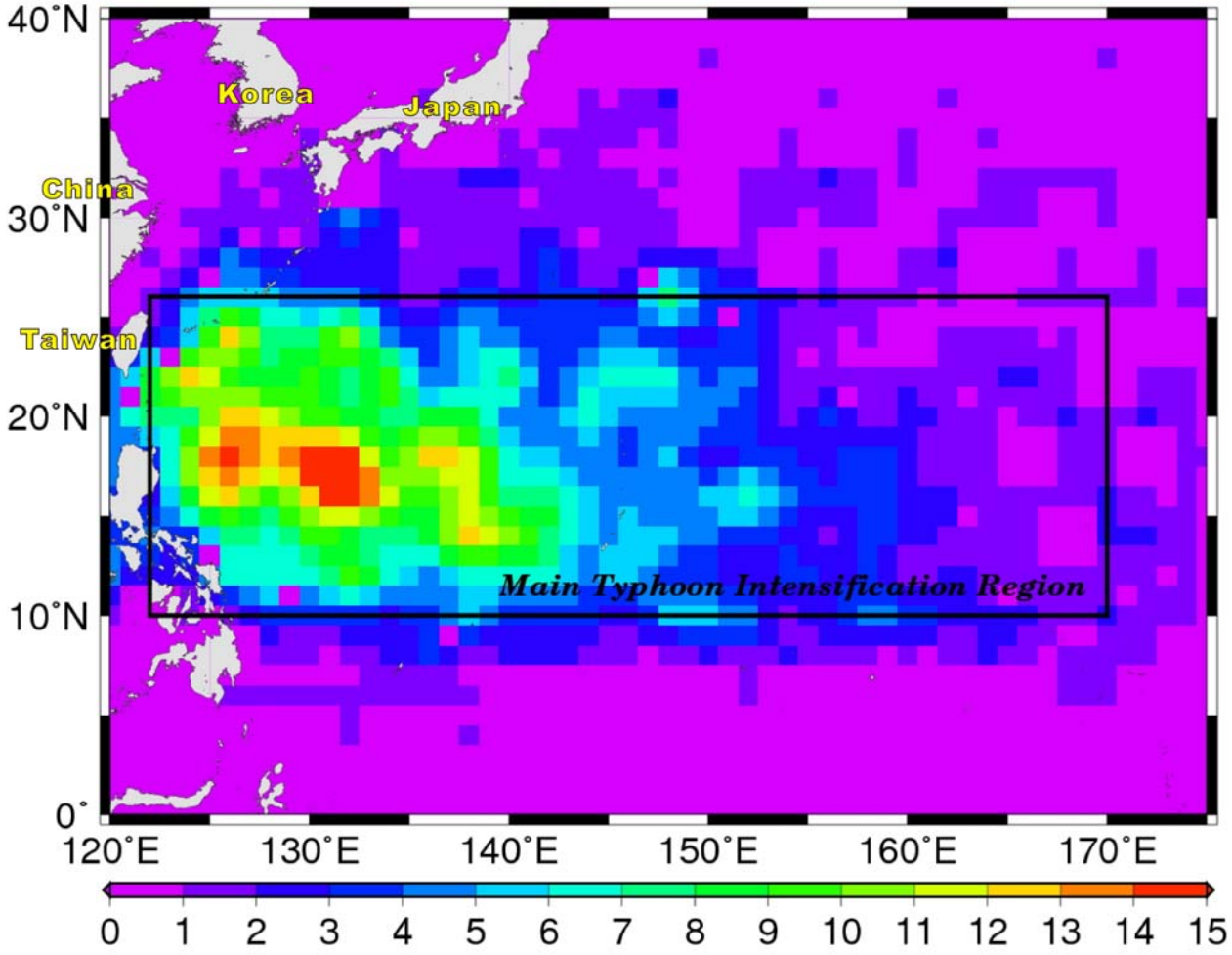

Figure 6.1: Geographical distribution of typhoon intensification in the western North Pacific Ocean. The map is calculated from the JTWC's 6-hour best track data from 1970-2008. Only the intensification segment (the first point of category 1 to peak) of the typhoon track is considered. The black box depicts the main typhoon intensification region, defined as 122-170°E, 10-26°N.

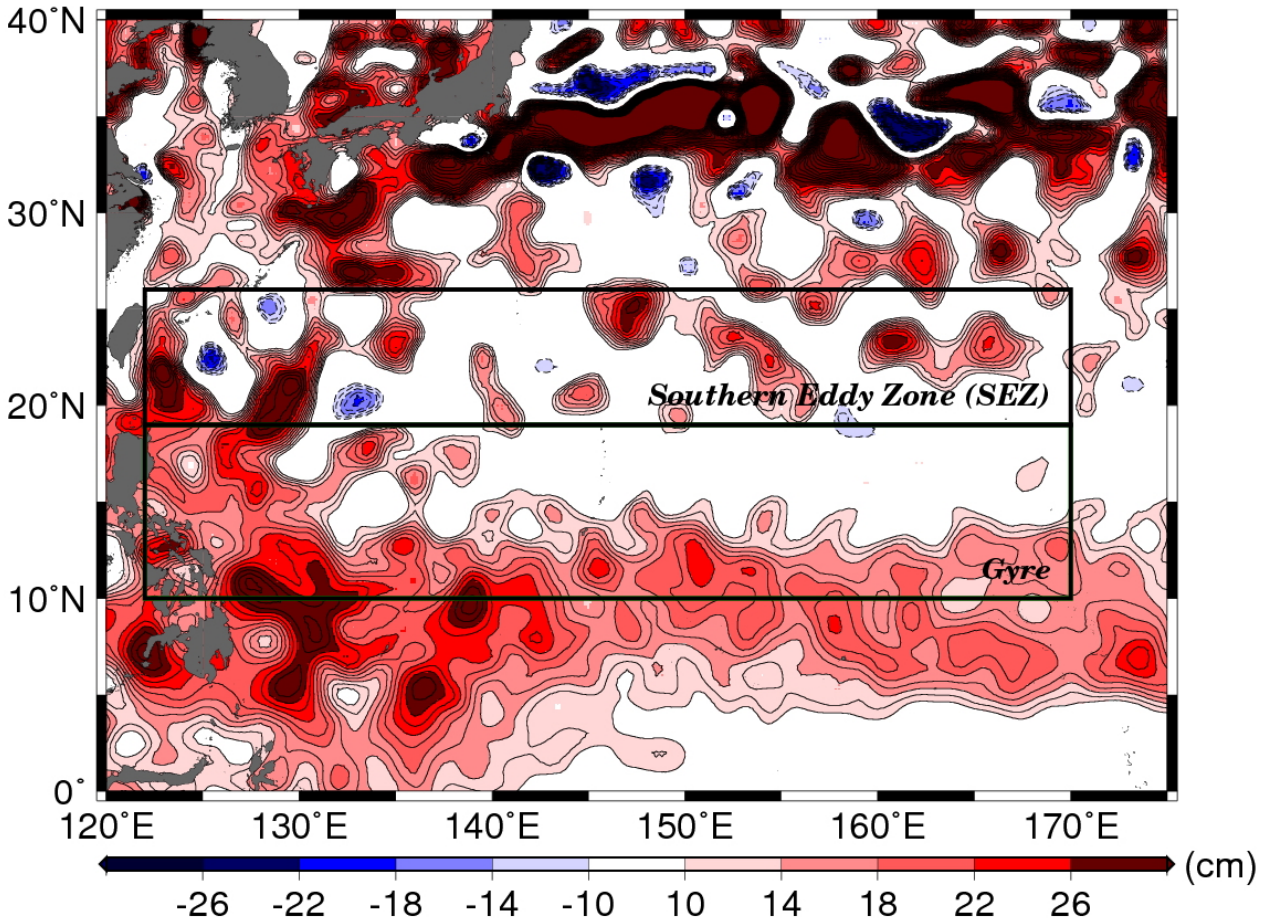

Figure 6.2: SSHA map from September 8, 2010 obtained from AVISO's DT Reference Series. The geographical locations of two sub-regions: Southern Eddy Zone (SEZ; 122-170°E, 19-26°N) and Gyre (122-170°E, 10-19°N) are depicted. The SSHA over +/-10 cm are shaded. The interval of the contour is 2 cm.

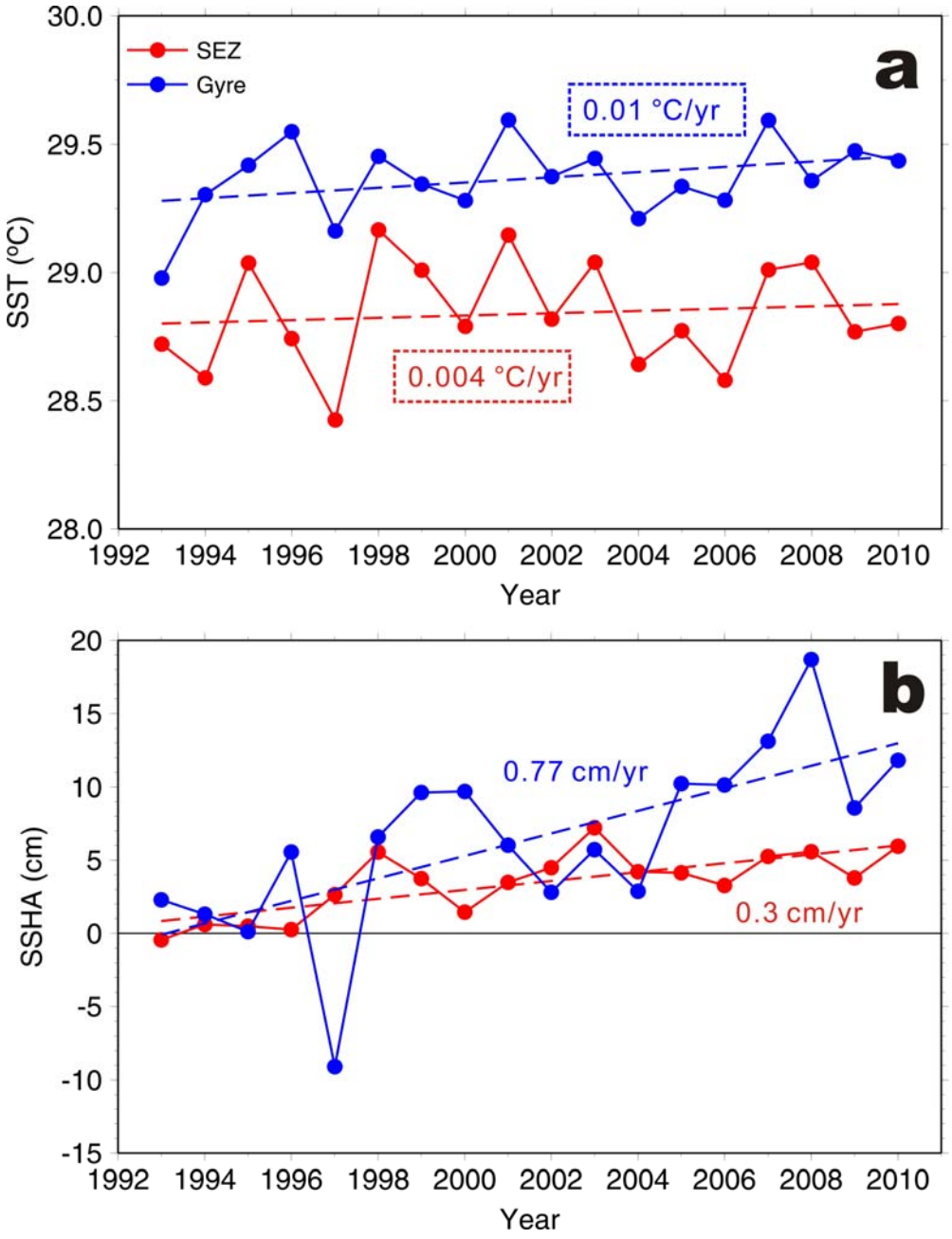

Figure 6.3: Time series of regional mean SST and SSHA. (a) Annual (June-October) regional mean SST for the SEZ (red dots) and Gyre (blue dots) between 1993 and 2010. The dashed lines are the linear trends calculated by the least squares fitting. The linear trend for the SEZ mean SST and Gyre mean SST are 0.004 and 0.01 °C yr^{-1}, respectively. (b) Same as (a), except for the SSHA. The linear trend for the SEZ mean SSHA and Gyre mean SSHA are 0.30 and 0.77 cm yr^{-1}, respectively. The horizontal line in (b) depicts the SSHA = 0 cm. The rate enclosed by the dashed box indicates the trend is less than 99% significant. Otherwise, the trend shown is at 99% significance level.

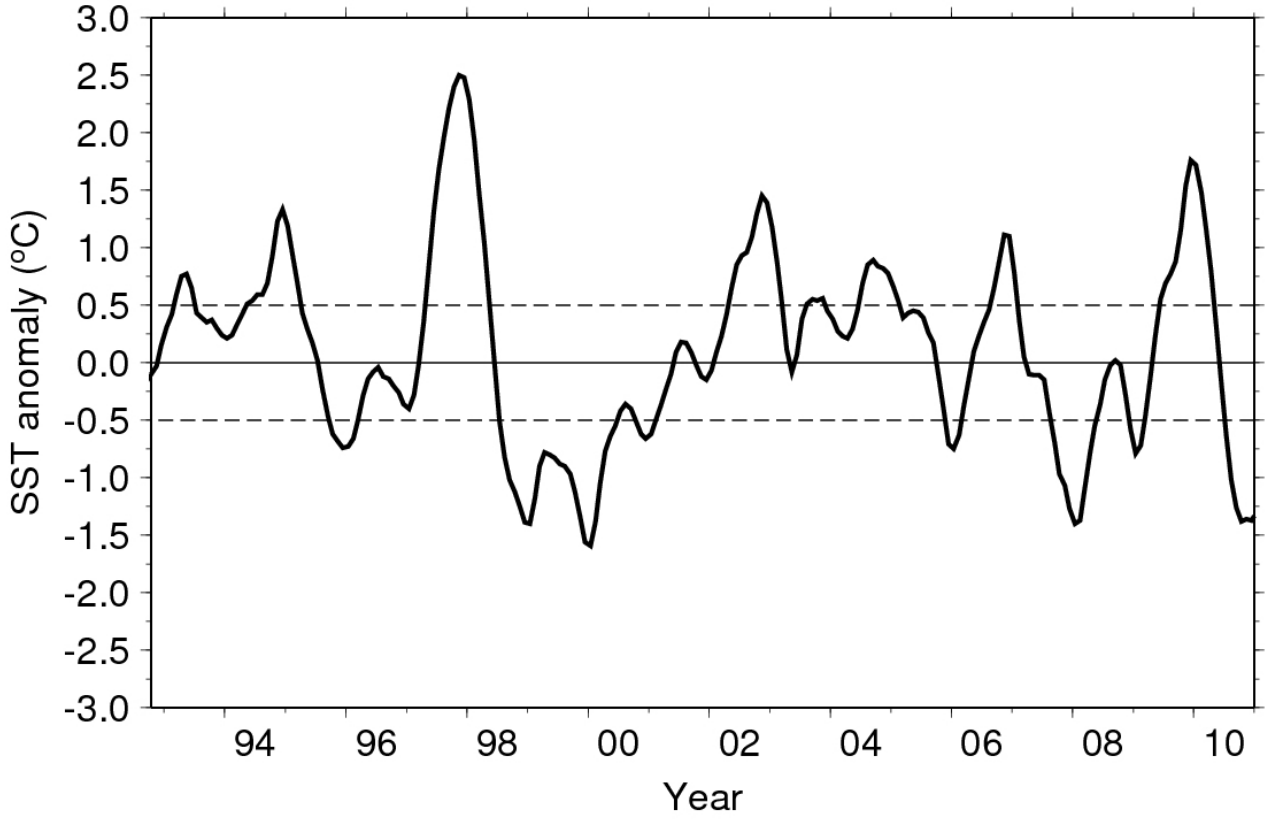

Figure 6.4: Ocean Niño Index (ONI) from NOAA Climate Prediction Center. The ONI is based on the SST anomaly in the Niño 3.4 region. A minimum of five consecutive months with SST anomaly of +/-0.5°C is considered an El Niño/ La Niña. The three horizontal lines depict the SST anomaly of +0.5, 0 and -0.5 °C.

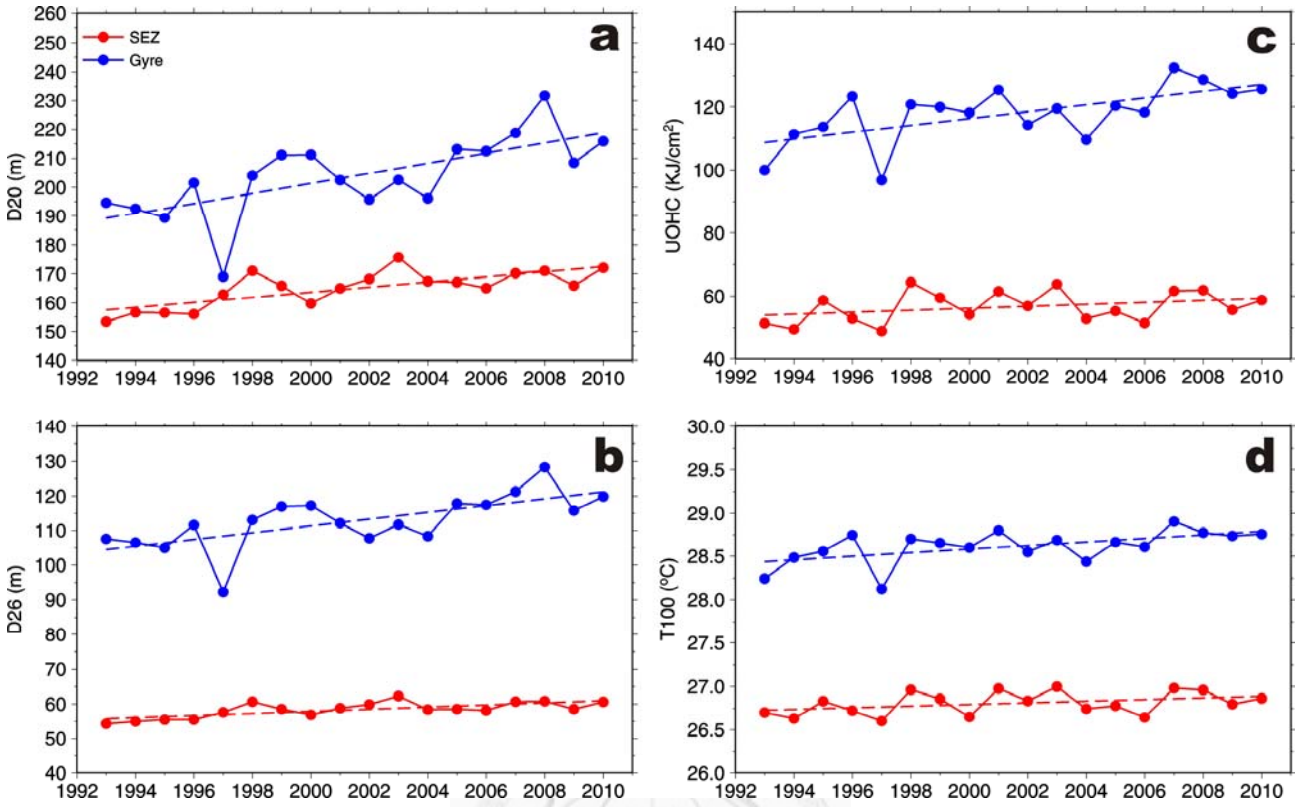

Figure 6.5: Time series of satellite-derived (a) D20, (b) D26, (c) UOHC, and (d) T100 during the 18-year (1993-2010) study period. All of the parameters are expressed by annual (June-October) regional means averaged over the SEZ (red dots) and Gyre (blue dots). The dashed lines show the linear trends calculated by the least squares fitting. The detailed changes in these four parameters are summarized in Tables 6.1 and 6.2.

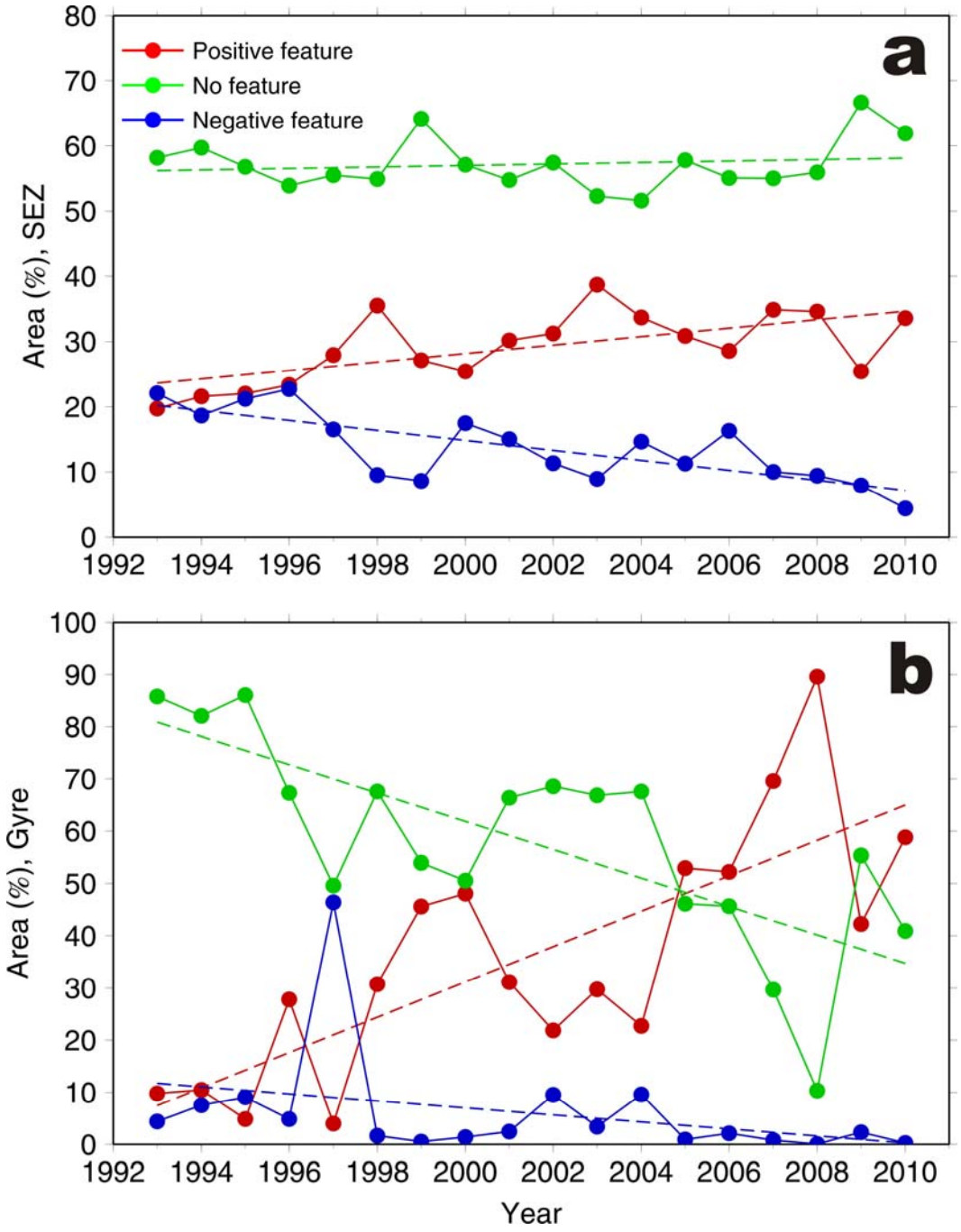

Figure 6.6: Percentage of total areas of oceanic features. Time series of annual percentage of total areas of positive (SSHA $\geqq$10 cm; red dots), negative (SSHA $\leqq$10 cm; blue dots) and no (SSHA within $\pm$10 cm; green dots) features in the (a) SEZ and (b) Gyre during the 18-year (1993-2010) study period. The dashed lines represent the linear trends. The detailed changes in the percentage of total area of the ocean features are summarized in Tables 6.3 and 6.4.

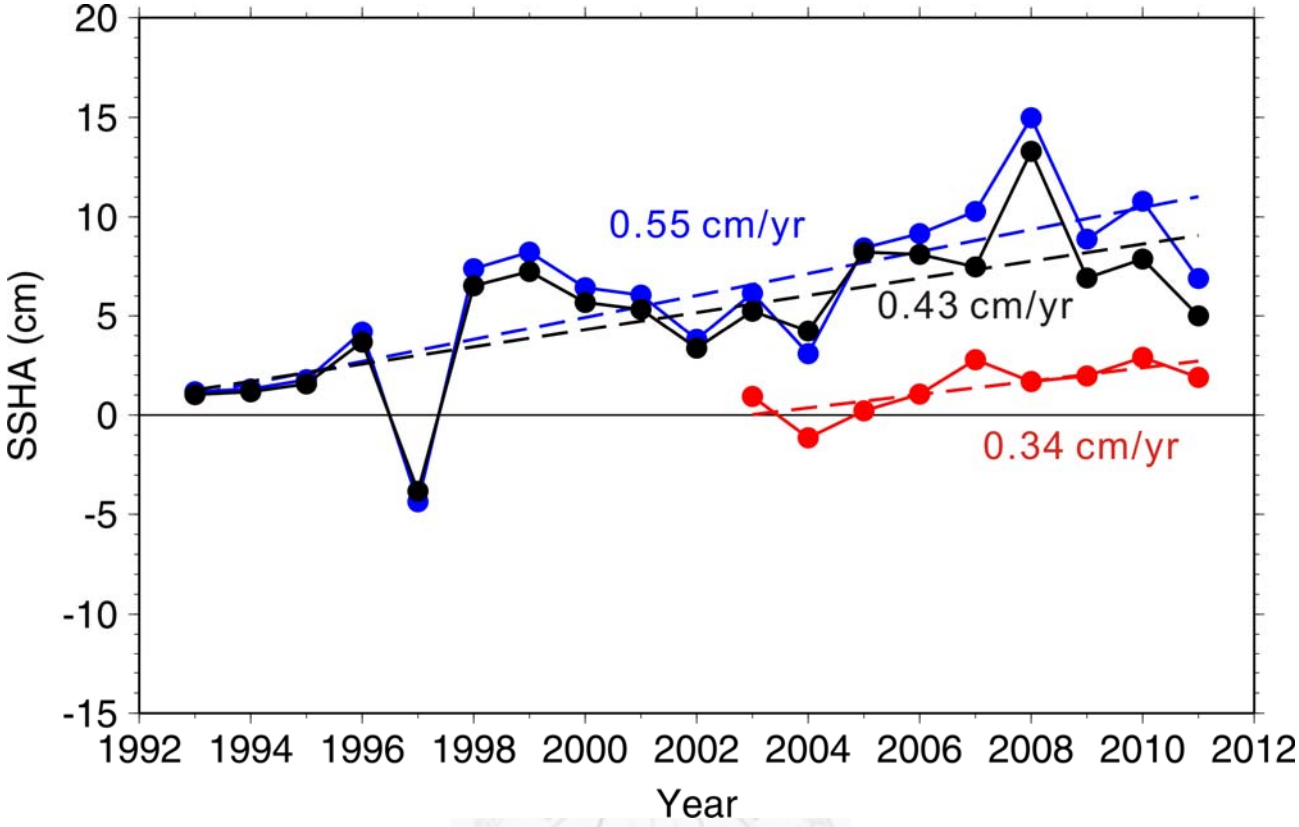

Figure 6.7: Time series of annual EWT (red curve), SSHA (blue curve) and SSHA corrected by EWT (black curve). The domain for these time series is 122-150°E, 10-26°N. In addition, the rates of changes are also shown.

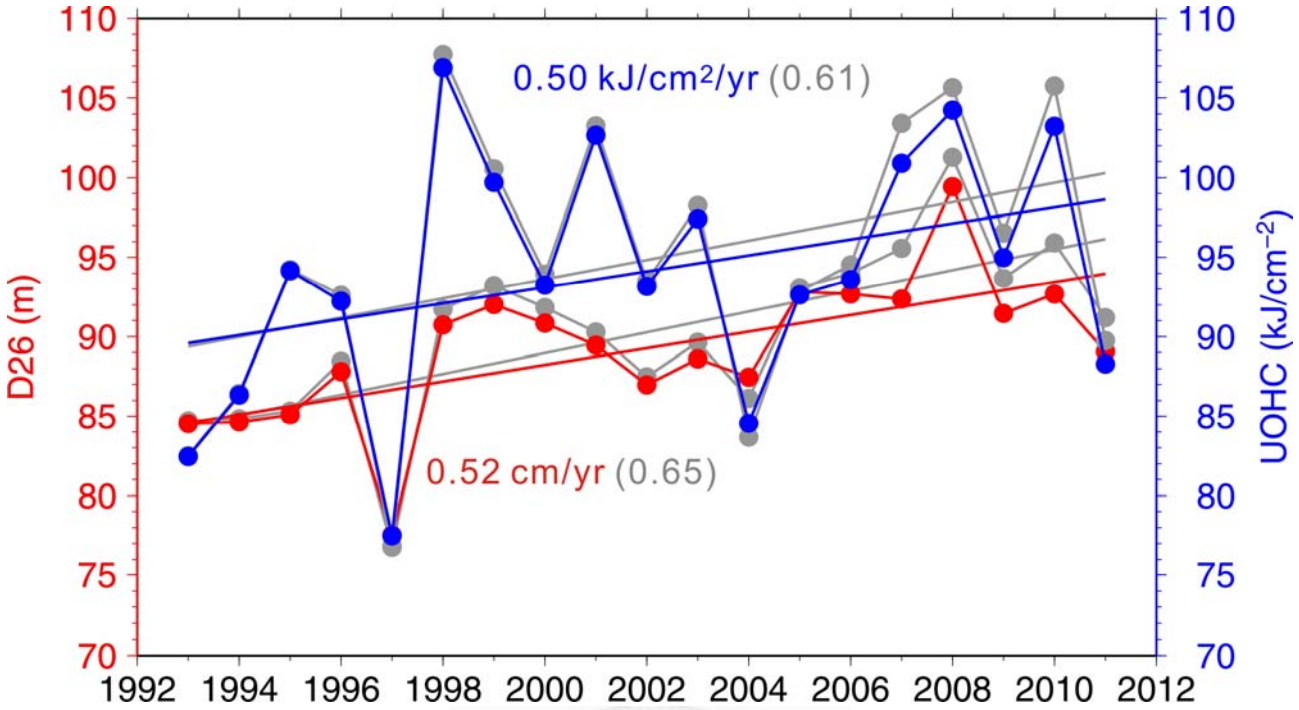

Figure 6.8: Time series of annual D26 (in red) and UOHC (in blue) with the mass correction for 1993-2010. The corresponding grey curves are the original D26 and UOHC without mass correction. The rates of changes are also shown.

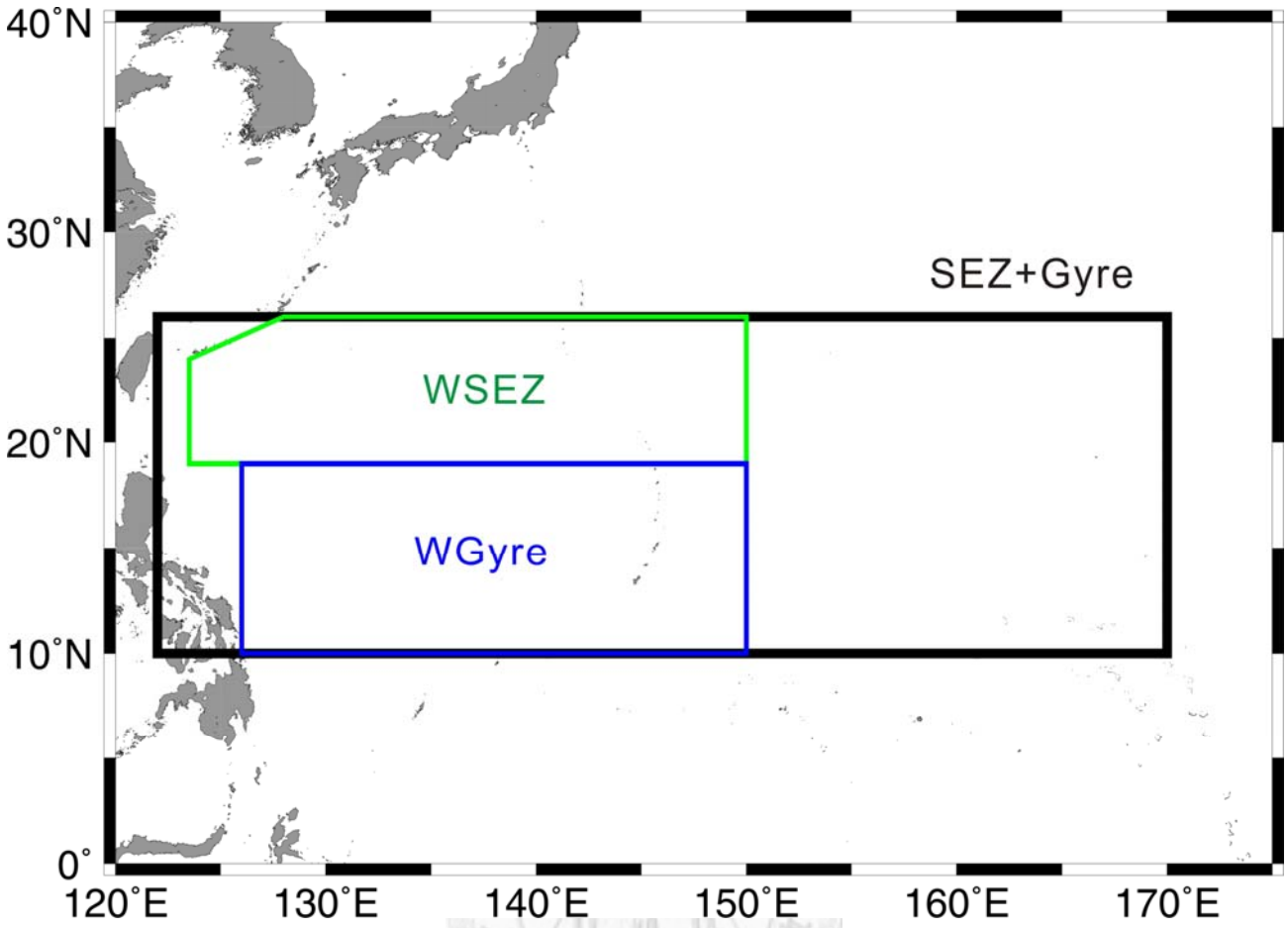

Figure 6.9: Three extra domains: 1) SEZ+Gyre, depicted by black box; 2) the western SEZ (WSEZ), depicted by green box; and 3) western Gyre (WGyre), depicted by blue box.

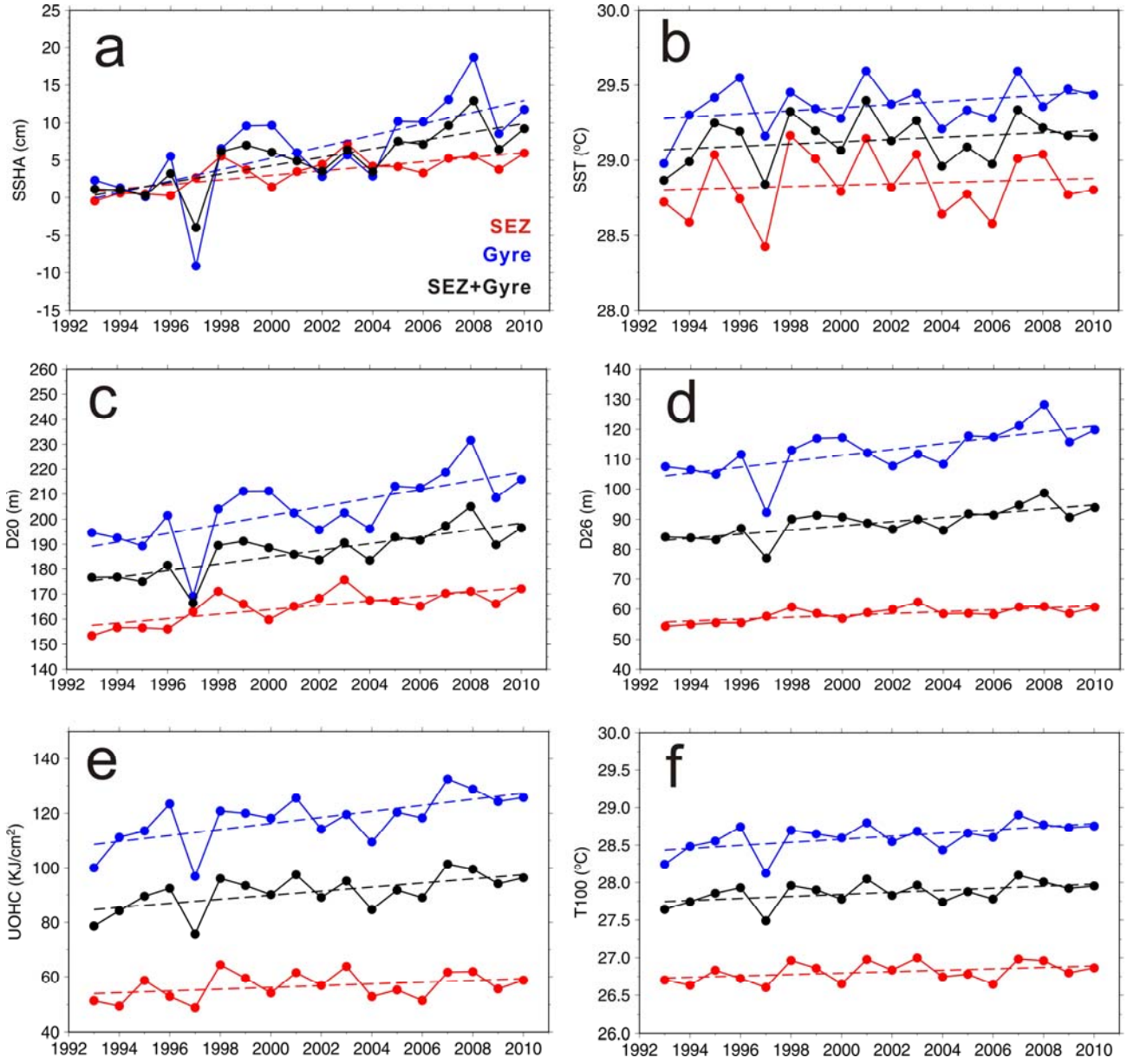

Figure 6.10: Comparison between results of SEZ (red), Gyre (blue) and SEZ+Gyre (black) for (a) SSHA, (b) SST, (c) D20, (d) D26, (e) UOHC, and (f) T100.

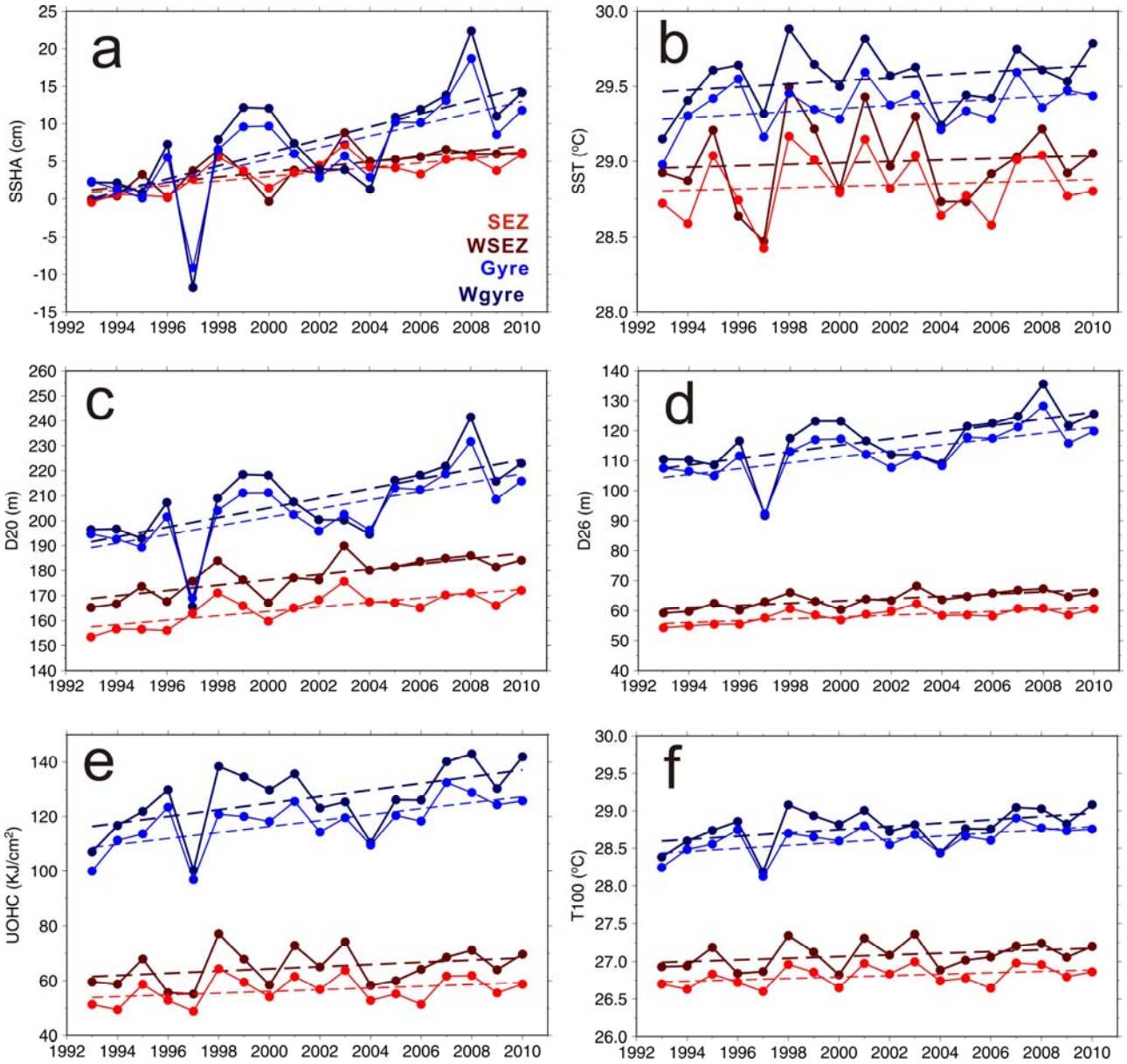

Figure 6.11: Comparison between results of SEZ (red), WSEZ (dark red), Gyre (blue) and WGyre (dark blue) for (a) SSHA, (b) SST, (c) D20, (d) D26, (e) UOHC, and (f) T100.

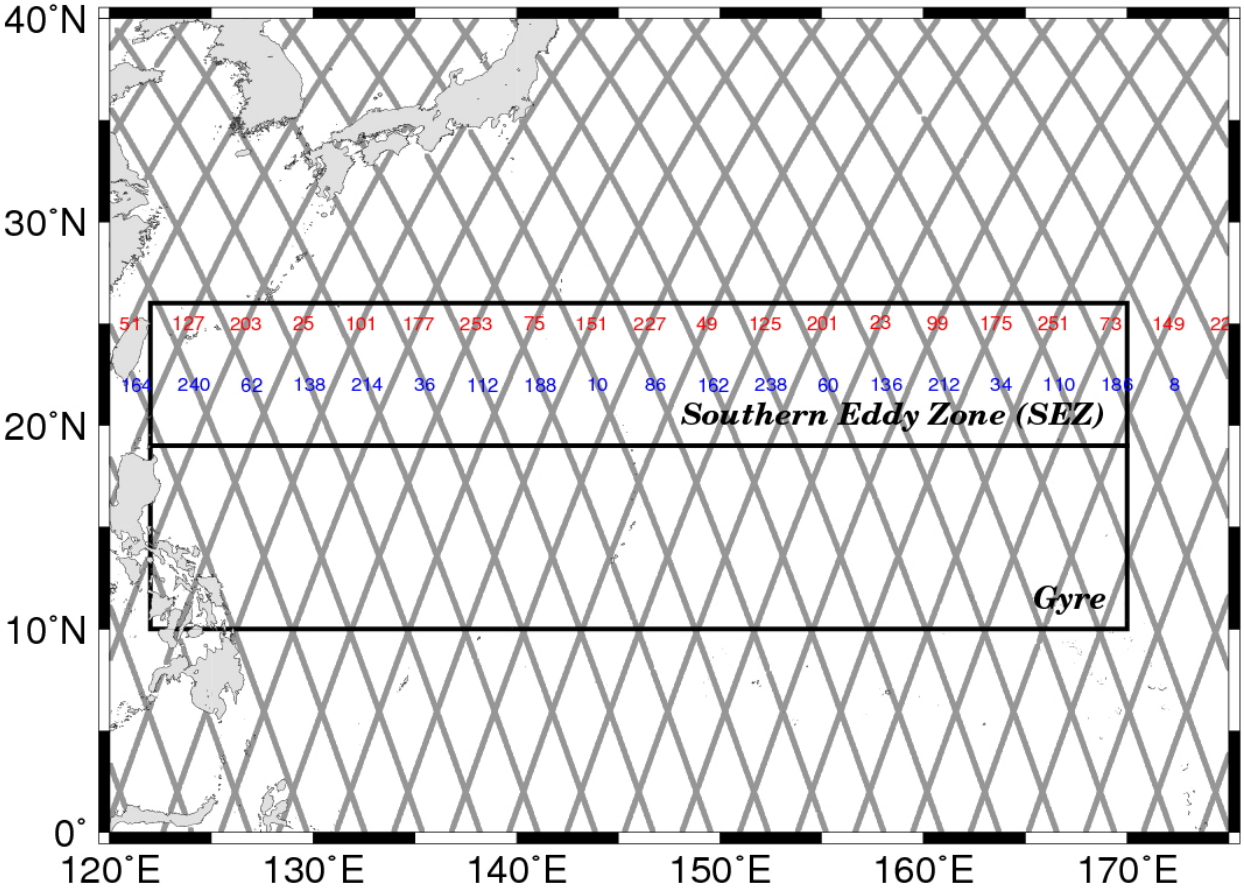

Figure 6.12: The regular ground tracks of TOPEX/Poseidon, Jason-1 and Jason-2. The pass numbers are shown; red and blue depict ascending and descending pass numbers, respectively.

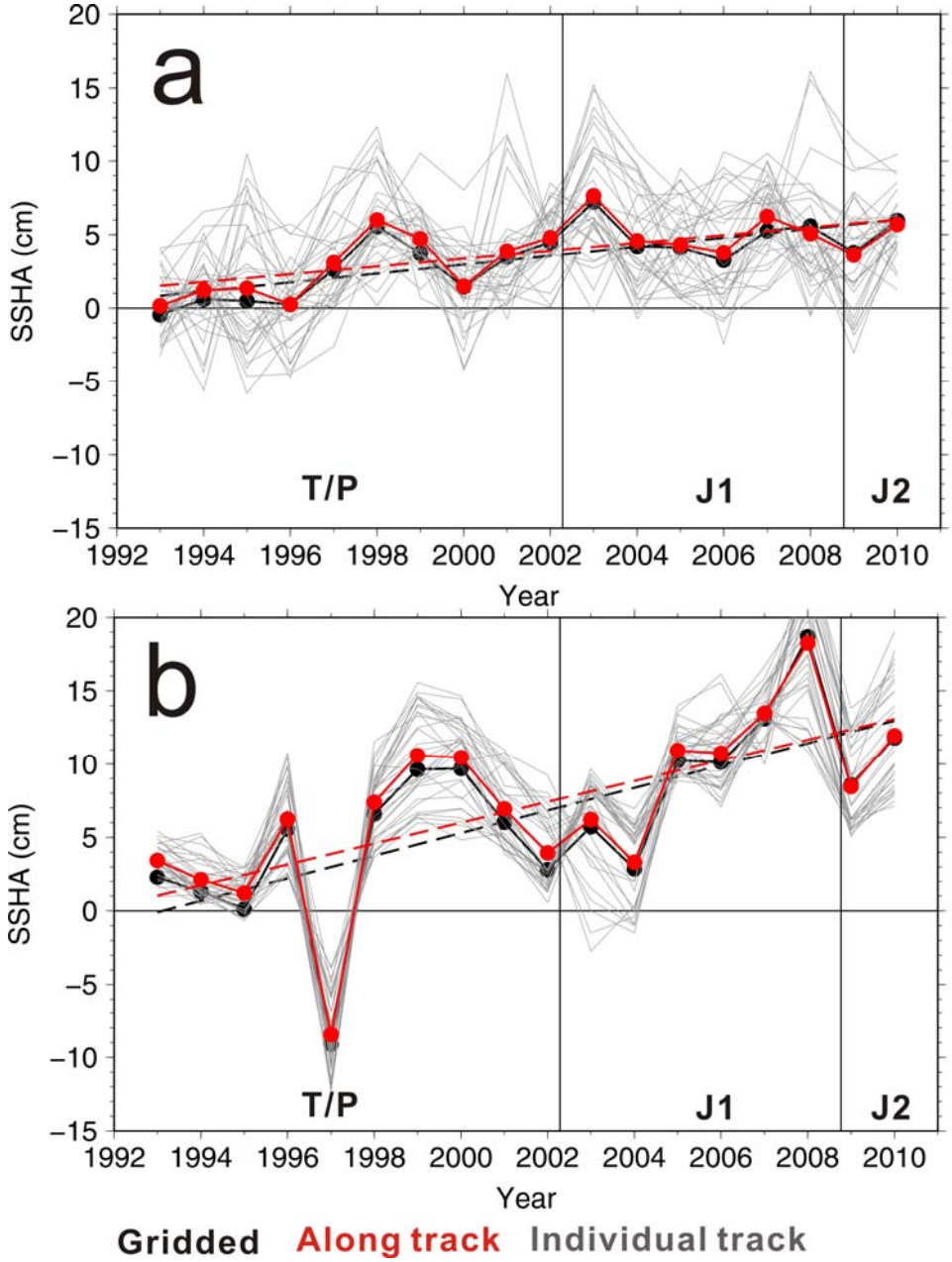

Figure 6.13: Annual SSHA time series calculated from the 32 regular passes and from gridded SSHA field for (a) the SEZ and (b) Gyre. Black curve depicts the time series computed by gridded SSHA, red curve depicts by along track SSHA, and grey curves depict by the 32 individual passes. T/P's observation is from 1993 to 2002, J1's from 2002 to 2008, and J2's from 2008 to 2010.